A MODULAR APPROACH TO BISTABLE MAGNETS: FROM EXTENDED ARCHITECTURES TO MOLECULES

A Dissertation

by

ANDREW JAMES BROWN

Submitted to the Office of Graduate and Professional Studies of
Texas A&M University
in partial fulfillment of the requirements for the degree of

DOCTOR OF PHILOSOPHY

Chair of Committee,	Kim R. Dunbar
Committee Members,	Timothy Hughbanks
	Marcetta Darensbourg
	Donald G. Naugle
Head of Department,	Francois Gabbai

December 2015

Major Subject: Chemistry

ABSTRACT

This dissertation describes structural and magnetic studies of three-dimensional Prussian Blue analogs (PBAs), one-dimensional single chain compounds, and discrete “zero-dimensional” molecules. All compounds that were studied are members of a large class of materials known as molecular nanomagnets which exhibit a barrier to spin reversal due to magnetic anisotropy which can surpass the superparamagnetic limit of classical materials. Single-molecule magnets (SMMs) which can exhibit long-lived relaxation times for their magnetic states are the prototype for the field and are poised for implementation in next generation nanoelectronic devices. The goal of this dissertation research was to determine sources of anisotropy in the quest for interesting magnetic properties.

Prussian Blue, $Fe^{III}_4[Fe^{II}(CN)_6]_3 \cdot 16H_2O$, exhibits ferromagnetic coupling with a Curie temperature of approximately 5 K. Different synthetic attempts historically yield slightly different formulations of the compound. We have revisited the structural analysis of this compound and have obtained the first crystal structure of Turnbull’s Blue, $KFe^{III}[Fe^{II}(CN)_6]$.

Capping ligands can reduce the dimension of PBAs while retaining their interesting properties. This strategy is presented by the reactions of tptz (tptz = 2,4,6-tris(2-pyridyl)-1,3,5-triazine) complexes of Cu(II), Co(II), and Fe(III) with $[M^V(CN)_8]^{3-}$ (M = Mo, W) anions which led to three new heterobimetallic chains based on ladder- or square structural motifs. The compound $\{[Fe^{III}(tptz)W^V(CN)_8] \cdot 2CH_3OH\}_\infty$ exhibits weak out-of-phase AC signals at low temperature, which indicates single-chain magnet behavior.

The blocking of all open coordination sites results in discrete molecules with the potential for SMM behavior. Underexplored transition and lanthanide metals with specific ligand fields afford single-ion anisotropies providing an easy-axis for the magnetization. In this regard, the new trigonally capped titanium(III) precursor, $[Et_4N][Tp^*Ti(CN)_3]$ (Tp* = tris(3,5-dimethylpyrazolyl)borohydride), was prepared. Concomitant hydrolysis, oxidation, and coordination of this titanium precursor affords a family of trinuclear carboxylate compounds, $\{(Tp^*Ti^{IV})(\mu_2\text{-}OAc)_2(\mu_2\text{-}O)M(\mu_2\text{-}O)(\mu_2\text{-}OAc)_2(Ti^{IV}Tp^*)\}$ (M = Cr^{III}, Mn^{II}, Co^{II}), with interesting magnetic properties.

The use of the equatorially coordinating bis(trimethylsilyl)amide ligand, $[N(SiMe_3)_2]^-$, enforces a trigonal pyramidal framework for the stabilization of prolate lanthanide SMMs. The compounds, $[Li(THF)_4]\{Ln^{III}[N(SiMe_3)_2]_3Cl\}$ (Ln = Er, Tm), exhibit single-molecule magnet behavior with the erbium analog showing magnetic hysteresis up to 3 K.

ACKNOWLEDGEMENTS

First and foremost, I would like to thank my advisor, Prof. Kim R. Dunbar for all of the years of mentorship and support. I am very grateful for her direction and patience in allowing me to develop, learn my field of research, and create my own research ideas. Her guidance has molded me into the chemist I am today. I feel fully prepared to tackle the next challenges I will face in life.

I would like to extend my gratitude to my committee members: Prof. Timothy Hughbanks, Prof. Marcetta Darensbourg, and Prof. Donald Naugle. Thank you for the encouragement and insightful discussions.

I would like to acknowledge all the past and current members of the Dunbar group that helped me grow scientifically and in friendship. They include Dr. Silvia Gómez-Coca, Dr. Maria Ballesteros Rivas, Dr. Hanhua Zhao, Dr. Mohamed Saber, Dr. Dawid Pinkowicz, Dr. Helen Chifotides, Dr. Yuan-zhu Zhang, Dr. Eric Reinheimer, Dr. Ian Giles, Dr. Heather Southerland, Dr. Zhongyue Zhang, Dr. Bruno Pena, Dr. Zhanyong Li, Dr. Nazario Lopez, as well as Amanda David, Ryan Coll, Jill Ellenbarger, Francisco Birk, David Kempe, Sayan Saha, Codi Sanders, Toby Woods, Kelsey Schulte, Haomiao Xie, and Xuan Zhang. Thanks for all the memories!

Finally, I would like to thank my mother and father for their continual advice in directing my future. Making them proud is my greatest accomplishment; the thought of which has propelled me to carry on even in times of doubt.

TABLE OF CONTENTS

LIST OF FIGURES

FIGURE Page

FIGURE Page

FIGURE Page

FIGURE Page

FIGURE Page

LIST OF TABLES

CHAPTER I

INTRODUCTION

Magnets in Nature and Society

One of the most interesting aspects of magnets is their use in nature. Migratory animals, or those that return to a similar location for nesting or breeding *e.g.*, birds, fish, insects, lobsters, and turtles are known to use the earth's magnetic field for magnetic homing.[1-6] For example, tiny concentrations of magnetite have been discovered in the beaks of pigeons. This iron oxide based magnet has been shown to communicate with the pigeon's brain through the ophthalmic branch of the trigeminal nerve.[7] Severing this nerve revealed that the pigeons lost their ability to recognize changes in an external magnetic field. Another interesting experiment involved displacing spiny lobsters from their home to a test location and monitoring the animal's progress on returning home.[5] In this experiment, the spiny lobsters were deprived of all orientation cues during transport. The eyes of the lobsters were covered with rubber caps. The boat was driven in a circuitous manner. The transport containers were even lined with magnets, some hanging from a string and swinging in spontaneous directions. Phenomenally, the spiny lobsters, on average, returned home.

Humans have also taken advantage of the earth's magnetic field, dating back as far back as 1100 A.D when the Chinese observed the attraction of iron to loadstone and made the first compass. Magnets are now ubiquitous in society. Nearly all electronics, motors, and generators extensively utilize magnets in their performance. Cosmetic, entertainment, transportation, and many other industries also revolve around the use of magnets. In 2013, the global permanent magnet market exceeded $15 billion in revenue and is expected to grow to over $30 billion by 2018 with a compound annual growth rate of 11.2%.[8,9] This overarching topic of this dissertation will be molecular nanomagnets - the smallest-sized magnets with potential for nano-scale device fabrication.

Basics of Magnetism

The foundation of magnetism is the presence of unpaired electrons in a material. The electrons exhibit spin and orbital motions, both are vector quantities which give rise to a magnetic moment via the vector sums of all of the individual electrons in an atom. In molecules, the magnetic moment is a function of the bonding and interactions between the atoms. In an externally applied magnetic field, electrons exhibit two types of responses. Paired electrons in bonds or within occupied molecular or atomic orbitals give rise to a diamagnetic response which causes a small temperature independent repulsion of the magnetic field. Unpaired electrons, on the other hand, in non-filled molecular or atomic orbitals will exhibit a paramagnetic response, in which the atom or molecule is attracted to a magnetic field. The vector sum of these components including other contributions, such as temperature independent paramagnetism, lead to the magnetic moment of the atom, molecule, or network solid, which is measured indirectly. The magnetic moment induced in a sample by an applied magnetic field is measured by the quantity known as magnetic susceptibility, χ. This dimensionless proportionality constant describes the magnetization, M, induced by an applied magnetic field, H, in a sample according to the equation:

$$\chi = \frac{\mathrm{M}}{\mathrm{H}}, \text{where } \chi = \chi^{\mathrm{P}} + \chi^{\mathrm{D}} \qquad \textbf{Equation 1.1}$$

The quantities χ^P and χ^D represent the paramagnetic and diamagnetic susceptibilities, respectively. Equation 1.1, is valid in the application of small external fields or high temperature. χ can be described in terms of the gram susceptibility:

$$\chi_g = \frac{\chi}{d} \qquad \textbf{Equation 1.2}$$

where d is the density of the material. The gram susceptibility can be converted to the molar susceptibility:

$$\chi_M = \chi_g M_W \qquad \textbf{Equation 1.3}$$

where M_W is the molecular weight of the material. Unless otherwise states, all magnetic susceptibilities in this dissertation are given as molar susceptibilities. The effective magnetic moment, μ_{eff}, of the material is then related by the following equation:

$$\mu_{eff} = \sqrt{\frac{3k_B\chi_M T}{N\mu_B{}^2}} \qquad \textbf{Equation 1.4}$$

where μ_{eff}, k_B, T, N, and μ_B represent the effective magnetic moment, the Boltzmann's constant, the temperature in Kelvin, Avogadro's number, and the Bohr magneton, respectively (in CGS units of the physical quantities).

In 1932, Van Vleck proposed an equation that correlates the energy of the different thermally populated states in a molecule with the macroscopic magnetic susceptibility. The equation applies in the limits of low fields and high temperatures, and is based on an expansion of exponential sums weighted according to the Boltzmann distribution law:

$$\chi = \frac{\mathrm{N}\sum_{\mathrm{n}}\left(\frac{\mathrm{E}_{\mathrm{n}}^{(1)2}}{\mathrm{kT}} - 2\mathrm{E}_{\mathrm{n}}^{(2)}\right)\exp\left(-\frac{\mathrm{E}_{\mathrm{n}}^{(0)}}{\mathrm{kT}}\right)}{\sum_{\mathrm{n}}\exp\left(-\frac{\mathrm{E}_{\mathrm{n}}^{(0)}}{\mathrm{kT}}\right)} \qquad \textbf{Equation 1.5}$$

where $\mathrm{E}_{\mathrm{n}}^{(0)}$ is the energy of level n in zero field, and $\mathrm{E}_{\mathrm{n}}^{(1)}$ and $\mathrm{E}_{\mathrm{n}}^{(2)}$ are the first- and second-order Zeeman coefficients, respectively. The Van Vleck formula allows for modeling of magnetic susceptibility, which is the basis for understanding all magnetic materials.[10]

Molecular Nanomagnets

Magnetic materials exhibit four different types of behavior, namely paramagnetic, ferromagnetic, antiferromagnetic, and ferrimagnetic. Paramagnets have no net magnetization in the absence of an external magnetic field. This is because thermal motion randomly orients all the spins in the material. There is no correlation between adjacent spins and no energy barrier to reorienting the direction of the spin, or if there is, the temperature is sufficiently high to overcome these types of interactions. However, when thermal energy becomes insufficient, adjacent spins can align. If this alignment is cooperative, the spins will orient their individual moments parallel to one another and in the same direction. Such a phenomenon is known as ferromagnetic interaction. In the case where the alignment of spins occur in an antiparallel fashion, where the adjacent spins are pointing in exactly opposite directions, the interaction is antiferromagnetic. This pairing of electrons is akin to a chemical bond and is attributed to orbital overlap between the orbitals housing the separate spins. If the individual spin moments are of equal magnitude, there is an overall cancellation of the spin and the ground state is nonmagnetic. If the magnitude of adjacent spins are not the same and the interaction is antiferromagnetic, then the behavior is said to be ferrimagnetic. These interactions can be observed in zero-dimensional molecules through three-dimensional compounds, which is different than magnetic ordering. In a network solid, if these pairwise interactions extend over a long-range, then there can be magnetic ordering. The spins in these materials are encompassed by domains, or regions within the material where all spins are strongly coupled. Domains are determined by a magnetocrystalline anisotropy and an exchange energy. At a critical temperature, the thermal energy will equate to the magnetic energy, which gives rise to ferro- or antiferromagnetic ordering. This temperature is known as the critical temperature. The critical temperature for a ferromagnetic material is known as the Curie temperature, T_c. The critical temperature for an antiferromagnetic material is known as the Neel temperature, T_N.

The interaction between spins in molecular materials is attributed to a "communication" between spin carriers by direct or superexchange mechanisms as described by the Goodenough Kanamori rules.[11,12] The latter involves spin polarization through a diamagnetic bridge. Both mechanisms require that the total wavefunction is antisymmetric relative to the interacting pair of electrons.[13] The strength of the interaction is quantified by the Heisenberg-Dirac-VanVleck effective exchange Hamiltonian, equation 4.4:

$$\widehat{\mathrm{H}}_{EX} = -2 \sum_{i<1}^{i,j\in N} J_{ij}\, \overrightarrow{S_i} \cdot \overrightarrow{S_j} \qquad \textbf{Equation 1.6}$$

where J_{ij} is the exchange coupling constant and S is the spin operator for sites i and j. Jij is positive for ferromagnetic interactions between spins i and j and negative for antiferromagnetic interactions. The energies from the exchange Hamiltonian can be plugged into the Van Vleck equation to model the magnetic susceptibility. The product of magnetic susceptibility with temperature plotted vs temperature (χT vs T) affords a qualitative evaluation of which form of interaction is predominate, Figure 1.1.

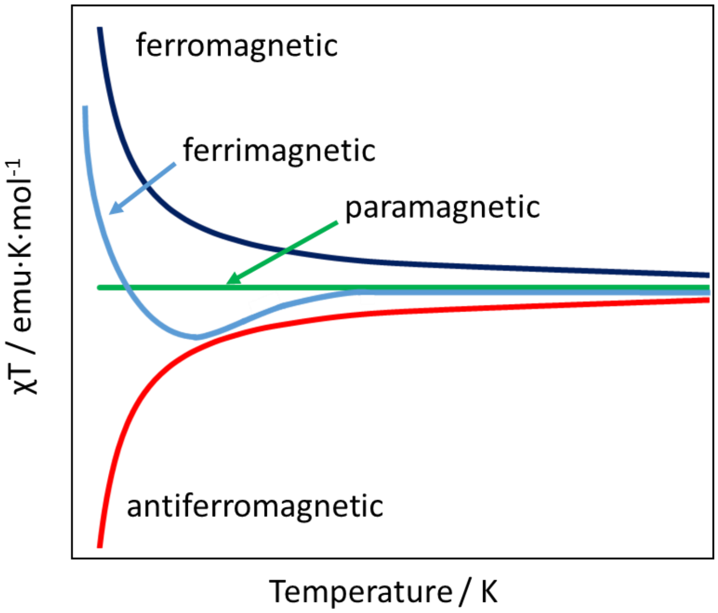

Figure 1.1 χT vs T plot depicting general behaviors in magnetic materials.

At high temperatures, where no interactions between spins are present and the material behaves as a simple paramagnet, the magnetic susceptibility can be determined by the Curie-Weiss law, equation 1.7:

$$\chi = \frac{T}{C - \theta} \qquad \textbf{Equation 1.7}$$

where T is the temperature, θ is the Weiss constant, and C is the Curie constant described by equation 1.8:

$$C = \frac{N_A g^2 \mu_B^2 S(S+1)}{3k_B}$$ **Equation 1.8**

where N_A is Avogadro's number, g is the Landé g-factor, μ_B is the Bohr magneton, S is the spin, and k_B is the Boltzmann constant. The Weiss constant accounts for deviation from Curie law between adjacent/pairwise spins. The value is extrapolated as the x-intercept using the slope of high temperature data in χ^{-1} vs T plots, Figure 1.2. A negative Weiss constant reveals antiferromagnetic coupling and a positive Weiss constant reveals ferromagnetic coupling. The Curie-Weiss law is only relevant to spin-only systems where other contributions, such as zero-field splitting, spin-orbit coupling, and temperature independent paramagnetism, can be ignored.

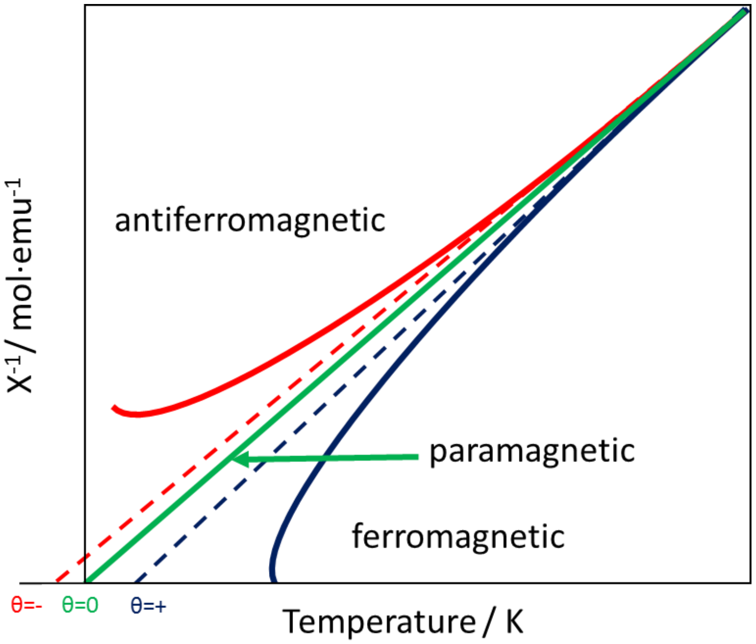

Figure 1.2 Representative plot of χ^{-1} vs T for a paramagnet (green line), antiferromagnet (red line), and ferromagnet (blue line). Curie-Weiss fit of high temperatures is represented by dotted lines for each scenario.

Another useful parameter that can be approximated is the phase transition temperature (paramagnetic to antiferromagnetic or paramagnetic to ferromagnetic transition):

$$\mathrm{T} = z|\mathrm{J}|\sqrt{\frac{\mathrm{C_A C_B}}{\mathrm{N_A} g^2 \mu_B^2}} \qquad \textbf{Equation 1.9}$$

where T is the phase transition temperature, z is the number of nearest neighbors, J is the exchange integral, C_A and C_B are the curie constants of the interacting spins, N_A is Avogadro's number, g is the Landé g-factor, and μ_B is the Bohr magneton. In the field of molecular magnets, equation 1.9 has been exploited to create high temperature magnets.

As mentioned above, the magnetic susceptibility correlates the magnetization with the applied field, $\chi = M/H$. However, when the external magnetic field becomes large or when temperature is low, M approaches a saturation value, M_S. This value is a general characteristic of magnets and is observed in hysteresis loops, Figure 1.3, if the magnetic energy is sufficient for being detected on the time scale of the experiment. In a hysteresis measurement, an external field is ramped, usually around 3.5 mT/s, from 0 through 3 T. The increasing field will eventually saturate the magnetization, M_S, at which point the applied field is reversed. A history dependence is observed and the material exhibits a remnant magnetization, M_R, after the field has returned to 0 T. In three-dimensional bulk magnets, M_R is due to the lag of the domain wall movement, whereas in lower dimensional 1D and 0D compounds the lag is due to an intrinsic energy barrier not dependent on long range ordering. Paramagnetic materials do not show remnant magnetization and are able to freely rotate with the changing field. For materials with a remnant magnetization, a negative field is required to return the magnetic moment of the material to zero. This field is known as the coercive field, H_C. The magnetization of the sample will then saturate in the negative fields, and the sweep back to positive, thereby completing the hysteresis loop. The value of H_C determines the strength of the magnet. A large H_C is called a hard magnet and a small H_C is a soft magnet. Each type of material has its own uses in technology.

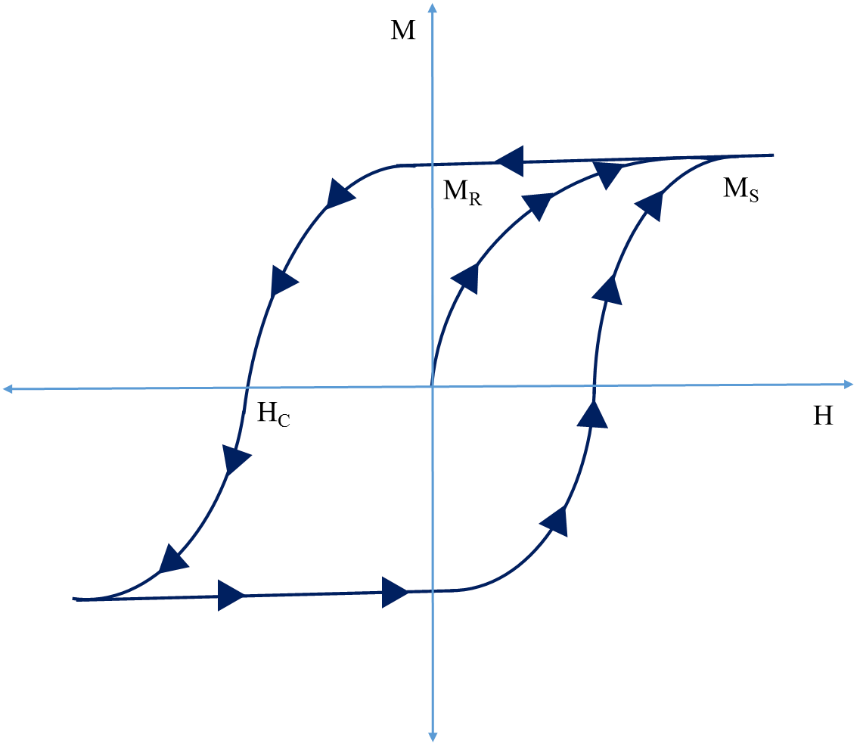

Figure 1.3 Representative hysteresis loop. Sweeping of field is shown by blue triangles.

Cyanide-Based Molecular Magnets

One class of materials that has emerged as an excellent candidate for molecular magnets is that of cyanide bridged compounds.[14] The cyanide ligand has proven to be a versatile bridging ligand capable of promoting moderate to excellent superexchange between a wide variety of transition metal ions. The versatility and predictability of this ligand is a result of its nonsymmetrical nature that allows for selective binding of different transition metals. The carbon bound metal ion will be in a low spin configuration due to the ligand field strength of cyanide, whereas the nitrogen end can coordinate with a metal that is high spin or low spin, depending on the metal. The linear configuration of the M-CN-M' unit in octahedral coordination environments allows for predictable exchange coupling by considering the symmetry of the magnetic orbitals on each spin center as depicted in Figure 1.4. Metal ions bridged by cyanide with unpaired electrons in orbitals with the same symmetry will form a bonding interaction leading to antiferromagnetic behavior. If the unpaired electrons reside in orthogonal orbitals with different symmetries there is no direct overlap and the interaction is ferromagnetic, similar to the case of non-bonding electrons. This principle was confirmed with the observation of ferromagnetic interactions in Ni as well as Cu containing Prussian Blue analogs.[15] Most three-dimensional transition complexes bridged by cyanide exhibit antiferromagnetic interactions. The different oxidation states and electronic configurations afforded by the transition metals have resulted in numerous complexes exhibiting interesting ferrimagnetic behavior. Most early examples of cyanide based magnets are Prussian Blue, $Fe^{III}_4[Fe^{II}(CN)_6]_3\cdot 14\text{-}16H_2O$, and its analogs, which make up an impressive family of three-dimensional ordered compounds, Table 1.1.

a) *Same Symmetry Magnetic Orbitals*
Anti-ferromagnetic Coupling

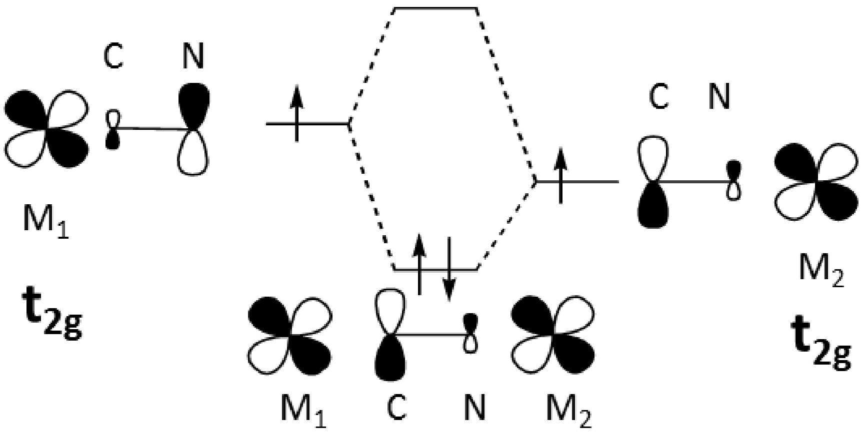

b) *Orthogonal Magnetic Orbitals*
Ferromagnetic Coupling

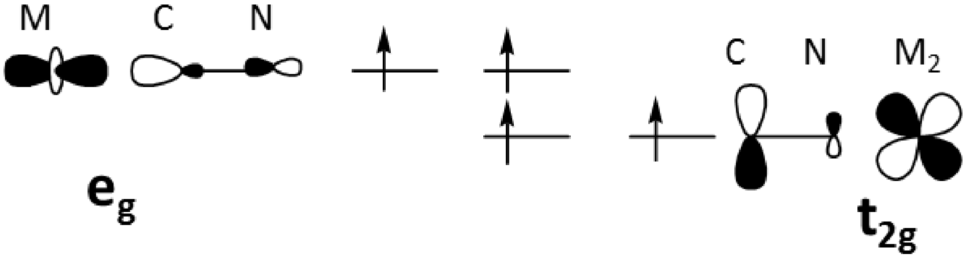

Figure 1.4 Orbital symmetry considerations directing superexchange between a) two octahedral metal ions with an electron in orbitals with the same symmetry and b) two octahedral metal ions with an electron in orthogonal orbitals.

Table 1.1 Compilation of critical temperatures in Prussian Blue analogs

Compound: $C_xA[B(CN)_6]z\cdot nH_2O^{(a)}$	**Ordering Nature**	T_C**/K**
$KV^{II}[Cr^{III}(CN)_6]$	Ferri	376
$V^{II}[Cr^{III}(CN)_6]_{0.86}\cdot 2.8H_2O$	Ferri	372
$K_{0.5}V[Cr(CN)_6]_{0.95}\cdot 1.7H_2O$	Ferri	350
$Cs_{0.8}V[Cr(CN)_6]_{0.94}\cdot 1.7H_2O$	Ferri	337
$V^{II}[Cr^{III}(CN)_6]_{2/3}\cdot 3.5H_2O$	Ferri	330
$V[Cr(CN)_6]_{0.86}\cdot 2.8H_2O$	Ferri	315
$Cr^{II}[Cr^{III}(CN)_6]_{2/3}\cdot 10/3H_2O$	Ferri	240
$(Et4N)_{0.4}Mn^{II}[V^{II}(CN)_5]_{4/5}\cdot 6.4H_2O$	Ferri	230
$Cs_{2/3}Cr^{II}[Cr(CN)_6]_{8/9}\cdot 40/9H_2O$	Ferri	190
$Cs_2Mn^{II}[V^{II}(CN)_6]$	Ferri	125
$(V^{IV}O)[Cr^{III}(CN)_6]_{2/3}\cdot 4.5H_2O$	Ferri	115
$CsMn^{II}[Cr^{III}(CN)_6]$	Ferri	90
$CsNi^{II}[Cr^{III}(CN)_6]\cdot 2\text{-}4H_2O$	Ferro	90
$Mn^{II}[Cr^{III}(CN)_6]_{2/3}\cdot 5–6H_2O$	Ferri	66
$Cu^{II}[Cr^{III}(CN)_6]_{2/3}\cdot 5–6H_2O$	Ferro	66
$Ni^{II}[Cr^{III}(CN)_6]_{2/3}\cdot 4H_2O$	Ferro	53
$(NMe_4)Mn^{II}[Cr^{III}(CN)_6]$	Ferri	59
$Mn^{II}[Mn^{IV}(CN)_6]$	Ferri	49
$CsNi^{II}[Mn^{III}(CN)_6]\cdot H_2O$	Ferro	42
$K_2Mn^{II}[Mn^{II}(CN)_6]\cdot 0.5H_2O$	Ferri	41
$Co^{II}_3[Co^{II}(CN)_5]_2\cdot 8H_2O$	Ferri	38
$Mn^{II}[Mn^{III}(CN)_6]_{2/3}\cdot 4H_2O$	Ferri	37
$Mn^{III}[Mn^{III}(CN)_6]$	Ferri	31
$Ni^{II}[Mn^{II}(CN)_6]_{2/3}\cdot 12H_2O$	Ferro	30
$Mn^{III}[Mn^{II}(CN)_6]_{2/3}\cdot$solvent	Ferri	29
$(Me_4N)Mn^{II}[Mn^{III}(CN)_6]$	Ferri	28.5
$V^{III}[Mn^{III}(CN)_6]$	Ferri	28
$Ni^{II}[Fe^{III}(CN)_6]_{2/3}\cdot nH_2O$	Ferro	23
$Cr^{III}[Mn^{III}(CN)_6]$	Ferri	22
$Cu^{II}[Fe^{III}(CN)_6]_{2/3}]\cdot nH_2O$	Ferro	20
$Co^{II}[Cr^{III}(CN)_6]_{2/3}]\cdot nH_2O$	Ferro	19
$Fe^{II}[Cr^{III}(CN)_6]_{2/3}\cdot 4H_2O$	Ferro	16
$Co^{II}[Fe^{III}(CN)_6]_{2/3}\cdot nH_2O$	Ferri	14
$Cr^{II}\ [Ni^{II}_2(CN)_4]_{2/3}\cdot nH_2O$	Ferri	12
$Fe^{III}[Fe^{II}(CN)_6]_{3/4}\cdot 3.7H_2O$	Ferro	5.6

[a] The formulae given in the table were rescaled from literature- site vacancies not included in formulations. Table adapted from reference[16] with permission.

The remarkable discovery that ferric ions in Prussian Blue couple ferromagnetically across a 10 Å bridge[17] led to an explosion of research on the topic of Prussian Blue analogs in which the iron ions are replaced by other paramagnetic metal spin centers.[16] The strategy was successful with many analogs exhibiting impressive critical temperatures, culminating with the $KV^{II}[Cr^{III}(CN)_6]$ compound that displays long range ordering up to 376 K - higher than the boiling point of water![18] Research on Prussian Blue and its analogs extend far beyond the search for high critical temperature magnets however. For example, the Prussian Blue analogs, $Rb_{0.8}Mn[Fe(CN)_6]_{0.93}\cdot 1.62\ H_2O$ and $Co_3[W(CN)_8]_2(pyrimidine)_4\cdot 6H_2O$, were shown to exhibit reversible changes in their optical and magnetic properties after application of an electric field.[19] Such systems are of interest for bistable devices. Prussian Blue itself has been incorporated into modified electrodes for oxidase enzyme-based biosensors in clinical, environmental, and food analysis.[20] Perhaps most importantly, Prussian Blue is the first cyanide compound and inspired the development of one of the largest fields in coordination chemistry.

Problems arise, however, in the characterization and modeling of the physical properties of Prussian Blue and its analogs. The rapid precipitation of an extended framework hinders formation of single crystals that exhibits randomly distributed vacancies dependent upon synthetic conditions. Cations, anions, or solvent molecules can be incorporated into the framework. These problems are undoubtedly dissuading researchers from further exploration or use of these materials and there is need for a foothold on the synthesis of Prussian Blue and its analogs. In this vein, chapter II of this dissertation revisits the structure of Prussian Blue to address these problems and presents a new method for making crystalline products.

Reducing the Dimensionality of Cyanide-Based Molecular Magnets

Motivated by a desire to prepare precise materials for modeling and for understanding the details of the properties, researchers are using capping ligands to prepare molecular clusters that mimic the properties of Prussian Blue parent compounds.[14] The molecular precursors used to design discrete compounds allow for geometric control through the use of a modular, or “building block approach.” Also known as the “bottom-up approach”, predetermined product geometry can be realized, making this technique ideal for the study of structure-property relationships. Greater structural control over molecular architectures is possible with cyanide compounds as opposed to the prevalent oxide clusters because cyanide chemistry allows for self-assembly.[21,22]

Among the important classes of molecular nanomagnets in this regard are one-dimensional single-chain magnets (SCMs) and zero-dimensional single-molecule magnets (SMMs).[21,23-27] By introducing blocking ligands to cyanide-based precursors, a large number of compounds consisting of different dimensionalities, nuclearities, and compositions have been realized with new potential for electronic and magnetic device application with precision at the nanoscale.[28] In particular, SCMs and SMMs have potential for high density data storage,[13,29,30] quantum computing [30-45], and molecular spintronics.[35,38,46-50] The remaining chapters of this dissertation will focus on the design of SCMs and SMMs which behave analogously to traditional bulk magnets in that they retain a preferential direction of the magnetic moment below a certain blocking temperature

(T_B). The organization of the chapters is in terms of decreasing dimensionality, although SMMs were historically realized before SCMs.

Single-Chain Magnets (SCMs)

SCMs, or "magnetic nanowires" as they were dubbed in the first paper describing the type of compound,[51] are exciting new materials that have the capability of giving rise to high blocking temperatures because of short range magnetic correlation along the chain direction in addition to an anisotropy barrier. The model behind the slow relaxation dynamics of SCMs was proposed by Glauber in 1963.[52] This process is described by the reversal of one spin in an infinite chain where all spins are aligned. In the Ising limit, this will cost an energy of $\Delta_E = 4|J|S^2$ due to the magnetic exchange interactions, J, between two neighboring spins. The domain wall created by the spin flip can propagate itself along the chain, or extinguish itself by reversing back the initial spin. This situation corresponds to the decay of the magnetization once the external magnetic field is removed, the analog of which is domain wall movement in three-dimensional network compounds. An additional anisotropy term for the individual magnetic repeat unit is given by $\Delta_A = S^2|D|$, where S is the spin ground state and D is the axial zero-field splitting parameter (as seen for SMMs discussed below). The total energy governing the orientation of the magnetic moment in SCMs is then given by, $\Delta_{total} = (8J + D)S^2$.[53] It is therefore a good strategy to synthesize chains consisting of anisotropic building blocks with the highest possible intrachain coupling. However, the systematic development of analogous models for Ising interactions has not yet been thoroughly developed as compared to the case of orbital models in rationalizing isotropic coupling constants and is awaiting experimental development.

The first example of a SCM was reported in 2001 by Caneschi and coworkers. The compound, {Co(hfac)$_2$[NIT(C$_6$H$_4$p-OMe)]} (hfac = hexafluoroacetylacetonate NIT(C$_6$H$_4$p-OMe) = 40-methoxy-phenyl-4,4,5,5-tetramethylimidazoline-1-oxyl-3-oxide radical) displays magnetic hysteresis of molecular origin below 4 K.[51] Interestingly, the authors discovered that hysteresis was only observed when the field was applied parallel to the molecular chain axis. The hysteresis loop, Figure 1.5, closes as temperature is increased or as the field direction is changed. The authors also reported AC magnetic susceptibility measurements, Figure 1.6, which also display characteristics of low-dimensional magnets and can be used to extrapolate the energy barrier, Δ_{total}.

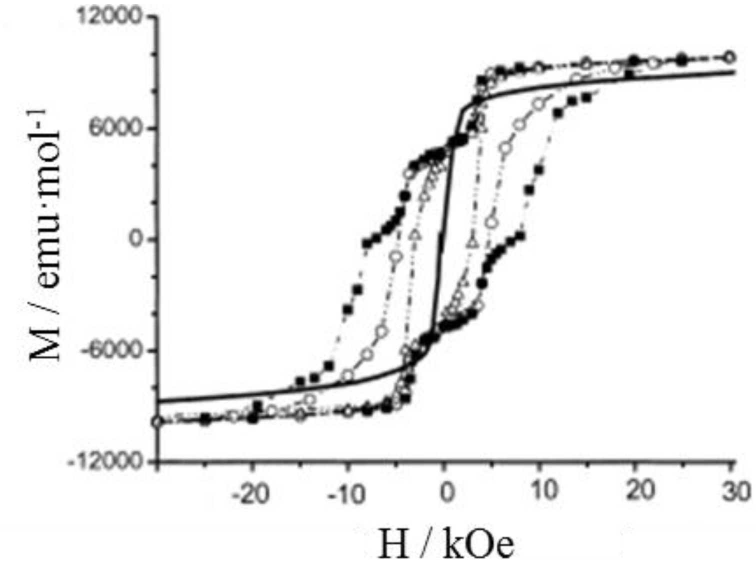

Figure 1.5 Hysteresis loops measured on a single crystal of **1** by applying the field parallel to the chain axis at 2.0 K (■), 3.0 K (○), 4.5 K (Δ), and at 2.0 K perpendicular to it (—). Reproduced from reference[51] with permission from John Wiley & Sons Ltd.

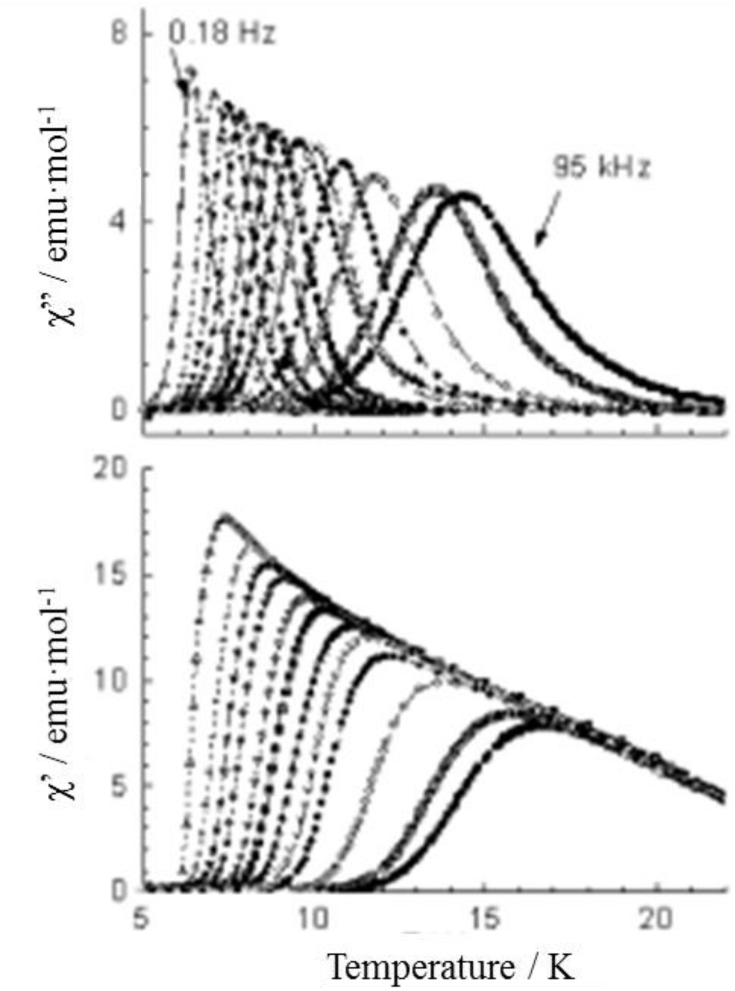

Figure 1.6 AC dynamic susceptibility measurements in zero-applied DC field showing the out-of-phase (top) and in-phase components (bottom) of the magnetic susceptibility as a function of temperature. Reproduced from reference[51] with permission from John Wiley & Sons Ltd.

In an AC magnetic susceptibility measurement a small oscillating field, typically 3-5 Oe, is applied to a sample over a collection of frequencies and temperatures. At a certain temperature, the frequency of the oscillating field is too rapid for the spins in the compound to follow the field. This leads to a lag time in the susceptibility response which is an “out-of-phase” (imaginary) component which is χ”. The “in-phase: component is χ’ and the relationship between the two is governed by equation 1.10.

$$\chi_{ac} = \chi' - i\chi'' \qquad \textbf{Equation 1.10}$$

The value of the out-of-phase susceptibility, χ”, reaches a maximum when the relaxation time of the compound is exactly equal to the frequency of the oscillating field. Thus, χ” shows an absorption-like maximum and the temperature at which this occurs is the “blocking temperature” at a given frequency. The collection of relaxation times are then plotted with the Arrhenius equation to obtain the barrier height, U_{eff}/k_B, which is further detailed in chapter IV. Arrhenius analysis of {Co(hfac)$_2$[NIT(C$_6$H$_4$p-OMe)]} led to an effective barrier height, U_{eff}/k_B = 154(2) K, which is much higher than the energy barriers of SMMs at the time, although the authors ignored the effects of infinite and finite domain regimes of SCMs which was not analyzed until after this early report.[54]

Since the discovery of {Co(hfac)$_2$[NIT(C$_6$H$_4$p-OMe)]} in 2001, many examples of slowly relaxing chain compounds have appeared in the literature that exhibit interesting and complex magnetic properties in addition to multifunctional behavior.[53-64] Chains based on the cyanide ligand[65-71] were sought due to the inherent linear nature of *trans*-cyano building blocks. One such example is (Et$_4$N)[Mn$_2$(5-MeOsalen)$_2$Fe(CN)$_6$] (5-MeOsalen^{2-} = N,N’-ethylenebis(5-methoxysalicylideneiminate)) which exhibits ferromagnetic coupling mediated by an easy-axis anisotropy along the chain propagation axis.[72] An easy-axis refers to magnetic anisotropy, which is a direction within a magnetic material that is easier to magnetize than all other directions. Trimer units are connected together through the phenolate oxygen to form 1D chains separated by layers of tetraethylammonium cations which serve to minimize the interchain interactions. Related work from the Dunbar group revealed a variation of structural motifs including one-dimensional chains, using the $[W(CN)_8]^{3-}$ anion in reactions with $[Mn^{II}(tptz)X_2]$ (tptz = tris(2-pyridyl)-1,3,5-triazine; X = Cl^-, NO_3^-) under different synthetic conditions.[73] The chemistry led to different products based on the W_2Mn_2 square repeat unit which are connected together to form chain complexes (W_2Mn_2 = $[Mn(tptz)(OAc)(H_2O)_2]_2[[Mn(tptz)(MeOH)_{1.58}(H_2O)_{0.42}]_2[W(CN)_8]_2]\cdot5MeOH\cdot9.85H_2O$; OAc = acetate). We were inspired by these results to prepare a family of cyanide bridged chain compounds using both $[W(CN)_8]^{3-}$ and $[Mo(CN)_8]^{3-}$ with different $[M(tptz)X_2]$ complexes which is the topic of chapter III. We envisioned that the use of the second and third row molybdenum and tungsten ions would induce significant anisotropy in the magnetic repeating units. The larger λ (spin-orbit coupling constant) of 4d and 5d transition metals have been reported to increase the orbital contribution leading to large anisotropy.[74-77] In addition, the diffuse orbitals of the second and third row (4d and 5d block) metals lead to enhanced overlap with the π and π^* orbitals of the cyanide ligand, which is known to improve superexchange properties for cyanide containing SCMs.[78,79]

Single-Molecule Magnets (SMMs)

In nanomagnetism, as the sizes of magnetic particles are reduced to the molecular level, a limit is reached when domain walls no longer exist and the particle exhibits single domain behavior, displaying superparamagnetic properties. The discovery that molecules themselves could behave in a similar fashion as tiny bar magnets below a critical temperature revolutionized the field of magnetism. This new class of materials, referred to as “single-molecule magnets” (SMMs), display magnetic hysteresis and slow relaxation dynamics due to individual molecules rather than the additive long range ordering effects through a network as in the case of three-dimensional magnets. SMMs arguably have the best potential for device implementations, even over SCMs because they are soluble and readily processed, and, indeed, great progress has been made recently towards the implementation of SMMs for quantum computing,[30,80-83] molecular spintronics,[80,84,85] and high density data storage.[86,87] Multiple studies have already shown that SMMs can be grafted onto surfaces[88-90] and deposited on carbon nanotubes[91] while still retaining their magnetic properties. At the molecular level, it is possible that SMMs can exhibit quantum properties such as superposition and entanglement of spin states. By controlling the spin of a molecule (up or down), a bit of information can be stored by taking advantage of the bistability of the system, assuming that the material can maintain its spin orientation. Additionally, a SMM’s spin state may also be a superposition or combination of spin up and spin down (Qubits) making them capable of performing multiple operations simultaneously, whereas the classical binary system of today’s transistor technology can only exist in a 1 or 0 state.

Assuming that a SMM has an easy axis for magnetization (Ising-type anisotropy) a barrier ($\Delta E = S^2|D|$ for integer spin systems and $\Delta E = (S^2-1/4)|D|$ for half-integer spin systems) exists for the reversal of the magnetic moment of spin states, which, in the classical case, is governed by a large negative value of the axial zero-field splitting parameter (D) as well as a large ground spin state (S).[92-94] The negative zero-field splitting parameter stabilizes the highest components of the spin microstates (M_S) leading to a thermal energy barrier which is related to the energy separation between the highest M_S and lowest M_S. This fact was experimentally determined for the first recognized SMM, $[Mn_{12}O_{12}(CH_3COO)_{16}(H_2O)_4]\cdot 2CH_3COOH\cdot 4H_2O$ (Mn12OAc), Figure 1.7, which exhibits an energy barrier that is proportional to $|D|S^2$.[95,96]

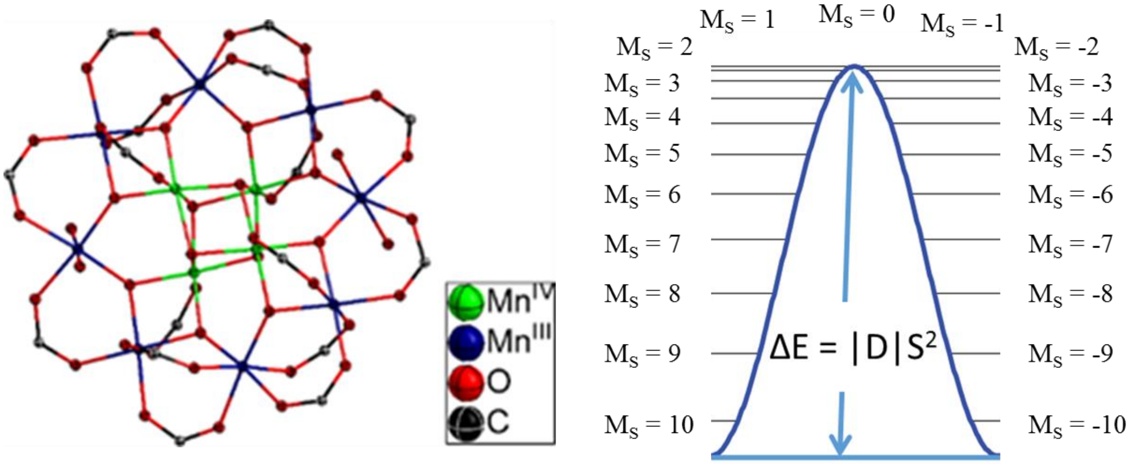

Figure 1.7 a) Structure of $Mn_{12}OAc$. Solvent and carbon atoms on acetate are omitted for the sake of clarity. b) Representative energy barrier for the reversal of the magnetic moment direction.

The structure of Mn12OAc consists of 8 outer Mn(III) (S=2) ions that engage in antiferromagnetic interactions with a central cubane of 4 Mn(IV) (S=3/2) ions, which leads to a ground state of S = 10 with D = -0.46 cm^{-1}. The anisotropy axes of the Jahn-Teller distorted Mn(III) ions align in a parallel fashion and, as a result, the molecule is Ising-type with a well-separated S = 10 spin ground state. $Mn_{12}OAc$ exhibits magnetic hysteresis up to 4 K, Figure 1.8. The step-wise behavior of the magnetization is due to quantum tunneling through the energy barrier which is advantageous for application in quantum computing.[97] The energy barrier, $U_{eff}/k_B = 62$ K, was determined by AC magnetic susceptibility and subsequent fitting with the Arrhenius equation.[30]

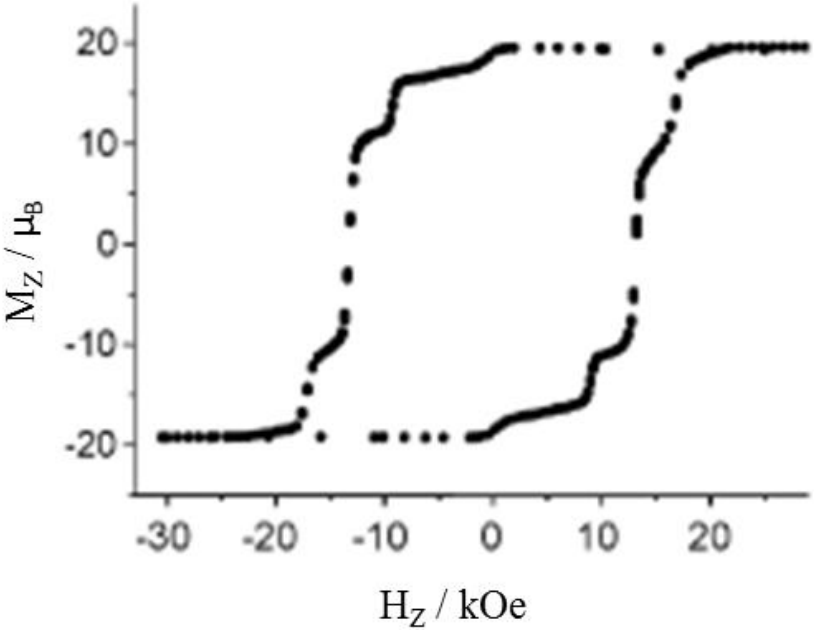

Figure 1.8 Magnetic hysteresis loop at 2.1 K for a single crystal of $Mn_{12}OAc$ with the field applied parallel to the tetragonal. Reproduced from reference[30] with permission from John Wiley & Sons Ltd.

To date, $Mn_{12}OAc$ remains one of the best SMMs among *polynuclear* transition metal complexes despite its discovery over 20 years ago. The primary reason progress has been somewhat stagnant is the presence of relaxation processes that are not related to thermally overcoming the energy barrier (Orbach process) in Figure 1.7b. At very low temperatures, depending on the applied magnetic field, quantum tunneling of the magnetization typically leads to faster relaxation rates than those obtained through the thermally activated pathway ($U_{eff}/k_B < \Delta_E$). The possible relaxation pathways for SMMs have been recognized as quantum tunneling, thermally-assisted quantum tunneling, single-phonon direct relaxation, two-phonon Raman relaxation, and a thermal Orbach relaxation.[98] Thus, a major challenge in this field is to design molecules that suppress all but the Orbach relaxation processes so that higher blocking temperatures can be achieved.[99,100]

Mononuclear Transition Metal SMMs

Mononuclear SMMs based on 3d transition metal ions became a subject of great interest in recent years because they are more easily modeled than larger molecules by the spin Hamiltonian, equation 1.11, with the single-ion zero-field splitting term involving the magnetic anisotropy:

$$\hat{\mathrm{H}} = \mathrm{D}\left(\hat{\mathrm{S}}_{\mathrm{Z}}^{2} - \frac{1}{3}\hat{\mathrm{S}}^{2}\right) + \mathrm{E}\left(\hat{\mathrm{S}}_{\mathrm{x}}^{2} - \hat{\mathrm{S}}_{\mathrm{y}}^{2}\right) \qquad \textbf{Equation 1.11}$$

where D is the axial zero-field splitting parameter, E is the rhombic zero-field splitting parameter, and $\hat{S}_i$ are the spin operators. A negative D value results in uniaxial type magnetic anisotropy and a positive D value results in an easy plane anisotropy. Mononuclear SMMs have been reported for both easy-axis and easy-plane systems,[101] although understanding the origin of slow relaxation in the latter type of complexes is a topic of debate.[102] The first mononuclear transition metal SMM was reported by Long and Freedman in 2010.[103] The compound is a high spin Fe(II) compound capped with a tris(pyrrolyl-α-methyl)amine ligand of general formula: $[(\mathrm{tpa}^{\mathrm{Mes}})\mathrm{Fe}]^{-}$ (Mes = mesityl). The geometry afforded by the ligand is trigonal pyramidal. This configuration leads to unquenched orbital angular moment due to the near degeneracy of the *xz* and *yz* orbitals. The strong orbital contribution leads to a large D value as evidenced by the non-superposition of the isofield curves collected from 1 – 7 T. Fitting the data with ANISOFIT 2.0 revealed a very large easy-axis D value of -39.6 cm^{-1} with E = -0.4 cm^{-1} and g = 2.21. Despite the impressive ZFS parameter, no χ" signals were observed with frequencies up to 1500 Hz and temperatures down to 1.8 K in the absence of an applied field. Application of a 1500 Oe DC field during the AC measurements, however, removed the ground state tunneling zero-field relaxation and led to an impressive energy barrier of 42 cm^{-1} with a pre-exponential factor of $\tau_o = 2 \text{ X } 10^{-9}$ s, on par with the $Mn_{12}Oac$ benchmark molecule. A major, but subtle, point the authors made was the explanation of not observing an AC signal in a zero applied DC field. In a purely axial system, the wavefunctions describing the ± M_s ground pair are orthogonal to each other, making the tunneling transition forbidden. However, the non-zero E value, which they ascribe to a slight lowering of symmetry, introduces a transverse magnetic anisotropy allowing for the mixing of the ± M_s ground states. Such observations have been noted for other SMMs in the literature.[30,104-106] Shortly after the work with $[(tpa^{Mes})Fe]^-$, the authors expanded upon the work by tuning the donor strength of the substituents group on the ligand to make a family of trigonal pyramidal Fe(II) pyrrolide complexes of general formula, $[M(solv)_n][(tpa^R)Fe]$ (M = Na, R = tert-butyl, phenyl, mesityl, 2,4,6-triisopropylphenyl, and 2,6-difluorophenyl).[107] The results revealed that the uniaxial ZFS parameter trended with the increasing ligand field strength at the Fe(II) center. Once again, an applied DC field during AC measurements was necessary to observe out-of-phase signals in the AC susceptibility measurements. Because of the fast relaxation at zero DC field, the authors performed Mössbauer spectroscopy which is on the time scale of approximately 0.01 μs. By monitoring the isomer shift and quadrupole splitting at different temperatures, the extent of line broadening could be fit to the Dattagupta and Blume formalism[108], which was used to construct an Arrhenius plot that is in good agreement with AC magnetometry fitting.

After the reports of the [(tpa^R)Fe] family, other research groups pursued mononuclear iron complexes as SMMs. One early report by Weismann and coworkers involves an aryl-Fe(II) complex with a cyclopentadienyl derivative.[109] The compound, [^{5}CpFe($C_6H_3iPr_3$-2,6)] exhibits a uniaxial anisotropy with D = -51.36 cm^{-1} as determined by a least squares fitting of M vs H/T curves by diagonalizing the spin Hamiltonian, equation 1.11. The rhombic splitting parameter is small (E = -0.32 cm^{-1}) and the average g value is 2.29. The molecular orbital diagram for [^{5}CpFe($C_6H_3iPr_3$-2,6)] indicates that unquenched orbital angular momentum is expected to lead to strong magnetic anisotropy. The D value was predicted to have a potential energy barrier of U_{eff} = 205 cm^{-1} based on the $S^2|D|$ equation. Therefore, AC susceptibility measurements were carried out, albeit in the presence of an applied DC field. Quite surprisingly, the authors noticed two different relaxation processes evolving at different applied DC fields. The two relaxation processes were fit to the Arrhenius law giving a U_{eff} = 40.3 K when the applied DC field is 750 Oe and a U_{eff} of 143.4K at 2500 Oe. The two barriers were designated as two different tunneling pathways that are suppressed at different DC fields. The temperature independent relaxation times for the process at 750 and 2500 Oe is on the order of 10^{-3} and 10^{-2} s, respectively. Because the first process exhibits faster tunneling it was ascribed to the transition between the ground M_s = ±2 states. The slower process was attributed to a thermally assisted quantum tunneling pathway through the M_S = ±1 manifold. The presence of any tunneling event was again attributed to the non-zero rhombic splitting parameter, E. These examples of Fe(II) SMMs are important in that they demonstrate that the relaxation barrier can be manipulated by the ligand field.

Other reports of mononuclear transition metal SMMs were made with the Co(II) ion. The first of this variety is the complex $(Ph_4P)_2[Co(SPh)_4]$ reported by Zadrozny and Long in 2011.[110] The tetrahedral complex has a $S = 3/2$ ground state with a uniaxial D value of $-70\ cm^{-1}$. More importantly, the AC susceptibility measurements revealed for the first time amongst mononuclear 3D SMMs signals in the χ" data without the necessity of an external DC field. As a Kramers ion, Co(II) has an non-integer spin which eliminates the mixing of the ground $\pm M_S$ levels by the rhombic splitting term, E. Other relaxation pathways that may still lead to fast quantum tunneling include hyperfine interactions and dipolar interactions.[30] The anisotropy of $[Co(SPh)_4]$ was attributed, like the previous examples, to a large spin-orbit coupling contribution between the ground and first excited state owing to the near degeneracy of the highest occupied and lowest half occupied d-orbitals. The AC magnetic studies were repeated with a diamagnetic zinc analog to magnetically dilute the compound and switch off dipolar interactions. Doing so revealed a disappearance of the quantum tunneling features at low temperatures. Nevertheless, the compound still exhibits a rather unimpressive barrier of $U_{eff} = 21\ cm^{-1}$, suggesting mixing with excited states or an unidentified relaxation process still predominating.

In 2012, two seminal papers emerged in the literature describing mononuclear SMMs exhibiting a positive D value. In the first report, Zadrozny and coworkers presented the magnetic study on the pseudo-tetrahedral complex, $[(3G)CoCl](CF_3SO_3)$ (3G = 1,1,1-

tris[2N-(1,1,3,3-tetramethylguanidino)methyl]ethane). Powder EPR data collected on the compound revealed three components, $g_z = 2.14$, $g_x = 5.28$, and $g_y = 3.81$, corresponding to transitions within the lowest $M_S = \pm 1/2$ Kramers doublets. Fitting the EPR data resulted in a $D = +12.7$ cm^{-1}, $E = 1.2$ cm^{-1}, and $g_z = 2.17$. Under an applied field of 1500 Oe, blocking temperatures were observed out to 2.6 K in AC measurements. The extracted barrier height from the Arrhenius fit gave $U_{eff} = 24$ cm^{-1} and $\tau_0 = 1.9 \text{ X } 10^{-10}$ s. Under a field of 1500 Oe, dipolar interactions are minimized but the ground state tunneling between the $M_S = \pm 1/2$ levels should still be operative. The authors attributed the slow relaxation in the complex to a lack of accessible phonon modes causing a phonon bottleneck and making the Orbach process through the excited state $M_S = \pm 3/2$ the dominant relaxation pathway. Not long after this result, Vallejo and coworkers published another Co(II) SMM but with a six-coordinate geometry. The compound, *cis*-$[Co^{II}(dmphen)_2(NCS)_2]\cdot 0.25EtOH$ (dmphen = 2,9-dimethyl-1,10-phenanthroline) contains a central Co(II) ion in a highly distorted environment with three sets of different bond lengths ranging from 2.038(3) – 2.275(3) Å leading to an overall rhombic C_{2V} symmetry. Investigations of the low temperature field-dependent magnetization data and EPR spectra were used to determine $D = +98$ cm^{-1}, $E = +8.4$ cm^{-1}, and $g = 2.78$. The AC magnetic studies of this compound revealed no out-of-phase signals in a zero-applied DC field. The compound did show strong frequency-dependent maxima in both χ' and χ'' under an applied DC field of 1000 Oe with an Arrhenius fit of the data yielding $U_{eff} = 18.1$ cm^{-1}. The authors admit that observing an energy barrier for an easy-plane systems is not readily understood and they propose that there may be an easy axis within the easy plane due to transverse anisotropy distinguishing between the x and y directions.

At this stage of the field, the modulation of spin-orbit coupling by ligand field effects was a well adopted strategy. Researchers began thinking of specific geometries to isolate a nearly- degenerate ground state. Bulky ligands with sufficient steric encumbrance were identified as a means to stabilize low-coordinate transition metals complexes with large spin-orbit coupling. In 2013, Poulten and coworkers reported a two-coordinate Ni^I complex with bulky N-heterocyclic carbene ligands.[111] The complex [Ni(6-Mes)2]Br (6-Mes = 1,3-bis(2,4,6-trimethylphenyl)-3,4,5,6-tetrahydropyrimi-din-2-ylidene) is the first mononuclear transition metal SMM with a metal other than Co(II) or Fe(II). Interestingly, the spin-orbit coupling was so large that magnetic susceptibility was modeled with unquenched orbital angular momentum J states, generating an energy barrier to the reversal of the magnetization in a nominally S = ½ transition metal. Under a 600 Oe applied DC field, the complex exhibits U_{eff} = 17 K and $\tau_0 = 4.6 \text{ X } 10^{-6}$ s. The authors reasoned that the small barrier is due to quantum tunneling from mixing of the ground state with excited states. Later in the same month that this publication appeared, another study was published by Zadrozny and coworkers on a family of linear, two-coordinate Fe(II) complexes.[112] The family includes $Fe[N(SiMe_3)(Dipp)]_2$, $Fe[C(SiMe_3)_3]_2$, $Fe[N(H)Ar']_2$, $Fe[N(H)Ar^*]_2$, $Fe(Oar')_2$ and $Fe[N(H)Ar^\#]_2$ (Dipp = C_6H_3-2,6-Pr^i_2; Ar′ = C_6H_3-2,6-(C_6H_3-2,6-$Pr^i_2)_2$; Ar* = C_6H_3-2,6-(C_6H_2-2,4,6-$Pr^i_2)_2$; $Ar^\#$ = C_6H_3-2,6-(C_6H_2-2,4,6-$Me_3)_2$). The complexes are listed in order of descending symmetry from rigorous $D_{\infty h}$ due to the ligand framework. *Ab initio* calculations revealed that the lowering of molecular symmetry reduces the amount of spin-orbit coupling to yield a lower energy barrier that was confirmed by AC magnetic studies (under an applied DC field). The compound $Fe[N(SiMe_3)(Dipp)]_2$ was most promising of the group with $U_{eff} = 181$ cm^{-1}. An important part of this work was the modeling of the relaxation processes. Even under an applied DC field, separate spin-reversal pathways can become accessible, such as the direct process, a Raman process, or thermally assisted quantum tunneling processes. These different pathways exhibit different dependencies on the strength of the applied DC field. The authors used equation 1.12 to determine which processes are operative in the AC measurements which was an important step in the future of the field. This same equation will appear in chapter 5 in the modeling of an erbium SMM.

$$\tau^{-1} = \mathrm{AH^2T} + \frac{\mathrm{B_1}}{1 + \mathrm{B_2H^2}} + \mathrm{BT^n} + \tau_{o}^{-1} \exp\left(\frac{-U_{\mathrm{eff}}}{\mathrm{k_BT}}\right) \qquad \textbf{Equation 1.12}$$

where $\mathrm{AH^2T} + \frac{\mathrm{B_1}}{1+\mathrm{B_2H^2}}$, $\mathrm{BT^n}$, and $\tau_o^{-1}\exp(-U_{eff}/k_BT)$ represent direct, Raman, and Orbach relaxation processes, respectively.

Zadrozny and workers went on after the previous study to study an Fe^I complex in a highly symmetric ligand field with the reasoning that it should provide a stronger spin-orbit coupling scenario and the possibility of observing AC signals in a zero DC applied field because Fe^I in this geometry is a Kramers $S = 3/2$ ion. Reducing the linear two-coordinate complex, $[Fe^{II}(C(SiMe_3)_3)_2]_2$, with potassium graphite in the presence of cryptand afforded $[K(crypt\text{-}222)][Fe^I(C(SiMe_3)_3)_2]$. The χT vs T data were analyzed and are in accord with first order spin-orbit coupling contributions; the AC measurements provided a barrier of $U_{eff} = 226\ cm^{-1}$ with $\tau_0 = 1.3(3) \times 10^{-9}$ s. The barrier height is the largest reported value for any transition metal SMM to date.

The preceding examples were selected out of the plethora of mononuclear metal complexes from the literature.[113] Recent theoretical calculations have confirmed that spin-orbit coupling greatly enhances ZFS which stems from second-order perturbation theory.[114,115] In fact, large magnetic anisotropy was shown to be predictable in transition metals complexes based on coordination number and electronic structure. This important computational work by Ruiz and Gomez-Coca and coworkers provides a roadmap for synthetic chemists in the search for the largest anisotropic systems. *Ab initio* CASSCF-RASSI calculations were conducted on the existing mononuclear transition metal SMMs to relate the D value to the splitting of the d-orbitals. The authors concluded that the magnitude of D is inversely proportional to the energy separations of the ground and excited states before the inclusion of spin-orbit coupling. Each transition contributes to the components of the D tensor, D_{zz}, $D_{xx,}$ or $D_{yy,}$ depending on which orbitals are involved in the transition leading to D and E parameters according to the following equation:

$$\mathrm{D} = D_{zz} - \frac{(D_{xx} + D_{yy})}{2}\ ;\ \mathrm{E} = \frac{(D_{xx} - D_{yy})}{2} \qquad \textbf{Equation 1.13}$$

Importantly, transitions between orbitals of the same magnetic quantum number, m_l, contribute to uniaxial zero-field splitting parameters, D_{zz}, which explains why spin-orbit coupling should be rigorously pursued. A qualitative model was then constructed to predict which geometries for a given electronic configuration will lead to large D values (Figure 1.9). This model was used as inspiration for the pursuit of the cobalt SMM,

$\{(Tp^{*}Ti^{IV})(\mu_2\text{-}OAc)_2(\mu_2\text{-}O)Co^{II}(\mu_2\text{-}O)(\mu_2\text{-}OAc)_2(Ti^{IV}Tp^{*})\}\cdot 4(CH_3CN)$, presented in chapter IV.

	d^1 / d^6	d^2 / d^7	d^3 / d^8	d^4 / d^9
linear-2	🟩	🟥	🟩	🟧
divacant tetrahedron-2	🟥	🟥	🟩	🟧
tetravacant octahedron or bent-2	🟩	🟥	🟥	🟦
trigonal planar-3	🟩	🟥	🟧	🟩🟦
vacant tetrahedron-3	🟩	🟥	🟧	🟩🟦
fac-trivacant octahedron-3	🟩🟥	🟩🟥	🟧🟦	🟧🟦
mer-trivacant octahedron-3	🟩	🟥	🟥	🟦
square-4	🟩	🟥	🟥🟧	🟦
tetrahedron-4	🟩🟥	🟩🟥	🟩🟥	🟩🟥
seesaw-4	🟥	🟩	🟧	🟧
trigonal pyramid-4	🟩	🟥	🟩	🟧
pentagon-5	🟩	🟥	🟧	🟩🟦
vacant octahedron-5	🟩	🟥	🟧	🟦
trigonal bipyramid-5	🟩	🟥	🟩	🟧
square pyramid-5	🟥	🟩	🟧	🟧
hexagon-6	🟩	🟥	🟧	🟩🟦
pentagonal pyramid-6	🟩	🟧	🟧	🟩🟦
octahedron-6	🟩🟥	🟩🟥	🟦🟧	🟦🟧
trigonal prism-6	🟧	🟩	🟧	🟩🟦
heptagon-7	🟩	🟥	🟧	🟩🟦
hexagonal pyramid-7	🟩	🟧	🟧	🟩🟦
pentagonal bipyramid-7	🟩	🟧	🟩🟦	🟧
capped octahedron-7	🟩	🟧	🟧	🟩🟦
capped trigonal prism-7	🟥	🟦	🟥🟧	🟥🟧
octagon-8	🟩	🟥	🟧	🟩🟦
heptagonal pyramid-8	🟩	🟧	🟧	🟩🟦
hexagonal bipyramid-8	🟩	🟧	🟩🟦🟧	🟩🟦🟧
cube-8	🟩	🟧	🟩🟦🟧	🟩🟦🟧
square antiprism-8	🟧	🟩	🟥	🟩🟦
dodecahedron-8	🟧	🟥	🟩	🟥🟧
biaugmented trigonal prism-8	🟧	🟥	🟩🟥	🟩🟥

Figure 1.9 Estimation of the *D* values for high-spin mononuclear transition-metal complexes with different electronic configurations and coordination modes using ammonia ligands (using the molecular orbitals of $Fe^{II}(NH_3)_x$ models). Green and blue squares indicate large and small negative values, in that order, while red and orange represent large and small positive values, respectively. Cases with more than one color indicate that the non-distorted structure has several degenerate orbits involved in the transition, and different options are possible depending on the symmetry of the Jahn–Teller distortion. Figure and caption reprinted with permission from reference.[115] Copyright 2013 American Chemical Society.

Mononuclear Lanthanide SMMs

"Single-ion" or mononuclear SMMs include transition metals,[115] actinides,[116,117] and lanthanides[98] with the latter receiving the most attention. The appeal is the simplicity of small molecules which affords better opportunities for structure/property relationships that can be more readily investigated computationally. In addition, these materials are easily tuned by systematic changes in the coordinating ligands. Lanthanide elements in general have received the most attention, due to their inherent single-ion anisotropy from 1st order spin-orbit coupling which leads to a barrier in such materials based on the splitting of the states by the crystal field. Because lanthanide elements exhibit strong angular dependence of their 4f orbitals that are well shielded by valence shell electron density, Figure 1.10, the free ion 4f electron density is distorted in either an oblate or prolate shape, as shown by quadrupole approximations for the trivalent lanthanides, Figure 1.11.[118]

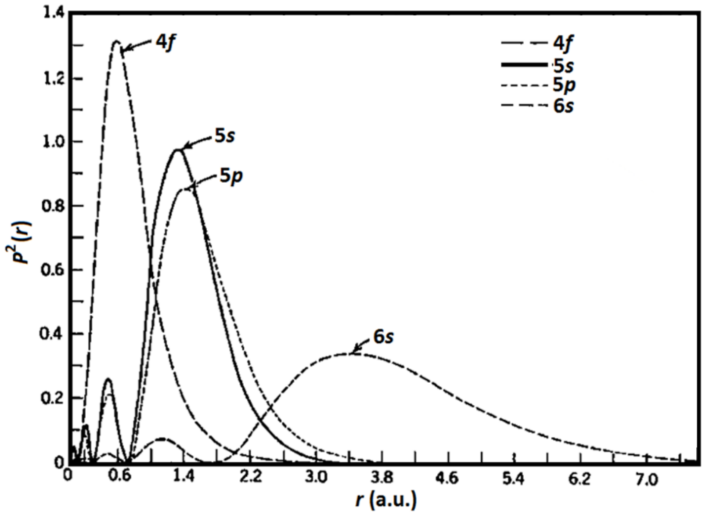

Figure 1.10 Radial distribution functions of lanthanide orbitals showing core 4f electrons are well shielded by the 5s, 5p, 5d, 6s, and 6p orbitals. Figure adapted from open access reference.[119]

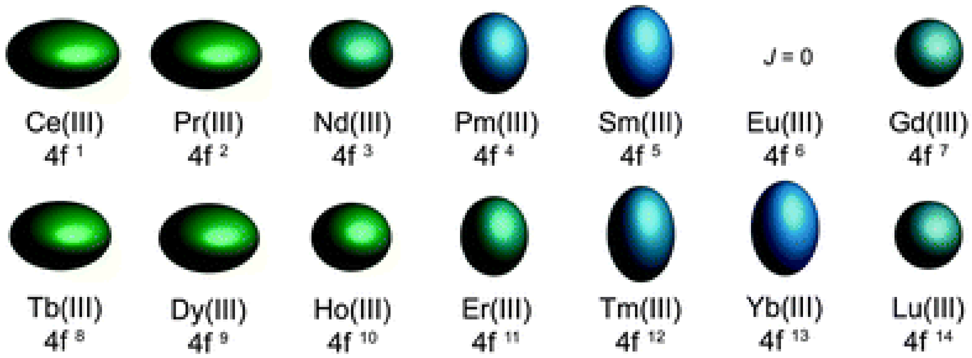

Figure 1.11 Shape of 4f electron density for trivalent lanthanide ions. Reproduced from reference[118] with permission of the Royal Society of Chemistry.

The near degeneracy of the 4f orbitals induce a large unquenched orbital contribution which leads to first order spin-orbit coupling. As a result, spin is no longer a good quantum number, and the electronic states are described by term symbols in the Russell-Saunders coupling scheme, $^{2S+1}L_J$, where S and L are the total spin and orbital angular momentum quantum numbers, respectively. J is the total angular momentum quantum number and takes on the values of |L+S| through |L-S| in integer increments. The spin-orbit coupling splits the different $^{2S+1}L_J$ multiplets into different energies according to equation 1.14:

$$E_{S.O.} = \left(\frac{\lambda}{2}\right)[J(J+1) - L(L+1) - S(S+1)] \qquad \textbf{Equation 1.14}$$

where λ is the spin-orbit coupling constant.[120] The ground-state multiplet is determined by the maximum S allowed by Hund's rule and the Pauli exclusion principle and L also takes on the maximum given that the rules for S remain. For lanthanide ions with less than half-filled orbitals, the smallest J is lowest in energy, whereas the largest J is lowest in energy for greater than half-filled subshells.[98] A given multiplet has 2J+1 levels characterized by the magnetic quantum number m_J which takes on the values of J through -J in integer increments. The m_J states are referred to a microstates or sublevels of a given J state.[118]

For a free lanthanide ion, the degenerate microstates split in a magnetic field with energy:

$$E_H = -g_J m_J \mu_B H \qquad \textbf{Equation 1.2}$$

where g_J is the Landé g-factor, μ_B is the Bohr magneton, and H is the applied magnetic field. For the cases when the lanthanide ion forms complexes with ligands, the degeneracy of the ground multiplet microstates is removed by the crystal field, Figure 1.12. The electrostatic field generated by the ligands is able to orient the the electron cloud of the lanthanide ion due to simple electronic repulsions based on a point charge model.[98] The implications of this is that microstates with the largest m_J value can be stabilized with a ligand framework of the appropiate symmetry that minimizes electronic repulsions between the lanthanide ions with the ligands. This is the source of magnetic anistropy in mononuclear lanthanide complexes where the barrier height is governed by the energy differences in the splitting of crystal field states.

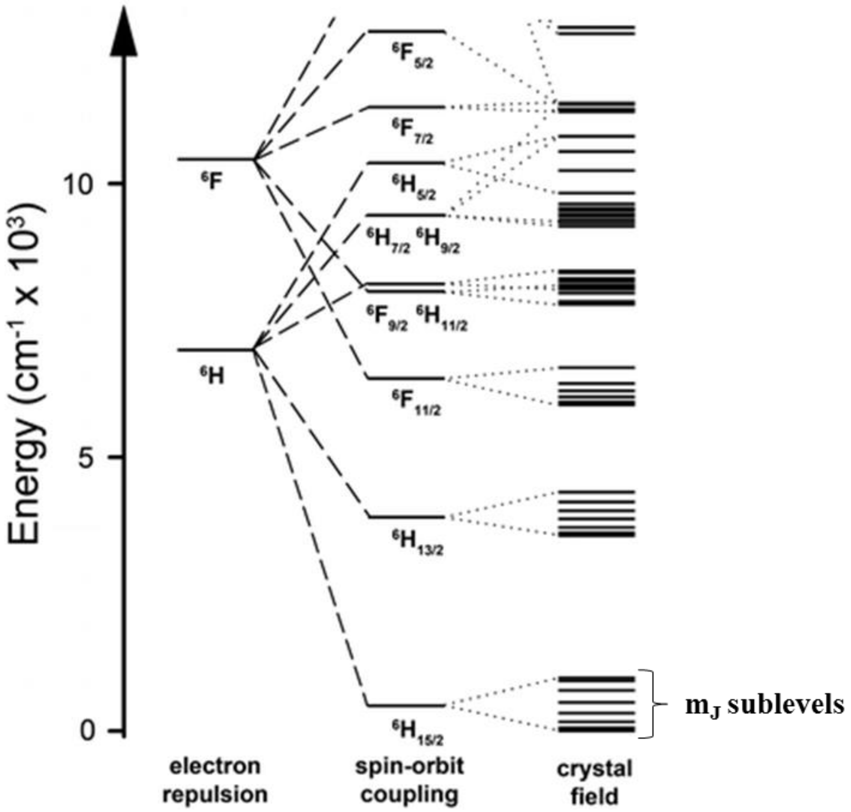

Figure 1.12 Splitting of ground-state of a dysprosium(III) ion due to the spin-orbit coupling (1st order) and the crystal field. Reproduced from reference[118] with permission of the Royal Society of Chemistry.

Fine-tuning the interaction between the lanthanide electron density with the crystal field environment is of upmost importance. For example, a lanthanide element with oblate electron density would be well suited with ligand fields of axial character. This was experimentally shown for the first mononuclear SMMs which are based on phthalocyanine double-decker compounds, $[LnPc_2]^-$ (Ln(III) = Tb, Dy, Ho, Er, Tm, and Yb), reported in 2003 by Ishikawa and coworkers.[121] Only the Tb and Dy analogs exhibit slow relaxation of the magnetization. The terbium analog TBA[$TbPc_2$] exhibits blocking temperatures below 50 K based on a 1000 Hz oscillating AC field and an effective barrier height of 230 cm^{-1}. This seminal work revealed that a single lanthanide ion could exhibit SMM behavior, far surpassing the transition metal polynuclear complexes where exploiting the co-alignment of anistropy is a challenging endeavor. The structural framework afforded by the Pc ligands in $[LnPc_2]^-$, Figure 1.13, was used as evidence of the validity of the simple oblate vs prolate theory.[118] Further studies on the phthalocyaninate family culminated with a heteroleptic octa(tert-butylphenoxy)-substituted Pc'Pc ligand framework in another Tb(III) complex, Figure 1.13b, which exhibits the largest effective energy barrier of any SMM iof U_{eff} = 652 cm^{-1}.[122] This barrier height is an order of magnetitude larger than that of $Mn_{12}OAc$.

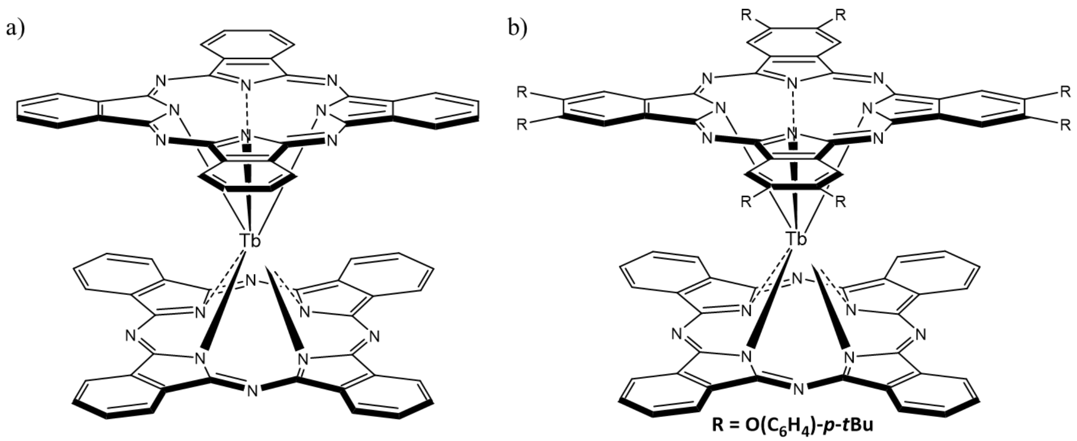

Figure 1.13 Structure of a) the first mononuclear lanthanide SMM, $[TbPc_2]^-$ and b) the derivatized analog, [TbPcPc'] (Pc' = R = octa(tert-butylphenoxy)) which exhibits the largest energy barrier to date.

Since Ishikawa's work in 2003, research in the field of mononuclear lanthanide SMMs has been prolific and continues to grow. [123-125] Most approaches revolve around polyoxometalates,[123] β-diketones,[126,127] and aromatic-based organometallic "sandwich" complexes.[128] These latter complexes show particular promise as the ligands can impose high symmetry- a crucial factor in realizing large effective energy barriers.[129] The mononuclear Er(III) sandwich complex, $[Li(DME)_3][Er^{III}(COT'')_2]$ (COT" = 1,4-bis(trimethylsilyl)cyclooctatetraenyl dianion) reported by Le Roy and coworkers exhibits hysteresis up to 8 K with an energy barrier of Ueff = 187 K.[130] The delocalized π cloud of the COT" ligands were reported to promote the crystal field perturbation on the lanthanide ion's ground-state which leads to a strictly axial anisotropic axis. This was a slightly surprising discovery given the oblate vs prolate theory; sandwich type compounds should better stabilize oblate 4f electron density. Through *ab initio* calculations the authors found that the equatorial nature of the ligands was responsible for the stabilization of the Er(III) ion and its intriguing magnetic data. The authors were able to expand on this work by tethering two Er(III) centers together in the triple decker compound, $[Er_2(COT")_3]$, which retains axial symmetry and exhibits a 4 K increase in the hysteresis temperature (matching the current hysteresis record[100] at 14 K) over its mononuclear analog, due to exchange coupling between the Er(III) ions.[131] The logical progression of aligning mononuclear SMMs into exchange-coupled systems represents the forefront of the field.

From the preceeding examples, it is evident that lathanide based SMMs are paving the way for SMM research, although one could argue this topic is becoming saturated with respect to two particular rare earth elements. Over 90% of the mononuclear lanthanide SMMs in the literature are based on Tb and Dy.[124] We were motivated by this statistic to pursue other prolate ions with a specific focus on Er(III) ion due to the results of the organometallic complexes. In addition, the study of Er(III) compounds are thus far limited to a handful of studies, Figure 1.14. The main premise, which will be discussed further in chapter 5, was to make a highly symmetric Er(III) complex using purely equatorial ligands.

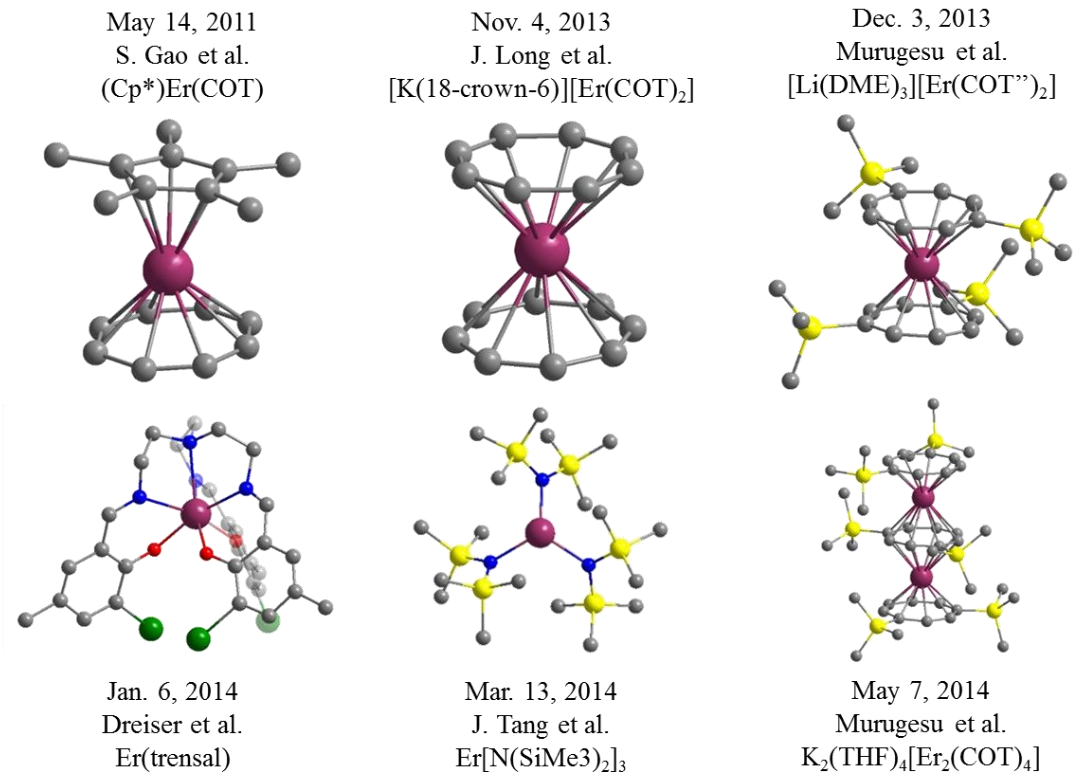
May 14, 2011
S. Gao et al.
(Cp*)Er(COT)

Nov. 4, 2013
J. Long et al.
[K(18-crown-6)][Er(COT)$_2$]

Dec. 3, 2013
Murugesu et al.
[Li(DME)$_3$][Er(COT'')$_2$]

Jan. 6, 2014
Dreiser et al.
Er(trensal)

Mar. 13, 2014
J. Tang et al.
Er[N(SiMe3)$_2$]$_3$

May 7, 2014
Murugesu et al.
K$_2$(THF)$_4$[Er$_2$(COT)$_4$]

Figure 1.14 Timeline of erbium-based mononuclear SMMs.

CHAPTER II

STRUCTURAL PROPERTIES OF PRUSSIAN BLUE

Introduction

Prussian Blue was discovered in 1704 by German pigment and dye producer, Johann Jacob Diesbach and reported anonymously.[132,133] The preparation was described twenty years later by Woodward and Brown.[134,135] Because of its long history in science, the compound which has the average formula, $Fe_4[Fe(CN)_6]_3 \cdot xH_2O$, has been coined, the "inorganic evergreen" and is known as the first coordination compound.[136] Once the brilliantly colored blue pigment was discovered to be an iron cyanide compound, a great deal of effort was expended to elucidate the chemical structure and connectivity.[137] Researchers discovered a wide array of compositions and this is true today even among commercially available compounds.[138]

The first problem encountered in literature regarding the composition of Prussian Blue was the identification of the oxidation states of the iron centers within the framework. Particularly, it was questioned whether the reaction of a ferric source ($Fe^{III}X_3$) with ferrocyanide ($[Fe^{II}(CN)_6]^{4-}$) produced the same product as the reaction of a ferrous ion ($Fe^{II}X_2$) with ferricyanide ($[Fe^{III}(CN)_6]^{3-}$). The presumption was that the compounds were different based on connectivity, Fe^{III}-NC-Fe^{II}-CN-Fe^{III} for the first case and Fe^{II}-NC-Fe^{III}-CN-Fe^{II} for the second case. The latter compound become known as Turnbull's Blue in the early to mid-1900s. At the time, textbooks printed the formula of Turnbull's Blue as $Fe^{II}_3[Fe^{III}(CN)_6]_2$.[139] With the advent of Mössbauer spectroscopy in 1957, Turnbull's Blue was found to be the same basic product as Prussian Blue in that the carbon bound iron is divalent and the iron coordinated to the nitrogen end of the cyanide ligand is trivalent in both compounds.[140] Numerous studies have confirmed this assessment.[137] Turnbull's Blue and Prussian Blue are thus distinguished as "soluble" and "insoluble" Prussian Blue, respectively, due to the presence of potassium in the interstitial channels in the former compound. Soluble Prussian Blue has the empirical formula, $KFe[Fe(CN)_6]$, and is termed "soluble" due to the compounds ability to form colloids and small particle sizes which makes the compound appear to be soluble although it is actually a finely dispersed suspension in water.[141]

In 1977, Buser, Schwarzenbach, Petter, and Ludi published the first crystal structure of Prussian Blue, Figure 2.1.[142] This report came after convincing powder X-ray data performed on samples from the same synthetic procedure.[143]

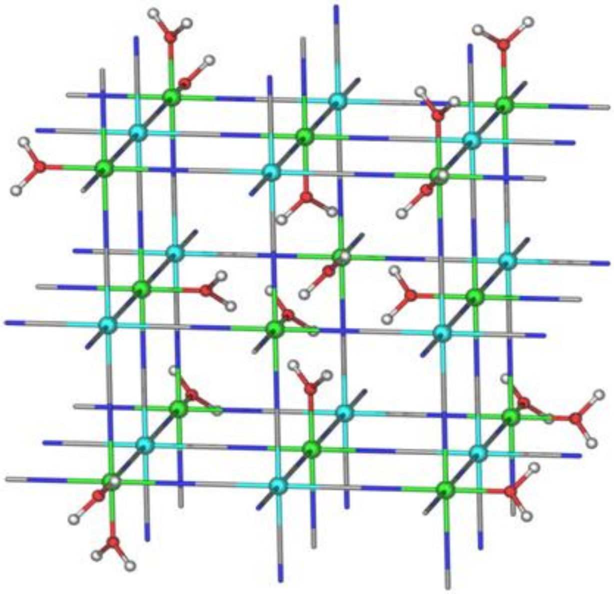

Figure 2.1 Representative crystal structure of Prussian Blue showing site defects inside the structure.

Crystals were grown by slow diffusion of water into concentrated HCl_{aq} solutions of Fe(II/III) with $K_4[Fe(CN)_6]\cdot 3H_2O$ or $H_4[Fe(CN)_6]$. An ion exchange column was used to eliminate the incorporation of potassium, which was shown to be 1-2% in the powder X-ray data. The resulting crystals diffracted in a cubic unit cell with non-face-centered reflections- deviating from the expected Fm3m space group due to the regularity of the defect sites. The resulting formula was determined to be $Fe_4[Fe(CN)_6]_3\cdot 14\text{-}16H_2O$. The four Fe(III) centers for every three $[Fe^{II}(CN)_6]^{4-}$ moieties make for a charge balanced molecular formula but does not accurately reflect the bonding (every $[Fe^{II}(CN)_6]^{4-}$ moiety is coordinated to six Fe(III) centrals in an octahedral environment to form the cubic structure). As such, the sight defects are not defects at all, and are actually necessary for charge balance throughout the three-dimensional network.[16] Every fourth $[Fe(CN)_6]^{4-}$ site is missing to form the defect and the Fe(III) ions at this site coordinate to water molecules.

Single-crystal X-ray analysis has not been previously reported for soluble Prussian Blue. In 1936, Keggin and Miles performed powder X-ray diffraction on a soluble Prussian Blue sample and determined that alkali atoms reside in the center of small alternating cubes, also known as octants, within the unit cell. The ferrous and ferric ions were arranged at the corners of the cell, with the cyanide ligands on the edges. The cubic lattice had a edge of 5.1 Å and uncoordinated water was suggested to exist in the remaining alternating octants. Later in 1973, Ludi and coworkers described experimental evidence suggesting a modification of the formula proposed by Miles and Keggins. In particular, a closer scrutiny of the lattice parameters, and densities prompted a new formulation, in which alkali metal ions are no longer present in alternating octants of the unit cell. A new formulation was made based on $[Fe^{II}(CN)_6]^{4-}$ vacancy sites. Infrared spectroscopy showing vibrational modes of coordinated water in Prussian Blue analogs corroborated the existence of vacancies. To account for the analytically determined water content, water not bound to the Fe(III) sites were reasoned to be hydrogen bonded to the coordinated water in the otherwise empty octants- making the uncoordinated water zeolitic in nature. Therefore the overall modified formulation proposed by Ludi was $\mathrm{M_k^A[M^B(CN)_6]_l \cdot xH_2O}$, where only the case of k = l = 1 would lead to the formulation proposed by Keggin and Miles.[137]

Presently, many more formulations have been recognized, although insoluble Prussian Blue remains the only compound with a reported crystal structure based on single-crystal X-ray experiments. The exact formulation of soluble Prussian Blue has received different opinions,[144,145] although recent evidence has provided some insight.[141] All other forms can be accessed through reduction or oxidation, which can be carried out on electrodeposited Prussian Blue films onto ITO glass working electrodes by galvanostatic or potentiostatic deposits.[146] Reduction of Prussian Blue occurs at +195 mV in reference to SCE electrode. The white, air-sensitive product contains iron in only the divalent oxidation state with the formula, $K_2FeFe(CN)_6$. This compound is known as “Prussian White” or Everitt’s salt. Oxidation of Prussian Blue occurs at 870 mV vs SCE and exhibits a light green color. Hence the name Berlin’s Green for this compound which is nominally $Fe^{III}Fe^{III}(CN)_6$ with all iron sites in the trivalent oxidation state.[147] Other reports describe “Berlin’s Green” as a compound resulting from partial oxidation of Prussian Blue and consisting of some ratio of an “all trivalent” and a mixed-valence compound, namely $[Fe^{III}Fe^{III}(CN)_6]$ and $[Fe_4[Fe^{II}(CN)_6]_3]_{1-\delta}$.[148] The oxidation at 1100 mV vs SCE is also debated. Oxidation of Berlin's Green forms a dark brown compound, known as "Prussian Yellow," which is described as $FeFe(CN)_6A_x$ (where A is a charge balancing anion and the oxidation states are either 3+ or 4+)[147] or $Fe^{III}Fe^{III}(CN)_6$ which is the full oxidation of Prussian Blue.[148] The exact formulation of Prussian Yellow is currently unclear, although the participation of counter ions is clear as electrogravimetric studies show a mass change in the conversion of Prussian Blue to Prussian Yellow.[149]

From the preceding discussion, it is evident that the chemistry of Prussian Blue is complicated. A systematic study of product formulation is required if we are to exactly understand the composition and accompanying properties. The biological applications of Prussian Blue are of particular importance as the compound has long been recognized as an antidote for internal contamination of radioactive isotopes of cesium[150,151] or thallium[152,153] or heavy element poisoning and is the active pharmaceutical ingredient of the current FDA approved drug product on the market with the trademark, Radiogardase®. After determining the drug to be safe from cyanide release following gastric exposure,[154,155] a fundamental challenge remained that the active pharmaceutical ingredient in the formulated drug product loses efficacy over time as a result of physiochemical changes in the Prussian Blue crystalline material.[150,152] This is important because the United States needs to have sufficient quantities of Prussian Blue in stockpile in preparation for a so-called "dirty bomb" and there is a great cost and waste associated with the cycle of replenishing expired drugs.[156] Thus, the evaluation of new hexacyanoferrate analogs by the FDA is essential for advancing our understanding of the stability and the critical quality attributes of Prussian Blue as a pharmaceutical.

Another area of research that is highly relevant to sample formulation is that of molecular magnetism. Prussian Blue is the first three-dimensional network solid to be studied for its magnetic properties. The Fe(III) centers are high spin, S = 5/2 and the Fe(II) centers are low spin with S = 0. It was found that the compound behaves as a ferromagnet below 5.6 K which was confirmed by coherent magnetic intensity superimposed on neutron powder diffraction peaks,[17] indicating that the spins on the Fe(III) centers are able to communicate via valence delocalization across the 10.17 Ǻ diamagnetic bridge. This superexchange mechanism is related to the mixed-valent charge transfer mechanism proposed by Mayoh and Day whom deem Prussian Blue was a class II[157] compound (explaining its dark blue color).[158] The mechanism relies on partial delocalization of electrons on the Fe(II) onto the neighboring Fe(III) center. Because Fe(III) has the t_{2g} and e_g orbitals exactly half occupied, only spin with a certain orientation will spend time on the Fe(III) site, which is the basis of ferromagnetic coupling calculated by Mayoh and Day.

Prussian Blue is the prototype for demonstrating the viability of the cyanide ion to be an effective bridging ligand for magnetic compounds. Pioneering work by the independent groups of Girolami and Verdaguer revealed that certain Prussian Blue Analogs (PBAs) exhibit spontaneous magnetization and bistability as high as 376 K.[16,159,160] Prussian Blue and its derivatives now constitute a substantial family of materials with interesting properties such as spin-crossover,[161] photo-switchable magnetism,[160,162-164] and charge-transfer induced spin transitions.[165-168] These tunable PBAs hold promise for the field of molecular electronics because the physical properties of these systems undergo reversible and controlled changes in response to external perturbations.

Because of the importance of Prussian Blue in medicinal chemistry and molecular magnetism, this chapter focuses on the intricate chemistry surrounding the preparation and subtle formulation of this important material. The goal is to analyze samples prepared via different synthetic conditions in light of the ambiguity in characterizing various phases of the compound that are known to form. Possible factors of structural variance include different incorporation of potassium and water within the structure.

Currently, the direct synthesis of “insoluble” Prussian Blue, $Fe_4[Fe(CN)_6]_3 \cdot 14\text{-}16H_2O$, involves the addition of a ferric salt (in excess) to potassium ferrocyanide. The excess of iron(III) in the reaction prevents the formation of “soluble” Prussian Blue which contains an alkali metal ion in the structure with the general formula being $MFe[Fe(CN)_6]$ ($M = Na^+, K^+$). However, even under the appropriate conditions, trace amounts of alkali metal ions may still be present using this direct method. To prevent the incorporation of alkali metal ions, early synthetic procedures reported in literature were carried out by adding excess of an acidified solution of a ferric salt to a solution of pure hydroferrocyanic acid or calcium ferrocyanide. More recent and commercially used methods provide an indirect preparation of Prussian Blue.[141] This two-step reaction starts by reacting an iron(II) salt with a hexacyanoferrate(II) salt to form “Prussian White” which has the formula $K_2Fe^{II}[Fe^{II}(CN)_6]$ This white precipitate is then treated with a powerful oxidizing agent such as hydrogen peroxide to give the final Prussian Blue material, $Fe_4[Fe(CN)_6]\cdot 14\text{-}16H_2O$. Single crystals of Prussian Blue were obtained by diffusing water into a concentrated hydrochloric acid solution of iron(II) and $K_4[Fe^{II}(CN)_6]$.[142] The structure reveals that water is bonded to the iron centers at the location of structural defects.

As a starting point for potassium containing Prussian Blue, we noted a recent paper in the literature that described the transformation in morphology of Prussian Blue from cubes to hexapods using microwave assisted oxidation of ferrocyanide in concentrated nitric acid.[169] We employed a similar synthetic procedure and discovered that, depending on the acidic concentration and time of microwave irradiation, formulations ranging from Prussian White to Prussian Blue are attainable. Such a study demonstrates that the term "Prussian Blue" more accurately refers to a continuum of compounds and that any one result is specific for that particular synthetic method. This work to a small extent contradicts the literature[132] in mistakenly referring to the "ideal" formula of Prussian Blue as $Fe_4[Fe(CN)_6]_3\cdot 14\text{-}16H_2O$. Such a case is only one adaptation of the spectrum of possibilities. This work also indicates that Prussian Blue can be tailored to specific formulations, which can provide a direct comparison of samples in the progression of this area of investigation which is of great interest to the FDA.

Experimental Section

Syntheses

The starting materials $FeCl_2$ (Alfa Aesar Lot# C06U005), $K_3[Fe(CN)_6]$ (Fisher Scientific Lot# 730144), $K_4[Fe(CN)_6]\cdot 3H_2O$ (Aldrich, 98.5%), $(NH_4)_2Fe(SO_4)_2$ (Alfa

Aesar), HCl (Macron Chemicals Lot# 11030) and HNO_3 (EMD Chemicals, Lot#52084) were used as received. Ethanol and methanol were of 200 proof ACS grade and used without further purification. All procedures were carried out in a fume hood. Microwave assisted oxidation procedures are adapted from the literature.[169]

Over the course of these studies we realized that the products are best described as an onion-like configuration i.e. containing different surface and core compositions. After the initial discovery that compound **1** exhibits the formula for Prussian White but has a blue color, the formula for the remaining compounds are described as a mixed composition of Prussian White and Prussian Blue: $\{K_2Fe^{II}[Fe^{II}(CN)_6]\}_1\{Fe_4[Fe(CN)_6]_3\cdot 14H_2O\}_X$. The value of X was determined by elemental analysis and/or energy dispersive x-ray spectroscopy. % yields are calculated based on limiting reactant and formula of the product listed.

Preparation of $K_2Fe^{II}[Fe^{II}(CN)_6]$ (1). In a Kimex 500 mL glass jar, 10 mmol (4.22 g) of $K_4[Fe(CN)_6]\cdot 3H_2O$ was dissolved in 495 mL of H_2O. Three jars were charged with starting materials and solvent under the same conditions. To each jar, 5mL of HNO_3 was added dropwise over a 3 minute period using a drop-funnel with manual stirring. Each jar was capped and manually shaken until all of the ferrocyanide dissolved. The caps were then removed from the jars, which were placed inside a conventional microwave oven. The solutions were irradiated at 30 s intervals (30 s on/30 s off) fifteen times. After the last 30 s interval, the samples were irradiated for 55 s intervals (55 s on/55 s off) fifteen times. Following the last 55 s interval, the samples were irradiated once more for 30 s intervals (30 s on / 30 s off) fifteen times. The contents of the jars were cooled to room temperature and left undisturbed for 12 hours. The blue products collected at the bottom of each jar. A 50 mL non-pyrogenic serological pipet was used to decant the clear supernatant. The remaining solids were combined and rinsed with 1000 mL of H_2O and 500 mL of EtOH. The product was collected by centrifugation and dried on a watch glass at 60 °C for 12 hours; yield 4.15 g (80% based on $K_4[Fe(CN)_6]\cdot3H_2O$). Elemental analysis: $K_2Fe_2C_6N_6$, Calc. C 20.90, H 0.00, N 24.29; Found: C 20.90, H 0.00, N 24.26.

Preparation of $\{K_2Fe^{II}[Fe^{II}(CN)_6]\}\{[Fe_4[Fe(CN)_6]_3\cdot14H_2O]_{0.03}\}$ (2). In Kimex 500 mL glass jars, 10 mmol (4.23 g) of $K_4[Fe(CN)_6]\cdot3H_2O$ was dissolved in 490 mL of H_2O. Using a drop funnel, 10 mL HNO_3 was added dropwise over a 3 minute period. The contents of the jars were manually shaken inside a fume hood until all the ferrocyanide had dissolved. The caps was removed from the jars which were placed inside a conventional microwave oven. The solutions were irradiated at 30 s intervals (30 s on / 30 s off) 45 times. The contents of the jars were cooled to room temperature and left to settle for 12 hours. During this time, a blue solid collected at the bottom of the jar. A 50 mL non-pyrogenic serological pipet was used to decant the colorless supernatant. The remaining solid was rinsed with 1 L of H_2O and 500 mL of EtOH. The product was collected by centrifugation and dried on a watch glass at 60 °C for 12 hours, yield: 1.52 g (77.3% based on $K_4[Fe(CN)_6]\cdot3H_2O$).

Preparation of $[K_2Fe^{II}[Fe^{II}(CN)_6]]\cdot[KFe[Fe(CN)_6]\cdot6.2H_2O]_{1.23}$ (3). In a Kimex 500 mL glass jar, 4.24 g of $K_4[Fe(CN)_6]\cdot3H_2O$ was dissolved in 495 mL of H_2O. To this jar was added 5 mL of HNO_3 dropwise over a 3 minute period using a drop funnel with manual stirring. The jar was capped and manually shaken until all the ferrocyanide had dissolved. The jar was placed in a conventional microwave oven after removing the cap. The solution was irradiated at 55 s intervals (55 s on/55 s off) twenty-five times. The contents of the jar were cooled to room temperature and left undisturbed for 12 hours. A blue product settled at the bottom of the jar. A 50 mL non-pyrogenic serological pipet was used to decant the clear supernatant. The remaining solid was rinsed with 1 L of H_2O and 500 mL of EtOH. The product was collected by centrifugation and dried on a watch glass at 60 °C for 12 hours, yield: 1.59 g (71.5% based on $K_4[Fe(CN)_6]\cdot 3H_2O$) Elemental analysis: $K_{3.23}Fe_{4.46}C_{13.38}N_{13.38}H_{15.25}O_{7.63}$, Calcd. C: 20.5; H: 0.7; N: 23.86 % Found C: 21.41; H: 0.16; N: 24.50%.

Preparation of $[K_2Fe^{II}[Fe^{II}(CN)_6]]\cdot[Fe_4[Fe(CN)_6]_3\cdot 14H_2O]_{0.14}$ (4). In a Kimex 500 mL glass jar, 10 mmol (4.23 g) of $K_4[Fe(CN)_6]\cdot 3H_2O$ was dissolved in 484 mL of H_2O. Using a drop funnel, 16 mL of HNO_3 was added dropwise over a 3 minute period. The contents of the jar were manually shaken inside a fume hood until all the ferrocyanide dissolved. The cap was removed from the jar which was placed inside a conventional microwave oven. The solution was irradiated at 30 s intervals (30 s on / 30 s off) 45 times. The contents in the jar were cooled to room temperature and left undisturbed for 12 hours which produced a blue precipitate. A 50 mL non-pyrogenic serological pipet was used to decant the clear supernatant and the solid was rinsed with 1000 mL 1 L of H_2O and 500 mL of EtOH. The product was collected by centrifugation and dried on a watch glass at 60 °C for 12 hours, yield: 1.2 g (62% based on $K_4[Fe(CN)_6]\cdot 3H_2O$).

Preparation of $[K_2Fe^{II}[Fe^{II}(CN)_6]]\cdot[Fe_4[Fe(CN)_6]_3\cdot 14H_2O]_{0.18}$ (5). In a Kimex 500 mL glass jar, 10 mmol (4.23 g) of $K_4[Fe(CN)_6]\cdot 3H_2O$ was dissolved in 492 mL of H_2O. Using a drop funnel, 8 mL of HNO_3 was added dropwise over a 3 minute period with manual stirring. The jar was capped and manually shaken until all the ferrocyanide had dissolved. The cap was then removed from the jar which was placed inside a conventional microwave oven The solution was irradiated at 30 s intervals (30 s on/30 s off) fifteen times. After the last 30 s interval, the sample was irradiated for 55 s intervals (55 s on/55 s off) fifteen times. Following the last 55 s interval, the samples were irradiated once more for 30 s intervals (30 s on/30 s off) fifteen times. The contents of the jars were cooled to room temperature and the contents were left to settle for 12 hours. A blue product collected at the bottom of the jar. A 50 mL non-pyrogenic serological pipet was used to decant the clear supernatant. The remaining solid was rinsed with 1 L of H_2O and 500 mL of EtOH. The product was collected by centrifugation and dried on a watch glass at 60 °C for 12 hours, yield 1.61 g (84% based on $K_4[Fe(CN)_6]\cdot 3H_2O$).

Preparation of $[K_2Fe^{II}[Fe^{II}(CN)_6]]\cdot[Fe_4[Fe(CN)_6]_3\cdot 14H_2O]_{0.26}$ (6). For this synthesis, 4.23 g of $K_4[Fe(CN)_6]\cdot 3H_2O$ was dissolved in 497 mL of H_2O in a Kimex 500 mL glass jar. To this jar was added 3 mL HNO_3 dropwise over a 3 minute period using a drop funnel with manual stirring. The jar was capped and shaken until all the ferrocyanide had dissolved. The yellow solution was stored undisturbed for an aging period of 8 hours. The jar was then placed in a conventional microwave oven after removing the cap. The solution was irradiated at 30 s intervals (30s on/30s off) ten times. The irradiation cycle was then changed to 55 s intervals (55s on/55 s off) 15 times. The contents of the jar were cooled to room temperature and after 12 hours a blue product had collected at the bottom of the jar. A 50 mL non-pyrogenic serological pipet was used to decant the clear supernatant. The remaining solid was rinsed with 1 L of H_2O and 500 mL of EtOH. The product was collected by centrifugation and dried on a watch glass at 60 °C for 12 hours, yield: 0.80 g (42% based on $K_4[Fe(CN)_6]\cdot 3H_2O$).

Preparation of $[K_2Fe^{II}[Fe^{II}(CN)_6]]\cdot[Fe_4[Fe(CN)_6]_3\cdot 14H_2O]_{0.44}$ (7). For this synthesis, 10 mmol (4.22 g) of $K_4[Fe(CN)_6]\cdot 3H_2O$ was dissolved in 497.4mL of H_2O in a Kimex 500 mL glass jar. Three jars were treated under the same conditions. To each jar was added 2.6 mL of HNO_3 dropwise over a 3 minute period using a drop funnel with manual stirring. Each jar was capped and shaken until all the ferrocyanide had dissolved. The caps were then removed from the jars, which were placed inside a conventional microwave oven. The solutions were irradiated at 30 s intervals (30 s on/30 s off) fifteen times. After the last 30 s interval, the samples were irradiated for 55 s intervals (55 s on/55 s off) fifteen times. Following the last 55 s interval, the samples were irradiated once more for 30 s intervals (30 s on/30 s off) fifteen times. The contents of the jars were cooled to room temperature and after 12 hours a blue solid was present. A 50 mL non-pyrogenic serological pipet was used to decant the clear supernatant. The remaining solids were combined and rinsed with 1 L of H_2O and 500 mL of EtOH. The product was collected by centrifugation and dried on a watch glass at 60 °C for 12 hours. The product was placed in a 500 mL Erlenmeyer flask and dissolved in 100 mL of concentrated HCl (Macron Chemicals, Lot# 11030). The resulting green solid and yellow solution turned into a yellow/blue solution after 24 hours. The solution was transferred to a 1 L Erlenmeyer flask containing 500 mL of water which led to the immediate precipitation of a blue precipitate. The resulting mixture was diluted up to 1 L with distilled H_2O. The product settled to the bottom of the flask and was collected using the same centrifugation procedure as described above, yield: 3.94 g (70% based on $K_4[Fe(CN)_6]\cdot 3H_2O$).

Preparation of $[K_2Fe^{II}[Fe^{II}(CN)_6]]\cdot[Fe_4[Fe(CN)_6]_3\cdot 14H_2O]_{18.3}$ (8). In a Kimex 500 mL glass jar, 10 mmol (4.23 g) $K_4[Fe(CN)_6]\cdot 3H_2O$ was dissolved in 464 mL of H_2O. Using a drop funnel, 36 mL HNO_3 was added dropwise over a 3 minute period. The contents of the jar were manually shaken inside a fume hood until all the ferrocyanide had dissolved. The cap was removed from the jar which was placed inside a conventional microwave oven. The solution was irradiated at 30 s intervals (30 s on/30 s off) for 45 times. The contents of the jars were cooled to room temperature and after 12 hours a blue product had collected at the bottom of the jar. A 50 mL non-pyrogenic serological pipet was used to decant the clear supernatant. The remaining solid was combined and rinsed with 1 L H_2O and 500 mL of EtOH. The product was collected by centrifugation and dried on a watch glass at 60 °C for 12 hours, yield: 1.4 g (77% based on $K_4[Fe(CN)_6]\cdot 3H_2O$).

$Fe^{III}_4[Fe^{II}(CN)_6]_3\cdot 27.7H_2O$ (9). Compound **9** was prepared by the addition of 45g (277 mmol) of $FeCl_3$ dissolved in 1 L of H_2O to 22g (59.7 mmol) $K_4Fe(CN)_6\cdot 3H_2O$ dissolved in 1 L of H_2O. which led to an instantaneous formation of a blue solution. The resulting mixture was vigorously stirred for 12 hours and the product was collected by filtration through a Buchner funnel equipped with Whatman 150 mm filter paper. The blue solid was in a 2 L Erlenmeyer flask and rinsed two times with 1500 mL OF H_2O and 300 mL of MeOH. Finally, the solid was collected on filter paper and ground with a mortar and pestle, yield: 8.0 g (69% based on $K_4[Fe(CN)_6]\cdot 3H_2O$). Elemental analysis: $Fe_7C_{18}N_{18}H_{55.4}O_{27.7}$, Calc. C 15.92, H 4.11, N 18.56; Found: C 15.61, H 3.48, N 17.94.

$Fe^{III}_4[Fe^{II}(CN)_6]_3\cdot 20.15\ H_2O$ (10). Sample **10** was prepared by heating sample **9** at 60°C on a glass Pyrex petri dish for 4 hours. The sample was then stored in a glass ampoule that was also heated to 60°C. The ampoule was sealed under a slight vacuum. To obtain elemental analysis, sample **10** was shipped to Atlantic Microlab INC., who were informed to heat the sample to 60°C for 4 hours before performing the analysis. Elemental analysis: $Fe_7C_{18}N_{18}H_{40.3}O_{20.15,}$ Calc. C 17.69, H 3.32, N 20.63; Found: C 17.45, H 2.55, N 19.85.

$Fe^{III}_4[Fe^{II}(CN)_6]_3\cdot 13.75H_2O$ (11). Compound **11** was prepared by heating sample **9** at 90°C on a glass Pyrex petri dish for 4 hours. The sample was then stored in a glass ampoule that was heated at 90°C for four hours. The ampoule was sealed under a slight vacuum. To obtain elemental analysis, sample **11** was shipped to Atlantic Microlab, INC., who were informed to heat the sample at 90°C for 4 hours before performing analysis. Elemental analysis: $Fe_7C_{18}N_{18}H_{27.5}O_{13.75}$, C 19.53, H 2.50, N 22.78; Found: C 18.99, H 1.74, N 22.01.

$Fe^{III}_4[Fe^{II}(CN)_6]_3\cdot 6H_2O$ (12). Iron powder, (2.23 g; 40 mmol), was added to 500 mL of 100 mM $HCl_{(aq)}$. The mixture was stirred vigorously in a 1 L mL Erlenmeyer flask. A solution of ferrocyanide (4.23 g; 10 mmol in 300 mL H_2O) was added to the stirring acid mixture which was refluxed with a condenser apparatus for 2 weeks, yielding Prussian White and then Prussian Blue in succession by the indirect method described in the introduction. The reaction mixture was slowly cooled to room temperature and the resulting precipitate was filtered and washed repeatedly with distilled water. Once the washings were colorless, the product was air-dried at room temperature, yield: 1.1 g (69%

based on $K_4[Fe(CN)_6]\cdot3H_2O$). Elemental analysis: $Fe_7C_{18}N_{18}H_{12}O_6$, Calc. C 22.35, H 1.25, N 26.08; Found: C 21.79, H 0.57, N 24.67.

$Fe^{III}_4[Fe^{II}(CN)_6]_3\cdot8H_2O$ (13). A 16.1 g (39.85 mmol) sample of $Fe(NO_3)_3.9H_20$ and 4.20 g (9.94 mmol) of $K_4Fe(CN)_6\cdot3H_20$ were each dissolved separately in 100 mL of water. The solution of $Fe(NO_3)_3.9H_20$ was added to the solution of $K_4Fe(CN)_6\cdot3H_2O$ with stirring. The mixture instantaneously turned blue in color. The mixture was stirred overnight at room temperature and then left undisturbed for a week. The resulting precipitate was filtered and washed repeatedly with distilled water and air dried at room temperature, yield: 1.0 g. (61% based on $K_4[Fe(CN)_6]\cdot3H_2O$). Elemental analysis: $Fe_7C_{18}N_{18}H_{16}O_{8,}$ Calc. C 21.54, H 1.60, N 25.13; Found: C 21.53, H 1.07, N 25.01.

$K_{1.975}[Fe^{III}_4Fe^{II}_{2.998}(CN)_{18}]\cdot\{10.285H_2O+1.975OH\}$ (14). Samples of 3.4 g (60.9 mmol) of Fe powder and 19.8 g (60.1 mmol) $K_3[Fe(CN)_6]$ were dissolved in 425 mL of a 3.5 M $HCl_{(aq)}$ solution in a 500 mL beaker. The beaker was carefully placed inside a desiccator of water which was sealed with grease and placed in a location where it would not be disturbed. The water slowly diffused into the $HCl_{(aq)}$ solution for two months. After this time period, purple crystals were observed floating on top of the mother liquor. The crystals were retrieved and sent to the Advanced Light Source at Lawrence Berkeley National Laboratory for analysis by synchrotron X-ray diffraction methods.

Instrumentation

Energy dispersive spectroscopic data were collected on an Oxford Instruments ATW type EDS detector with an INCA Energy TEM platform for chemical analysis of elements with Z >/= 5 and elemental mapping using the INCA Semi-STEM mode. The microscope model is a JEOL JEM-2010 transmission electron microscope and was operated at a 200 kV accelerating voltage with a LaB_6 filament. Images were acquired with a Gatan SC1000 ORIUS CCD camera (Model 832), 4008 x 2672 pixels image size (the CCD active area is 36 x 24 mm). Samples for TEM-EDS analysis were prepared by evaporation of colloidal solutions onto 200 Mesh Ted Pella Formvar copper grids.

Magnetic susceptibility measurements were collected using a Quantum Design MPMS-XL SQUID magnetometer. Elemental analyses were performed by Atlantic Microlab, Inc. Thermogravimetric analysis was performed on a Shimadzu TGA-50 Analyzer.

This research was carried out using resources of the Advanced Light Source. The Advanced Light Source is supported by the Director, Office of Science, Office of Basic Energy Sciences, of the U.S. Department of Energy under Contract No. DE-AC02-05CH11231. Data were collected at the research beamline 11.3.1 with the assistance of Dr. Kevin Gagnon at Lawrence Berkeley National Laboratory.

Physical Methods

Single crystal X-ray data were collected at 100 K using Synchrotron radiation ($\lambda = 0.41328$ Å) and a CCD detector. Single crystal X-ray data sets were recorded as ω-scans at 0.5° step width. Integration was performed with the Bruker SAINT Software package and absorption corrections were empirically applied using SADABS.[170] Using Olex2,[171] the structure was solved with the ShelXT[172] structure solution program using Direct Methods and refined with the ShelXL[173] refinement package using Least Squares minimization. Images of the crystal structure were rendered using the crystal structure visualization software DIAMOND.[174]

DC magnetic susceptibility measurements were performed under an applied field of 1000 Oe over the temperature range 2-300 K. The data were corrected for diamagnetic contributions of the sample holder and the sample calculated from Pascal's constants.

Results and Discussion

The first part of this chapter involves the structural studies of potassium containing or "soluble Prussian Blue", as analyzed by TEM-EDS and elemental analysis. The second part covers the TGA and elemental analysis of insoluble Prussian Blue. The primary goal of these studies was to verify the importance of the exact synthetic procedure in order to obtain a specific product formulation. The final portion of this chapter describes the first single-crystal X-ray structure of the so-called "soluble Prussian Blue" the results of which are compared to recent synchrotron powder X-ray data reported in the literature.[145]

Syntheses

Lee and coworkers recently reported that "soluble" Prussian Blue can be made by microwave-assisted oxidation of ferrocyanide.[169] Prussian Blue products were prepared from this method using different concentrations of HNO_3. A continuum of possible product formulations were reported, ranging from "soluble Prussian Blue", $KFe^{III}[Fe^{II}(CN)_6]$, when 80 mM HNO_3 was used to "insoluble Prussian Blue", $Fe^{III}_4[Fe^{II}(CN)_6]_3\cdot14H_2O$, when 570 mM HNO_3 was used in the synthesis. The authors compared the powder patterns of the products with insoluble Prussian Blue and also $KMn^{3+}[Fe^{2+}(CN)_6]$, because they claimed they could not find any structural powder data on soluble Prussian Blue in the literature despite the existence of such data.[145] Importantly, using HNO_3 at intermediate concentrations (160-480 mM) led to XRD peaks of both soluble and insoluble Prussian Blue, results that imply the formation of "onion-like" particles consisting of layers of soluble and insoluble Prussian Blue according to the data reported in this chapter. An increase in the nitric acid concentration was found to alter the morphology of the particles by specific preferential etching along the {111} planes of the crystal. This preference also suggests that the portions of the particle that do not lie along the {111} plane may remain unchanged giving rise to a layered or multi-configurational formulation.

Armed with the above information as a backdrop, we adapted the microwave-assisted synthesis of soluble Prussian Blue the results of which demonstrate that the amount of potassium ions in the framework can be tuned. We have also prepared insoluble Prussian Blue samples using both the direct and indirect methods to show that the level of hydration can vary. Thermal gravimetric analysis has been reported for Prussian Blue in literature.[175] From these TGA data and the crystal structure it is known that some water molecules are coordinated to the iron centers inside the structure while a varying amount can be present in the zeolitic-like positions.[175]

Characterizations of Soluble Prussian Blue

Transmission electron microscopy equipped with Energy-dispersive X-ray spectroscopy (TEM-EDS) is a powerful analytical technique that can be used for elemental analysis. The basic idea involves the interaction of an incident electron beam with the sample. An incident electron bombards the sample ejecting an inner (K)-shell electron leaving behind a hole. Outer-shell electrons fill this hole, generating X-rays with characteristic wavelengths of the element in accord with the difference in energy between the two shells. The TEM has a particular advantage over other microscopes, such as SEM that also employ EDS, in that the electron beam can be focused to a particular location on a given sample. The technique therefore does not provide elemental mapping, but rather local elemental compositions.

$K_2Fe^{II}[Fe^{II}(CN)_6]$ (1). The reported procedure of the microwave assisted oxidation of ferrocyanide results in the formulation of Turnbull's Blue, $KFe^{III}[Fe^{II}(CN)_6]$.[169] Following a similar synthesis as detailed for **1** resulted in a different product formulation than expected. The potassium to iron ratio was in perfect agreement with the formula for Prussian White, Figure 2.2. These results were surprising because of the light blue hue of compound **1**, which is contrary to the reported air-sensitive all iron(II) compound. In addition, the elemental analysis of CHN content complements the EDS data suggesting one potassium atom per iron atom, Table 2.1. The reported SEM-EDS analysis on an analogous product is actually in agreement with our formulation. Lee and Huh report EDS data with the following observed (calculated) atomic %: C, 31.6 (40.0%); N, 42.4 (40.0%); K, 12.3 (6.7%); Fe, 13.7 (13.3%); O, 0.0 (0.0%).[169] The potassium content is nearly double the value of what they calculated. Additionally, the potassium ions in soluble Prussian Blue does not fully occupy the channels, which should therefore contain water molecules. The reported oxygen content is 0%, which further undermines their conclusions.

Table 2.1 Elemental analysis for compound **1**.

Element	Calculated	Found
C	20.83	20.90
H	0.00	0.00
N	24.29	24.26

Elemental Analysis: The experimental carbon, hydrogen, and nitrogen content are in accord with the formula assignment. Calculated column is for $K_2Fe^{II}[Fe^{II}(CN)_6]$.

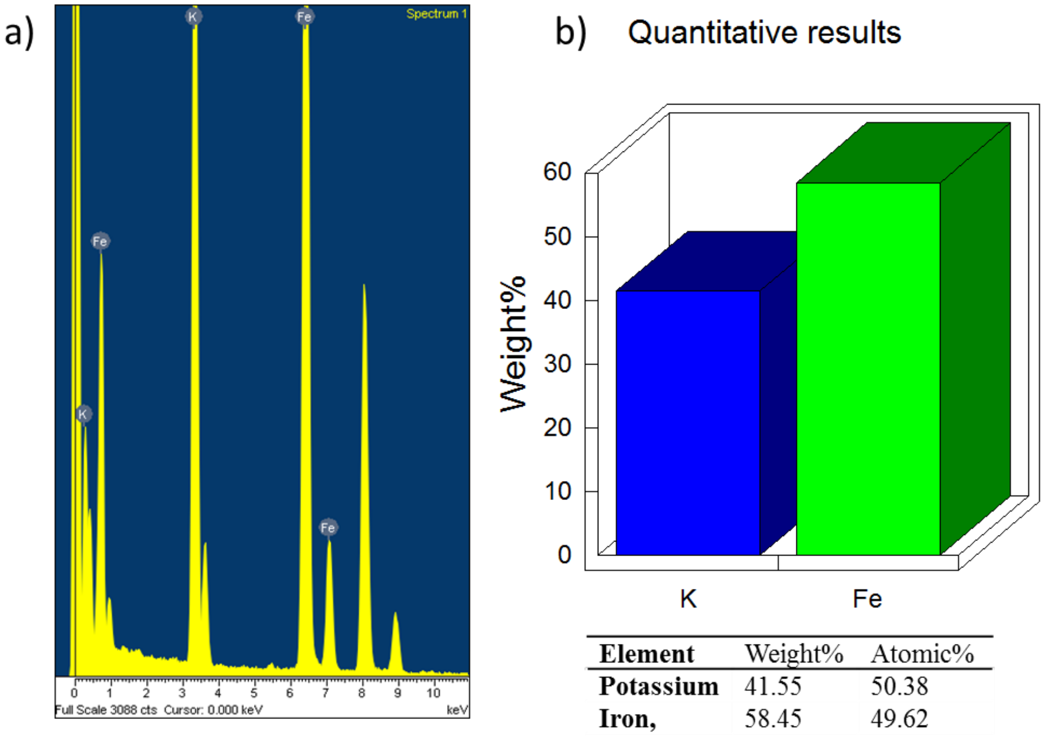

Element	Weight%	Atomic%
Potassium	41.55	50.38
Iron,	58.45	49.62

Figure 2.2 a) EDS spectrum of compound **1** and b) relative weight % of potassium and iron based on peak intensities in spectrum. Corresponding atomic % for K^+ and Fe(II) are 50.38 % and 49.62 %, respectively. The experimental composition of the sample is consistent with the formula $K_2Fe[Fe(CN)_6]$.

Given that compound **1** is air-stable, we propose that a small surface layer of Prussian Blue protects the inner composition of the particles in a similar fashion to the layers of an onion. Scanning electron microscopy, Figure 2.3, shows that soluble Prussian

Blue particles are cubic in shape with polydisperse micron to sub-micron dimensions. The electron microprobe imaging, Figure 2.4, shows that the particles form aggregates composed of layers which supports the theory of an onion-like structure. The potassium ions may also play a vital role in protecting the integrity of the internal structure. Thermal gravimetric analysis performed on compound **1**, Figure 2.5, revealed no water loss and minimal sample decomposition over the temperature range of 25-300 ^{o}C. This observation is contrary to the hydration studies of Prussian Blue which indicate that the compound decomposes after ~150 ^{o}C.[175] The structure of insoluble Prussian Blue is associated with 14-16 moles of water due to the presence of site defects and open zeolitic positions in the channels.[142] The structure of “Prussian White” has potassium ions in every cavity, which occupies most of the space that water could occupy in similar compounds, such as Turnbull’s Blue as described above, which has potassium ions located in tetrahedral holes of the cubic framework.

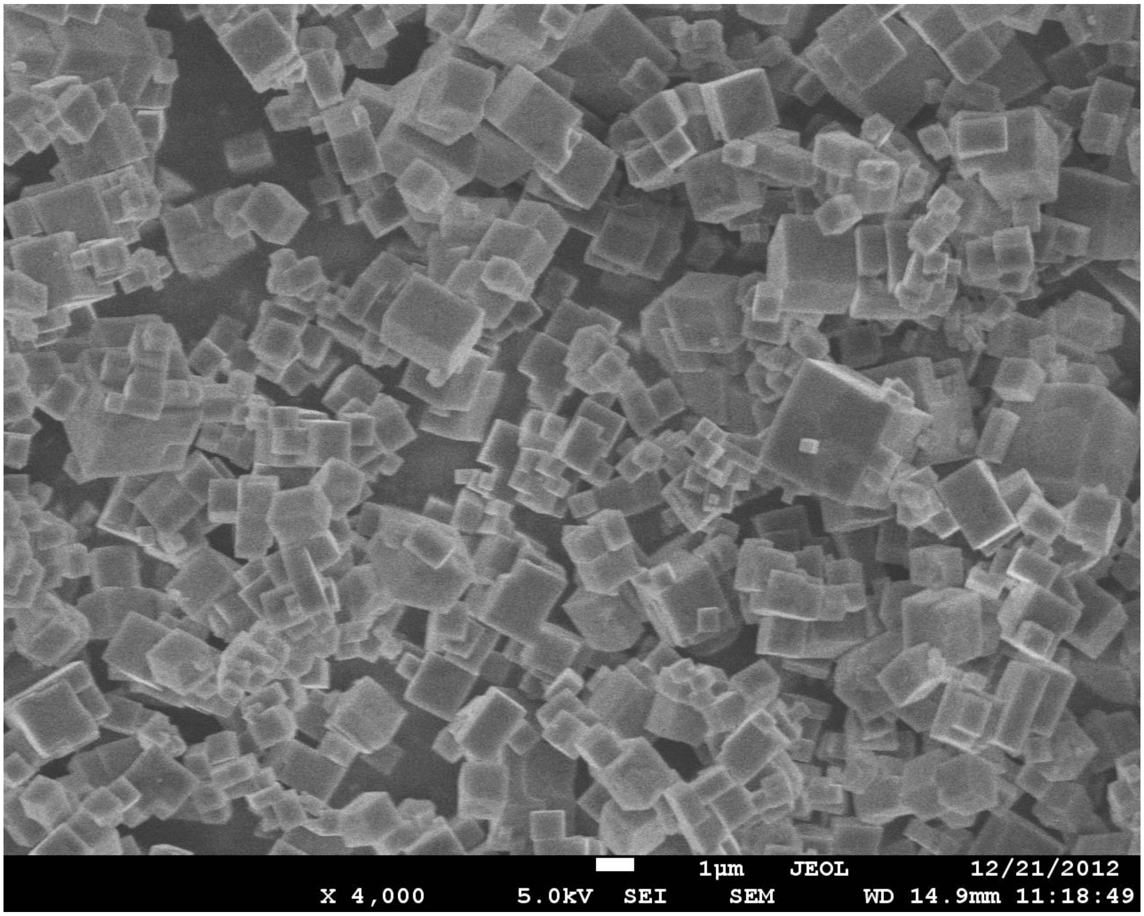

Figure 2.3. SEM image of bulk particles of compound **1** which are cubic and in the micrometer regime. The measuring bar is in the bottom-middle of image and is 1 micrometer.

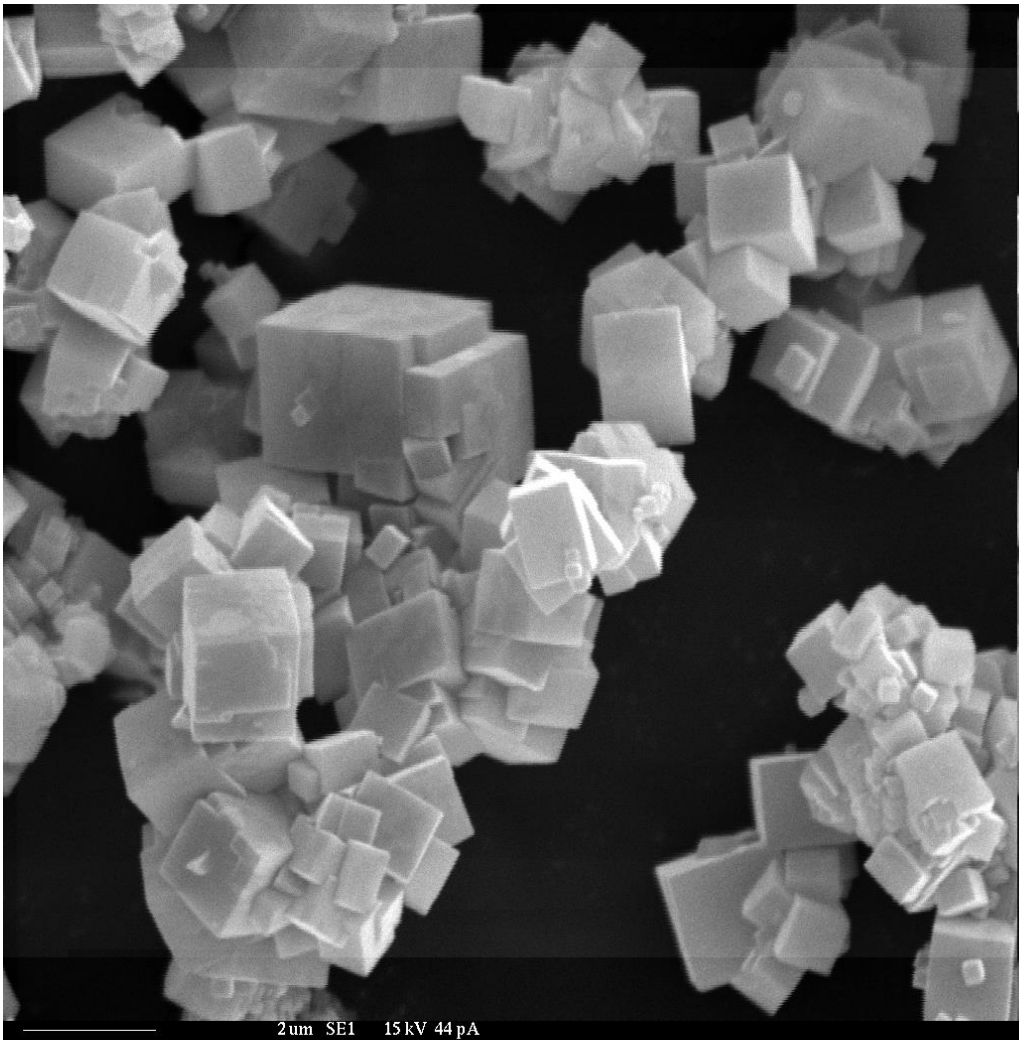

Figure 2.4 Electron Microprobe image of **1** that shows particle conglomeration. Measuring bar in bottom left corner is 2 micrometers in length.

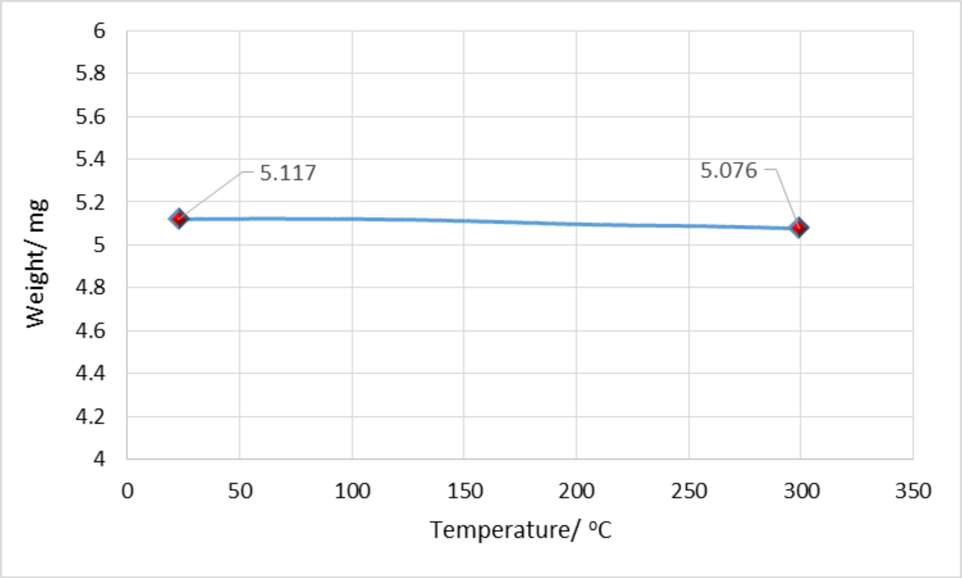

Figure 2.5 Thermal gravimetric analysis of compound **1** showing negligible weight loss from 25 to 300 °C.

Because the blue color of the compound indicates mixed-valency for the Fe centers, magnetic data were collected on the sample in an attempt to ascertain the spin states. The χT vs T plot is shown in Figure 2.6. The magnetic susceptibility at room temperature is 4.31 emu·K·mol^{-1} based on the formula weight of Prussian White, $K_2Fe[Fe(CN)_6]$. As the temperature is decreased, the χT value remains constant until approximately 25 K at which point there is an abrupt increase to 32.8 emu·K·mol^{-1}. The 1/ χ vs T plot was fit with a Weiss constant, $\theta = +3.5$. These results indicate ferromagnetic interactions consistent with the Prussian Blue material. The room temperature χT value can be modeled with a high spin Fe(II) center (S = 2, g = 2.44), but this does not account for the white versus blue color when comparing reports of “Prussian White” with **1**. Another possibility for the formulation of **1** is $K_2Fe^{III}[Fe^{II}(CN)_6]\cdot(OH^-)$. The hydroxide ion counters the extra positive charge from making the nitrogen bound iron trivalent. The potassium ions could occupy all octants of the unit cell, or may also be located in the defect sites. The formula is similar to Turnbull's Blue, $KFe^{III}[Fe^{II}(CN)_6]\cdot xH_2O$, except there is an extra potassium ion and the water becomes hydroxide. Adjusting the molecular weight to include the hydroxide ion raises the χT plot to a room temperature value of 4.53 emu·K·mol^{-1}, which is in close agreement with $S = 5/2$ and $g = 2.04$. The formula, $K_2Fe^{III}[Fe^{II}(CN)_6]\cdot(OH^-)$, therefore corroborates the magnetic and TEM-EDS data, but the elemental analysis is slightly off: Calc. $K_2Fe_2C_6N_6O_1H_1$, C: 19.85; H: 0.28; N: 23.15%, Found: C: 20.90; H: 0.00; N: 24.26 %. The light blue color is consistent with a mixture of dark blue and white from Prussian Blue and Prussian White, respectively.

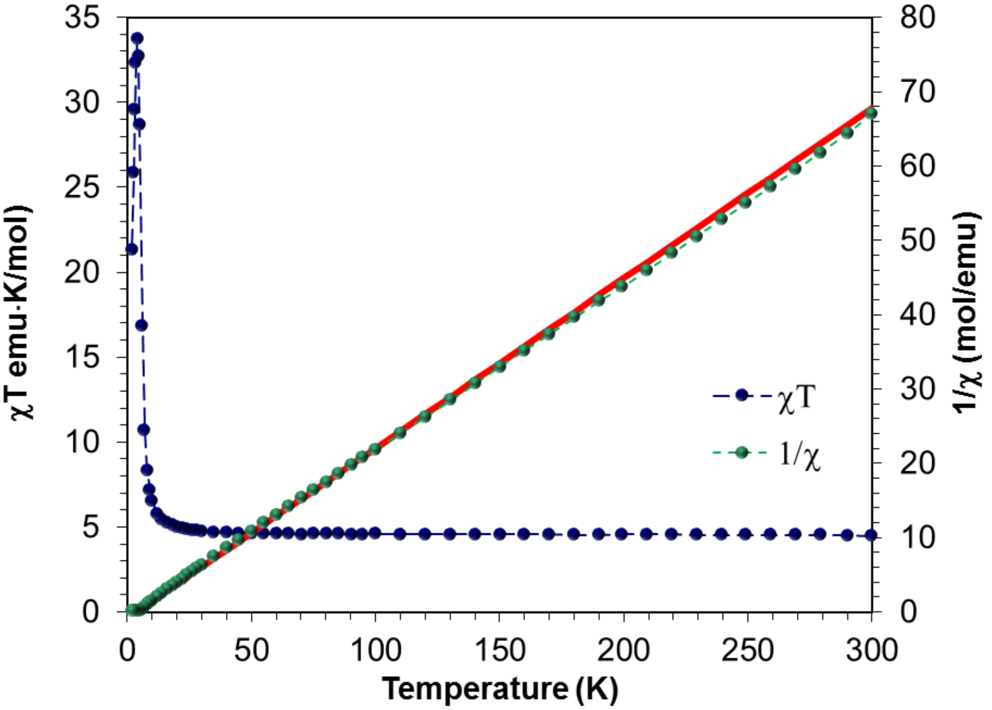

Figure 2.6 χT vs T plot and 1/ χ vs T plot for compound **1**. Red lines correspond to the best fit with Curie-Weiss law with θ = 3.5.

$[K_2Fe^{II}[Fe^{II}(CN)_6]]\cdot[Fe_4[Fe(CN)_6]_3\cdot 14H_2O]_{0.11}$ (2). The TEM-EDS analysis for compound **2** gives potassium and iron weight % of 39.07 and 60.93 %, respectively. These values are between the expected values for Prussian White and Turnbull's Blue, Figure 2.7, but closer to Prussian White. The increased concentration of nitric acid used in the synthesis leads to a greater extent of oxidation of the Fe(II) ions. Because of the proposed onion-like structure, the formulation for the compound is identified as being similar to reports of "Berlin's Green",[148] in that the material exists as a ratio of "Prussian Blue" to "Prussian White". Using the TEM-EDS results, the formula for **2** was determined to be $[K_2Fe^{II}[Fe^{II}(CN)_6]]\cdot[Fe_4[Fe(CN)_6]_3\cdot 14H_2O]_{0.11}$.

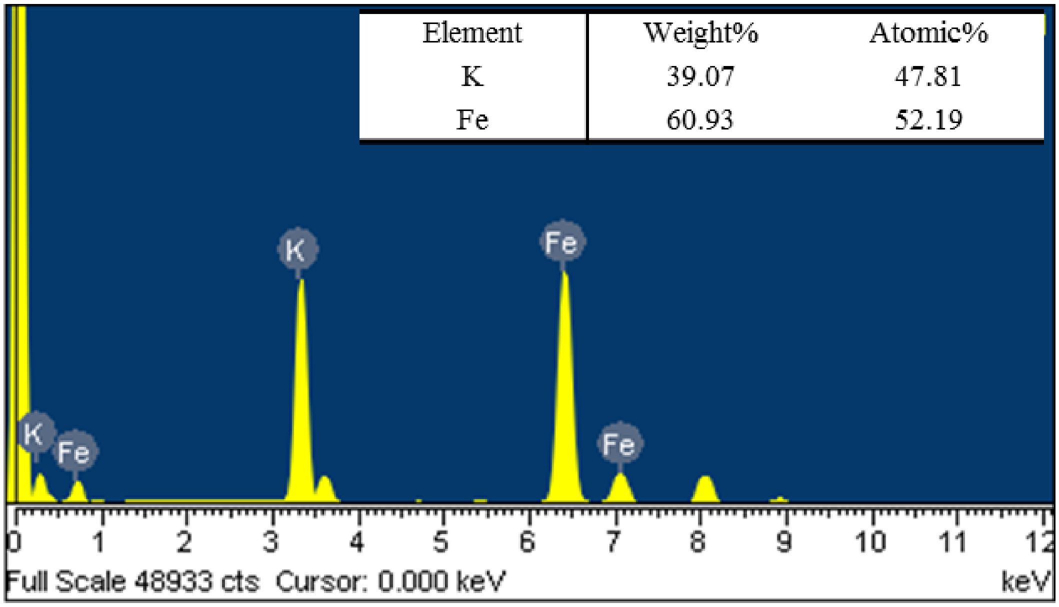

Element	Weight%	Atomic%
K	39.07	47.81
Fe	60.93	52.19

Figure 2.7 TEM-EDS data for compound **2**. Relative weight and atomic % are given in the inset, which were determined by Cliff Lorimer thin ratio section quantitation method.

$[K_2Fe^{II}[Fe^{II}(CN)_6]]\cdot[KFe[Fe(CN)_6]\cdot6.2H_2O]_{1.23}$ (3). The TEM-EDS data for compound **3**, Figure 2.8, resulted in a potassium and iron weight % of 32.15 and 67.85, respectively. These values are intermediate for “Prussian White” and “Turnbull’s Blue”. The formula, $[K_2Fe^{II}[Fe^{II}(CN)_6]]\cdot[Fe_4[Fe(CN)_6]_3\cdot14H_2O]_{0.11,}$ was proposed based on the weight % but elemental analysis resulted in CHN content that did not equate to the proposed formula. A combination of the expected water content from elemental analysis with the ratios from TEM-EDS suggest that 6.2 moles of water are present in the structure. Prussian Blue has more 14-16 water molecules and, therefore, the product formula was adjusted as a combination of Prussian White and soluble Prussian Blue: $[K_2Fe^{II}[Fe^{II}(CN)_6]]\cdot[KFe[Fe(CN)_6]\cdot6.2H_2O]_{1.23}$. The calculated CHN content are now much closer to experimental data: Calcd. C: 21.98; H: 0.16; N: 25.63 % Found C: 21.41; H: 0.16; N: 24.50%.

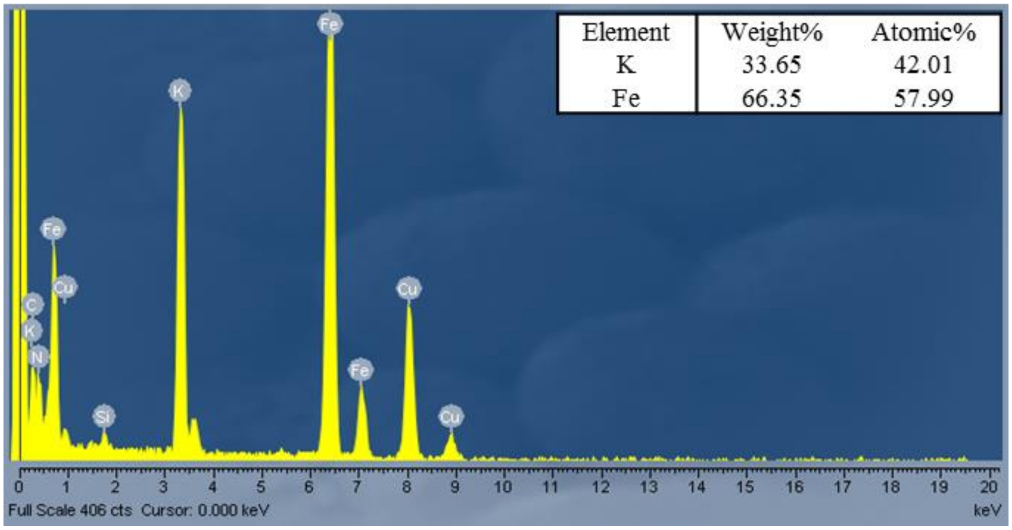

Element	Weight%	Atomic%
K	33.65	42.01
Fe	66.35	57.99

Figure 2.8 TEM-EDS data for compound **3**. Relative weight and atomic % are given in the inset, which were determined by Cliff Lorimer thin ratio section quantitation method.

$[K_2Fe^{II}[Fe^{II}(CN)_6]]\cdot[Fe_4[Fe(CN)_6]_3\cdot14H_2O]_{0.14}$ (4). The potassium and iron weight % for compound **4** provide convincing evidence of a layered structure for Prussian Blue prepared by microwave irradiation. The edge of a particle was analyzed as shown in Figure 2.9 and then the electron beam was focused over the bulk of the particle which caused the crystalline cubic particle to crack. EDS spectra were then acquired on the freshly exposed surfaces, revealing a different composition than the first obtained spectrum. The electron beam causing sample destruction has been noted in literature.[176] Originally, the edge of the particle exhibited a weight percent ratio of 8.02 and 91.98 for potassium and iron respectively. After fracturing, the particle was measured at two different locations within the broken plane. The potassium and iron content changed to 28.11 and 71.89 and 32.15 and 67.85, respectively. The formulations for these inner shell compositions were determined to be $[K_2Fe^{II}[Fe^{II}(CN)_6]]\cdot[Fe_4[Fe(CN)_6]_3\cdot14H_2O]_{0.23}$ and $[K_2Fe^{II}[Fe^{II}(CN)_6]]\cdot[Fe_4[Fe(CN)_6]_3\cdot14H_2O]_{0.14}$, respectively. Both are quite different from each other, suggesting a very complex internal structure. Another possibility is that the difference in measurement time between the two exposed surfaces caused different amounts of oxidation between the two sites but this is not as plausible as the conclusion that the internal surface is of a very different composition.

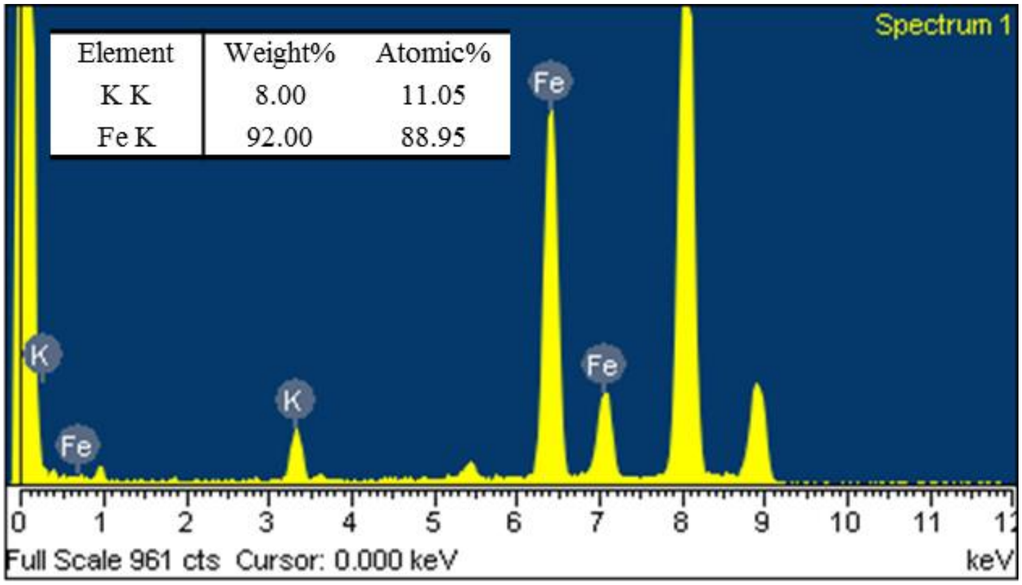

Element	Weight%	Atomic%
K K	8.00	11.05
Fe K	92.00	88.95

Figure 2.9 TEM-EDS data for the particle edge of compound **4**. Relative weight and atomic % are given in the inset, which were determined by the Cliff Lorimer thin ratio section quantitation method.

$[K_2Fe^{II}[Fe^{II}(CN)_6]]\cdot[Fe_4[Fe(CN)_6]_3\cdot 14H_2O]_{0.18}$ (5). The reaction procedure for **5** was identical to that of compound **1**, except a 265 mM $HNO_{3(aq)}$ solution was used instead of 83 mM $HNO_{3(aq)}$. The potassium and iron content, Figure 2.10, of 30.15 and 69.85 %, respectively, for **5** is consistent with a higher concentration of Fe(III) ions, although the quantities are still less than what is expected for Turnbull's Blue formulation. The best fit for the EDS data provided the formula of 0.18 insoluble Prussian Blue molecules for every Prussian White molecule. An 80 mM $HNO_{3(aq)}$ is reported to yield soluble Prussian Blue.[169]

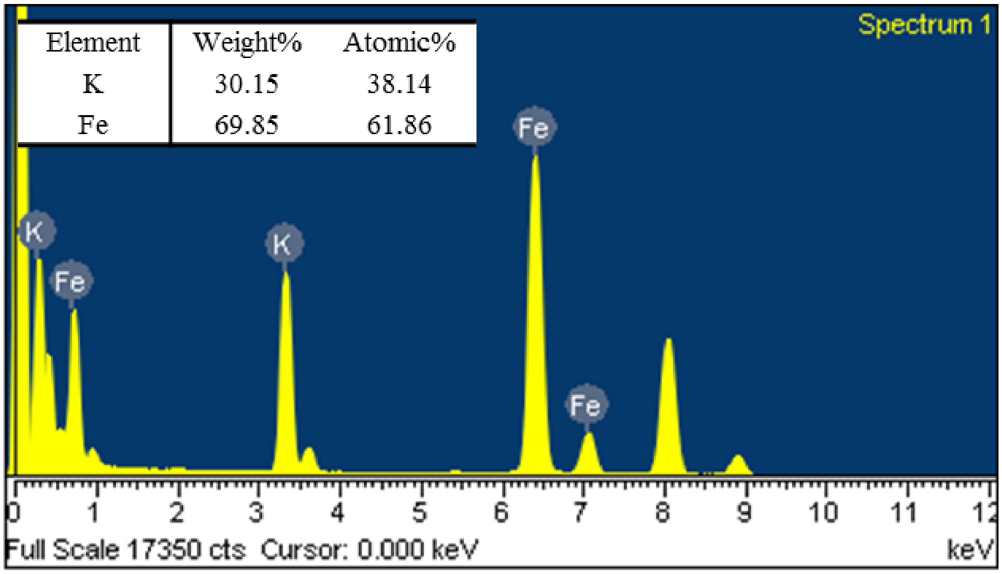

Element	Weight%	Atomic%
K	30.15	38.14
Fe	69.85	61.86

Figure 2.10 TEM-EDS data for outer-shell of compound **5**. Relative weight and atomic % are given in the inset which were determined by the Cliff Lorimer thin ratio section quantitation method.

$[K_2Fe^{II}[Fe^{II}(CN)_6]]\cdot[Fe_4[Fe(CN)_6]_3\cdot14H_2O]_{0.21}$ (6). The synthesis of compound **6** was performed in a 50 mM $HNO_{3(aq)}$ ferrocyanide solution. Despite a lower concentration of nitric acid, compound **6** has a higher Fe(III) content and, in fact, the potassium and iron content (28.71% and 71.29%, Figure 2.11) is closer to the formula of Turnbull's Blue. This result is attributed to an intermediate aging period during which the iron atoms are slowly oxidized. This assertion is based on literature reports of product synthesis being affected by the relative proportion of the starting reagents, the atmosphere, the rate of formation of the intermediate Berlin White, and the aging of the precipitate before oxidation.[141]

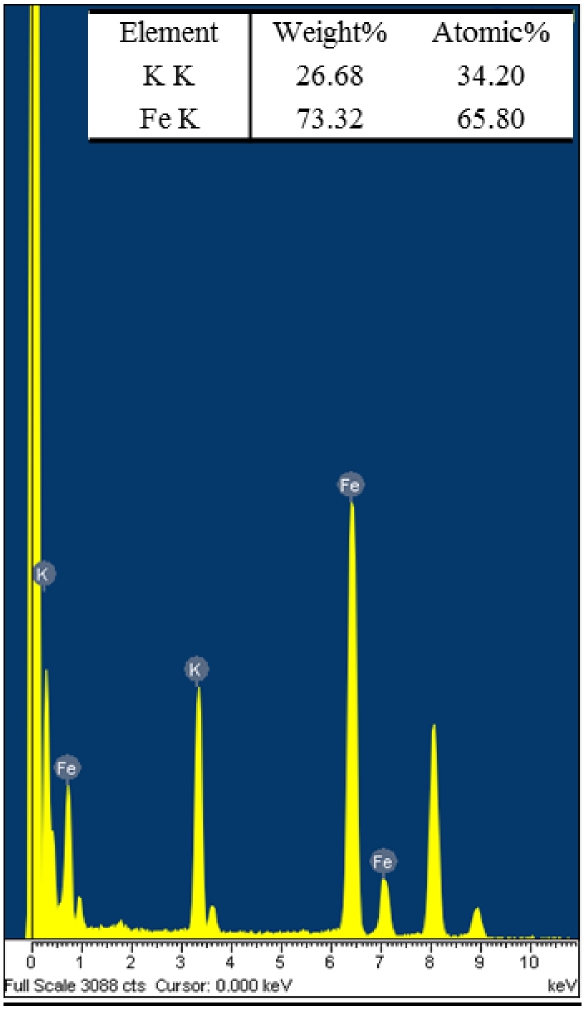

Element	Weight%	Atomic%
K K	26.68	34.20
Fe K	73.32	65.80

Figure 2.11 TEM-EDS data for outer-shell of compound **6**. Relative weight and atomic % are given in the inset, which were determined by the Cliff Lorimer thin ratio section quantitation method.

$[K_2Fe^{II}[Fe^{II}(CN)_6]]\cdot[Fe_4[Fe(CN)_6]_3\cdot 14H_2O]_{0.44}$ (7). Samples of **7** indicate the formation of Berlin's Green with the recrystallization step performed in concentrated $HCl_{(aq)}$. The mixture of Berlin's Green transformed back to Prussian Blue after sitting for 24 hours. Precipitation of the product was achieved in water. The EDS analysis, Figure 2.12, of the dark blue pigment led to potassium and iron weight % values of 21.47% and 78.53%, respectively, along with substantial chloride content. Previous literature had reported that the presence of the chloride ion is unimportant and, in fact, the Cl^- ion was completely neglected in the discussion of product formation, despite an EDS analysis revealing the presence of this anion in the products.[145] The reasoning was that the locations of the Cl^- ions were impossible to pinpoint and that they do not play a role in the ionic mechanism of potassium incorporation into the site defect locations. Ignoring the chloride content gives the formula $[K_2Fe^{II}[Fe^{II}(CN)_6]]\cdot[Fe_4[Fe(CN)_6]_3\cdot 14H_2O]_{0.44}$ for **7**. However, more recent evidence revealed that a KCl electrolyte solution does participate in the Prussian Blue formation process - a conclusion reached after monitoring *in situ* electrochemical reactions inside carbon nanotubes by electrochemical quartz crystal microbalance measurements.[177] Therefore, the potential for chloride incorporation into these materials represents a new direction for this field and another level of complexity. Reports on soluble Prussian Blue suggest that hydroxide ions are incorporated in the structure to charge balance excess potassium.[141,145] It is reasonable to expect that the charge balancing OH^- ions are replaced by Cl^- ions upon treatment with a chloride source such as KCl or $HCl_{(aq)}$.

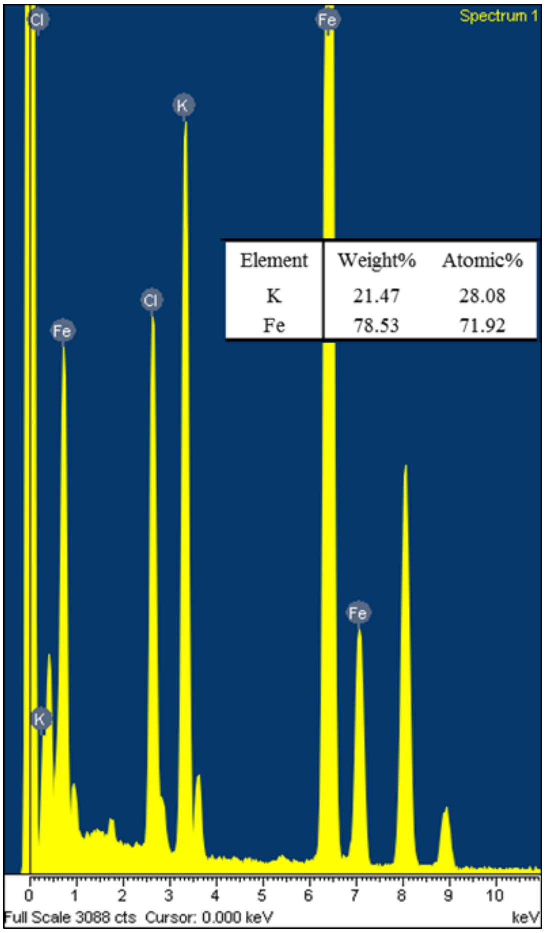

Element	Weight%	Atomic%
K	21.47	28.08
Fe	78.53	71.92

Figure 2.12 TEM-EDS data for the outer-shell of particles of compound **7**. Relative weight and atomic % are given in the inset, which were determined by the Cliff Lorimer thin ratio section quantitation method.

$[K_2Fe^{II}[Fe^{II}(CN)_6]]\cdot[Fe_4[Fe(CN)_6]_3\cdot 14H_2O]_{18.3}$ (8). A 1725 mM solution of nitric acid solution was prepared in the synthesis of **8**. The EDS spectrum, Figure 2.13, shows a very small level of potassium content with a potassium to iron weight % of 1.07 to 98.93%. The compound is perhaps better described as Prussian Blue with a small amount of potassium absorbed. The best fit based on the EDS data suggest there are 18.3 molecules of Prussian Blue for every molecule of Prussian White. The color of the compound is dark purplish blue.

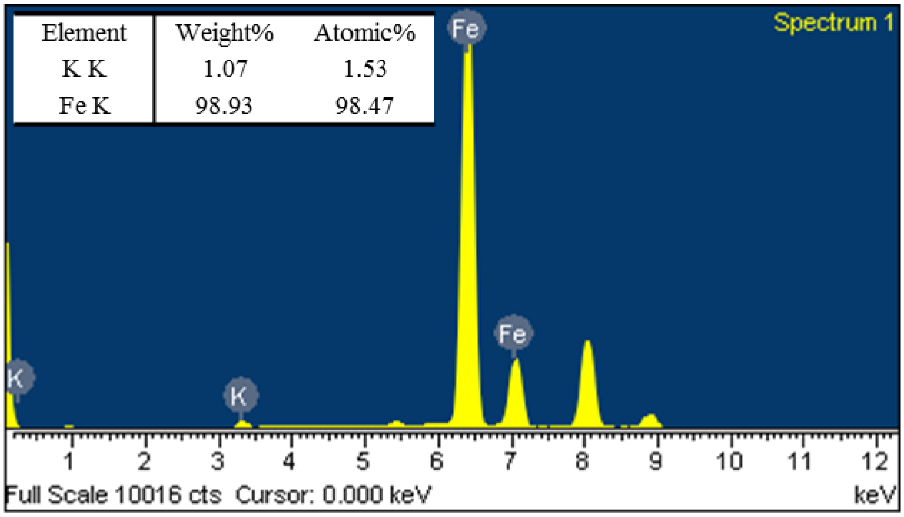

Element	Weight%	Atomic%
K K	1.07	1.53
Fe K	98.93	98.47

Figure 2.13 TEM-EDS data for the outer-shell of particles of compound **8**. Relative weight and atomic % are given in the inset, which were determined by the Cliff Lorimer thin ratio section quantitation method.

The compilation of EDS data is given in Table 2.2. It is clear that a spectrum of possibilities in product formation are possible. The novel aspect of this work is the fact the Prussian White can be synthesized and be made air-stable with an apparent small outer layer of Prussian Blue preventing its decomposition. With all other factors being constant, the microwave-assisted syntheses of different soluble Prussian Blue analogs is directly related to the concentration of the nitric acid. Compound **6** reveals that the aging step, or rate at which the Fe(II) ions in ferrocyanide dissociate and oxidize, is of vital importance. The source of composition variance in Prussian Blue analogs can be attributed to this aging process. Dissolving soluble Prussian Blue in concentrated hydrochloric acid can incorporate chloride anions into the structure upon recrystallization in water, but there is currently no model to account for this problem.

Table 2.2 Product formulae based on relative ratio (weight %) of potassium to iron.

TEM-EDS Weight Percentages			
Compound	**Formula**	**Potassium**	**Iron**
	Prussian Blue*	0	100
8	$[K_2Fe^{II}[Fe^{II}(CN)_6]]\cdot[Fe_4[Fe(CN)_6]_3\cdot 14H_2O]_{18.3}$	1.07	98.93
4	$[K_2Fe^{II}[Fe^{II}(CN)_6]]\cdot[Fe_4[Fe(CN)_6]_3\cdot 14H_2O]_{2.0}$	8.02	91.98
7	$[K_2Fe^{II}[Fe^{II}(CN)_6]]\cdot[Fe_4[Fe(CN)_6]_3\cdot 14H_2O]_{0.44}$	21.47	78.53
	Turnbull's Blue*	25.92	74.07
6	$[K_2Fe^{II}[Fe^{II}(CN)_6]]\cdot[Fe_4[Fe(CN)_6]_3\cdot 14H_2O]_{0.26}$	26.68	73.32
4	$[K_2Fe^{II}[Fe^{II}(CN)_6]]\cdot[Fe_4[Fe(CN)_6]_3\cdot 14H_2O]_{0.23}$	28.11	71.89
5	$[K_2Fe^{II}[Fe^{II}(CN)_6]]\cdot[Fe_4[Fe(CN)_6]_3\cdot 14H_2O]_{0.18}$	30.15	69.85
4	$[K_2Fe^{II}[Fe^{II}(CN)_6]]\cdot[Fe_4[Fe(CN)_6]_3\cdot 14H_2O]_{0.14}$	32.15	67.85
3	$[K_2Fe^{II}[Fe^{II}(CN)_6]]\cdot[KFe[Fe(CN)_6]\cdot 6.2H_2O]_{1.23}$	33.65	66.35
2	$[K_2Fe^{II}[Fe^{II}(CN)_6]]\cdot[Fe_4[Fe(CN)_6]_3\cdot 14H_2O]_{0.03}$	39.07	60.93
	Prussian White*	41.18	58.82
1	$K_2Fe^{II}[Fe^{II}(CN)_6]$	41.55	58.45

*Calculated weight ratios for Prussian Blue, Turnbull’s Blue, and Prussian White. Fill color designates approximate color of the products surrounding the particular analog.

Characterizations of Insoluble Prussian Blue

Our goal in this part of the research was two-fold: (1) to show that the water content can be controlled through heating insoluble Prussian Blue, and (2) to show that different sample preparations lead to products with different levels of hydration. An overarching goal of this chapter is to emphasize that discussions about Prussian Blue must acknowledge structural variance in order to conclude anything definitive with regards to structure and composition. To ignore the reality of how complex these materials are is to add only more conflicting reports to the ones already present in the literature. Much of the previous work on Prussian Blue has been carried out with oversimplification of the results.

Two important studies in the literature have previously addressed the issue of hydration levels in Prussian Blue.[17,175] The first report was published in 1980 by Herren and coworkers who used powder neutron diffraction on four different hydrated states of Prussian Blue, including deuterated forms. Of the 14-16 molecules from the crystal structure, 6 were found to be coordinated to the Fe(III) sites in the vacant positions of ferrocyanide. The remaining water molecules were found to reside at the center of the cell octants, or hydrogen bonded to coordinated water molecules within the interstitial channels. Moreover, the structure of Prussian Blue was refined as a superposition of ordered substructures. Because the exact hydrogen bonding network could not be determined due to large incoherent background scattering of the protons, the authors used a stepwise approach of determining the solution of the structures of dehydrated, 33% deuterated, fully deuterated, and protonated samples with consecutive application of difference Fourier calculations. The data were refined in the Fm-3m space group, as the distribution of light atoms are less affected by vacancies when using powder neutron diffraction.[17]

The second literature report covering the hydrated forms of Prussian Blue was reported by Sanjukta and coworkers in 1983. In this study, time-dependent rehydration studies led to four distinct levels of hydration and the activation energies were determined using ^{1}H-NMR spectroscopy. The Prussian Blue sample was cycled twice between room temperature and 150 ^{o}C. The sample was then cooled back to room temperature over the course of 2 hours in air. After 3 cycles of rehydration, the TGA changed from showing a continuous loss of water to a step-like plot with three regions of stability. The authors concluded that due to the loss of water and step-like TGA curve, Prussian Blue can exist as well defined hydrates.

Herein, we report our hydration studies of Prussian Blue taking into account the heating of one sample, and the variance across samples prepared by different synthetic methods. The temperature range for the TGA studies was ramped from 25 to 400 ^{o}C at 2^{o}C per minute. The weights of the samples were monitored as a function of temperature. Data points of interest on the TGA curves corresponding to plateaus or near-zero slopes are marked in red diamonds. The tables accompanying each figure shows the calculated amount of water corresponding to a given weight-loss percentage between two red diamonds, as well as the weight loss between the first red diamond and the green square (starting at lowest temperature). The green squares represent the water content calculated from the mass loss that would be needed to obtain the corresponding water content from elemental analysis.

$Fe^{III}_4[Fe^{II}(CN)_6]_3 \cdot 27.7H_2O$ (9). Most synthesis procedures of Prussian Blue involve the use of acidic solutions to obtain crystalline materials. In the synthesis of **9**, two water soutions of ferrocyanide and ferric chloride were added together and stirred for 12 hours. While this procedure is noted to yield amophorous products, the elemental and TGA formulations, Figure 2.14, suggest that a large amount of water can be incoroprated into the channels and defect sites. This particular synthetic procedure shows that approximately 30 water molecules are incorporated into the material. The last step of grinding with a mortar and pestal may play a vital role in exposing more surface area for water to be absorbed. The elemental analysis suggest that water still remains in the framework after the first plateau at 220 °C. The reason is due to the tightly bound water molecules in the defect sites which are bonded to the Fe^{III} ions. Unfortunately, the decrease in weight loss after 220 °C is continuous, thus rendering water loss and sample decomposition indiscernible from each other.

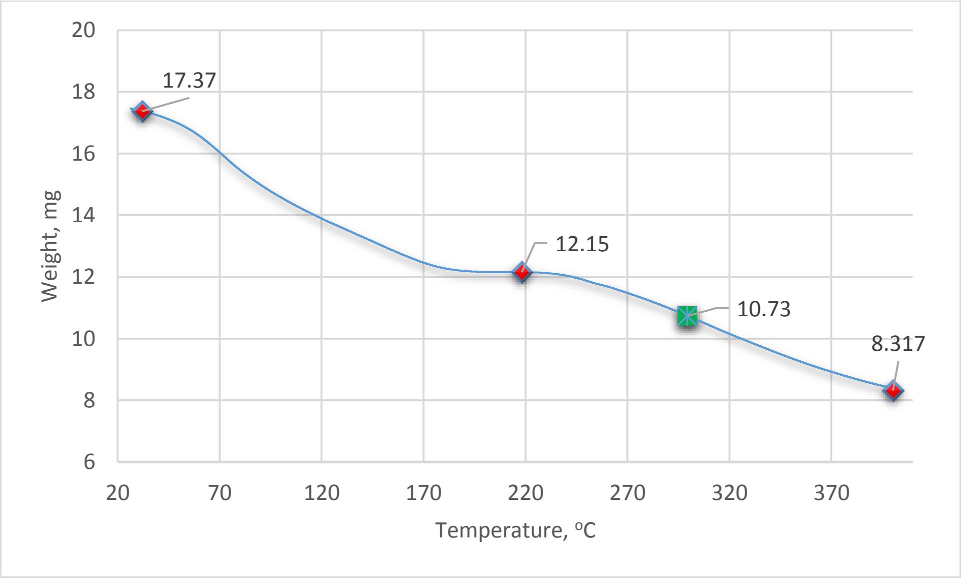

Weight Loss Range	Number of water molecules
17.37 – 12.15 mg	20.49
17.37 – 10.73 mg	29.51

Figure 2.14 Combined TGA and elemental analysis for compound **9**.

$Fe^{III}_4[Fe^{II}(CN)_6]_3\cdot 20.15H_2O$ (10). Compound **10** was prepared by heating compound **9** at 60 °C for 4 hours. The sample was quickly transferred to the TGA instrument at room temperature under a blanket of N_2. The resulting plot, Figure 2.15, shows little reabsorption between 20-60 °C. The TGA curve is very similar to the one in Figure 2.15 except that now the mass loss is consistent with 11.6 water molecules in the interstitial channels and 6.6 molecules presumably bound to the Fe^{III} centers at the $[Fe(CN)_6]^{4-}$ vacancy locations.

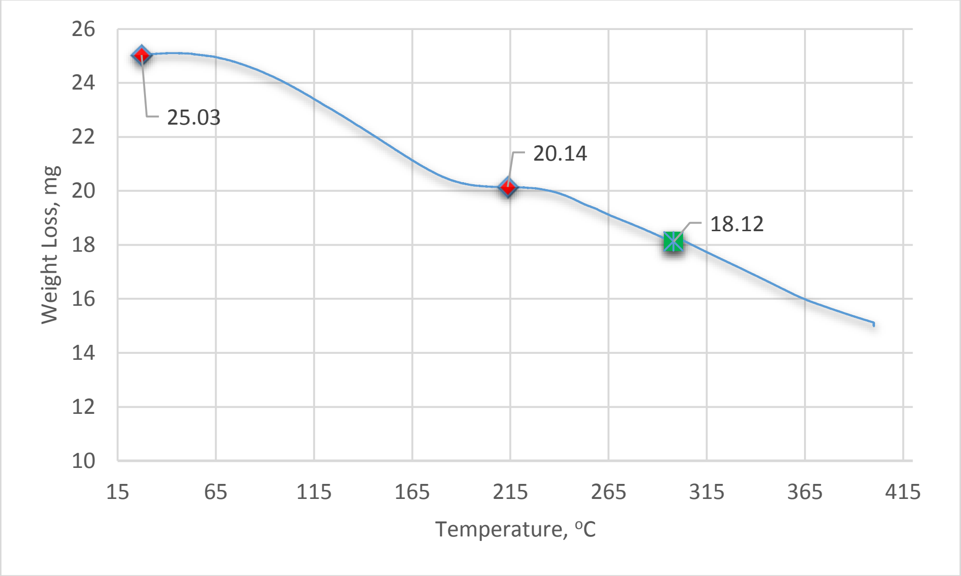

Weight Loss Range	Number of water molecules
25.03 – 20.14 mg	11.58
25.03 – 18.12 mg	18.19

Figure 2.15 Combined TGA and elemental analysis for compound **10**.

$Fe^{III}_4[Fe^{II}(CN)_6]_3\cdot 13.75H_2O$ (11). Compoud **9** was reheated to 90 °C for 4 hours. The sample was prepared for TGA the same as described for compound **10**. The data in Figure 2.16 reveal that compound **11** has approximately 13 total water molecules inside the framework with 5.7 molecule bound to the Fe^{III} centers inside the vacancies, which is approximately one water less than compound **10**. The feature at 275 °C is an artifact in the TGA experiment and not due to solvent loss.

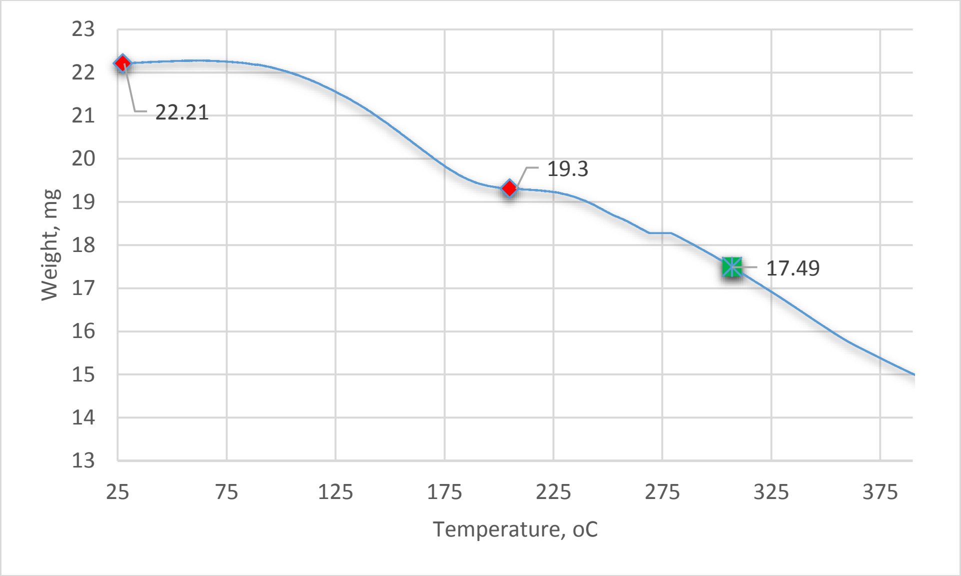

Weight Loss Range	Number of water molecules
22.21 – 19.30 mg	7.19
22.21 – 17.49 mg	12.87

Figure 2.16 Combined TGA and elemental analysis for compound **11**.

$Fe^{III}_4[Fe^{II}(CN)_6]_3 \cdot 6H_2O$ (12). Compound **12** was synthesized by an indirect method involving the oxidation of iron powder using concentrated hydrochloric acid. The formation of Prussian Blue is believed to go through a Prussian White intermediate. The TGA curve for this compound, Figure 2.17, is quite different than the previous compounds in that there are only 1.6 water molecules in the interstitial channels. We believe this is due to the presence of potassium ions, given that the reaction proceeds through a Prussian White intermediate. After 250 °C there is an abrupt weight loss. Once again, the weight loss in this region is continuous and a distinction between bound water and sample decomposition cannot be made. Elemental analysis results show that the loss of coordinated water is complete at approximately 300 ^{o}C, which is approximately in the middle of the continuous weight loss in the 250 – 350 ^{o}C temperature range.

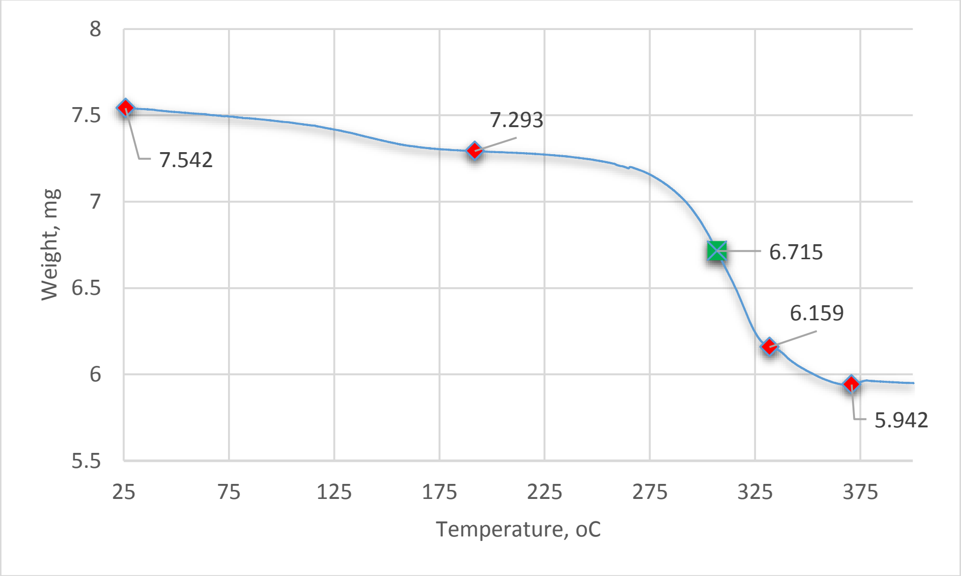

Weight Loss Range	Number of water molecules
7.542 – 7.293 mg	1.63
7.542 – 6.715 mg	5.87

Figure 2.17 Combined TGA and elemental analysis for compound **12**.

$Fe^{III}_4[Fe^{II}(CN)_6]_3\cdot8H_2O$ (13). The final sample of insoluble Prussian Blue was prepared using a differnt source of ferric ions. The nitrate anion would have a different absoption profile compared to chloride, which should have a direct effect on the amount of water moelcules absorbed in the structre. The TGA and elemental analysis, Figure 2.18, reveals moderate water loss from 25–225 ^{o}C that corresponds to 5.4 water molecules in the zeolitic positions of the Prussian Blue framework. As observed for compound **12**, there is a rather abrupt drop in the weight loss profile after 250 °C. The elemental results indicate that the coordinated water is liberated at the beginning of this decline in weight around 280 °C.

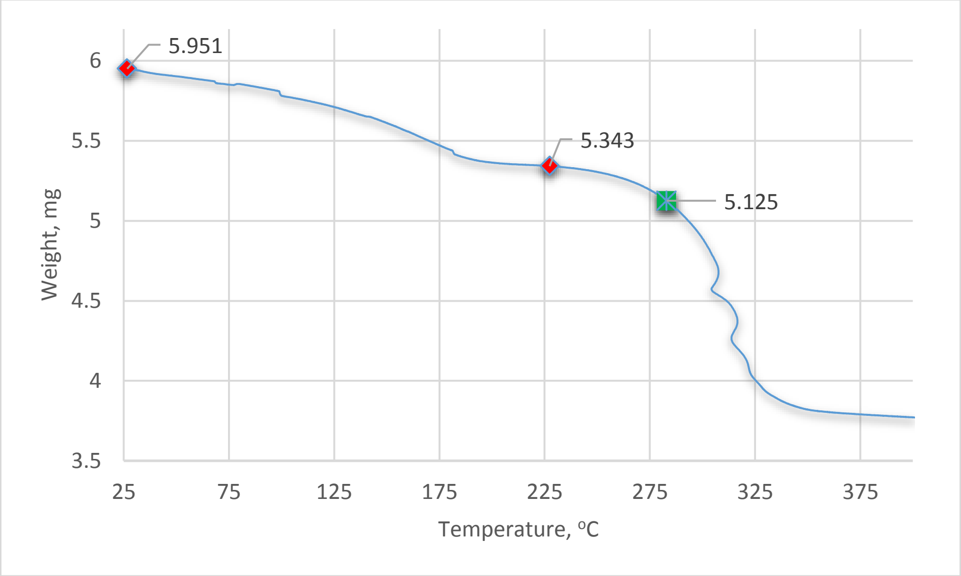

Weight Loss Range	Number of water molecules
5.951 – 5.343 mg	**5.43**
5.951 – 5.125 mg	**7.69**

Figure 2.18 Combined TGA and elemental analysis for compound **13**.

In summary, we have made Prussian Blue samples with hydration levels ranging from 6-28 moles of water, Table 2.3. Unfortunately, we are unable to dehydrate the sample as the internal water molecules are strongly bound. Attempting to heat the sample above 225 °C resulted in decomposition. Thermal decomposition products are Fe_2O_3 nanoparticles and $HCN_{(g)}$ when exposed to high temperature in air.[178] Under inert gas, the decomposition products are a cocktail of iron metal, iron carbide species, graphite, and cyanogen.[179] Both reports claim that, before these decomposition products are realized, the bound water is released. We believe our elemental results combined with TGA analysis to be an accurate determination of the bound water content. Interestingly, the elemental analysis results give on average 5.8 more water molecules than what is expected from thermal gravimetric analysis, Table 2.3, which is in accord with the known amount of bound water in Prussian Blue.[141] For each sample, the relative change in the amount of free and bound water molecules varied, which suggests disorder in the site defects. The TGA graphs show water loss from approximately 25-250 ^{o}C. There is then a plateau usually occurring from 250-275^{o}C and after this temperature range there is a constant decrease up to 400^{o}C.

Table 2. 3 Summary of water content in Prussian Blue samples

Sample	*TGA	**Elemental	Bound Water	% Difference
9	20.49 H_2O	27.7 H_2O	7.21	29.9
10	11.58 H_2O	20.15 H_2O	8.57	54.0
11	7.19 H_2O	13.75 H_2O	6.56	62.7
12	1.63 H_2O	5.87 H_2O	4.24	113.1
13	5.43 H_2O	7.69 H_2O	2.26	34.5

*TGA column represents the water content corresponding to the first plateau marked by the second red diamond in the Figures 2.14-2.18. **Elemental column represents the water content calculated from the H content from elemental analysis assuming base formula of $Fe_4[Fe(CN)_6]_3$.

X-ray Crystallographic Studies on Soluble Prussian Blue

To date, X-ray structural studies on soluble Prussian Blue have only been achieved using powder data. In 1936, Keggin and Miles proposed the first structure based on powder data and elemental analysis to be the typical formulation in the literature, namely

$KFe^{III}[Fe^{II}(CN)_6]$. The formula is charge balanced, not requiring defects, and contains potassium ions in the zeolitic-like positions at the center of alternating octants that make up the unit cell (Wcykoff position *8g* in the space group Pm3m). The space group Pm3m corresponds to a lower symmetric space group in which the site defects are ordered, as was discovered for the case of insoluble Prussian Blue in 1977.[142] In 2008, Bueno and coworkers determined a potential structure (referred to hereafter as the Bueno Model) for soluble Prussian Blue that was prepared electrochemically.[145] Using X-ray synchrotron powder diffraction and Rietveld refinement methods, they found that soluble Prussian Blue also contained approximately 25% vacancies of the ferrocyanide ions - thereby invalidating the conventional formula of $KFe^{III}[Fe^{II}(CN)_6]$ and revealing that the only difference between the soluble and insoluble entities was the alkali metal content. Using Fourier maps and previous electrogravimetirc analysis,[180,181] the alkali metal ions were determined to exist in the water crystalline substructure. In other words, the potassium ions were determined to reside on the Fe-CN-Fe linkage axes at the site of point defects- a surprising conclusion given the open zeolitic framework. The *8c* and *32f* sites in the interstitial channels were determined to be occupied by uncoordinated water, or water participating in hydrogen bonding with the water coordinated to Fe(III) ions. The schematic representation of the crystal structure is shown in Figure 2.19.

The refinement of the crystal data was carried out in the Fm-3m space group with a lattice parameter, a = 10.1783(3) Å. Because of the potassium ions in the substructure, the authors proposed that some of the water molecules are in fact OH^- ions which allow for charge balance, thereby modifying the so-called soluble Prussian Blue formula to $Fe_4^{III}[Fe^{II}(CN)_6]_3\cdot[K_h^+\cdot OH_h^-\cdot(mH_2O)]$.

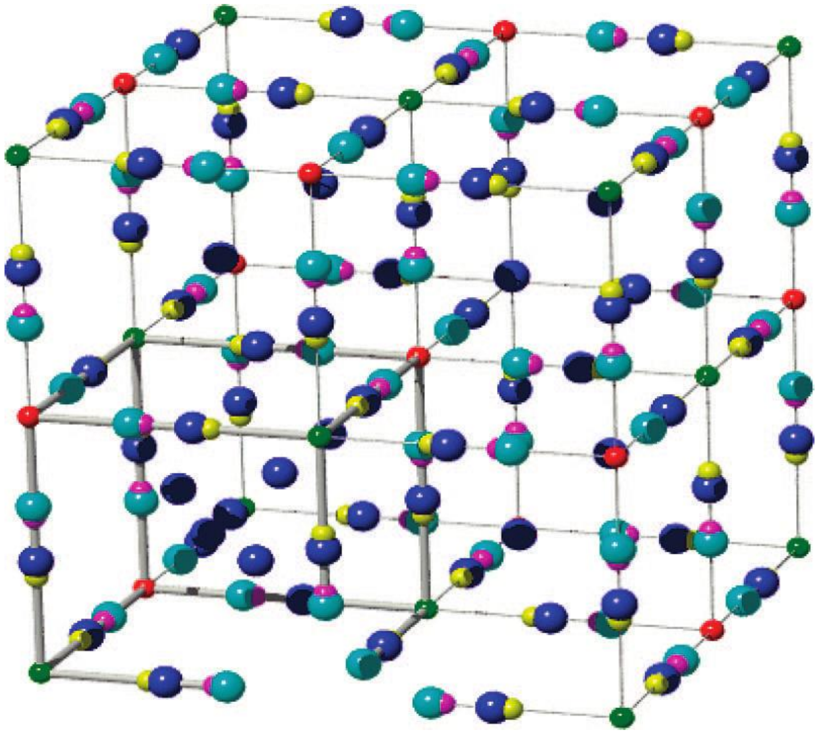

Figure 2.19 Schematic representation of the soluble Prussian Blue after the final refinement cycle. Green, red, magenta, yellow, blue, and cyan circles represent Fe(III), Fe(II), C, N, O, and K. Only one octant is represented with 5 atoms at sites 32f and 8c. The atoms in the other octants were removed for clarity. A ferrocyanide group was removed at the bottom of the structure to emphasize the vacant sites. Figure reprinted with permission from reference.[145] Copyright 2008, American Chemical Society.

This new formula was revisited in 2013 by Samain and coworkers (hereafter referred to as the Samain Model), who performed a systematic study on soluble and insoluble Prussian Blue products in relation to their behavior in paint layers using an array of analytical techniques, including TGA, high-energy powder X-ray diffraction, atomic absorption and flame emission, electronic spectroscopy, iron-57 Mössbauer, iron K-edge X-ray absorption, and Raman spectroscopies.[141] From TGA experiments, the water molecules for soluble Prussian Blue were found to range from 1-5, whereas for insoluble Prussian Blue, the range was 14-16 moles per formula unit. The authors reported that, based on iron K-edge X-ray absorption spectra and pair distribution analysis, soluble Prussian Blue crystallizes in the Pm-3m space group with a lattice parameter of 10.2178(1) Å.

The water molecules were found to exhibit large displacement parameters which was posited to result from displacement disorder of the oxygen atoms in conjunction with different chemical environments, (i.e. OH^- vs H_2O and coordinated vs uncoordinated water throughout the framework). Rietveld refinements of the high resolution powder X-ray data revealed 11.2 oxygen atoms, six of which are located at the *6e*, *6f*, and *12h* sites in the Pm-3m space group. These six water molecules reside in the site defects, which were also found to be 25% occupied in accord with the Bueno model. The remaining uncoordinated water molecules are on the *8g* sites in the interstitial channels. The authors' attempts at refining weak reflections using the Bueno Model in the Fm-3m space group had failed, thus leading to some ambiguity in the actual structure in terms of occupancies of defects and locations of potassium ions. The potassium ions in the Samain Model were found to reside on the *8g* positions in the center of the octants. This is similar to the structure described by Keggin and Miles,[144] but now includes 75% occupancy of the ferrocyanide ions. The validity of the recent model was attributed to the fact that the high resolution powder pattern exhibited 50 reflections, whereas the Bueno Model was constructed from 13-15 reflections. This large difference in the quality of data lends credence to the Samain Model, which would have lower incoherent scattering.[141]

While the Samain Model initially separated the positions of zeolitic water and potassium ions, the comparison of potassium content as inferred from flame emission spectroscopy led to less potassium ions that needed and a surplus of oxygen. The Samain Model was altered to account for potassium and water occupying the same *8g* positions. After this adjustment, the water and potassium content were in good agreement with TGA and flame emission spectroscopy. The results pointed towards 2.9(2) uncoordinated oxygen atoms and 6.01(1) coordinated oxygen atoms, along with 1.9(2) potassium ions. Using the same formula unit proposed via the Bueno Model, the revised formula of soluble Prussian Blue is: $K_{1.9(2)}[Fe^{III}_4Fe^{II}_{3.00(2)}(CN)_{18.0(1)}]\cdot\{7.0(2)H_2O+1.9(2)OH\}$. Despite the different locations of the potassium ions in the two models, the resulting conclusions were congruent; soluble Prussian Blue is the same structural motif as insoluble Prussian Blue because of the 25% ferrocyanide vacancies. As such, the terms soluble Prussian Blue versus insoluble Prussian Blue now have even less of a chemical meaning.

Over the course of our work with soluble Prussian Blue, we discovered that sufficiently large X-ray quality crystals could be grown by slowly diffusing water into concentrated $HCl_{(aq)}$ solutions of ferricyanide and iron powder. After 50-60 days, crystals of **14** grew to a suitable size for single-crystal diffraction at the synchrotron facility at Lawrence Berkeley National Laboratory. This marks the first time single-crystal data has been reported on soluble Prussian Blue. A comparison of our structural parameters with the previously described models is provided in Table 2.4.

Table 2.4 Comparison of unit cell and bond lengths for structure **14** with literature models.

	14	**Bueno Model**	**Samain Model**
Formulation	$K_{1.975}[Fe^{III}_4Fe^{II}_{2.998}(CN)_{18}]\cdot\{10.285H_2O+1.975OH\}$	$Fe_4[Fe(CN)_6]_3\cdot[K^+_h\cdot OH^-_h\cdot mH_2O]$	$K_{1.9(2)}[Fe^{III}_4Fe^{II}_{3.00(2)}(CN)_{18.0(1)}]\cdot\{7.0(2)H_2O+1.9(2)OH\}$
Space group	Fm-3m	Fm-3m	Pm-3m
a/Å	10.1461(16)	10.1780(8)	10.2059(1)
Volume/Å^3	1044.5(5)	1054.3(2)	1063.1
Fe(III)-N/Å	1.992(6)	1.92(3)	1.926(4)
Fe(III)-O*/Å	2.220(16)	2.22(6)	2.568(15)
Fe(III)-K/Å	3.427(3)	3.30(7)	Not Applicable
Fe(II)-C/Å	1.901(6)	2.00(30)	1.947(5)
Fe(II)-K/Å	1.65(11)	1.79(7)	Not Applicable
C-N/Å	1.180(9)	1.18(20)	1.155(5)
C-O/Å	0.952(17)	0.88(9)	Not Applicable

Ironically, our best refinement suggests both models are needed for the full description of the structure. Compound **14** crystallizes in the Fm-3m space group. The space group, Pm-3m, was attempted, but the asymmetric unit consisted of only one iron atom, one carbon atom, and one potassium atom. This smaller unit cell was accounted for by assigning different site occupancies and assuming the carbon and nitrogen readily isomerized, but the refinement statistics were not satisfactory. Thus, in our particular case, the space group Fm-3m was used. The asymmetric unit consist of a full Fe^{III}-NC-Fe^{II} moiety in the unit cell, notably shorter than either of the previous models at a = 10.1461(16) Å. The $[Fe^{II}(CN)_6]^{4-}$ unit was constrained to 75% occupancy given the findings of both previous models. Applying this restraint gave two distinct Q-peaks with large intensities at the *24e* positions - one closer to Fe(III) center and one closer to Fe(II). Consistent with the Bueno model, these Q-peaks were assigned at 25% occupancy to a coordinated water moelcule and potassium ion, respectively. Another potassium ion was found in the interstital, zeolitic *8g* positions and was assigned to a second free variable and allowed to refine freely. A PART 2 command was used to assign an oxygen atom at this same position, which was allowed to refine freely to a third free variable. Hydrogen atom Q-peaks were evident around this *8g* position, suggesting both water and potassium occupancies, which is in aggrement with the Samain Model. The remaining Q-peaks were at or below 1.0 e Å^{-3} and were ignored. All non-hydrogen atoms were refined anisotropically until convergence. With these restraints, the data refinement produced a goodness of fit = 1.235 and R1 = 4.28%. The crystal structure is shown in Figure 2.20. Additional structural parameters are given in Table 2.5. The final refinement led to the following formula (being consistent with the previous models): $K_{1.975}[Fe^{III}_{4}Fe^{II}_{2.998}(CN)_{18}]\cdot\{10.285H_2O+1.975OH\}$. It is our hope that this formulation will be confirmed when the efforts of synthetic chemists lead to larger crystals in the future. However, as this chapter exemplifies, each synthesis no matter how subtly different, will yield different product formulations.

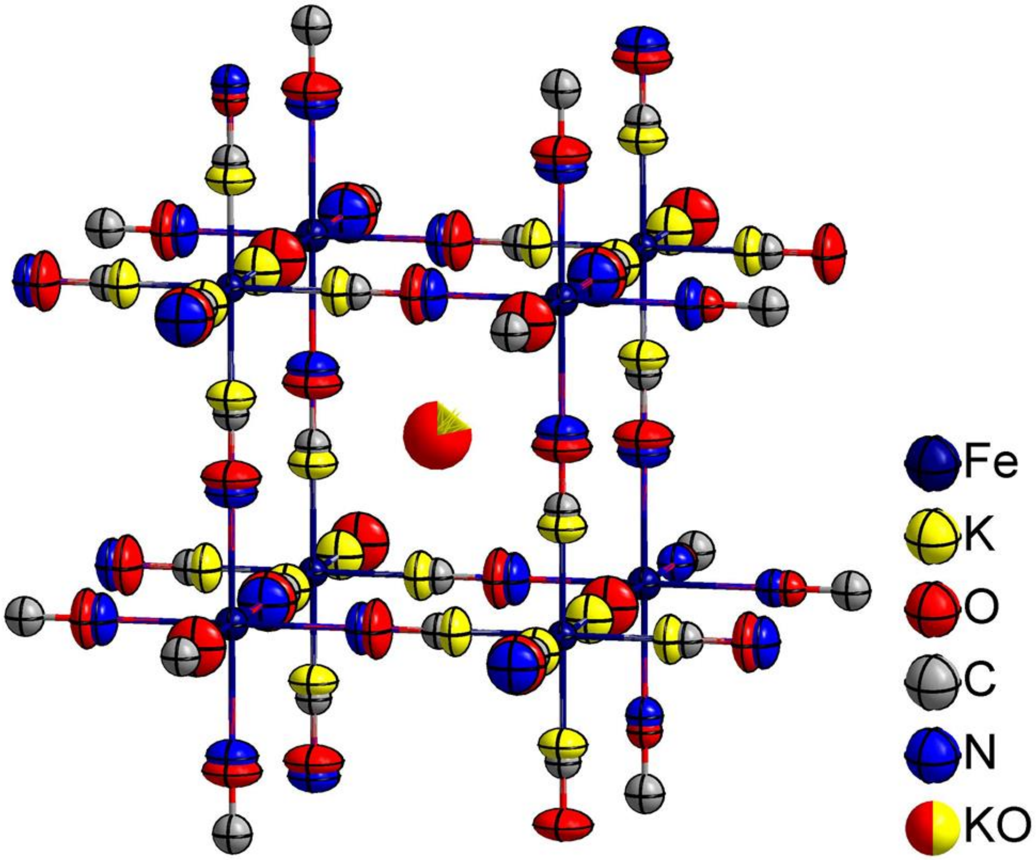

Figure 2.20 The first single crystal X-Ray structure of soluble Prussian Blue. Hydrogen atoms omitted for clarity. Ellipsoids rendered at 50% probability.

Table 2.5 Crystal and structural refinement data for soluble Prussian Blue, **14**.

	14
Empirical formula	$C_{18}N_{18}O_{12.26}Fe_7K_{1.98}H_{32}$
Formula weight	1164.83
Temperature/K	100
Crystal system	cubic
Space group	Fm-3m
a/Å	10.1461(16)
b/Å	10.1461(16)
c/Å	10.1461(16)
α/°	90
β/°	90
γ/°	90
Volume/Å^3	1044.5(5)
Z	1
ρ_{calc}g/cm^3	1.852
μ/mm^{-1}	2.631
F(000)	584.0
Radiation	Synchrotron (λ = 0.41328 Å)
2Θ range for data collection/°	6.956 to 60.68
Index ranges	$-14 \leq h \leq 14, -13 \leq k \leq 14, -14 \leq l \leq 14$
Reflections collected	2815
Independent reflections	109 [R_{int} = 0.0589, R_{sigma} = 0.0259]
Data/restraints/parameters	109/48/21
Goodness-of-fit on F^2	1.235
Final R indexes [I>=2σ (I)]	R_1 = 0.0390, wR_2 = 0.0998
Final R indexes [all data]	R_1 = 0.0428, wR_2 = 0.1053
Largest diff. peak/hole / e Å^{-3}	0.70/-1.00

$^{a}R = \sum||F_o|-|F_c||/\sum|F_o|$. $^{b}wR = \{\sum[w(F_o^2 - F_c^2)^2]/\sum w(F_o^2)^2]\}^{1/2}$. ^{c}Goodness-of-fit = $\{\sum[w(F_o^2 - F_c^2)^2]/(n-p)\}^{1/2}$, where n is the number of reflections and p is the total number of parameters refined.

Concluding Remarks

Prussian Blue has been known for over 3 centuries and yet research on it’s composition is still being actively pursued and published in the current literature. The results described in this chapter provide an appreciation of the inherent complexity of Prussian Blue and it is imperative that researchers focus on comparing multiple samples with different structural compositions with regards to water and potassium content, particles size, and the number of vacancies within the structure. Such factors can lead to stark differences in the compounds properties such as ion uptake in the treatment of radioactive cesium and thallium poisoning.

The work discussed in this chapter revealed that potassium and water content can vary significantly depending on the sythetic route. The incorporation of the chloride ion in soluble Prussian Blue has been noted and is a topic that needs to be further investigated by the research community in future studies. Insoluble Prussian Blue can contain nearly double the amount of water molecules than what was suggested by the crystal structure reported in 1977. Slow diffusion methods of water into highly accidic solutions of iron powder mixed with ferricyanide results in single crystals, yielding the first single-crystal X-ray diffraction study on soluble Prussian Blue.

CHAPTER III

ONE-DIMENSIONAL ARCHITECTURES INCORPORATING OCTACYANOMETALLATES OF MOLYBDENUM AND TUNGSTEN [*]

Introduction

An important direction in the field of molecular magnetism is the study of chain compounds, a sub-set of which behave as one-dimensional analogues of single-molecule magnets (SMMs) and are known as single-chain magnets (SCMs)[182]. These "magnetic nanowires" are exciting new soft materials that, in principle, have the capability of producing higher blocking temperatures for molecular paramagnets due to the exchange coupling (J) between adjacent metal centers in the chain giving rise to an energy term, known as the correlation energy (Δ_ξ), along with the classical anisotropy energy in SMMs[52,67,183]. In addition, it is well established that the cooperative alignment of the individual single-ion easy axes enhances the energy barrier for an array of connected SMMs.[184,185] Linear SCMs have the advantage of being a natural platform for the parallel alignment of the local easy axes of each chain repeat unit along the unique chain orientation. By taking advantage of this large uniaxial magnetic anisotropy inherent in SCMs, it is conceivable that information recording and storage devices could be constructed from them.[13,186]

Among the SCMs that have appeared in the literature[54] are those which incorporate flexible cyanometallates equipped with different blocking ligands. Octacyanometallates

---

[*] Reprinted with permission from "One-dimensional square- and ladder-type architectures incorporating octacyanometallates of molybdenum(V) and tungsten(V)" by Hanhua Zhao, Andrew J. Brown, Andrey V. Prosvirin, and Kim R. Dunbar, 2013. Polyhedron, 64, 321-327, Copyright [2013] by Elsevier. http://dx.doi.org/10.1016/j.poly.2013.06.006

of tungsten and molybdenum have already proven to be two such appropiate choices for the rational design of SMMs.[187,188] These anions possess diffuse 4d/5d orbitals for enhanced coupling across the cyanide bridge and also exhibit coordination flexibility through facile interconversion between three different coordination geometries, *viz*., square antiprism, dodecahedron, and bicapped trigonal prism.[189,190] The combination of these properties promoted a great diversity of topologies and magnetic properties.[191-194] In one example pertinent to this work, the reaction of Cu(II) complexes of cyclam derivatives with $[M^{V}(CN)_8]^{3-}$ (M = Mo, W) led to the formation of materials with different dimensionalities depending on the substituents on the cyclam ligand.[195] When the unsubstituted $[Cu(cyclam)]^{2+}$ precursor was used, a 1D ladder-type chain compound, $[Cu^{II}(cyclam)]_3[W^{V}(CN)_8]_2{\cdot}5H_2O$, was obtained. This structural motif and other dimensionalities have been reported for compounds containing capping ligands on the 3d metal center.[196-207] Another strategy that has been devised is the replacement of the 3d metal ions with lanthanide elements.[208-211] Variation to the structure can be achieved as demonstrated by another noteworthy example wherein a one-dimensional chain of Mn_2W_2 squares was obtained by incorporating a bridging Mn(II) center.[212]

Several years ago our group initiated the use of the *mer*-tridentate planar ligand tptz (tptz = 2,4,6-tris(2-pyridyl)-1,3,5-triazine), Chart 1.1, in reactions of complexes of Mn(II) ions with the octacyanometallate anions $[W(CN)_8]^{3-/4-}$. This work led to a structurally diverse series of heterobimetallic complexes, some of which exhibit antiferromagnetic coupling between Mn(II) and W(V) ions giving rise to ferrimagnetic ground states.[73] The structural variation in the products ranged from discrete molecular complexes to one-dimensional networks with the common feature being that all are derived from the same basic square fragment, W_2Mn_2. This work exemplifies the structural adaptability afforded by the octacyanometallate building block. As part of our ongoing efforts involving these types of building blocks we focused on the combination of $[M^V(CN)_8]^{3-}$ ions (M = Mo, W) with mononuclear tptz complexes of transition metal ions with higher single-ion anisotropies. In this chapter, three new one-dimensional metal-tptz polymers $\{[Cu^{II}(tptz)Mo^V(CN)_8]^-\cdot(H_3O)^+\cdot CH_3OH\}_\infty$ (2), $\{[Co^{II}_2(tptz)_2(H_2O)_2W_2{}^V(CN)_{16}Co^{II}(H_2O)_4]\cdot 2H_2O\}_\infty$ (3), and $\{[Fe^{III}(tptz)W^V(CN)_8]\cdot 2CH_3OH\}_\infty$ (4), along with the structure of a new precursor compound $[Cu^{II}(tptz)(CF_3SO_3)_2(CH_3OH)]\cdot 2H_2O$ (1) which was used to prepare compound 2, are described. Although no extraordinary magnetic properties were encountered in this study, compound 3 does exhibit the beginning of out-of-phase signals at low temperatures which hints at SCM behavior. Moreover the structural motifs are interesting for future studies that involve different combinations of 3d/4d and 3d/5d metal ions.

Experimental Section

Syntheses

The reagents 2,4,6-tris(2-pyridyl)-1,3,5-triazine (tptz, Sigma-Aldrich; Chart 1.1), $Cu(CF_3CO_2)_2$ (Sigma-Aldrich), $CoCl_2\cdot 6H_2O$ (Sigma-Aldrich), $Fe(ClO_4)_3\cdot 6H_2O$(Fisher) and reagent grade solvents (methanol, tetrahydrofuran and dimethylformamide) were used as received. The compounds $[(C_4H_9)_3NH]_3M^V(CN)_8$ (M = Mo, W)[213] and $Co_4Cl_8(THF)_6$[214] were prepared by following reported procedures.

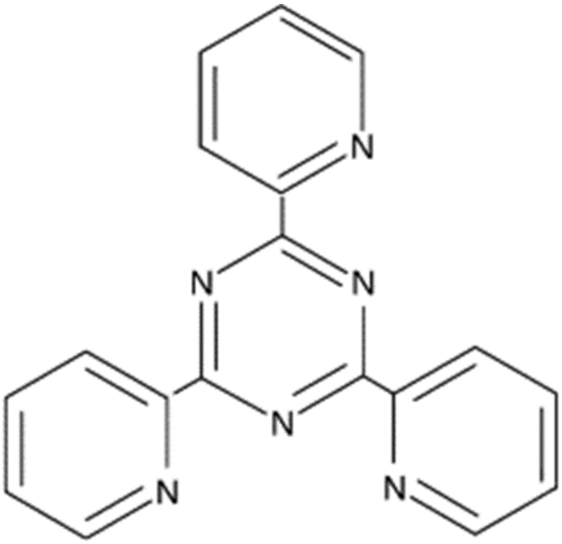

Chart 1.1 Schematic drawing of 2,4,6-tris(2-pyridyl)-1,3,5-triazine (tptz).

Preparation of [Cu^{II}(tptz)(CF_3SO_3)$_2$(CH_3OH)]·2H_2O (15). A solution of tptz (94 mg, 0.30 mmol) in 8 mL of methanol was added dropwise to a solution of Cu(CF_3CO_2)$_2$ (108 mg, 0.30 mmol) in 8 mL of methanol, stirred for 30 minutes and then left to stand undisturbed for 12 hours. The resulting bright green solution was slowly diffused with 20 mL of diethyl ether to yield green crystals after 1 week. Single crystal X-ray diffraction studies revealed the crystals to be a mixture of [Cu^{II}(tptz)(CF_3SO_3)$_2$(CH_3OH)]·2H_2O **(15)** (Fig. 1) and a [Cu^{II}(tptz)$_2$(CH_3OH)$_2$](CF_3SO_3)$_2$ impurity. The impurity was removed by recrystallization from methanol to give a polycrystalline form of **15**. Yield: 80 mg (36% based on Cu(CF_3CO_2)$_2$). Calcd. for **15** ($C_{21}H_{19}N_6O_9F_6S_2Cu$): C, 34.04; H, 2.58; N, 11.34. Found: C, 34.51; H, 3.20; N, 11.77; (%). The elemental analysis results indicate loss of one water molecule for the dried sample (Calcd. for $C_{21}H_{17}N_6O_8F_6S_2Cu$: C, 34.88; H, 2.37; N, 11.62.).

Preparation of $\{[Cu^{II}(tptz)Mo^{V}(CN)_8]^{-}\cdot(H_3O)^{+}\cdot CH_3OH\}_\infty$ (16). A solution of compound **15** (74 mg, 0.10 mmol) in 8 mL of methanol was layered in the absence of light with a solution of $[(C_4H_9)_4N]_3Mo(CN)_8$ (136 mg, 0.10 mmol) in 10 mL of methanol. Blue-green crystals were obtained after two weeks. Yield: 23 mg (32% based on $[(C_4H_9)_4N]_3Mo(CN)_8$). Elemental analysis: Calcd. for **16** ($C_{27}H_{20}N_{14}O_2Cu_1Mo_1$): C, 44.30; H, 2.75; N, 26.79. Found: C, 43.62; H, 2.77; N, 27.13%. IR (Nujol), ν(C≡N), cm^{-1}: 2122, 2138, 2150. The elemental analysis results indicate partial loss of the interstitial methanol molecule for the dried sample, viz., $\{[Cu^{II}(tptz)Mo^{V}(CN)_8]^{-}\cdot(H_3O)^{+}\cdot 0.4CH_3OH\cdot 0.7H_2O\}_\infty$ (Calc.: C, 43.71; H, 2.64; N, 27.03).

Preparation of $\{[Co^{II}_2(tptz)_2(H_2O)_2W_2^{V}(CN)_{16}Co^{II}(H_2O)_4]\cdot 2H_2O\}_\infty$ (17). A solution of tptz (124 mg, 0.40 mmol) in 15 mL of THF was added dropwise to a solution of $Co_4Cl_8(THF)_6$ (95 mg, 0.10 mmol) in 15 mL of THF with constant stirring. The mixture was stirred for 30 minutes and then left to stand undisturbed for 12 hours to yield a green solid which was recovered by vacuum filtration, washed with THF, and dried in air. The green solid was then dissolved in 10 mL of a solution containing $Co(BF_4)_2\cdot 6H_2O$ (34 mg, 0.10 mmol) in DMF and ethanol (1:1 v/v). This solution was layered in the absence of light with a solution of 95 mg (0.10 mmol) of $[(C_4H_9)_3NH]_3W(CN)_8$ in 10 mL of ethanol and methanol (1:1 v/v). Red crystals were obtained after two weeks and were collected by filtration, washed with methanol, and dried in vacuo. Yield: 36 mg (42% based on $[(C_4H_9)_3NH]_3W(CN)_8$). Calcd. for **17** ($C_{52}H_{40}N_{28}O_8Co_3W_2$) (%): C, 36.11; H, 2.33; N, 22.68. Found: C, 35.70; H, 2.69; N, 23.25. IR (Nujol), ν(C≡N), cm^{-1}: 2145, 2161, 2184. Elemental analysis are in accord with three water molecules, namely

$\{[Co^{II}_2(tptz)_2(H_2O)_2W_2^V(CN)_{16}Co^{II}(H_2O)_4]\cdot 3H_2O\}_\infty$ (Calc. for $C_{52}H_{42}N_{28}O_9Co_3W_2$: C, 35.74; H, 2.42; N, 22.44), which is reasonable if all three water were not located in the final refinement.

Preparation of $\{[Fe^{III}(tptz)W^V(CN)_8]\cdot 2CH_3OH\}_\infty$ (18). A solution of tptz (63 mg, 0.20 mmol) in 5 mL of methanol was added dropwise to a yellow-brown solution of $Fe(ClO_4)_3\cdot 6H_2O$ (71mg, 0.20 mmol) in 7 mL of methanol and DMF (5:2 v/v). The solution was stirred for 30 minutes and a blue solution was observed to form. To this solution was added $\{(C_4H_9)_3NH\}_3[W(CN)_8]$ (95 mg, 0.10 mmol) in 10 mL of methanol with stirring. A brown by-product immediately precipitated and was removed by filtration. The blue filtrate was collected and treated with diethyl ether by diffusion. The resulting blue product was washed with methanol and dried *in vacuo*. Yield: 15 mg (19% based on $[(C_4H_9)_3NH]_3W(CN)_8$). Elemental analysis: Calcd. for **18** ($C_{28}H_{20}N_{14}O_2Fe_1W_1$): C, 40.80; H, 2.45; N, 23.79. Found: C, 42.05; H, 2.71; N, 24.32%. IR (Nujol), ν(C≡N), cm^{-1}: 2143, 2162. Single crystals were obtained after two weeks by slow diffusion of diethyl ether into a concentrated solution of **18** in methanol and DMF (5:2 v/v). Elemental data reflect the presence of DMF molecules of crystallization that were not located in the structural refinement and fit best to the fractional formula $\{[Fe^{III}(tptz)W^V(CN)_8]\cdot 2CH_3OH\cdot 0.65C_3H_7NO\}_\infty$ (Calc.: C, 41.26; H, 2.84; N, 23.54).

Physical Methods

Magnetic susceptibility and magnetization measurements were collected on crushed polycrystalline samples using a Quantum Design MPMS-XL SQUID magnetometer. DC magnetic susceptibility measurements were performed at an applied field of 1000 Oe over the temperature range 2-300 K. DC magnetization data were collected at 1.8 K under a range of DC fields from 0-7 T. AC magnetic susceptibility measurements were performed in a 3 Oe AC field at operating frequencies of 1-1000 Hz. The data were corrected for diamagnetic contributions as calculated from the Pascal constants.[215]

Single crystal X-ray data were collected at 110 K on Bruker SMART 1000 (**15**), Bruker APEX (**15** and **18**) and Bruker-AXS GADDS (**16** and **17**) diffractometers equipped with CCD detectors. The data sets were recorded as ω-scans at 0.3° step width. Integration was performed with the Bruker SAINT[216] software package and absorption corrections were empirically applied using SADABS.[170] The crystal structures were refined using the SHELX[173] suite of programs and the graphical interface XSEED.[217] Images of the crystal structure were rendered using the crystal structure visualization software DIAMOND.[174] All of the structures were solved by direct methods. Remaining non-hydrogen atoms were located by alternating cycles of least squares refinements and difference Fourier maps. All hydrogen atoms were placed at calculated positions except for some water molecules for which the hydrogen atoms were located by difference Fourier maps. The bond lengths of disordered solvent molecules were restrained to chemically meaningful values. Anisotropic thermal parameters were added for all non-hydrogen atoms unless there was a disorder involved. In such cases, the atoms were refined isotropically. For compound **17**, a two part disorder was included for the water ligands of the bridging cobalt cations, which were then refined isotropically.

Infrared (IR) spectra were measured as Nujol mulls placed between KBr plates on a Nicolet 740 FT-IR spectrometer. Elemental analyses were performed by Atlantic Microlab, Inc.

Results and Discussion

Syntheses

Reactions between $[M^{V}(CN)_8]^{3-}$ (M = Mo, W) anions and $[M(tptz)]^{2+/3+}$ (M = Cu(II), Co(II), Fe(III)) complexes afford a series of one-dimensional cyanide-bridged compounds. The use of the mononuclear precursor **15** resulted in the isolation of compound **16** in which square units share opposite edges to form a molecular ladder. Compound **17** was prepared from the starting material $Co_4Cl_8(THF)_6$ because the only tractable product that was isolated using $CoCl_2{\cdot}6H_2O$ was $[Co(tptz)_2]Cl_2$. The use of $Co_4Cl_8(THF)_6$ slows the rate of the reactions and leads to the formation of compound **17** in good yields and minimizes the formation of the bis-tptz impurity. In an analogous fsahion, the preparation of compound **18** resulted in low yields due to the formation of $[Fe(tptz)_2]^{3+}$, but the product can be separated from the impurity when $Fe(ClO_4)_3{\cdot}6H_2O$ is used as a starting material.

Crystallographic Studies

Crystallographic data for compounds **15-18** are listed in Table 3.1. Selected bond distances and angles are provided in Table 3.2.

Table 3.1 Crystal and structural refinement data for **15-18**.

	15	**16**	**17**	**18**
Empirical formula	$C_{22}H_{20}CuF_6N_6O_8S_2$	$C_{27}H_{20}CuMoN_{14}O_2$	$C_{52}H_{24}Co_3N_{28}O_9W_2$	$C_{28}H_{20}FeN_{14}O_2W$
Formula weight	738.10	732.05	1729.48	824.28
Temperature/K	110(2)	110(2)	110(2)	173(2)
Crystal system	Monoclinic	Monoclinic	Triclinic	Monoclinic
Space group	$P2_1/c$	$P2_1/n$	P-1	$P2_1/n$
a/Å	8.1853(16)	10.665(2)	10.733(2)	10.135(2)
b/Å	15.074(3)	17.956(4)	13.380(3)	17.939(4)
c/Å	23.177(5)	17.194(3)	17.141(3)	17.231(3)
α/°	90.00	90.00	100.06(3)	90.00
β/°	91.91(3)	96.19(3)	96.15(3)	96.55(3)
γ/°	90.00	90.00	112.15(3)	90.00
Volume/$Å^3$	2858.1(10)	3273.3(11)	2204.2(8)	3112.3(11)
Z	4	4	1	4
$\rho_{calc}g/cm^3$	1.715	1.485	1.303	1.759
F(000)	1492.0	1468.0	833.0	1608.0
Radiation	MoKα (λ = 0.71073)	CuKα (λ = 1.54184)	CuKα (λ = 1.5418)	MoKα (λ = 0.71073)
2Θ range for data collection/°	3.52 to 57.7	3.28 to 46.86	3.68 to 48.68	4.46 to 57.54
Index ranges	$-10 \leq h \leq 10$, $-20 \leq k \leq 20$, $-30 \leq l \leq 29$	$-11 \leq h \leq 11$, $-19 \leq k \leq 19$, $-19 \leq l \leq 19$	$-12 \leq h \leq 12$, $-15 \leq k \leq 15$, $-18 \leq l \leq 19$	$-13 \leq h \leq 13$, $-24 \leq k \leq 24$, $-22 \leq l \leq 23$
Reflections collected	29259	23430	15622	33876
Independent reflections	7036 [R_{int} = 0.0800]	4553 [R_{int} = 0.1167]	6221 [R_{int} = 0.1255]	7622 [R_{int} = 0.0730]
Data/restraints/parameters	7036/0/452	4553/6/419	6221/6/408	7622/0/417
Goodness-of-fit	1.037	0.988	0.919	1.057
Final R indexes [all data]	R_1 = 0.0976, wR_2 = 0.1390	R_1 = 0.1084, wR_2 = 0.1910	R_1 = 0.1770, wR_2 = 0.2328	R_1 = 0.0706, wR_2 = 0.1169
Largest diff. peak/hole / e $Å^{-3}$	0.89/-0.75	1.41/-0.92	1.47/-2.02	2.25/-1.21

$R_1 = \Sigma||F_o| - |F_c||/ \Sigma|F_o|$. $wR_2 = [\Sigma w(|F_o| - |F_c|)^2/|\Sigma w(F_o)^2]^{1/2}$. $w = 0.75/(\sigma^2(F_o)+0.00010F_o^2)$. Goodness-of-fit = $\{\sum[w(F_o^2 - F_c^2)^2]/(n-p)\}^{1/2}$, where n is the number of reflections and p is the total number of parameters refined.

Table 3.2. Selected bond distances (Å) and angles (°) for compounds **15- 18**. *Indicates second domain for a two-part disorder in compound **17**.

15				**16**			
Bond	Distance (Å)	Angle	Degrees (°)	Bond	Distance (Å)	Angle	Degrees (°)
Cu(1)–N(1)	2.065(3)	N(1)–Cu(1)–N(3)	157.5(1)	Cu(1)–N(1)	1.942(8)	N(1)–Cu(1)–N(2)	93.1(3)
Cu(1)–N(2)	1.913(3)	N(1)–Cu(1)–N(2)	78.8(1)	Cu(1)–N(2)	2.269(9)	N(1)–Cu(1)–N(3)	86.5(3)
Cu(1)–N(3)	2.079(3)	N(2)–Cu(1)–N(3)	78.7(1)	Cu(1)–N(3)	2.429(8)	N(2)–Cu(1)–N(3)	174.7(3)
Cu(1)–O(1)	2.280(3)	O(1)–Cu(1)–O(7)	91.0(1)	Cu(1)–N(9)	2.080(7)	N(2)–Cu(1)–N(9)	90.1(3)
Cu(1)–O(4)	2.461(3)	O(1)–Cu(1)–O(4)	172.91(8)	Cu(1)–N(10)	1.938(7)	N(2)–Cu(1)–N(10)	89.7(3)
Cu(1)–O(7)	1.937(2)			Cu(1)–N(11)	2.063(7)	N(2)–Cu(1)–N(11)	88.1(3)
				Mo(1)–C(1)	2.145(9)	N(3)–Cu(1)–N(9)	84.8(3)
				Mo(1)–C(2)	2.152(11)	N(3)–Cu(1)–N(10)	90.7(3)
				Mo(1)–C(3)	2.174(10)	N(3)–Cu(1)–N(11)	97.2(3)
				Mo(1)–C(4)	2.184(11)	Cu(1)–N(1)–C(1)	173.3(7)
				Mo(1)–C(5)	2.157(11)	Cu(1)–N(2)–C(2)	156.7(8)
				Mo(1)–C(6)	2.167(11)	Cu(1)–N(3)–C(3)	140.2(7)
				Mo(1)–C(7)	2.147(10)	Mo(1)–C(1)–N(1)	175.4(7)
				Mo(1)–C(8)	2.192(10)	Mo(1)–C(2)–N(2)	178.7(9)
				C(1)–N(1)	1.153(10)	Mo(1)–C(3)–N(3)	177.6(8)
				C(2)–N(2)	1.146(11)	C(6)–N(6)	1.167(11)
				C(3)–N(3)	1.141(11)	C(7)–N(7)	1.141(11)
				C(4)–N(4)	1.143(12)	C(8)–N(8)	1.140(11)
				C(5)–N(5)	1.151(11)		

Table 3.2 Continued.

17				**18**			
Bond	Distance (Å)	Angle	Degrees (º)	Bond	Distance (Å)	Angle	Degrees (º)
Co(1)–N(1)	2.150(14)	N(1)–Co(1)–N(6)	90.9(5)	Fe(1)–N(1)	1.926(5)	N(1)–Fe(1)–N(7)	91.9(2)
Co(1)–N(6)	1.992(17)	N(1)–Co(1)–O(1)	172.9(5)	Fe(1)–N(7)	1.912(5)	N(7)–Fe(1)–N(8)	88.4(2)
Co(1)–N(9)	2.142(16)	N(6)–Co(1)–O(1)	90.6(5)	Fe(1)–N(8)	1.918(6)	N(1)–Fe(1)–N(8)	177.1(2)
Co(1)–N(10)	2.045(15)	N(1)–Co(1)–N(9)	95.7(5)	Fe(1)–N(9)	1.978(6)	N(1)–Fe(1)–N(9)	89.3(2)
Co(1)–N(11)	2.168(15)	N(1)–Co(1)–N(10)	89.2(5)	Fe(1)–N(10)	1.861(6)	N(1)–Fe(1)–N(10)	87.3(2)
Co(1)–O(1)	2.136(11)	N(1)–Co(1)–N(11)	85.8(5)	Fe(1)–N(11)	1.990(5)	N(1)–Fe(1)–N(11)	88.2(2)
Co(2)–N(2)	2.06(2)	N(2)–Co(2)–O(2)	92.6(18)	W(1)–C(1)	2.157(7)	N(8)–Fe(1)–N(9)	93.5(2)
Co(2)–O(2)	2.32(7)	N(2)–Co(2)–O(2)*	87.4(19)	W(1)–C(2)	2.168(7)	N(8)–Fe(1)–N(10)	92.4(2)
Co(2)–O(2)*	2.32(7)	N(2)–Co(2)–O(3)	89.4(7)	W(1)–C(3)	2.147(7)	N(8)–Fe(1)–N(11)	88.9(2)
Co(2)–O(3)	2.101(14)	N(2)–Co(2)–O(3)*	90.6(7)	W(1)–C(4)	2.176(6)	Fe(1)–N(1)–C(1)	167.5(5)
Co(2)–O(3)	2.239(15)*	O(2)–Co(2)–O(3)	87.3(6)	W(1)–C(5)	2.167(7)	Fe(1)–N(7)–C(7)	175.5(5)
W(1)–C(1)	2.123(18)	O(2)–Co(2)–O(3)	92.7(6)	W(1)–C(6)	2.160(7)	Fe(1)–N(8)–C(8)	166.4(6)
W(1)–C(2)	2.05(3)	Co(1)–N(1)–C(1)	158.2(12)	W(1)–C(7)	2.138(7)	W(1)–C(1)–N(1)	176.0(6)
W(1)–C(3)	2.12(2)	Co(1)–N(6)–C(6)	174.9(17)	W(1)–C(8)	2.153(7)	W(1)–C(7)–N(7)	175.5(6)
W(1)–C(4)	2.17(2)	Co(2)–N(2)–C(2)	167.5(19)	C(1)–N(1)	1.135(8)	W(1)–C(8)–N(8)	170.6(6)
W(1)–C(5)	2.18(2)	W(1)–C(1)–N(1)	174.9(15)	C(2)–N(2)	1.140(9)	C(6)–N(6)	1.137(9)
W(1)–C(6)	2.19(2)	W(1)–C(2)–N(2)	179(2)	C(3)–N(3)	1.154(9)	C(7)–N(7)	1.152(8)
W(1)–C(7)	2.11(2)	W(1)–C(6)–N(6)	177.0(17)	C(4)–N(4)	1.131(8)	C(8)–N(8)	1.154(8)
W(1)–C(8)	2.182(19)	C(5)–N(5)	1.11(2)	C(5)–N(5)	1.146(9)		
C(1)–N(1)	1.157(18)	C(6)–N(6)	1.13(2)				
C(2)–N(2)	1.23(3)	C(7)–N(7)	1.16(2)				
C(3)–N(3)	1.17(2)	C(8)–N(8)	1.14(2)				
C(4)–N(4)	1.11(2)						

[Cu^{II}(tptz)(CF$_3$SO$_3$)$_2$(CH$_3$OH)]·2H$_2$O (15). Compound **15** is a mononuclear Cu(II) complex whose coordination environment consists of a tridentate tptz ligand, two coordinated triflate anions and a methanol solvent molecule, Figure 3.1. The triflate ligands are arranged in trans positions with each other, with the methanol molecule being trans to a central N atom of the tptz ligand. The Cu–N distances to the coordinated nitrogen atoms of the tptz molecule and the Cu–O bond lengths are listed in Table 3.2.

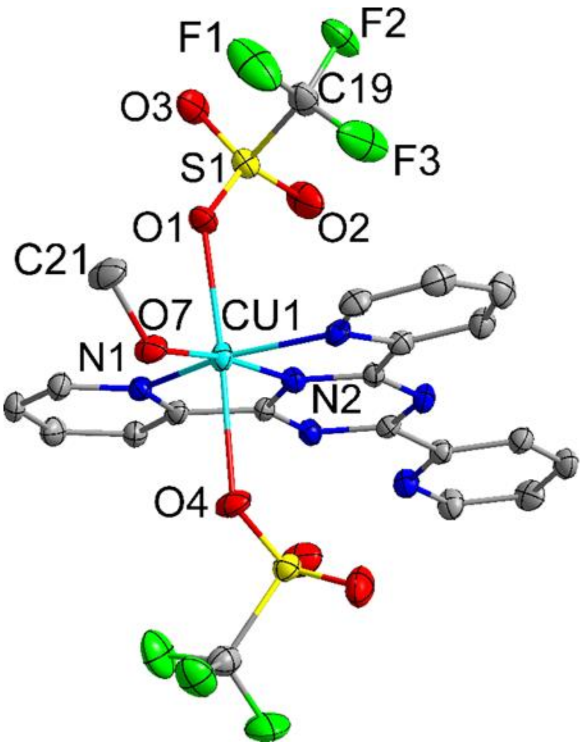

Figure 3.1 Molecular structure of [Cu(tptz)(CF$_3$SO$_3$)$_2$(CH$_3$OH)]·2H$_2$O, **15**. Ellipsoids are plotted at the 50% probability level; H atoms are omitted for the sake of clarity.

{[Cu^{II}(tptz)Mo^{V}(CN)$_8$]$^-$·(H$_3$O)$^+$·CH$_3$OH}$_\infty$, (16). The crystal structure of **16** contains Cu$_2$Mo$_2$ square fragments that are connected through shared edges. The structure consists of a one-dimensional "ladder" extending along the crystallographic a axis, Figure 3.2. The Cu(II) ions are in an octahedral environment that consists of one tridentate tptz ligand and three bridging $CN^–$ ligands which replace the positions of the triflate anions and the methanol molecule in **15**. The change in the coordination environment of the Cu(II) centers has little effect on the bond lengths between the Cu(II) ion and the nitrogen atoms of tptz ligand (2.080(7), 1.938(7), and 2.063(7) Å in **16**, as compared to 2.079(3), 1.913(3), and 2.065(3) Å in **15** (See Table 3.2)). The $[Mo^V(CN)_8]^{3–}$ anion adopts a square antiprismatic geometry with three bridging and five terminal $CN^–$ ligands. The combination of Cu(II) cations and $[Mo^V(CN)_8]^{3–}$ in **16** requires an extra positive charge to achieve neutrality. It is conceivable that the coordinated pyridyl moiety in tptz is protonated,[218,219] but the crystal structure indicates that the inter-chain interactions contain weak hydrogen bonding between H_3O^+ cations and $[Mo^V(CN)_8]^{3–}$ anions, Figure 3.3 and Figure 3.4. The hydrogen bond distances connecting adjacent chains alternate between 2.76 and 2.82 Å.

$\{[Co^{II}_2(tptz)_2(H_2O)_2W_2^V(CN)_{16}Co^{II}(H_2O)_4]\cdot 2H_2O\}_\infty$ (17). Chains of cyanide-bridged alternating arrays of Co_2W_2 squares and $[Co(H_2O)_4]^{2+}$ fragments comprise **17**, Figure 3.5. As compared to the ladder-type structure of **16**, the square fragments of Co_2W_2 are interconnected by $[Co(H_2O)_4]^{2+}$ ions through the CN^- ligand on the $[W^V(CN)_8]^{3-}$ moiety to construct an infinite chain of squares. The chain exhibits a zig-zag motif with interstitial water molecules located between the chains. The Co1 ion is bound to one tptz ligand, two CN^- ligands from $[W^V(CN)_8]^{3-}$ and one oxygen atom from water. The octahedral environment of the Co1 ion deviates from ideal 90° angles: N1-Co1-N6 90.9(5)°, N6-Co1-

O1 90.6(5)°, N1-Co1-N9 95.7(5)°, N1-Co1-N10 89.2(5)°, N1-Co1-N11 85.8(5)°, N1-Co1-O1 172.9(5)°. By comparison, the angles of the Co2 ion also deviate from 90°: N2-Co2-O2 92.6(18)°, N2-Co2-O3 89.4(7)°. The chains run parallel to the c axis, Figure 3.6, and H_2O molecules are situated between the chains which interact with each other through hydrogen bonding of the W-C≡N···HO and Co-O···HO types. The closest interchain distance in 9.6 Å, Figure 3.7.

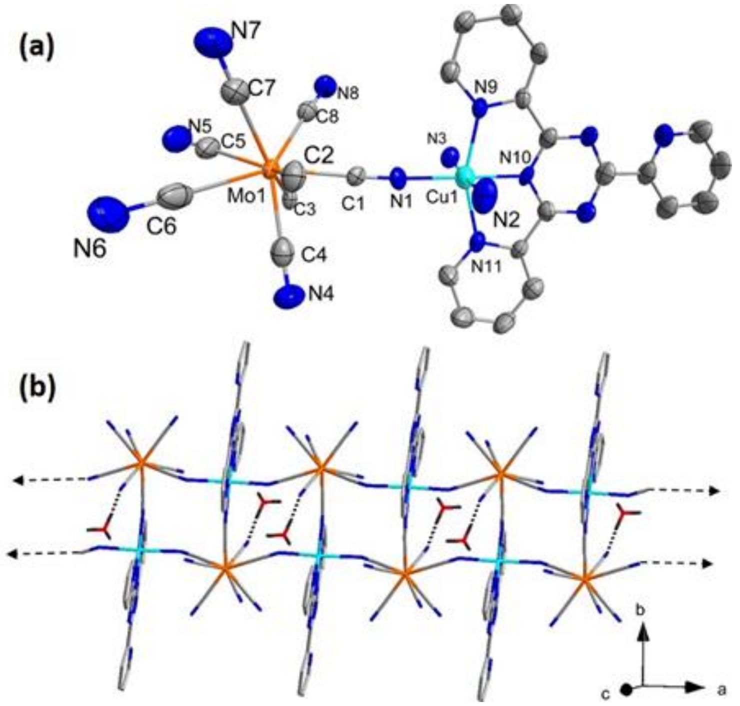

Figure 3.2 (a) Depiction of the asymmetric unit of **16** with thermal ellipsoids plotted at the 50% probability level; H atoms are omitted for the sake of clarity. (b) View of one-dimensional chain structure of **16** approximately along *a* axis. The figure depicts hydrogen bonding of the C≡N···HO type between H_3O^+ cations and $[Mo^V(CN)_8]^{3-}$ anions. Arrows indicate direction of chain propagation.

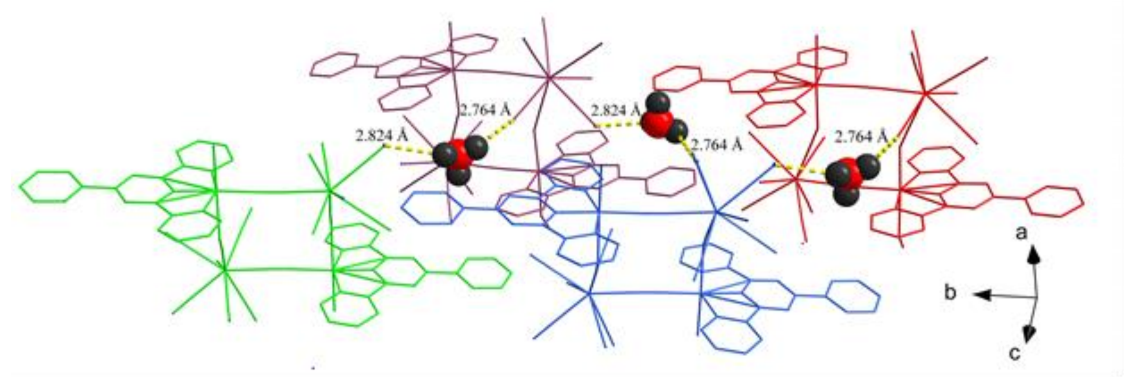

Figure 3.3 Representation of **16** emphasizing the inter-molecular hydrogen bonds (indicated by dotted yellow lines) between neighboring 1D ladder-type chains. Methanol molecules are omitted for clarity. H_3O^+ cations are represented by enlarged ball and stick models and different chain units are represented by different colors. Hydrogen bond lengths are labeled. Each chain unit extends along the *a* axis.

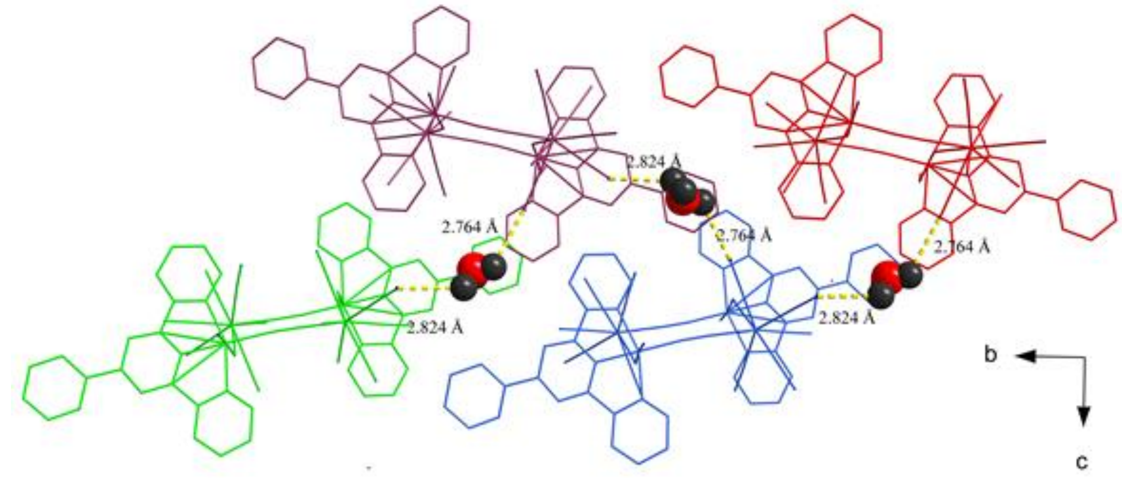

Figure 3.4 Packing diagram of **16** looking down the *a* axis.

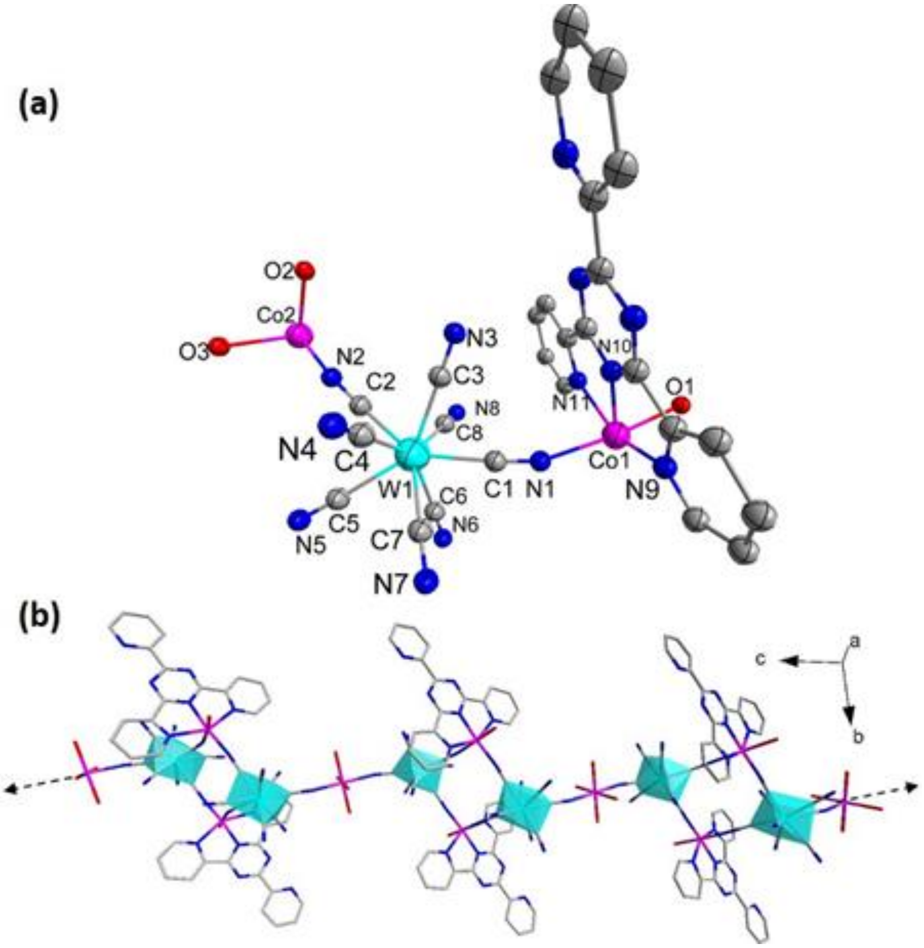

Figure 3.5 (a) Depiction of the asymmetric unit of **17** with thermal ellipsoids plotted at the 50% probability level; H atoms and solvent molecules are omitted for the sake of clarity. (b) View of the one-dimensional chain structure of **17** approximately along *c* axis. Octacyanotungstate anions are depicted with superimposed teal polyhedra. Arrows indicate directions of chain propagation.

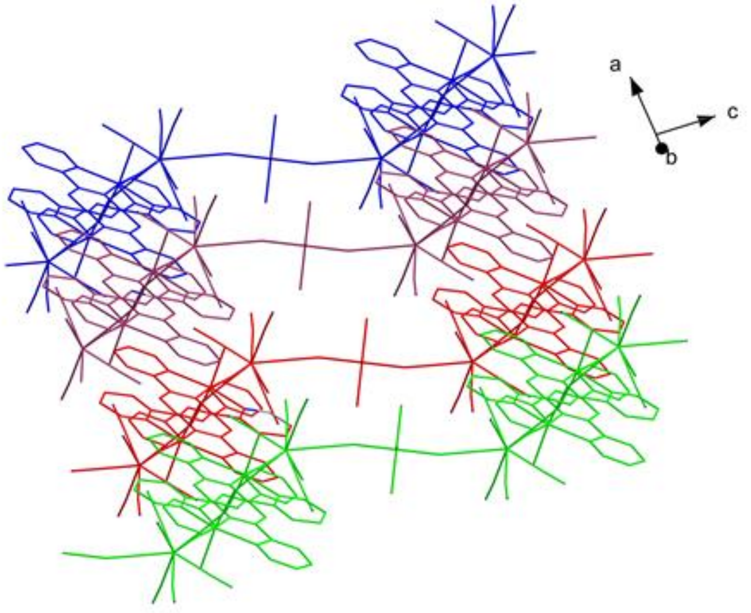

Figure 3.6 Packing diagram of **17** along selected axis.

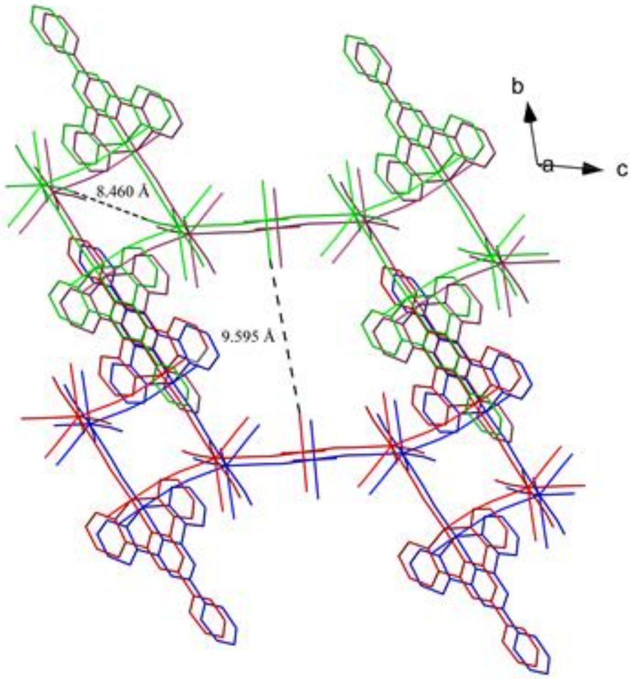

Figure 3.7 Packing diagram of **17** along *a* axis. The bond distances are shown between chains through the aqua ligands of the bridging Co(II) moiety on neighboring chains and within a square unit of the chain through the nitrogen atoms of the closest cyanide ligands.

$\{[\mathrm{Fe^{III}(tptz)W^{V}(CN)_8]\cdot 2CH_3OH}\}_\infty$ (18). Compound **18** is isostructural with **16** and has the same asymmetric unit consisting of M_2W_2 fragments that form a zigzag chain of cyanide-bridged Fe(III) and W(V) ions. The Fe(III) ions are in an octahedral environment that consists of one tridentate tptz ligand and three bridging CN^- ligands. As in the case of **16**, the $[W^V(CN)_8]^{3-}$ anion in **18** is in a square antiprismatic conformation with three bridging and five terminal CN^- ligands. The W(V) centers connect two adjacent squares via edge-sharing of Fe-N≡C-W, thus resulting in the ladder motif, Figure 3.8. In considering the driving force for the formation of the different structural motifs, it is reasonable to suggest that the formation of **18** is aided by the neutrality of the resulting phase which facilitates crystallization. The compound crystallizes with interstitial methanol molecules, Figure 3.9 and Figure 3.10.

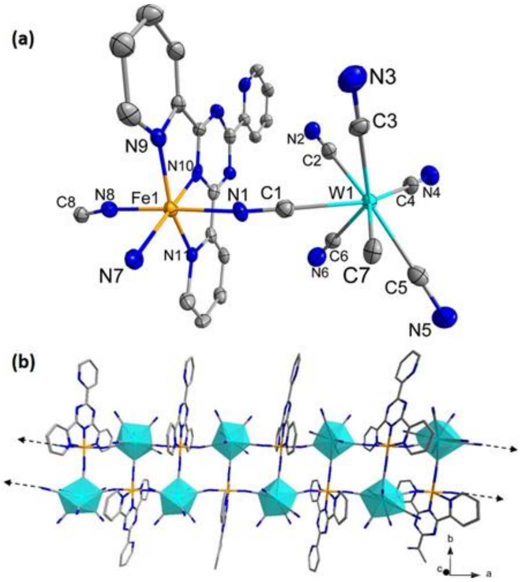

Figure 3.8 (a) Depiction of the asymmetric unit of **18** with thermal ellipsoids plotted at the 50% probability level; H atoms are omitted for the sake of clarity. (b) Packing diagram for **18**.

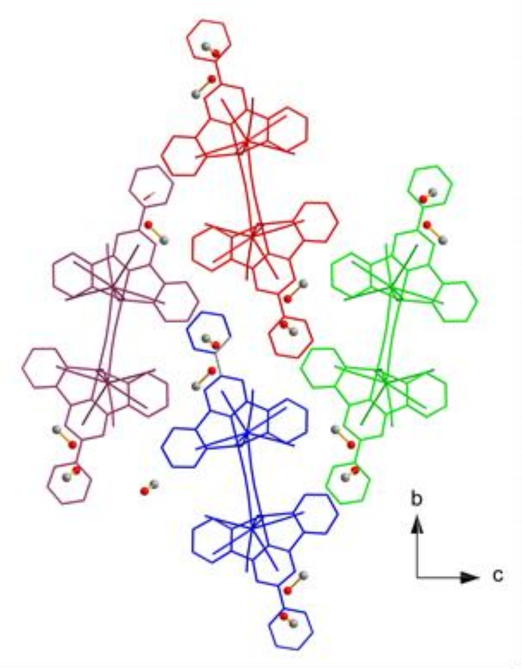

Figure 3.9 Packing diagram of four chain units of **18** along *a* axis. Chain propagation is along *a* axis. Methanol molecules are represented as ball and stick.

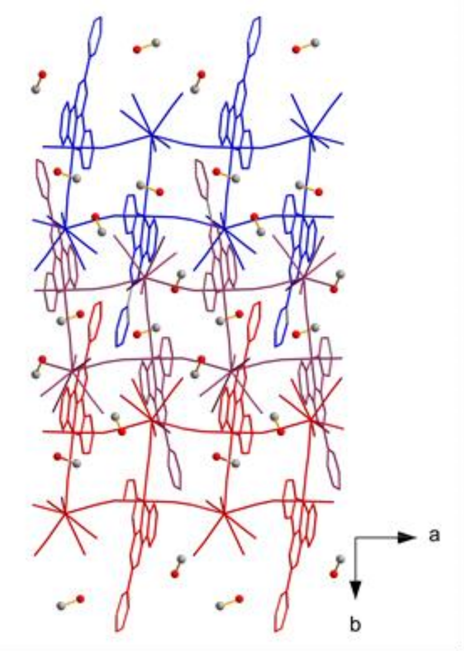

Figure 3.10 Packing diagram of four chain units of **18** along *c* axis. Chain propagation is along *a* axis. Methanol molecules are represented as ball and stick.

Magnetic Properties

{[Cu^{II}(tptz)Mo^{V}(CN)$_8$]$^-$·(H$_3$O)$^+$·CH$_3$OH}$_\infty$ (16). The χT and 1/χ versus T plots for **16** are shown in Figure 3.11. The value of χT at 300 K is 0.76 emu·mol^{-1} K, in accord with the expected value for two non-interacting spins S = 1/2, g = 2.0 (χT = 0.75 emu·mol^{-1} K). The temperature dependence of 1/χ between 300 and 20 K approximates Curie-Weiss behavior with C = 0.755 emu·mol^{-1} K and θ = 4 K. The increase of χT upon cooling and positive sign of the Curie-Weiss constant indicates the presence of ferromagnetic interactions between Cu(II) and Mo(V) centers.

Well-isolated Cu(II)-Mo(V) chains are the dominant magnetic units in this material. The magnetic data were fit to a ferromagnetic chain model[220] (the Hamiltonian is written as $H = -\Sigma J_i J_{i-1}$). Weak inter-chain antiferromagnetic interactions were accounted for by applying the molecular field approximation, equation 3.1, where χ_{chain} is the magnetic susceptibility of the chain, zJ' is the exchange parameter, N is Avogadro's constant, g is the Landé g-factor, and β is the Bohr Magneton)[10]:

$$\chi = \frac{\chi_{chain}}{1-(zJ' / Ng^2\beta^2)\chi_{chain}}$$ **Equation 3.1**

This model produces a good fit to the experimental data over the whole temperature range with the parameters J = +4 cm^{-1}, g = 2.0, and zJ' = -0.9 cm^{-1}.

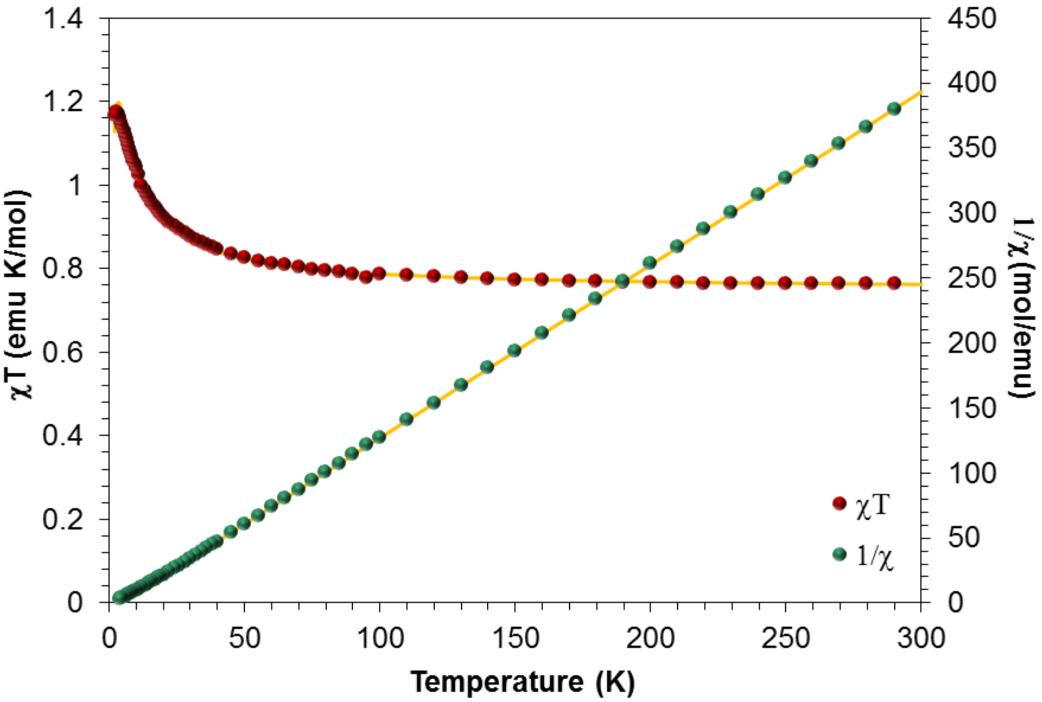

Figure 3.11 Temperature dependence of χT and 1/χ for **16**. The solid yellow line corresponds to the best fit to a ferromagnetic *S* = 1/2 chain model; the red line is the Curie-Weiss fit.

$\{[Co^{II}_2(tptz)_2(H_2O)_2W_2^V(CN)_{16}Co^{II}(H_2O)_4]\cdot 2H_2O\}_\infty$ (17). The χT and 1/χ versus T plots for **17** are provided in Figure 3.12. The value of χT at 300 K is 10.9 emu·mol^{-1} K, which is close to the expected value (χT = 11.0 emu·mol^{-1} K) for the sum of two W(V) ions (S = ½, g=2.0) and three Co(II) ions (S = 3/2, g =2.7). The temperature dependence of 1/χ between 300 and 60 K approximates Curie-Weiss behavior with C = 11 emu·mol^{-1} K and θ = -8 K. The decrease of χT upon cooling and the negative sign of the Curie-Weiss constant is due to spin-orbit coupling of Co(II) ions. Starting from 20 K, the χT value increases from 9.6 to 9.8 emu·mol^{-1} K at 10 K, which may indicate the presence of weak ferromagnetic interactions between the Co(II) and W(V) centers. Below 10 K, the χT value decreases to 8 emu·mol^{-1} K. A weak out-of-phase AC signal appears at low temperature which suggests possible SCM behavior for this compound, Figure 3.12 inset.

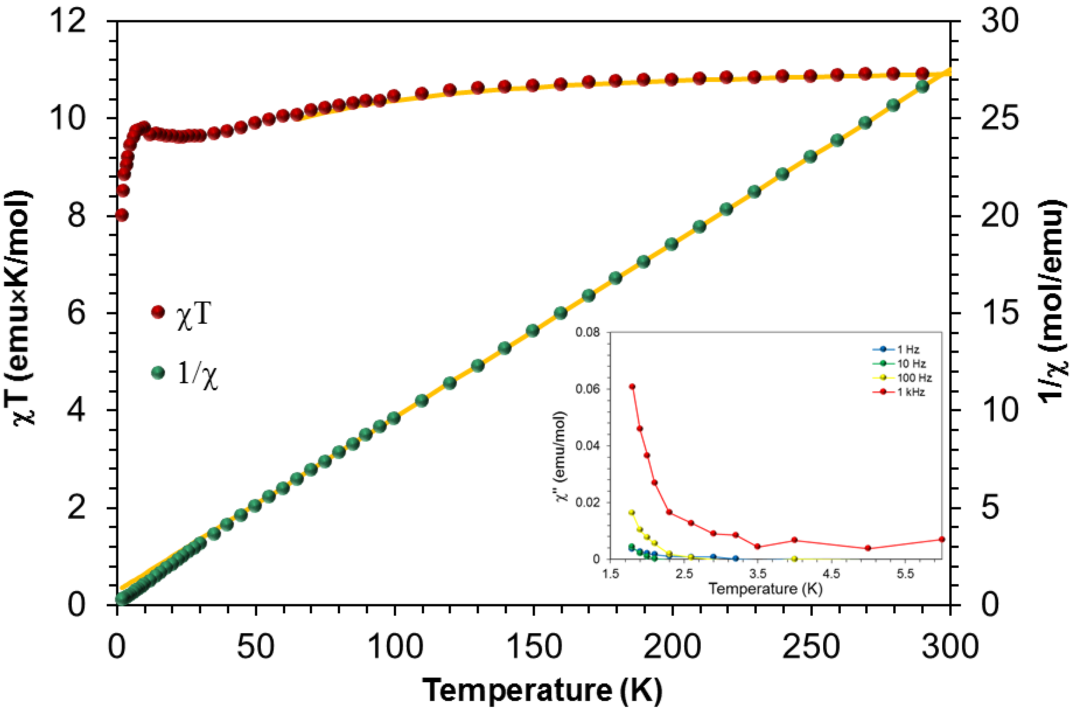

Figure 3.12 Temperature dependence of χT and 1/χ for **17**. The solid lines correspond to the best fit to the Curie-Weiss law. Inset: Out-of-phase AC susceptibility.

$\{[Fe^{III}(tptz)W^{V}(CN)_8]\cdot 2CH_3OH\}_\infty$ (18). The χT and 1/χ versus T plots for **18** are shown in Figure 3.13. The value of χT at 300 K is 0.85 emu·mol^{-1} K, which equates to the expected value (χT = 0.85 emu·mol^{-1} K) for the sum of a W(V) ion (S = 1/2, g=2.0) and Fe(III) ion (S = 1/2, g =2.25). The temperature dependence of 1/χ between 300 and 30 K approximates Curie-Weiss behavior with C = 0.87 emu·mol^{-1} K and θ = -4 K. The prominent factor for the decrease of χT upon cooling and the negative sign of the Curie-Weiss constant is the spin-orbit coupling contribution from the Fe(III) ion. Additionally, weak antiferromagnetic interactions between W(V) and Fe(III) centers are operative.

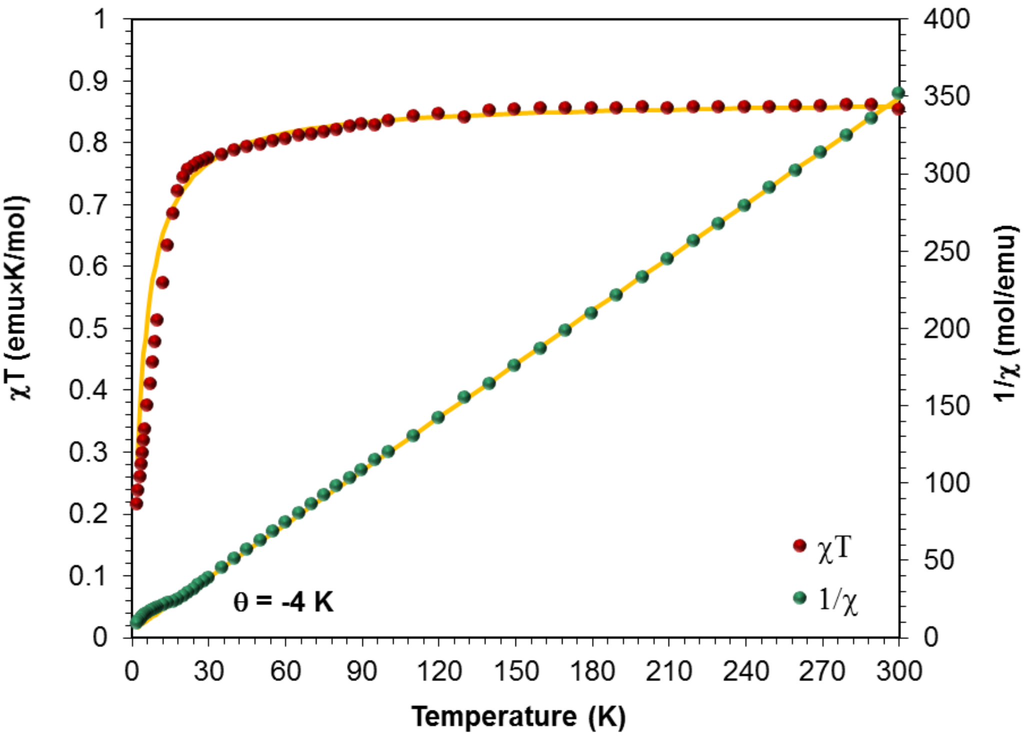

Figure 3.13 Temperature dependence of χT and 1/χ for **18**. The solid lines correspond to the best fit to the Curie-Weiss law.

Concluding Remarks

Three new heterobimetallic chains $\{[Cu^{II}(tptz)Mo^{V}(CN)_8]^{-}\cdot H_3O^{+}\cdot CH_3OH\}_\infty$ (**16**), $\{[Co^{II}_2(tptz)_2(H_2O)_2W_2^{V}(CN)_{16}Co^{II}(H_2O)_4]\cdot 2H_2O\}_\infty$ (**17**) and $\{[Fe^{III}(tptz)W^{V}(CN)_8]\cdot 2CH_3OH\}_\infty$ (**18**) are reported. Compounds **16** and **18** are composed of an infinite ladder of edge-sharing squares. Compound **17** is composed of molecular squares bridged by $[Co(H_2O)_4]^{2+}$ cations. The magnetic behavior of **16** is dominated by ferromagnetic coupling between Cu(II) and Mo(V) ions, as opposed to isostructural **18** which exhibits weak antiferromagnetic coupling between Fe(III) and W(V) centers. In the case of **17**, the magnetic data indicate a ferromagnetic interaction between Co(II) and W(V) centers and a weak out-of- phase AC signal at low temperature, which may indicate single-chain magnet behavior. Importantly, this work exemplifies the building block approach towards reducing dimensionality in the rational design of molecular magnetic materials.

CHAPTER IV

MAGNETIC STUDIES OF TITANIUM-CONTAINING MAGNETIC MOLECULES

Introduction

The field of single-molecule magnets (SMMs) has witnessed a full-circle transformation in regards to the molecules studied for magnetic anisotropy. After the seminal $Mn_{12}OAc$ compound was discovered to exhibit slow paramagnetic relaxation, many synthetic efforts focused on synthesizing giant spin clusters in hopes of increasing the spin-reversal barrier.[221-225] In fact our group reported one such example, namely a $\{Mo_8Mn_{14}\}$ docosanuclear cluster exhibiting an S = 31 ground state which is the highest spin value known for cyanide-bridged clusters.[226] Despite these efforts, which include the largest ground spin state ever achieved which is S = 83/2 for $[Mn^{III}_{12}Mn^{II}_{7}(\mu_{4}\text{-}O)_{8}(\mu_{3},\eta^{1}\text{-}N_{3})_{8}(H_{3}L)_{12}(MeCN)_{6}]Cl_{2}\cdot 10MeOH\cdot MeCN$ (H_3L=2,6-bis(hydroxymethyl)-4-methylphenol), higher barriers and ordering temperatures have remained elusive. Theoretical evidence began to emerge which indicated that incorporation of highly anisotropic building blocks with first order spin-orbit coupling would be a more effective means for enhancing the energy barrier in SMMs.[227-232] Many researchers directed their attention to the lanthanide elements which are inherently anisotropic due to strong spin-orbit coupling which leads to barriers based on the splitting of M_J states.[118,131] This appears to be the current trend, as many records are being made in the subset of SMMs known as mononuclear lanthanide SMMs (the topic of chapter V). The main caveats regarding lanthanide SMMs are two-fold: (1) coupling with other spins through ligands is minimal due to shielding of the 4f electrons and (2) despite impressive barriers based on AC susceptibility measurements, hysteresis temperatures remain low due to fast quantum tunneling and other complex modes of relaxation. The current hysteresis record is held by two different lanthanide SMMs at just 14 K.[100,131]

In addition to lanthanide and actinide SMM research, the pursuit of underexplored transition metal ions or common transition metal ions with exotic oxidation states or geometries is an active direction for the area.[113,233-235] It was recently shown that large spin-orbit coupling can be achieved by controlling the ligand field in the unsaturated two-coordinate complex of iron(I), $[Fe(C(SiMe_3)_3)_2]_2$. This molecule exhibits blocking temperatures below 29 K with an effective spin reversal barrier Ueff = 226 cm^{-1} as well as magnetic hystersis up to 4.5 K- results that are comparable to lanthanide SMMs. Researchers where then inspired to pursue molecules with degeneracy of the ground state orbitals. Recent computations show that a large contribution to D_z, or the uniaxial easy-axis direction of the magnetic moment, can be realized when the first excited state involves a transition between orbitals with the same m_l quantum number compared with the ground state.[115] This type of scenario can be accomplished, as our theory collaborator Prof. Boris Tsukerblat showed over 10 years ago, by increasing the trigonal distortion in the geometry of the transition metal ion in cyanide-based SMMs.[236]

Previous work in our group reported magnetic compounds based on a trigonally distorted $[Re(triphos)(CN)_3]^-$ building block, the results of which produced a family of cyanide bridged compounds 3d metal ions of general formula $[\{MX\}_4\{Re(triphos)(CN)_3\}_4]$ (M = Mn, Fe, Co, Ni, Zn; X = Cl, I, $-OCH_3$; triphos = 1,1,1-tris(diphenylphosphinomethyl)ethane). These molecules were found to exhibit interesting electrochemical and magnetic properties[237] and the Mn(II) analog displays single molecule magnetic behavior albeit with a fast tunneling relaxation process at zero-field as determined by micro-SQUID measurements. The iron derivative exhibits six one-electron reversible redox couples and two closely spaced one-electron quasi-reversible processes, behavior that is of great interest for applications in electronic devices.

With the preceding discussion in mind, a research goal of mine has been to induce a trigonal field in underexplored transition metal complexes that exhibit the possibility for orbital degeneracy in the ground state. In this vein, the d^1 titanium(III) ion was targeted in the trigonal field of the anionic scorpionate ligand tris(3,5-dimethyl-1-pyrazolyl)borohydride (Tp*) depicted in Chart 4.1, as it has a proven track record as a convenient facial capping ligand in cyanide clusters.[185] A perusal of the literature indicates that Tp* is useful in trivalent titanium chemistry,[237-244] although it has been noted that the scorpionate ligand can decompose in the presence of this ion.[245]

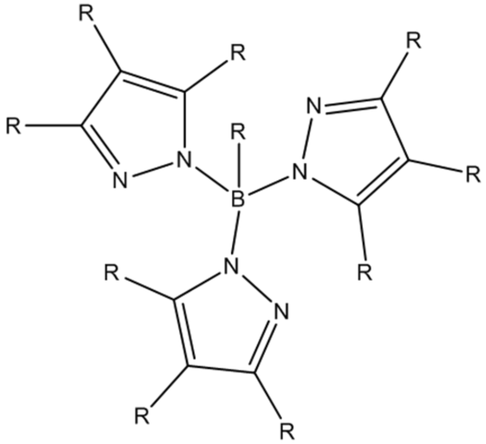

Chart 4.1 General structure of a pyrazolylborate ligand. The R groups indicate that substitution is possible on 10 carbon centers. Coordination to metal ions occur through three nitrogen atoms on the pyrazole moieties.

To date, there are very few discrete heterometallic molecules containing titanium(III) in the literature and no cases of SMMs.[246-252] This is likely is due to the high sensitivity towards water and oxygen, as well as their propensity to act as catalysts. The most well-studied examples of titanium(III) compounds include homonuclear salts of urea,[253,254] hexaaqua,[255-258] and halide[246,247,251,259-267] complexes. Of interest in the context of my project is the fact that the titanium(III) ion has been predicted to offer the advantage of ferromagnetic interactions in designed cyanide-bridged heterometallic compounds with exchange constants ranging from J = +37 and +161 cm^{-1} for Ti^{III}-CN-Cr^{III} and Ti^{III}-CN-V^{II} linkages, respectively.[268] The result of unquenched orbital angular momentum was demonstrated in the magnetic properties of the homoleptic $[Ti_2Cl_9]^{3-}$ anion for which an effective spin-orbit coupling Hamiltonian with low-symmetry components of the crystal field was used to accurately account for the magnetic properties.[269] An additional effect of comparable magnitude is the Jahn-Teller distortion, which can lift the degeneracy of the ground state and couple with low-lying vibronic states, which mix into the ground state through the magnetic field. This situation has been shown to occur in Ti(III) model complexes.[256]

This chapter is divided into two parts. The first section focuses on the synthesis of the new titanium cyanide building block, $[(CH_3CH_2)_4N][Tp^*Ti(CN)_3]$, as well as its chloride precursor with full magnetic and theoretical considerations. Attempts to incorporate this new cyanide building block into heteronuclear molecules are then discussed. All attempts to obtain a multinuclear cluster containing the intact $[Tp^*Ti(CN)_3]^-$ anion have been unsuccessful but among the numerous reactions studied, several very interesting decomposition products were obtained. Most notably, a family of trinuclear compounds of general formula, $\{(Tp^*Ti)(\mu_2\text{-}OAc)_2(\mu_2\text{-}O)M(\mu_2\text{-}O)(\mu_2\text{-}OAc)_2(TiTp^*)\}\cdot x(CH_3CN)$, (M = Cr^{III}, Mn^{II}, Co^{II}; x = 1-4; OAc = acetate) was obtained by hydrolysis of the precursor, the results of which are described in the second part of this chapter. This structural motif places the central metal ion in a pseudo-octahedral environment with slight axial compression. Such a geometry was recently predicted to be an excellent case for large uniaxial magnetic anisotropy with certain transition metal ions.[115] A comparison of the compounds $\{(Tp^*Ti^{IV})(\mu_2\text{-}OAc)_2(\mu_2\text{-}O)M^{II}(\mu_2\text{-}O)(\mu_2\text{-}OAc)_2(Ti^{IV}Tp^*)\}\cdot 4(CH_3CN)$ (M = Mn, Co) validates this theoretical prediction of engendering large D-values in geometrically designed transition metal complexes.

Experimental Section

Syntheses

The reagents $TiCl_3(THF)_3$ (97%, Sigma-Aldrich), KTp* (98%, TCI Chemicals), $[(CH_3CH_2)_4N]Cl$ (>98%, Sigma-Aldrich), $[(CH_3)_3Si]CN$ (98%, Sigma-Aldrich), anhydrous solvents diethyl ether (HPLC >99.9% inhibitor free, Sigma-Aldrich), and dimethylformamide (99.8%, Sigma-Aldrich) were purchased and used as received. Acetonitrile and tetrahydrofuran (ACS grade) were pre-dried over 3 Å molecular sieves and distilled under a dinitrogen atmosphere. The compound, $[(CH_3CH_2)_4N]CN$, was prepared by metathesis of $[(CH_3CH_2)_4N]Cl$ with NaCN in methanol followed by an extraction into CH_3CN, concentration, and precipitation with THF. Before using $[(CH_3CH_2)_4N]CN$ it was dried for 24 hours at ambient temperature in a distillation apparatus containing P_2O_5. The reagents $Cr_2(C_2H_3O_2)_4$,[270] $[Cr(CH_3CN)_4][BF_4]_2$,[271]

$Tp^*Ni(NO_3)$,[272] and $Tp^*Co(NO_3)$[272] was prepared following published procedures. All glassware was coated with Glassclad 18 and heated in an oven before use to minimize residual surface water. All reactions were conducted using standard Schlenk-line techniques or inside a nitrogen filled glovebox.

Preparation of $[(CH_3CH_2)_4N][Tp^*TiCl_3]$ (19). In a nitrogen purged glovebox, 5.0 g of $TiCl_3(THF)_3$, 4.45g KTp*, and 2.2g $[(CH_3CH_2)_4N]Cl$ were added to a 200 mL Schlenk flask and charged with 100 mL CH_3CN. The dark purplish blue mixture was stirred for 24 hours and then filtered through a 30 mL glass fritted medium porosity frit to remove KCl. The filtrate was concentrated to ~ 30 mL which led to the precipitation of the first crop of blue product. The remaining filtrate was concentrated to dryness, redissolved in a minimal amount of acetonitrile, filtered through a 30 mL medium porosity frit and treated with 150 mL of diethyl ether to produce a second crop of blue solid. At this stage, the filtrate was pinkish purple in color and slow evaporation led to crystals of the by-product $[Tp^*TiCl_2pz^*]pz^*$ (pz* = 3,5-dimethylpyrazole). Adding a stoichiometric amount of $[(CH_3CH_2)_4N]Cl$ to an acetonitrile solution of $[Tp^*TiCl_2pz^*]pz^*$ led to a third crop of blue solid which was collected on a 30 mL medium porosity frit. All three crops of solid were combined and redissolved in a minimal volume of acetonitrile. The blue solution was filtered and the filtrate was stored at -15 ^oC for 24 hours to give a crystalline product in a final yield of 6.3 g (80% based on $TiCl_3(THF)_3$). IR (Nujol), ν(BH), cm^{-1}: 2513; ν(CH), cm^{-1}: 3129. Large block-shaped crystals of $[(CH_3CH_2)_4N][Tp^*TiCl_3]$ were grown by slow diffusion of diethyl ether into an acetonitrile solution of $[(CH_3CH_2)_4N][Tp^*TiCl_3]$ in a Schlenk tube after 1 week.

Preparation of [Tp*TiCl$_2$pz*]pz* (20). Compound **20** was originally isolated as a side product to the preparation of compound **19**. In initial efforts to react Tp*TiCl$_2$(THF) with [(CH$_3$CH$_2$)$_4$N]CN in THF, both compound **19** and **20** crystallized from the reaction mixture after layering with benzene.

Preparation of [(CH$_3$CH$_2$)$_4$N][Tp*Ti(CN)$_3$] (21). In the most successful experiment, 0.51 g [(CH$_3$CH$_2$)$_4$N]CN were dissolved in 20 mL CH$_3$CN and added slowly via pipette transfer to a stirring solution of 0.63g [(CH$_3$CH$_2$)$_4$N][Tp*TiCl$_3$] dissolved in 25 mL CH$_3$CN. The resulting reaction mixture was stirred for 15 hours during whic time a color transformation occurred from blue to green to brown and finally to orange. The reaction mixture was filtered through a 30 mL medium porosity gla frit to remove a dark blue impurity. The bright orange filtrate was concentrated to ~ 10 mL and treated with 90 mL of diethyl ether. The bright orange crude precipitate collected by filtration: yield 0.55 g (92% based on [(CH$_3$CH$_2$)$_4$N][Tp*TiCl$_3$]). IR (Nujol), ν(CN), cm^{-1}: 2116, 2103; ν(BH), cm^{-1}: 2521; ν(CH), cm^{-1}: 3110. Crystals of [(CH$_3$CH$_2$)$_4$N][Tp*Ti(CN)$_3$] were obtained from a 5mM solution of the crude powder containing 30% by volume acetonitrile in diethyl ether. Elemental analysis: Calcd. for **21** (C$_{26}$H$_{42}$B$_1$N$_{10}$Ti$_1$): C, 56.54; H, 7.48; N, 25.36. Found: C, 55.43; H, 7.44; N, 23.39; Cl, 0.00 %. By reacting [(CH$_3$CH$_2$)$_4$N][Tp*TiCl$_3$] with 13 molar equivalents of [(CH$_3$CH$_2$)$_4$N]CN, a different polymorph was found from layering of the acetonitrile solution with diethyl ether in a thin tube.

Preparation of [(CH$_3$CH$_2$)$_4$N]{(Tp*Ti(CN)$_2$)$_2$(μ-CN)} (22). In a 100 mL Schlenk flask, 1.0 g [(CH$_3$CH$_2$)$_4$N][Tp*TiCl$_3$] was dissolved in 20 mL of acetonitrile. To this intense blue solution was added 3 mL of $[(CH_3)_3Si]CN$. The reagent $[(CH_3)_3Si]CN$ readily hydrolyzes in air producing $HCN_{(g)}$ therefore great care was taken when transferring the $[(CH_3)_3Si]CN$ solution via syringe to the $[(CH_3CH_2)_4N][Tp^*TiCl_3]$ solution. After the addition, the reaction solution was heated to 80 ^oC in an oil bath and allowed to stir for 24 hours and then cooled to room temperature and reduced to dryness under vacuum. The resulting residue was treated with 50 mL of acetonitrile and stirred for 2 hours. The resulting mixture contained a bright orange filtrate and a brownish tan powder. The powder was collected on a 30 mL glass medium porosity frit and rinsed with 3 X 10 mL portions of acetonitrile. IR (Nujol), ν(CN), cm^{-1}: 2137, 2116, 2103; ν(BH), cm^{-1}: 2521; ν(CH), cm^{-1}: 3120. The resulting powder was insoluble in all common organic solvents and attempts slow the rate of formation did not lead to crytals of the product.

Preparation of $[(CH_3CH_2)_4N]_4[\{CoCl\}_4\{Ti(CN)_6\}_4]\cdot 16THF$ (23). Layering THF mixtures of 10mM $[(CH_3CH_2)_4N][Tp^*Ti(CN)_3]$ and 10 mM $CoCl_2$ with a buffer of toluene in a thin tube led to the isolation of large blue crystals that are stable in air over the course of 1 year. The structure was tentatively solved as a cube of formula $[(CH_3CH_2)_4N]_4[\{CoCl\}_4\{Ti(CN)_6\}_4]$. Insufficient tetraethylammonium cations were found in the structure to suggest trivalent titanium ions. IR (Nujol), ν(CN), cm^{-1}: 2170 and 2135. Performing the direct reaction of $[(CH_3CH_2)_4N]_3[Ti(CN)_6]$ with $CoCl_2$ was unsuccessful, presumably due to time sensitive nature of crystal growth. The direct reaction produced amorphous solids, which resulted in IR spectra that did not match the spectrum of **23**.

Preparation of $[(CH_3CH_2)_4N]\{(Tp^*Ti^{III})(\mu_2\text{-}OAc)_2(\mu_2\text{-}O)Cr^{III}(\mu_2\text{-}O)(\mu_2\text{-}OAc)_2(Ti^{III}Tp^*)\}\cdot(CH_3CN)$ (24). In a 50 mL Schlenk tube, 0.124 g $Cr_2(C_2H_3O_2)_4$ were dissolved in 10 mL of 1:1 CH_3CN/DMF. In a separate glass vial, 0.40 g $[(CH_3CH_2)_4N][Tp^*Ti(CN)_3]$ were dissolved in 10 mL acetonitrile. The bright orange titanium solution was layered over the reddish brown chromium solution. After sitting undisturbed for 24 hours, small green needle-like crystals had formed at the interface of the two solutions. The crystals were obtained by filtration through a 15 mL medium porosity frit; yield: 0.22 g (48% based on $Cr_2(C_2H_3O_2)_4$). IR (Nujol), ν(BH), cm^{-1}: 2520; ν(CH), cm^{-1}: 3111.

Preparation of $\{(Tp^*Ti^{IV})(\mu_2\text{-}OAc)_2(\mu_2\text{-}O)Mn^{II}(\mu_2\text{-}O)(\mu_2\text{-}OAc)_2(Ti^{IV}Tp^*)\}\cdot4(CH_3CN)$ (25). In a 100 mL Erlenmeyer flask, 0.124 g $Mn(C_2H_3O_2)_2\cdot4H_2O$ were dissolved in 40 mL of DMF. In a separate Schlenk flask inside the glove box, 0.51 g $[(CH_3CH_2)_4N][Tp^*Ti(CN)_3]$ was dissolved in 20 mL of CH_3CN. The bright orange titanium solution was removed from a glovebox, and quickly dumped into the Erlenmeyer containing $Mn(C_2H_3O_2)_2\cdot4H_2O$. The reaction miture was mechanically shaken for 30 seconds and then the flask was stored undisturbed for 24 hours. Yellowish orange, air-stable crystals were harvested from the bottom of the flask and rinsed with DMF followed by CH_3CN until the washings were colorless. Yield: 0.25g (46% based on $[(CH_3CH_2)_4N][Tp^*TiCN_3]$). Elemental analysis: Calcd. for **25** ($C_{46}H_{68}B_2N_{16}O_{10}Ti_2Mn$): C, 46.92; H, 5.82; N, 19.03. Found: C, 46.92; H, 5.81; N, 19.08%. IR (Nujol), ν(BH), cm^{-1}: 2527; ν(CH), cm^{-1}: 3116.

Preparation of {(Tp*Ti^{IV})(μ_2-OAc)$_2$(μ_2-O)Co^{II}(μ_2-O)(μ_2-OAc)$_2$(Ti^{IV}Tp*)}·4(CH_3CN) (26). In a 100 mL Erlenmeyer flask, 0.048 g $Co(C_2H_3O_2)_2 \cdot 4H_2O$ were dissolved in 20 mL of DMF to give a purple solution. In a separate Schlenk flask inside the glove box, 0.105 g $[(CH_3CH_2)_4N][Tp^*Ti(CN)_3]$ were dissolved in 20 mL of CH_3CN. The bright orange titanium solution removed from the glovebox and placed under a nitrogen purge on the Schlenk line. The flask was opened under nitrogen gas and rapidly transferred into an Erlenmeyer flask containing $Co(C_2H_3O_2)_2 \cdot 4H_2O$. The reaction miture was mechanically shaken until the solution color was a dark greenish blue. A rubber septum was placed on the erlenmeyer and the solution was stored undisturbed for 24 hours. Yellow, air-stable crystals were harvested from the bottom of the flask and rinsed with DMF followed by CH_3CN until the washings were colorless. Yield: 0.072g ((64% based on $[(CH_3CH_2)_4N][Tp^*Ti(CN)_3]$). Elemental analysis: Calcd. for **26** ($C_{46}H_{68}B_2N_{16}O_{10}Ti_2Co$): C, 46.77; H, 5.80; N, 18.97. Found: C, 46.86; H, 5.88; N, 19.12%. IR (Nujol), ν(BH), cm^{-1}: 2520 ν(CH), cm^{-1}: 3118.

Physical Methods

Infrared (IR) spectra were measured as Nujol mulls placed between KBr plates on a Nicolet 740 FT-IR spectrometer. Elemental analyses were performed by Atlantic Microlab, Inc. Thermogravimetric analysis was performed on a Shimadzu TGA-50 Analyzer. AC and DC magnetic susceptibility and magnetization measurements were collected using a Quantum Design MPMS-XL SQUID magnetometer. DC magnetic susceptibility measurements were performed at an applied field of 1000 Oe over the temperature range 2-300 K. DC magnetization data were collected at 1.8 K under a range of DC fields from 0-7 T. AC magnetic susceptibility measurements were performed in a 3 Oe AC measuring field at operating frequencies of 1-1500 Hz. The data were corrected for diamagnetic contributions as calculated from Pascal constants.[215] Single-cystal X-ray crystallographic data were collected on Bruker APEX diffractometers equipped with CCD detectors. The data sets were recorded as ω-scans at a 0.3° step width. Integration was performed with the Bruker SAINT[216] software package and absorption corrections were empirically applied using SADABS.[170] The crystal structures were refined using the SHELX[173] suite of programs.[217] Images of the crystal structure were rendered using the crystal structure visualization software DIAMOND.[174] All of the structures were solved by direct methods. Any remaining non-hydrogen atoms were located by alternating cycles of least squares refinements and difference Fourier maps. All hydrogen atoms were placed at calculated positions. The bond lengths of disordered solvent molecules were restrained to chemically meaningful values. Anisotropic thermal parameters were added for all non-hydrogen atoms.

Computational Details

Single-point *ab initio* calculations on **19** and **21** were performed by Dr. Alessandro Soncini and Dr. Willem Van den Heuvel from the University of Melbourne using the crystallographic geometries provided in the .cif files. The electronic configuration of Ti(III) is d^1 which gives rise, in the ligand field, to five spin doublet states. These were obtained from a Complete Active Space Self Consistent Field calculation (CASSCF), followed by a second order perturbation calculation (CASPT2). CASSCF gives wavefunctions and energies for ground and excited states. CASPT2 corrects the energies for electron correlation effects. The CASSCF/CASPT2 method does not include spinorbit coupling (SOC). SOC was introduced in the next step in which the SOC Hamiltonian was diagonalized in the basis of the CASSCF wavefunctions. The spin-orbit wavefunctions were used to calculate *g*-factors and the temperature dependence of the paramagnetic susceptibility. All these computations were performed with MOLCAS 7 software.

Single-point calculations on **26** were performed by Dr. Silvia Gomez-Coca, a post-doc in the Dunbar Group at Texas A&M University, using the crystallographic geometries provided in the .cif files. The *ab initio* calculations were performed using the two-step approach implemented in the ORCA 3.0.3 program in which the spin-orbit coupling (SOC) and spin-spin coupling (SSC) relativistic effects are included a posteriori.[273] In the first step, several solutions of the non-relativistic Born-Oppenheimer Hamiltonian were calculated using a complete active space self-consistent field (CASSCF). The electronic configuration of Co(II) is d^7, so the selected active space CAS(7,5) contains 7 electrons in the 5 essentially atomic d orbitals. In a second step the effect of SOC and SSC are taken into account using the quasi-degenerate perturbation theory (QDPT). To evaluate the effects of the dynamic correlations N-Electron Valence Perturbation Theory (NEVPT2) was employed by substituting the diagonal elements of the QDPT matrix with the NEVPT2 corrected state energies. The Karlsruhe polarized triple-z basis set (TZVP),[274] and the auxiliary def2-TZV/J basis set[275] for resolution of identity (RI) approximation were employed.

Results and Discussion

Syntheses

Originally attempts at preparing the starting material Tp*$TiCl_2$(THF) was sought by reacting equimolar amounts of $(THF)_3TiCl_3$ with potassium tris(3,5-dimethyl-1-pyrazolyl)borohydride in THF at low temperatures.[238] The resulting purple solid exhibited a υ(BH) stretching mode at 2548 cm^{-1} with a shoulder at 2513 cm^{-1} and a υ(CH) stretch at 3116 cm^{-1}. The purple powder was then reacted with three equivalents of $[(CH_3CH_2)_4N]CN$ and recrystallized from THF and benzene. Two crystals were obtained by this process and characterized by single crystal X-ray methods as compounds **19** and **20**. It is interesting to note that the products did not contain coordinated cyanide and that the B-N bond has been cleaved. This is not entirely surprising considering prior evidence for such decomposition reactions.[245] In lieu of these results, addition of $[(CH_3CH_2)_4N]Cl$ to the reaction of $TiCl_3$ with KTp* was performed to selectively favor the formation of **19**. Even under these conditions, a purple filtrate is obtained. Slow evaporation of this filtrate also yields crystals of **20**. Further treatment of **20** with $[(CH_3CH_2)_4N]Cl$ affords the desired trichloro substituted derivative of **19.** Substitution of the chloride ligands with cyanide ligands was achieved after stirring a solution of **19** in the presence of a slight excess of $[(CH_3CH_2)_4N]CN$ in acetonitrile for 48 hours. Recrystallization of the orange product proved to be difficult and was highly dependent on solvent composition and concentration in addition to the product being highly air sensitive. Crystals of **21** were obtained by making a 5mM solution containing 30% by volume acetonitrile in diethyl ether. Under conditions of excess cyanide, a different polymorph was found by the layering of the acetonitrile solution with diethyl ether in a thin tube, which produced orange block crystals that had to be mechanically separated from co-crystallizing crystals of $[(CH_3CH_2)_4N]CN$. The former polymorph exhibits ν(C≡N) at 2106 cm^{-1} and 2115 cm^{-1}, whereas the latter polymorph shoes only one ν(C≡N) stretch at 2063 cm^{-1}. If only 3 equivalents or less of $[(CH_3CH_2)_4N]CN$ are used, incomplete substitution can occur as verified by elemental analysis and X-ray crystallography. Other attempted routes to **21** involved the use of trimethylsilycyanide in an effrot eliminate contaminating side products. Both $[(CH_3)_3Si]Cl$ and $[(CH_3)_3Si]CN$ are liquid and volatile rendering them easily removeable from the reaction. Reactions of **19** with $[(CH_3)_3Si]CN$ yields the orange product **21** but also an insoluble brownish tan powder which is a titanium-bridged species, **22**. While the crystal structure of this tan solid has not been achieved, compound **22** is worth mentioning as it shows for the first time, that coupling that can be obtained across the cyanide ligand with titanium(III). The overall synthetic routes are depicted in Chart 4.2.

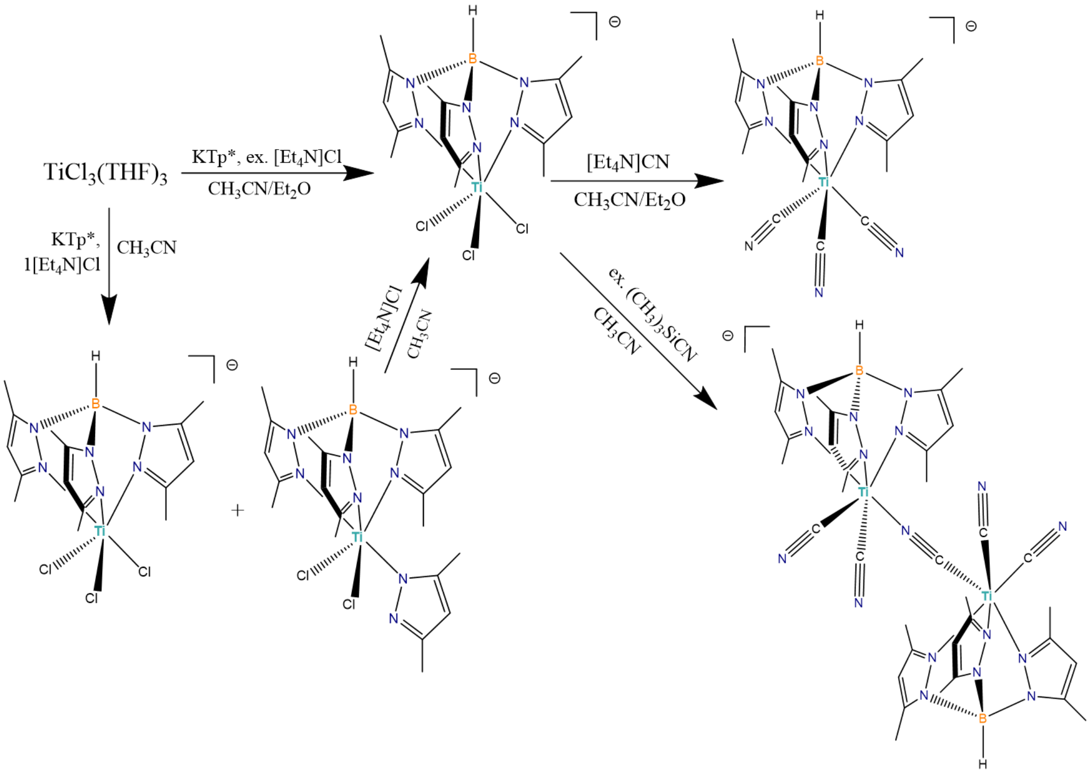

Chart 4.2 Synthetic routes of titanium starting materials.

Reactions of **21** with other divalent metal sources did not produce isolable crystals. Powders obtained from various reactions exhibit IR spectra that indicate a bridging cyanide species was being formed. In this regard, reacting **21** with $[Cr^{II}(CH_3CN)_4][BF_4]_2$, Tp*Ni($NO_3$), or Tp*Co($NO_3$) represent the best candidates for future studies. Reactions of acetonitrile solutions of Tp*Ni(NO_3) or Tp*Co(NO_3) with **21** yielded dark green reaction solutions. The products were highly soluble even after addition of crystallizing solvents, which is surprising because the expected cubic molecule would be charge neutral with formula, $[\{M^{II}Tp^*\}_4\{Tp^*Ti(CN)_3\}_4]$ (M = Co, Ni) or $[\{M(MeCN)_x\}_4\{Tp^*Ti(CN)_3\}_4]$ (M = Cr; x = 1 or 3). The solvent was slowly evaporated, and other crystallization methods were attempted but no crystals were obtained.

An interesting discrete molecule was obtained from the reaction of **21** with $CoCl_2$ in THF layered with toluene. A serendipitous reaction ensued in thin crystallizing glass tubes that had been undisturbed for a year in which compound **21** loses coordination of the Tp* ligand and scavenges three other cyanide ligands in the process of coordinating with $CoCl_2$. This is clearly not an ideal situation but it is mentioned here because it is the first example of the incorporation of the hexacyanotitanate ion into a compound (including 3-D frameworks).[276] Compound **23** is a testament to the flexibility of the cyanide ligand to allow for a tetrahedron and octahedron to form alternating corners of a cube. The infrared spectrum of the crystals shows two cyanide stretching frequencies in accord with the terminal and bridging cyanide groups.

In the presence of water, reactions of **21** with metal acetate complexes afford acetate and oxo- bridged trinuclear compounds by hydrolysis. The first example was observed in the reaction of **21** with dichromium tetraacetate which was prepared by a new literature method.[270] A small amount of moisture was apparently introduced although the reaction solution was performed in the glovebox with dry CH_3CN/DMF solvents. A layering of the two solutions in a Schlenk tube led to the formation of a green solution at the interface and the formation of crystals of $[(CH_3CH_2)_4N]\{(Tp^*Ti^{III})(\mu_2\text{-}OAc)_2(\mu_2\text{-}O)Cr^{III}(\mu_2\text{-}O)(\mu_2\text{-}OAc)_2(Ti^{III}Tp^*)\}\cdot(CH_3CN)$ over the course of 24 hours. Because of the presence of a $[(CH_3CH_2)_4N]^+$ cation, compound **23** exhibits at least one titanium center in the trivalent oxidation state, which adds to the very limited collection of small molecules containing a titanium(III). Given that this reaction was also able to cleave the dimeric dichromium tetraacetate, the direct reactions of hydrated transition metal acetates were pursued. After some optimization, the reaction proved to be robust and facile. Crystals could be obtained without stringent air-free conditions by the quick mixing in air (to prevent decomposition of **21** into TiO_2) of **21** and $MnOAC\cdot 4H_2O$ in a MeCN/DMF, to produce crystals of **24** within 24 hours. Compelled by the synthetic ease and the theory predicting the magnitude of anisotropy in mononuclear SMMs[115] (Figure 4.1) the cobalt analog was targeted as a potentially intriguing magnetic compound. Compound **26** was prepared analogously to the manganese analog. A convenient aspect of the reaction procedure is that pure starting material **21** is not needed to obtain the products. A single-pot reaction of $TiCl_3$, KTp*, $[CH_3CH_2N]CN$, and $M(C_2H_3O_2)_2\cdot 4H_2O$ ($M = Mn^{II}, Co^{II}$) will produce crystals after initial mechanical stirring and then 24 hours of crystallization in an undisturbed environment. An additional benefit is the insolubility of the products which allows them to be purified by repeated washings of CH_3CN and/or DMF. It is important that the final washing be acetonitrile, however, as the DMF is not removed easily even under vacuum which can cause problems with the magnetic susceptibility data analysis. While this chemistry was unplanned at first, we quickly shifted our focus from trying to keep the titanium center trivalent to capitalizing on the synthetic ease of the reaction to afford a platform for testing the “mononuclear” magnetic properties of the central metal ion. The oxidation of the titanium center therefore affords an “inorganic” capping ligand, $\{Tp^*Ti^{IV}\}$, which will help isolate the central metal ion from dipolar intermolecular relaxation pathways.

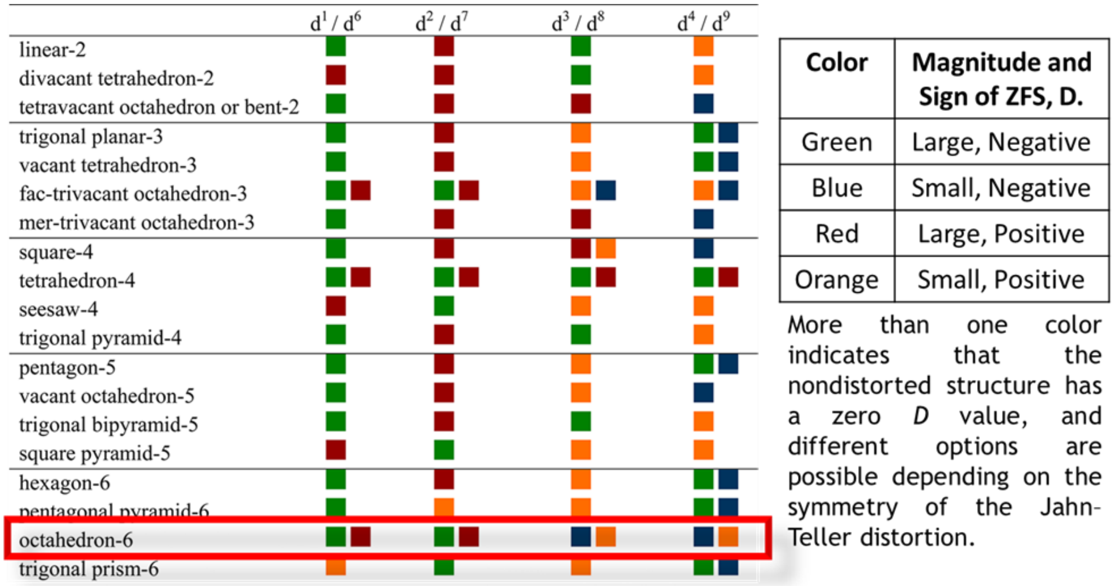

	d^1 / d^6	d^2 / d^7	d^3 / d^8	d^4 / d^9
linear-2	🟩	🟥	🟩	🟧
divacant tetrahedron-2	🟥	🟥	🟩	🟧
tetravacant octahedron or bent-2	🟩	🟥	🟥	🟦
trigonal planar-3	🟩	🟥	🟧	🟩🟦
vacant tetrahedron-3	🟩	🟥	🟧	🟩🟦
fac-trivacant octahedron-3	🟩🟥	🟩🟥	🟧🟦	🟧🟦
mer-trivacant octahedron-3	🟩	🟥	🟥	🟦
square-4	🟩	🟥	🟥🟧	🟦
tetrahedron-4	🟩🟥	🟩🟥	🟩🟥	🟩🟥
seesaw-4	🟥	🟩	🟧	🟧
trigonal pyramid-4	🟩	🟥	🟩	🟧
pentagon-5	🟩	🟥	🟧	🟩🟦
vacant octahedron-5	🟩	🟥	🟧	🟦
trigonal bipyramid-5	🟩	🟥	🟩	🟧
square pyramid-5	🟥	🟩	🟧	🟧
hexagon-6	🟩	🟥	🟧	🟩🟦
pentagonal pyramid-6	🟩	🟧	🟧	🟩🟦
octahedron-6	🟩🟥	🟩🟥	🟦🟧	🟦🟧
trigonal prism-6	🟧	🟩	🟧	🟩🟦

Color	Magnitude and Sign of ZFS, D.
Green	Large, Negative
Blue	Small, Negative
Red	Large, Positive
Orange	Small, Positive

More than one color indicates that the nondistorted structure has a zero *D* value, and different options are possible depending on the symmetry of the Jahn-Teller distortion.

Figure 4.1 Theoretical predictions of magnitude of *D* for mononuclear transition metal-based complexes. Red box represents geometry of central ion in trinuclear compounds **24**, **25**, and **26**. Figure reprinted with permission from reference,[115] copyright 2012 American Chemical Society.

Infrared Spectroscopy

The Tp* ligand exhibits two characteristic stretching frequencies in the 2500-3200 cm^{-1} window, namely the C-H stretch within the pyrazolyl rings and the B-H stretch. The latter is more useful in these studies because the C-H stretch overlaps with NUJOL oil. However, these absorptions are not very sensitive to a coordination changes of the metal center. The cyanide ligand is a superb reporter, however, with resonances typically appearing in the range of 2000-2200 cm^{-1}. The highest occupied molecular orbital on the cyanide ligand is weakly antibonding in character and is composed mainly of carbon character (68%). Therefore, coordination through the carbon end of the cyanide ligand (σ-donor) reduces the antibonding character of the ligand, making the stretching frequency occur at higher energy. On the other hand, the trend is reversed when considering *d-p* back-bonding interactions. Donation of electron density from the metal centers into the π* molecular orbital of cyanide engenders an increase in antibonding character and therefore a decrease in the CN bond strength.[277] Another factor affecting the cyanide stretching frequency is the so-called kinematic effect, in which binding a second metal center to cyanide causes a mechanical constraint on motion, which increases the energy of the absorption.[278]

Compound **21** exhibits a υ(BH) stretching frequency at 2518 cm^{-1} and a υ(CH) mode at 3120 cm^{-1}. Two cyanide stretching modes, υ(CN), are located at 2115 and 2106 cm^{-1}. The reaction of **19** with $[(CH_3)_3Si]CN$ leads to a tan powder which exhibits three cyanide stretching frequencies located at 2110, 2123, and 2137 cm^{-1}, as shown in Figure 4.2. The additional cyanide mode at 2137 cm^{-1} is believed to be from the formation of a multinuclear titanium compound which is further supported by data provided in the magnetic section.

The infrared spectra of products obtained by the reaction of **21** with $Tp^*Ni(NO_3)$, $Tp^*Co(NO_3)$, $Cr^{II}(MeCN)_4[BF_4]_2$, and $CoCl_2$ are shown in Figures 4.3 – 4.6. In all cases, a shift in the cyanide stretching mode to higher energies is observed as compared to the spectrum of **21**. Such results imply that bridging Ti^{III}-CN-M^{II} (M = Ni, Co, Cr) bonds are being formed. The target compounds in all cases are molecular cubes- analogs of previously published work with the anisotropic building block, $[Re(triphos)(CN)_3]^-$.[237] The reaction of compound **21** with $Tp^*Co(NO_3)$, resulted in a green amorphous solid exhibiting cyanide stretching frequencies at 2167 and 2136 cm^{-1}, Figure 4.3. The reaction of compound **21** with Tp*Ni(NO_3) proceeds in the same manner, resulting in a dark green solid. The IR spectrum of this reaction, Figure 4.4, shows cyanide stretching mode shifts from 2115 and 2106 cm^{-1} in compound **21** to a broad absorption at 2171 cm^{-1}. Acetonitrile υ(CN) stretching frequencies are also present in the 2250-2320 cm^{-1} window which may be a result of the formation of a multinuclear compound with open channels for solvent, such as a molecular cube. The reaction with $[Cr(CH_3CN)_4][BF_4]_2$, exhibits a shift in the cyanide stretching mode shifts from 2115 and 2106 cm^{-1} in **21** to a very broad absorption at 2148 cm^{-1}, Figure 4.5. Acetonitrile υ(CN) stretching frequencies are also present in the 2240-2300 cm^{-1} window. In this case, a molecular cube with acetonitrile molecules bound to the Cr(II) center would be a nice candidate for attachment to surfaces via ligand substitution for device applications. Compound **23** demonstrates a valid example for monitoring the shift in cyanide stretching frequencies as a bridging cyanide bond is formed, since the crystal structure has also been determined for this compound. The reaction with $CoCl_2$, shows a shift in the cyanide stretching mode shifts from 2115 and 2106 cm^{-1} in **21** to two υ(CN) stretching frequencies at 2170 and 2135 cm^{-1} consistent with bridging and terminal cyanide ligands in **23**, Figure 4.6. The disappearance of the υ(BH) stretching frequencies is also observed.

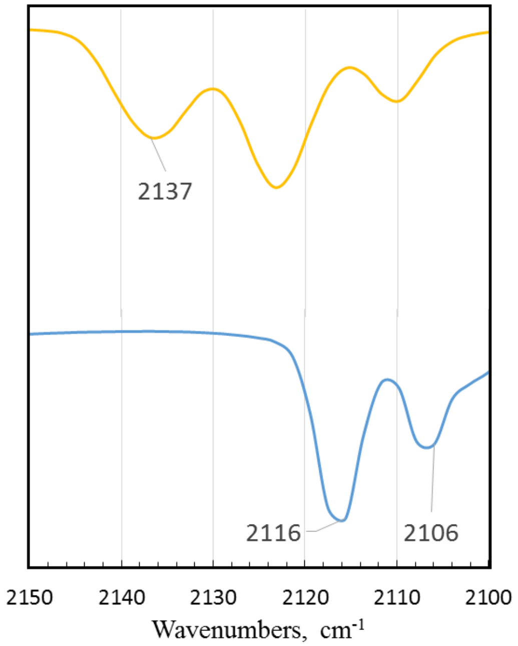

Figure 4.2 Spectral overlay of compound **21** (blue line) and **22** (yellow line) depicting the presence of a bridging cyanide stretching mode in **22** that is absent in **21**.

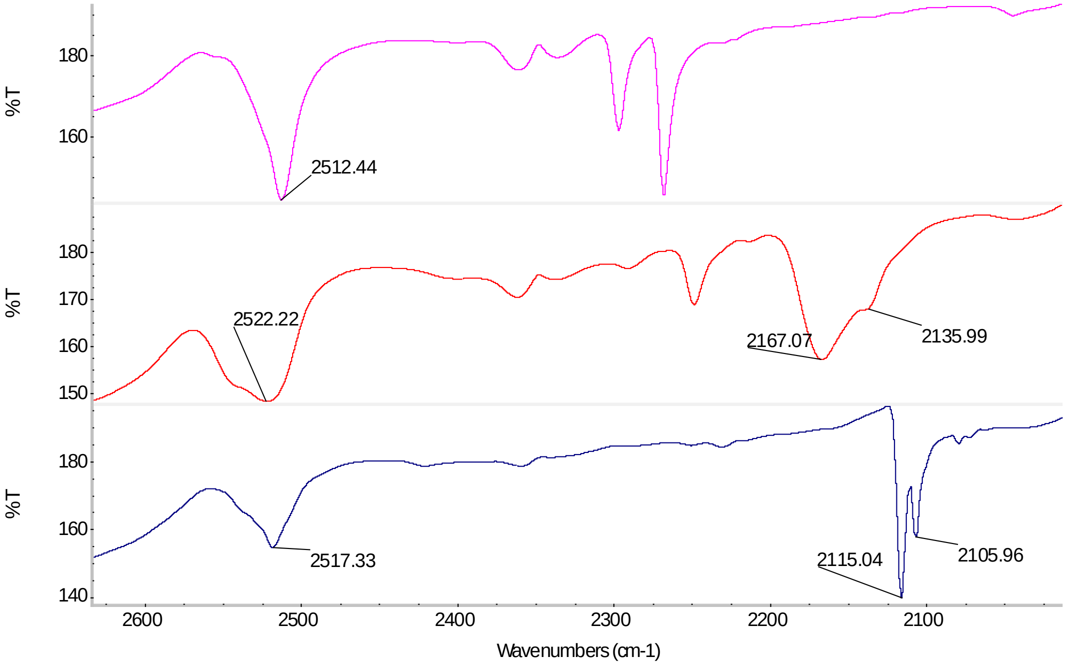

Figure 4.3 Spectral overlay of compound **21** (blue line), Tp*Co(NO_3) (pink line), and reaction product (red), which is presumably [{CoTp*}$_4${Tp*Ti(CN)$_3$}$_4$]. The red line depicts the presence of a bridging cyanide stretching mode.

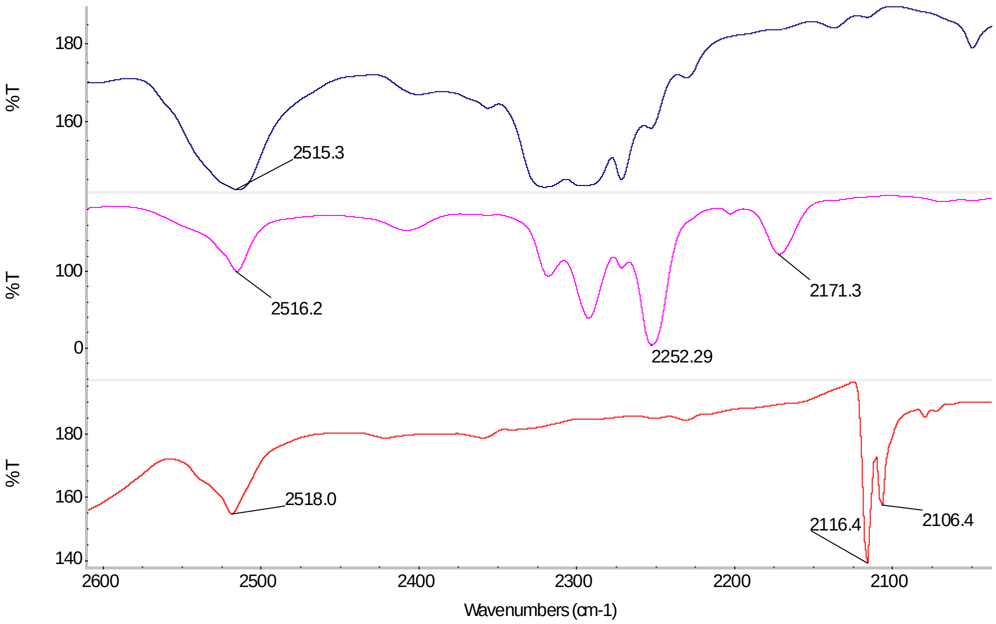

Figure 4.4 Spectral overlay of compound **21** (red line), $Tp^*Ni(NO_3)$ (blue line), and reaction product (pink), which is presumably $[\{NiTp^*\}_4\{Tp^*Ti(CN)_3\}_4]$. The red line depicts the presence of a bridging cyanide stretching mode.

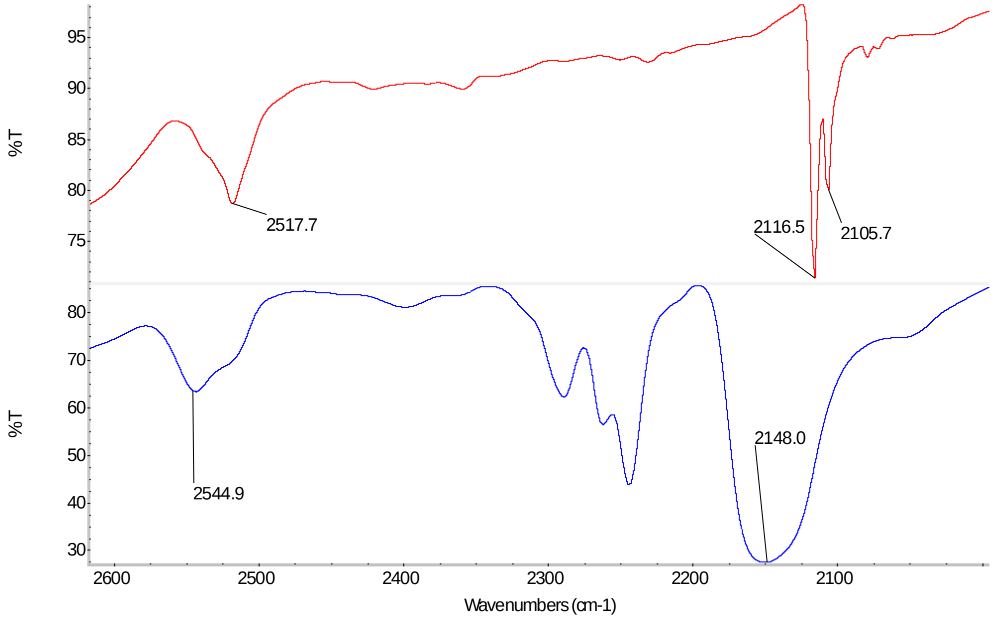

Figure 4.5 Spectral overlay of compound **21** (red line) and reaction product (red), which is presumably $[\{M(MeCN)_x\}_4\{Tp^*Ti(CN)_3\}_4]$ (M = Cr; x = 1 or 3). The blue line depicts the presence of a bridging cyanide stretching mode.

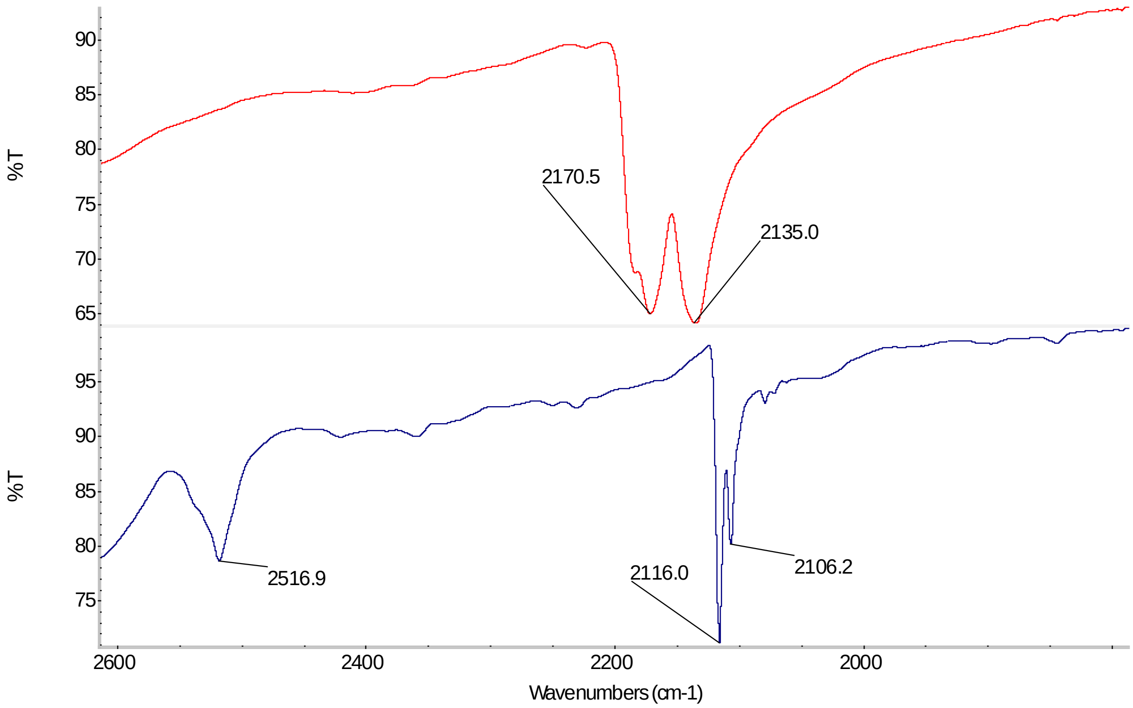

Figure 4.6 Spectral overlay of compound **21** (blue line) and **23** (red line). The red line depicts the presence of a bridging and terminal cyanide stretching modes, consistent with the crystal structure of **23**.

Crystallographic Studies

Crystallographic data for selected compounds **19-26** are listed in Table 4.1 and Table 4.2. This research used resources of the Advanced Photon Source, a U.S. Department of Energy (DOE) Office of Science User Facility operated for the DOE Office of Science by Argonne National Laboratory under Contract No. DE-AC02-06CH11357. Data for compund **24** were collected at the X-ray Operations and Research beamline 15-ID-B at the Advanced Photon Source, Argonne National Laboratory.

Table 4.1 Crystal and structural refinement data for **19-21**.

	19	**20**	**21**
Empirical formula	$C_{23}H_{42}BN_7TiCl_3$	$C_{22.5}H_{33.5}BN_9TiCl_2$	$C_{26}H_{42}BN_{10}Ti$
Formula weight	581.69	559.17	553.40
Temperature/K	110.0	110.0	110.0
Crystal system	monoclinic	monoclinic	orthorhombic
Space group	Cc	C2/c	$Pmn2_1$
a/Å	17.669(4)	20.462(4)	11.634(2)
b/Å	10.410(2)	10.763(2)	8.1814(16)
c/Å	17.024(3)	25.135(5)	15.620(3)
α/°	90	90	90
β/°	111.44(3)	97.57(3)	90
γ/°	90	90	90
Volume/Å^3	2914.6(12)	5488(2)	1486.8(5)
Z	4	8	2
ρ_{calc}g/cm^3	1.326	1.3536	1.236
F(000)	1228.0	2341.3	590.0
Radiation	MoKα (λ = 0.71073)	Mo Kα (λ = 0.71073)	MoKα (λ = 0.71073)
2Θ range for data collection/°	4.63 to 57.14	3.26 to 46.5	4.366 to 57.208
Index ranges	-23 ≤ h ≤ 23, -13 ≤ k ≤ 13, -21 ≤ l ≤ 22	-22 ≤ h ≤ 22, -11 ≤ k ≤ 11, -27 ≤ l ≤ 27	-15 ≤ h ≤ 15, -10 ≤ k ≤ 10, -20 ≤ l ≤ 21
Reflections collected	13853	19049	16509
Independent reflections	6617 [R_{int} = 0.0737, R_{sigma} = 0.1152]	3735 [R_{int} = 0.0510, R_{sigma} = 0.0411]	3736 [R_{int} = 0.0207, R_{sigma} = 0.0206]
Data/restraints/parameters	6617/8/330	3735/0/350	3736/1/270
Goodness-of-fit on F^2	1.002	1.073	1.030
Final R indexes [all data]	R_1 = 0.0924, wR_2 = 0.1710	R_1 = 0.0604, wR_2 = 0.1128	R_1 = 0.0265, wR_2 = 0.0704
Largest diff. peak/hole / e Å^{-3}	0.65/-0.87	0.61/-0.58	0.31/-0.16

$R_1 = \Sigma||F_o| - |F_c||/ \Sigma|F_o|$. $wR_2 = [\Sigma w(|F_o| - |F_c|)^2/|\Sigma w(F_o)^2]^{1/2}$. $w = 0.75/(\sigma^2(F_o)+0.00010F_o^2)$. Goodness-of-fit = $\{\sum[w(F_o^2 - F_c^2)^2]/(n-p)\}^{1/2}$, where *n* is the number of reflections and *p* is the total number of parameters refined.

Table 4.2 Crystal and structural refinement data for **23-26**.

	23	**24**	**25**	8
Empirical formula	$C_{120}H_{208}BN_{28}O_{16}Ti_4Co_4Cl_4$	$C_{54}H_{88}B_2N_{15}O_{10}Ti_2Cr$	$C_{46}H_{68}B_2N_{16}O_{10}Ti_2Mn$	$C_{46}H_{68}B_2N_{16}O_{10}Ti_2Co$
Formula weight	2868.25	1276.81	1177.52	1181.51
Temperature/K	110.15	110.0	110.0	110.0
Crystal system	tetragonal	triclinic	monoclinic	monoclinic
Space group	I-4	P-1	$P2_1/n$	$P2_1/n$
a/Å	17.4538(11)	9.8246(6)	19.325(8)	19.185(5)
b/Å	17.4538(11)	10.2973(7)	15.767(6)	15.938(4)
c/Å	24.678(2)	15.0983(10)	21.486(8)	21.901(5)
α/°	90	81.809(2)	90	90.00
β/°	90	84.915(2)	115.801(5)	115.537(3)
γ/°	90	79.644(2)	90	90.00
Volume/Å^3	7517.8(11)	1484.12(17)	5894(4)	6043(3)
Z	2	1	4	4
ρ_{calc}(g/cm^3)	1.267	1.429	1.327	1.299
Radiation	MoKα (λ = 0.71073)	synchotron (λ = 0.41328 Å)	MoKα (λ = 0.71073)	MoKα (λ = 0.71073)
2Θ range	4.668 to 48.706	5.464 to 57.932	2.37 to 50.426	2.36 to 49.18
Index ranges	$-20 \leq h \leq 20$, $-20 \leq k \leq 20$, $-28 \leq l \leq 28$	$-11 \leq h \leq 13$, $-14 \leq k \leq 14$, $-20 \leq l \leq 20$	$-23 \leq h \leq 22$, $-18 \leq k \leq 18$, $-25 \leq l \leq 25$	$-22 \leq h \leq 22$, $-18 \leq k \leq 18$, $-25 \leq l \leq 25$
Reflections collected	34706	46132	56369	53753
Independent reflections	6176 [R_{int} = 0.0255]	7450 [R_{int} = 0.0975]	10553 [R_{int} = 0.0662]	10105 [R_{int} = 0.0469]
Data/restraints/parameters	6176/80/222	7450/0/393	10553/0/722	10105/0/714
Goodness-of-fit	1.056	1.059	1.047	1.080
Final R indexes [all data]	R_1 = 0.0474, wR_2 = 0.1346	R_1 = 0.0790, wR_2 = 0.2127	R_1 = 0.0727, wR_2 = 0.1108	R_1 = 0.1174, wR_2 = 0.2993
Largest diff. peak/hole / e Å^{-3}	0.97/-0.48	1.05/-1.33	0.37/-0.38	1.91/-1.64

$R_1 = \Sigma||F_o| - |F_c||/ \Sigma|F_o|$. $wR_2 = [\Sigma w(|F_o| - |F_c|)^2/|\Sigma w(F_o)^2]^{1/2}$. $w = 0.75/(\sigma^2(F_o)+0.00010F_o^2)$. Goodness-of-fit = $\{\sum[w(F_o^2 - F_c^2)^2]/(n-p)\}^{1/2}$, where n is the number of reflections and p is the total number of parameters refined.

[(CH$_3$CH$_2$)$_4$N][Tp*TiCl$_3$] (19). The Ti(III) ion in compound **19** is in a trigonally distorted octahedral environment from the 3 nitrogen atoms of the Tp* ligand and three terminal chloride ligands, Figure 4.7. The negative charges of the Tp* and chloride ligands require a charge balancing [(CH$_3$CH$_2$)$_4$N]$^+$ cation. The molecule and cation are bisected by a glide plane in the C_C space group. The average Ti-Cl bond length is 2.389(2) Å and the average Ti-N bond length is 2.200(5) Å. The pyrazol ligands exhibit a staggered conformation with the chloride ligands as viewed along the Ti-B axis. The three trans N-Cl bond distances are 4.569(5), 4.577(5), and 4.590(5) Å. The average N-Ti-N bond angle is 84.35(2)^o and the average Cl-Ti-Cl angle is 95.08(6)^o.

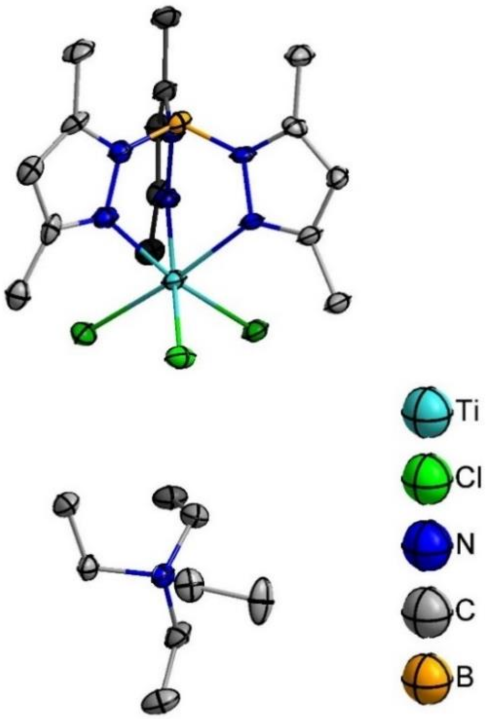

Figure 4.7 Molecular structure of [(CH$_3$CH$_2$)$_4$N][Tp*TiCl$_3$], **19**. Ellipsoids are plotted at the 50% probability level; H atoms are omitted for the sake of clarity.

{(Tp*TiCl$_2$pz)}[pz] (20). In compound **20**, the titanium center is coordinated to two chloride ligands and 4 pyrazolyl moieties, one of which has been scavenged from a sacrifical titanium species, Figure 4.8. Another pyrazole is located in the periphery to the scavenged pyrazole and the two participate in a hydrogen bonding competition. The free pyrazole molecule resides on a two-fold rotation axis in the C2/c space group modeled for disorder. Compound **20** is distored from octahedral due to the pyrazole group. The average Ti-Cl bond length is 2.3727(12) Å and the average Ti-N bond length is 2.173(3) Å. The Ti-N$_{pz}$ bond length is 2.186(3) Å. The average N-Ti-Cl total length is 4.544(3) Å, while the N-Ti-N$_{pz}$ total length is shorter at 4.345(4) Å. The Cl-Ti-Cl bond angle is 95.41 Å and the average N-Ti-N anlge is 85.71(10)^o. The average Cl-Ti-N$_{pz}$ bond anlge is 90.32(8)^o.

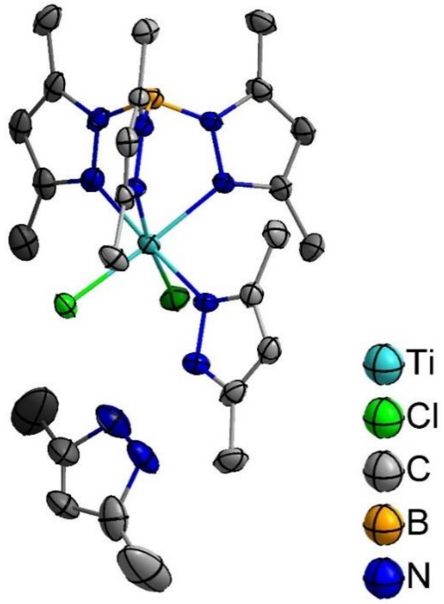

Figure 4.8 (a) Depiction of the asymmetric unit of [Tp*TiCl$_2$pz*][pz*], **20**. with thermal ellipsoids plotted at the 50% probability level; H atoms are omitted for the sake of clarity. Cooridinated and uncoordinated pyrazole ligands are depicted which are evidence of Ti(III) reactivity in cleaving the Tp* ligand.

[$(CH_3CH_2)_4N$][Tp*Ti$(CN)_3$] (21). Compound **21** crystallizes in the space group, $Pmn2_1$. The structure is shown in Figure 4.9 which is similar to the chloride analog and trigonally distorted due to the presence of the Tp* ligand. The $[(CH_3CH_2)_4N]^+$ cation and the [Tp*Ti$(CN)_3$] anion are bisected by a mirror plane. The average Ti-C bond length is 2.175(2) Å and the average Ti-N bond length is 2.154(2) Å. The N-Ti-C distances are 4.326(2) Å, 4.315(3) Å, and 4.326(2) Å which means that one axis which is slightly compressed. The average N-Ti-N bond angle is 85.82º, whereas the average C-Ti-C bond angle is 92.59º. A different crystal structure was obtained from a reaction in which an excess of $[(CH_3CH_2)_4N]CN$ was not used. In this case, the crystal structrue solved for only 90% substitution of chloride for cyanide at one of the positions, Figure 4.10.

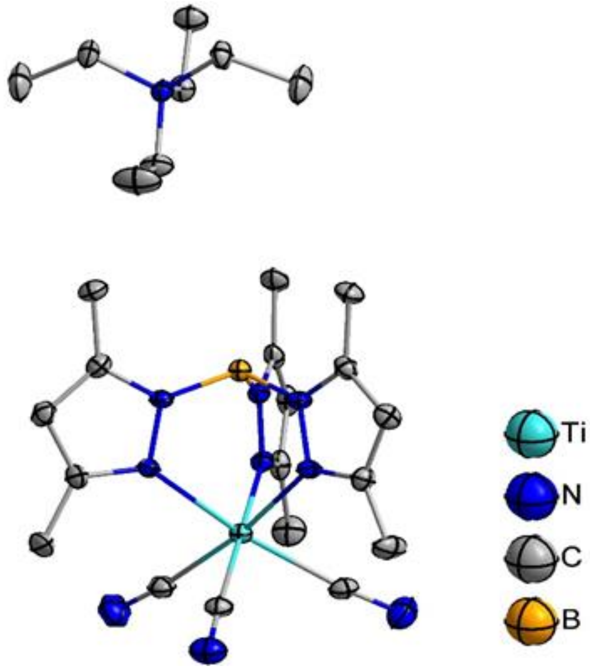

Figure 4.9 Crystal structure of a new trivalent heteroleptic titanium cyanide building block, [$(CH_3CH_2)_4N$][Tp*Ti$(CN)_3$], **21**. Thermal ellipsoids are plotted at the 50% probability level; H atoms are omitted for the sake of clarity.

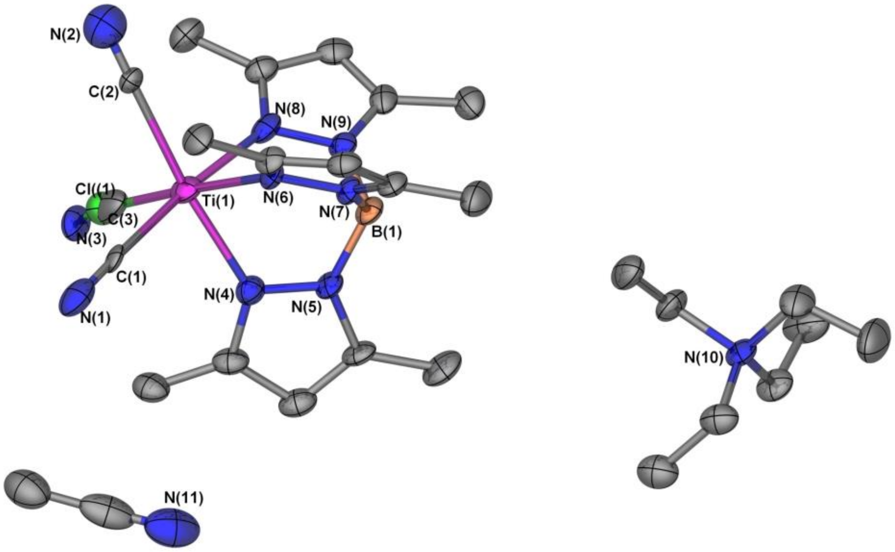

Figure 4.10 Incomplete substitution of the three chloride ligands for cyanide, with one coordination site containing 90% cyanide and 10% chloride. Thermal ellipsoids are plotted at the 50% probability level; H atoms are omitted for the sake of clarity.

$[(CH_3CH_2)_4N]_4[\{CoCl\}_4\{Ti(CN)_6\}_4]\cdot 16$ THF (23). Compound **23** crystallizes in the I-4 symmetric space group. The unit cell has eight tetra-ethylammonium cations surrounding a central $[\{CoCl\}_4\{Ti(CN)_6\}_4]$ cube. One-eighth of a $[\{CoCl\}_4\{Ti(CN)_6\}_4]$ moeity resides at the corner of the unit cell, resulting in a Z =2. Disordered THF solvent molecules were removed with the SQUEEZE program in Platon.[279] The calculated electron density and void spaces are consistent with approximately 32 THF molecules per unit cell, or 16 per $[\{CoCl\}_4\{Ti(CN)_6\}_4]$. The asymmetric unit consists of one edge of a cube. Figure 4.11 shows one fully constructed cubic molecule. The cobalt center is in a tetrahedral environment and is coordinated to one terminal chloride and three bridging cyanide ligands though the nitrogen atoms. The Co-Cl bond length is 2.212(1) Å and the average Co-N bond length is 1.955(11) Å. The titanium ion is coordinated to six cyanide ligands and has an average Ti-C bond length of 1.903(1) Å, which is shorter than what was reported for the trivalent hexacyanotitanate ion (2.20 Å), suggesting tetravalent titanium centers.[280]

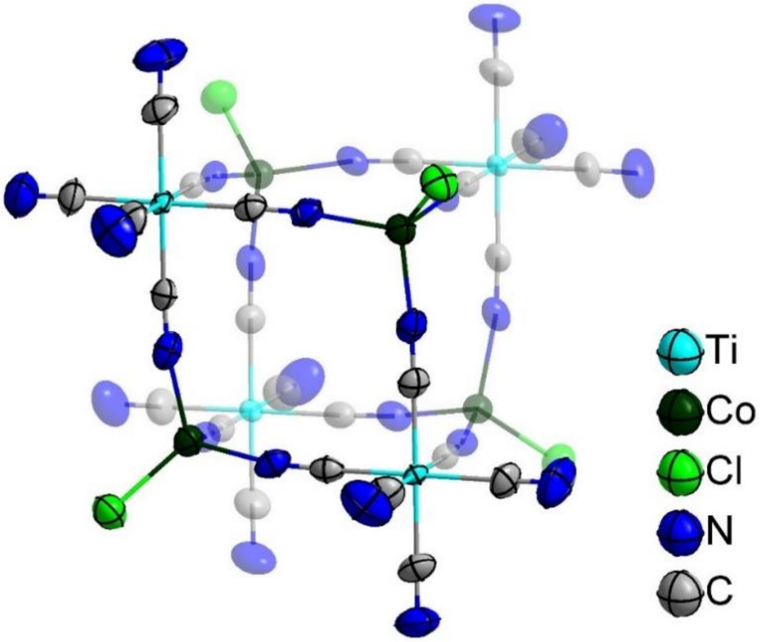

Figure 4.11 Crystal structure of compound **23**. Thermal ellipsoids are plotted at the 50% probability level; H atoms and solvent molecules are omitted for the sake of clarity.

$[(CH_3CH_2)_4N]\{(Tp^*Ti^{III})(\mu_2\text{-}OAc)_2(\mu_2\text{-}O)Cr^{III}(\mu_2\text{-}O)(\mu_2\text{-}OAc)_2(Ti^{III}Tp^*)\}\cdot(CH_3CN)$ (24). The trinuclear compound containing titanium and chromium, Figure 4.12, crystallizes in a low symmetry triclinic unit cell in the P-1 space group. The small needle-like crystals were measured using synchotron radiation at the Argonne National Laboratories Advanced Photon Source. The $[(CH_3CH_2)_4N]^+$ cation and the trinuclear compound both reside on an inversion center. As evidenced by the presence of the

$[(CH_3CH_2)_4N]^+$ cation, one of the Ti(III) centers is not oxidzed. The cyanide ligands from the titanium starting material have been lost presumeably as HCN gas from hydrolysis leaving behind an oxide bridging ligand to both the titanium and chromium centers. The central Cr(III) ion is coordinated to two *trans* oxide ligands and four *trans* acetate ligands, which places it in a slightly compressed octahedral geometry. The Cr-O bond length is 1.9146(1) Å and the Cr-$O_{acetate}$ bond lengths average to 2.1155(1) Å. The Ti-O bond length is 1.7842(1) Å and the average Ti-$O_{acetate}$ bond length is 2.0833(1) Å.

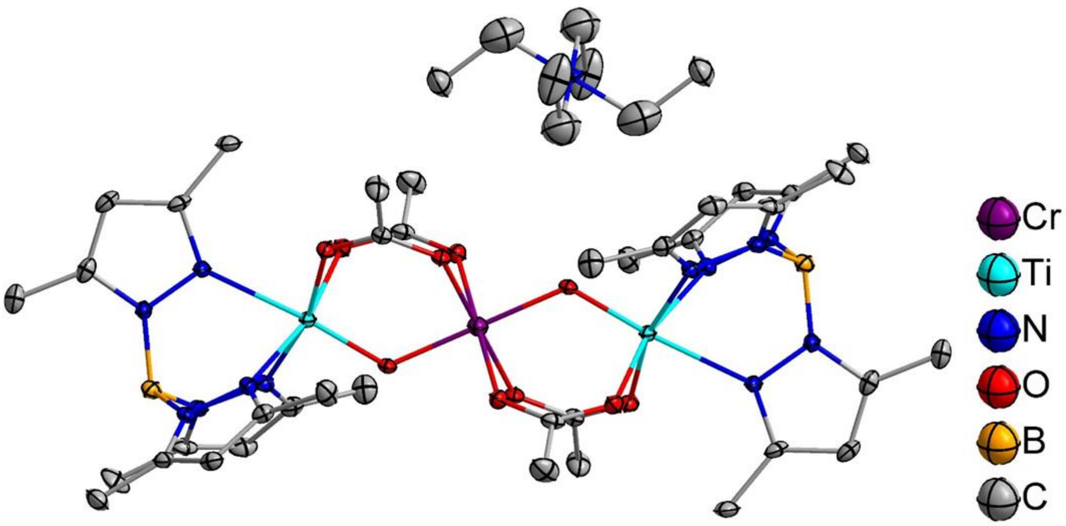

Figure 4.12 Crystal structure of compound **24**. Thermal ellipsoids are plotted at the 50% probability level; H atoms and solvent molecules are omitted for the sake of clarity.

$\{(Tp^*Ti^{IV})(\mu_2\text{-}OAc)_2(\mu_2\text{-}O)Mn^{II}(\mu_2\text{-}O)(\mu_2\text{-}OAc)_2(Ti^{IV}Tp^*)\}\cdot 4(CH_3CN)$ (25). The manganese trinuclear compound, Figure 4.13, crystallizes in the monoclinic crystal system in the $P2_1/n$ space group. The asymmetric unit consists of an entire molecule as well as four acetonitrile solvent moelcules. The molecule is isostructural to **24** except that **25** is charge neutral and does not require an additional $[(CH_3CH_2)_4N]^+$ cation, as both titanium centers are in the tetravalent state. The average Ti-O bond distance is 1.672(2) Å. The average Ti-$O_{acetate}$ bond distance is 1.988(2) Å. The shorter titanium-oxo bond distancs in **25** as compared to **24** is consistent with the oxidation state of titanium changing from trivalent to tetravalent. The Mn-O average bond distance is 2.127(2) Å and the average Mn-$O_{acetate}$ bond distance is 2.177(2).

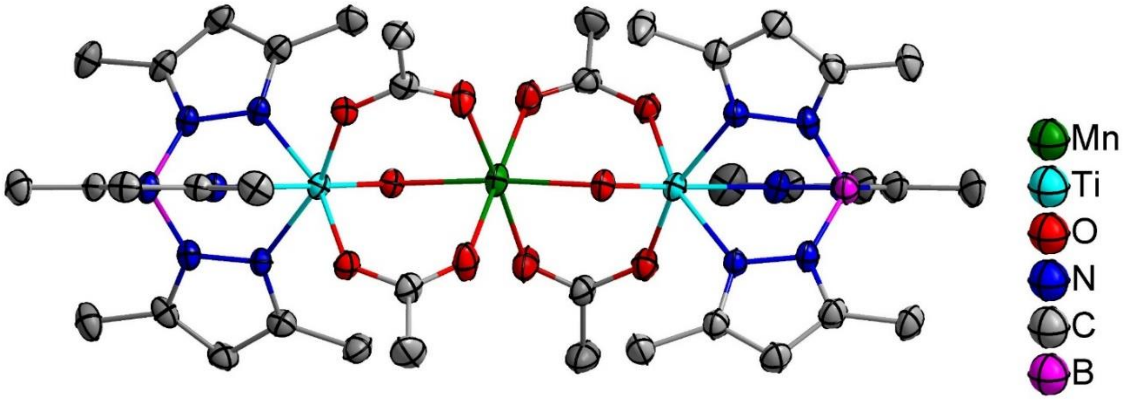

Figure 4.13 Crystal structure of compound **25**. Thermal ellipsoids are plotted at the 50% probability level; H atoms and solvent molecules are omitted for the sake of clarity.

{(Tp*Ti^{IV})(μ_2-OAc)$_2$(μ_2-O)Co^{II}(μ_2-O)(μ_2-OAc)$_2$(Ti^{IV}Tp*)}·4(CH$_3$CN) (26). The cobalt analog is isostructural with compound **25** including the number of solvent molecules in the crystal lattice. Compound **26**, depicted in Figure 4.14, crystallizes in the monoclinic $P2_1/n$ space group. A two-fold screw axis bisects the Tp* ligands. The average Ti-O bond distance is 1.665(3) Å, which is indicative of Ti(IV) oxidation states. The average Ti-

$O_{acetate}$ bond distance is 1.9843(4) Å. The average Co-O bond length is 2.0452(5) Å and the average Co-$O_{acetate}$ bond distance is 2.0979(4) Å.

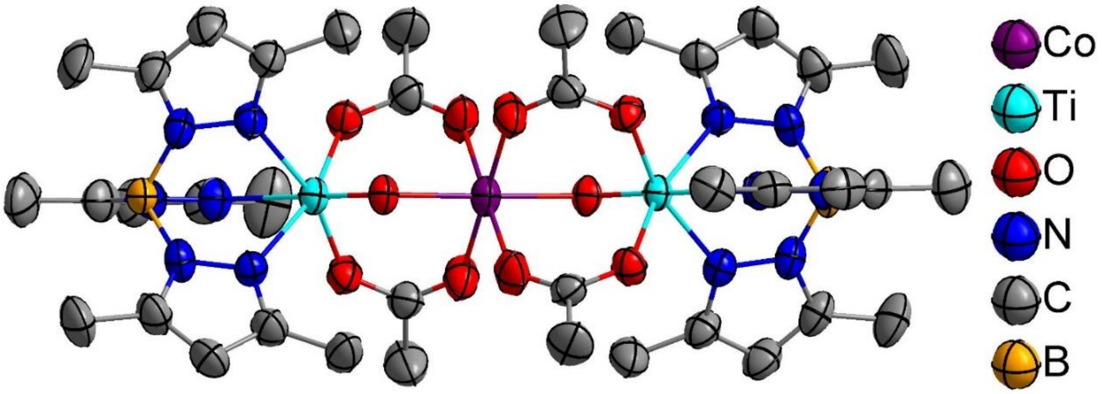

Figure 4.14 Crystal structure of compound **26**. Thermal ellipsoids are plotted at the 50% probability level; H atoms and solvent molecules are omitted for the sake of clarity.

Magnetic Properties

For general sources describing the equations cited in this section, the reader is directed to the references cited herein.[13,281-284]

$[(CH_3CH_2)_4N][Tp^*TiCl_3]$ (19). The temperature dependence of the magnetic susceptibility is given by the Curie law, equation 4.1:

$$\chi_M = \frac{N_A g^2 \mu_B^2}{3k_B T} S(S+1) \qquad \textbf{Equation 4.1}$$

where χ_M is the molar susceptibility, N_A is Avogardo's constant, g is the Lande g-factor, μ_B is the Bohr magneton, k_B is the Boltzmann constant, T is temperature, and S is the spin quantum number. Therefore, the expected χT value for a S = ½ Curie paramagnet would be a horizontal line with a y-intercept at 0.375 emu·Kmol^{-1}. Compound **19** deviates from ideal Curie behavior because of a Van Vleck temperature independent paramagnetism contribution, or TIP, which is a mixing of the ground and excited states through a Zeeman perturbation. Compound **19** exhibits an experimental TIP of $3.0\cdot10^{-4}$ cm^{3}mol^{-1}. Because of this effect, the χT product gradually decreases as temperature is lowered, Figure 4.15. At high temperatures and low magnetic fields, the magnetization has a linear relationship with the magnetic field, $M = \chi H$. As the field becomes substantial, the magnetization becomes saturated according the the relationship: $M = \mu_B N_A S g$. With a free electron g-value of 2.0023, rearranging gives the following equation 4.2:

$$\frac{M}{N_A} \approx 2S\mu_B \qquad \textbf{Equation 4.2}$$

From equation 4.2, it is deduced that the high field saturation value should approach the number of unpaired spins in the molecule in units of μ_B. Compound **19** shows near saturation of 0.85 μ_B at 7 tesla, Figure 4.16. The saturation value for a perfect Curie paramagnet with S = ½ would be 1 μ_B. The reason for the lower value is that the g-value of the titanium ion in this trigonally distorted environment at low temperature is less than 2.0. The magnetization from 0-7 T was fit with to the Brillouin function in equations 4.3-4.5. The best fit occurs when g = 1.77.

$$M = \mu_B N_A S g B \qquad \textbf{Equation 4.3}$$

$$\text{where } B = \frac{2S+1}{2S}\coth\left(\frac{2S+1}{2S}x\right) - \frac{1}{2S}\coth\left(\frac{x}{2S}\right), \qquad \textbf{Equation 4.4}$$

$$\text{and } x = \frac{\mu_B S g}{k_B T} \qquad \textbf{Equation 4.5}$$

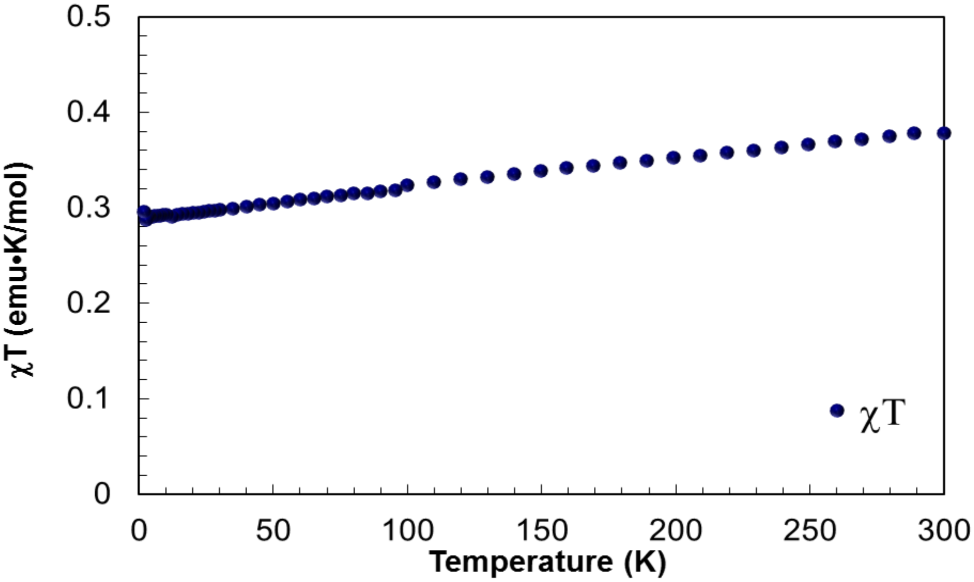

Figure 4.15 Temperature dependence of χT for **19**. The steady decrease in the χT product is due to van Vleck temperature independent paramagnetism (TIP).

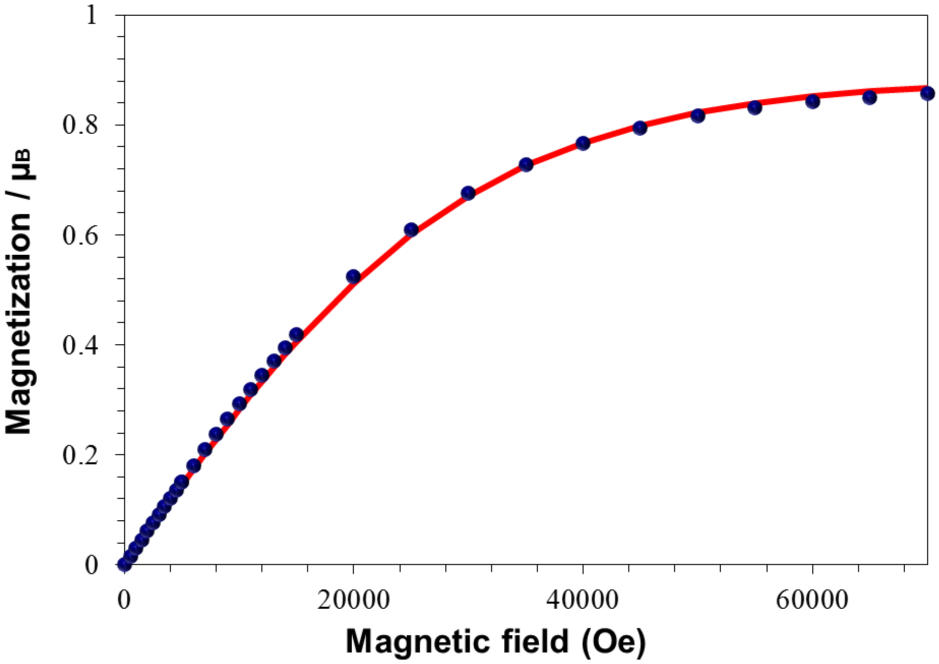

Figure 4.16 Best fit of the magnetization (blue data points) data for **19** to the Brillouin function (red line) at 1.8 K. The best fit suggests leads to a g value of ~ 1.77 at this temperature.

[$(CH_3CH_2)_4N$][$Tp^*Ti(CN)_3$] (21). The χT versus T plot and magnetization plots for **21** are shown in Figure 4.17 and Figure 4.18, respectively. The magnetic properties are quite similar to those of compound **19**. The value of χT at 300 K is 0.38 emu·mol^{-1} K which is close to the expected value (χT = 0.375 emu·mol^{-1} K) for an isotropic Ti(III) ion (S = ½, g = 2.0). The decrease of χT upon cooling is due to TIP with a value of $2.9 \cdot 10^{-4}$ cm^{3}mol^{-1}. The magnetization plot at 1.8 K saturates at a value of 0.83 μ_B, which as already mentioned is due to the g value being less than 2.0 at this temperature. The best fit to the Brillouin function gives g = 1.80.

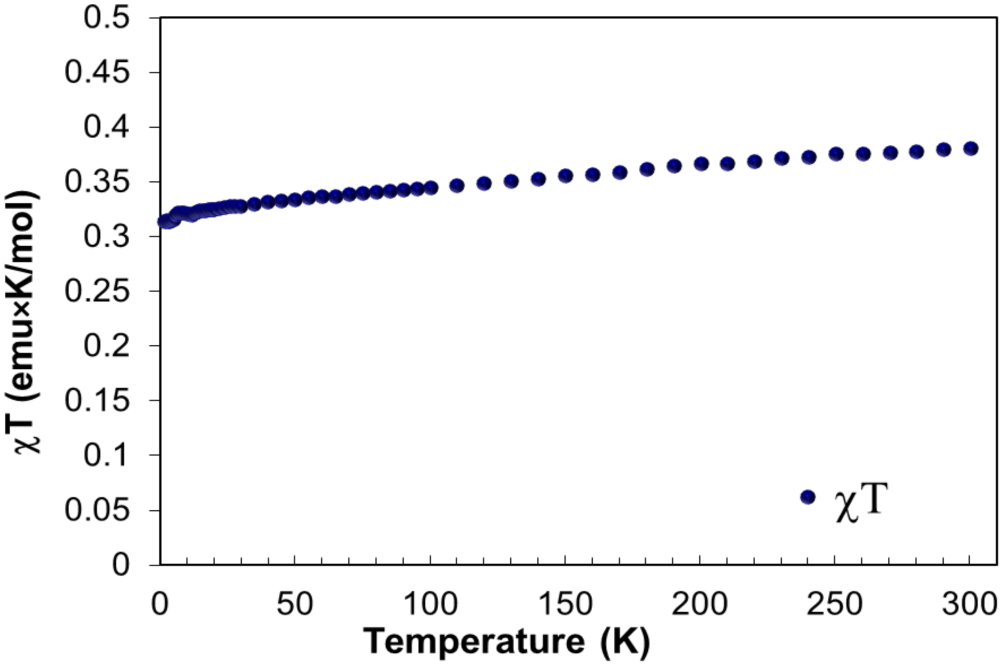

Figure 4.17 Temperature dependence of χT for **21**. The steady decrease in the χT product is due to van Vleck temperature independent paramagnetism (TIP).

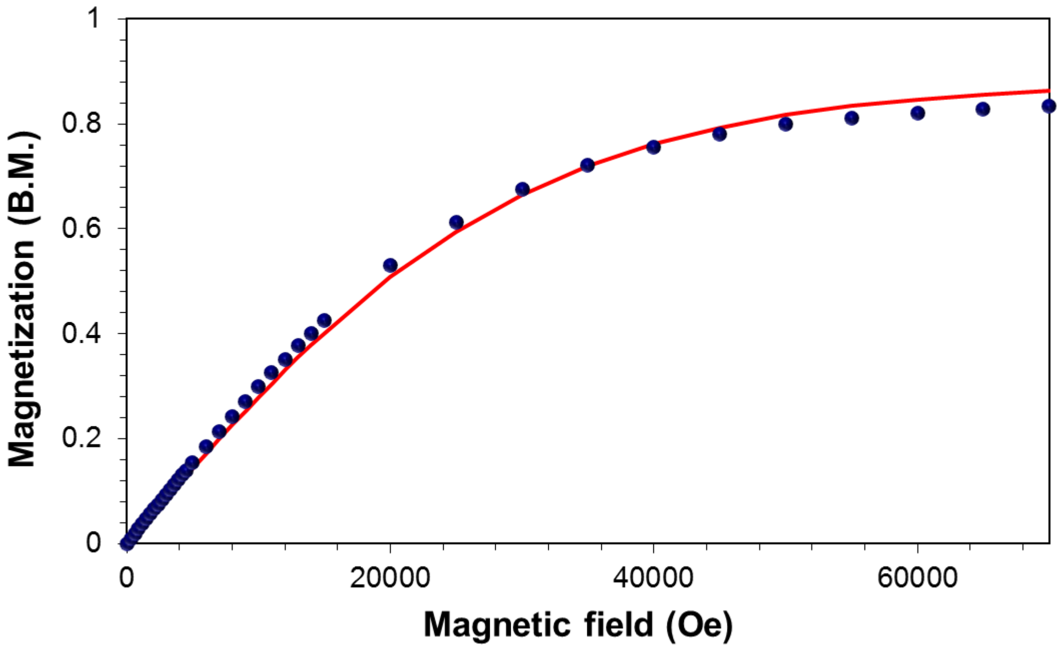

Figure 4.18 Magnetization vs magnetic field plot for **21**. The red line represents the best fit to the Brillouin function.

[$(CH_3CH_2)_4N$]{($Tp^*Ti(CN)_2$)$_2$(μ-CN)} (22). The IR spectroscopic data for compound **22** suggests that the product is a homonuclear cyanide bridged species. The magnetic data in Figure 4.19 strongly support this conclusion. The room temperature χT value of 0.73 emu·K·mo1^{-1} is close to the sum of two S = ½ paramagnets (0.735 emu·K·mo1^{-1}). As the temperature is lowered, χT decreases precipitously and is consistent with antiferromagnetic superexchange interactions through the cyanide bridge. The χT value at low temperatures is not going to zero, which signifies either spin canting or weak intermolecular interactions. To ascertain the strength of the coupling, the susceptibility data were fit with the Hsisenberg-Dirac-Van Vleck effective exchange Hamiltonian, equation 4.6, using the PHI magnetic fitting program.[285] The best fit parameters led to the values J = -71 cm^{-1} and g = 1.98 revealing strong coupling of the titanium ions across the cyanide bridge which in accord with the expected excellent overlap of earlier transition metal ions with the π^* orbitals of cyanide.

$$\hat{\mathrm{H}}_{EX} = -2\sum_{i<1}^{i,j\in N} J_{ij}\,\overrightarrow{\hat{S}_i}\cdot\overrightarrow{\hat{S}_j} + \mu_B g\hat{S}H \qquad \textbf{Equation 4.6}$$

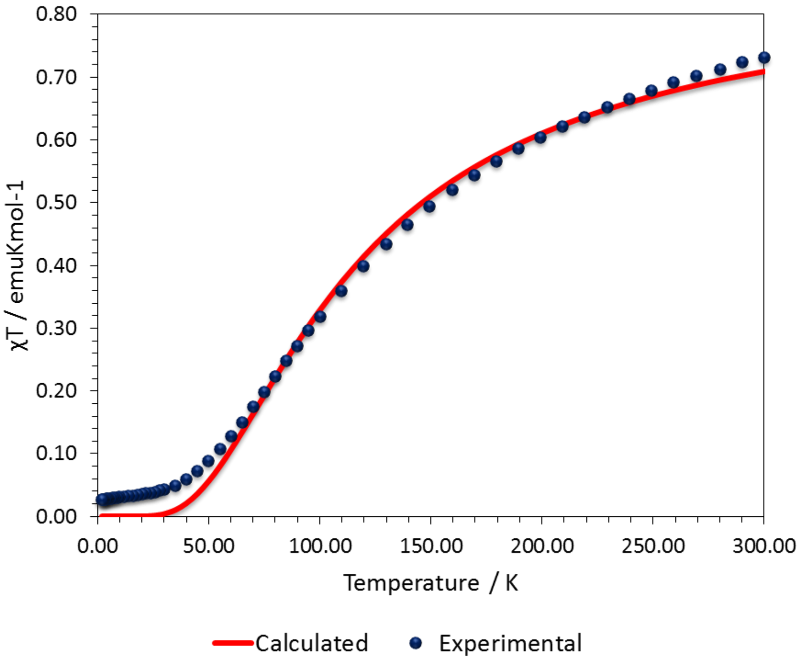

Figure 4.19 Temperature dependence of χT and 1/χ for **22**. The solid lines correspond to the best fit using the PHI magnetic program[38] according the the Hamiltonian in equation 4.6.

$[(CH_3CH_2)_4N]_4[\{CoCl\}_4\{Ti(CN)_6\}_4]\cdot 16THF$ (23). The χT vs T plot for compound **23** is depicted in Figure 4.20. The molecular weight was calculated in accordance with the number of THF solvent molecules in the crystal structure. The magnetic data were obtained on crushed crystals of the same sample that was used to collect the X-ray crystallographic data. The room temperature value of 7.6 emu·K·mo1^{-1} is reasonable for the sum of four S = 3/2 cobalt ions with the expected value of χT for four uncoupled isotropic S = 3/2, g = 2.0 centers, namely 7.5 emu·mol^{-1} K. The rapid decrease in χT at low temperatures is due to depopulation of zero-field split states and/or antiferromagnetic intermolecular interactions.

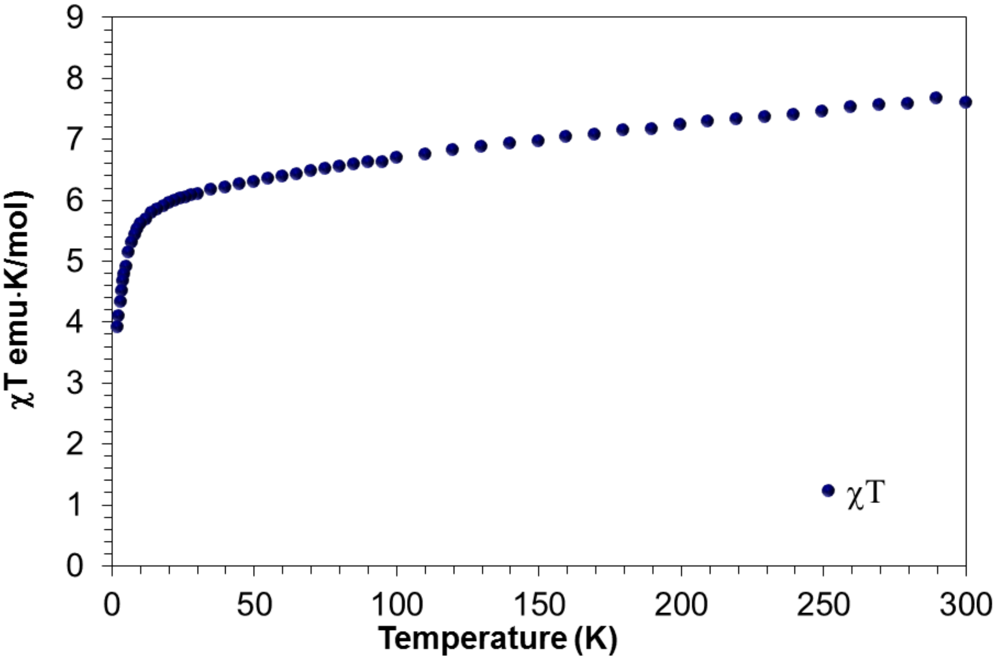

Figure 4.20 Temperature dependence of χT for **23**.

[(CH$_3$CH$_2$)$_4$N]{(Tp*Ti^{III})(μ_2-OAc)$_2$(μ_2-O)Cr^{III}(μ_2-O)(μ_2-OAc)$_2$(Ti^{III}Tp*)}·(CH$_3$CN) (24). The magnetic data for the highly air-sensitive compound **24** were collected on crushed crystals. The χT versus T plot in Figure 4.21 reveals a large linear decrease in χT as temperature is lowered which is indicative of substantial TIP contributions from the titanium centers in conjunction with antiferromagnetic interactions between the Cr(III) center and the Ti(III) centers. Two Ti(III), S = ½ centers coupled with the S = 3/2 center on Cr(III) should result in a ground state of S = ½ (Curie law χT = 0.375 emu·mol^{-1}) at low temperatures. The χT value at 1.8 K is much lower than the expected value at 0.13 emu·mol^{-1} which is attributed to intermolecular dipolar interactions.

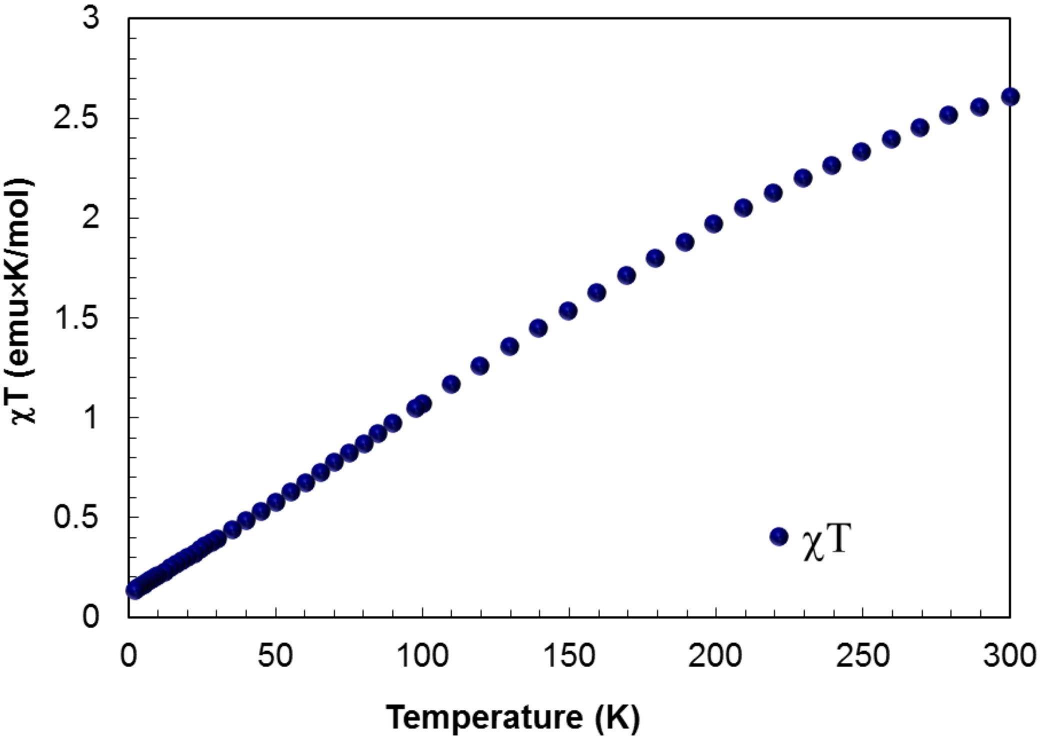

Figure 4.21 Temperature dependence of χT for **24**.

{(Tp*Ti^{IV})(μ$_2$-OAc)$_2$(μ$_2$-O)Mn^{II}(μ$_2$-O)(μ$_2$-OAc)$_2$(Ti^{IV}Tp*)}·4(CH$_3$CN) (25). The χT versus T plot for **25** is shown in Figure 4.22. The value of χT at 300 K is 4.37 emu·mol^{-1} K which equates to the expected Curie value (χT = 0.4375 emu·mol^{-1} K) for a single Mn(II) center with S= 5/2 and g = 2. Upon lowering the temperature the χT value remains constant which is indicative of a simple Curie paramagnt which is typical of high spin Mn(II) ions in an octahedral ligand field. The magnetization plot, Figure 4.23, saturates at the expect value of 5 μ_B. This result which was serendiptious at first led us to realize that this structure is an excellent scaffold for exploring mononuclear SMM properties of the cental metal ion. Given that it has been predicted that a d^7 mononuclear compound in a distorted octahedral environment can give rise to a large D values,[115] the Co(II) analogue was targeted.

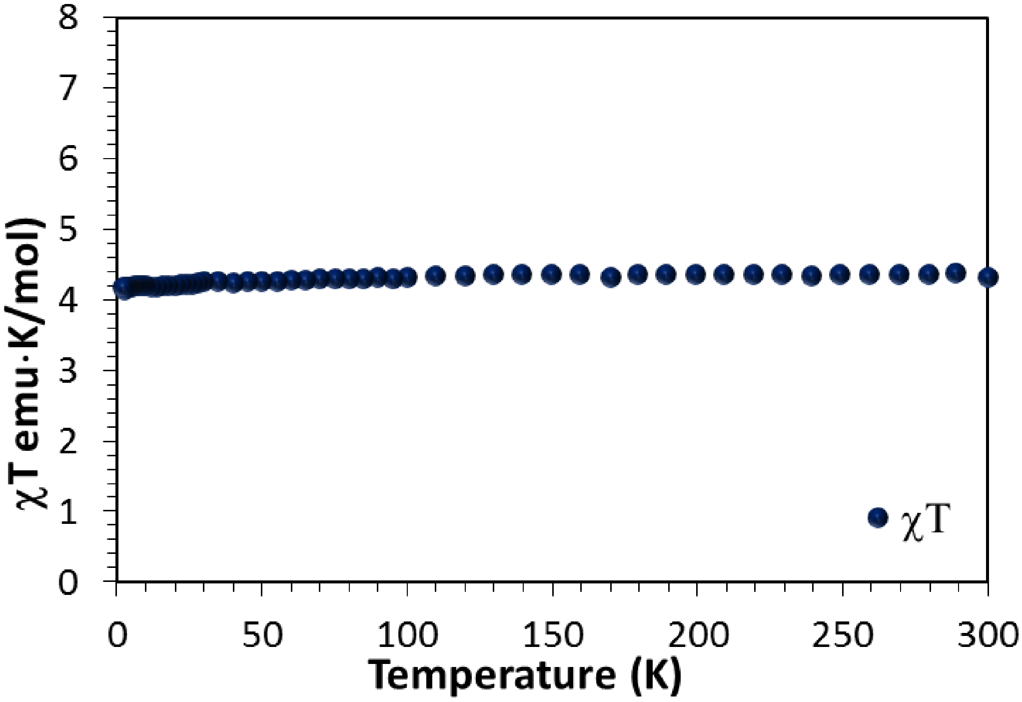

Figure 4.22 Temperature dependence of χT for **25**.

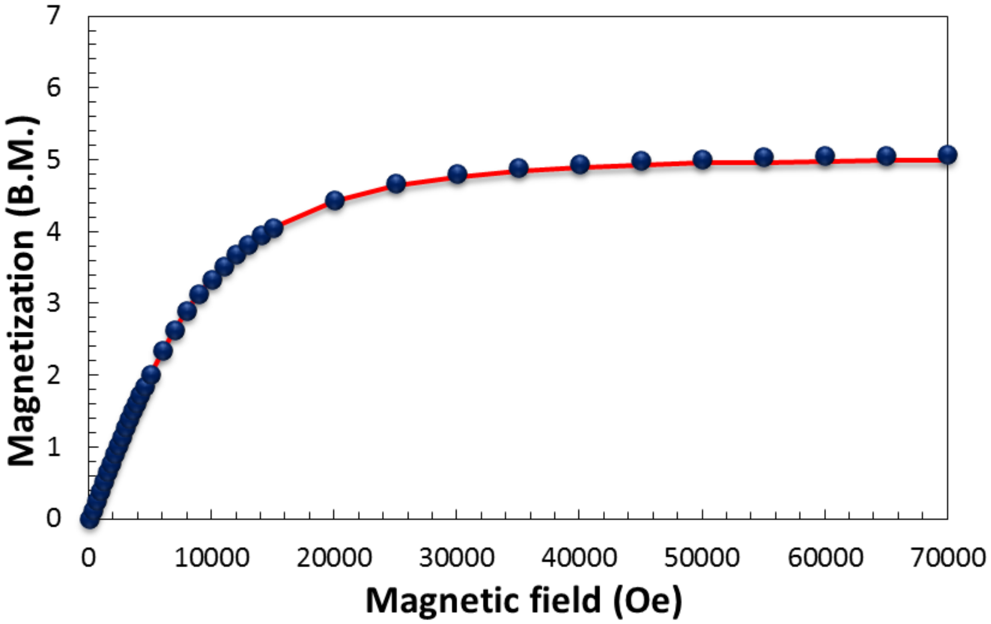

Figure 4.23 Magnetization vs magnetic field plot for **25**. The red line represents the best fit to the Brillouin function.

{(Tp*Ti^{IV})(μ$_2$-OAc)$_2$(μ$_2$-O)Co^{II}(μ$_2$-O)(μ$_2$-OAc)$_2$(Ti^{IV}Tp*)}·4(CH$_3$CN) (26). The expected χT for an S = 3/2, g = 2 Curie paramagnet is 1.875 emu·mol^{-1} K. The χT vs T plot for compound **26** provided in Figure 4.24 shows a room temperature χT value of 3.15 emu·mol^{-1} K which is indicative of a very large zero-field splitting parameter. The decrease in χT as the temperature is lowered is consistent with depopulation of ZFS states and an orbital contribution attributed to spin-orbit coupling, which mixes the near degenerate orbitals of the ground state. The entire temperature range was fit using the PHI magnetic fitting software with the following Hamiltonian,[285] equation 4.7:

$$\hat{\mathrm{H}} = \sum_{i=1}^{N}\sum_{j=1}^{2S_i}\lambda_{j_i}\left(\sigma_i\overrightarrow{\hat{L}_j}\cdot\overrightarrow{\hat{S}_i}\right)^{j} + \sum_{i=1}^{N}\sum_{k=2,4,6}\sum_{q=-k}^{k}B_{k_i}^{q}\theta_k\hat{O}_{k_i}^{q}$$

Equation 4.7

$$+\ \mu_B\sum_{i=1}^{N}\sum_{\alpha\in x,y,z}\left(\sigma_i\hat{L}_{i\alpha} + g_{i\alpha}\hat{S}_{i\alpha}\right)B_\alpha$$

where the first, second, and third terms account for the spin-orbit interaction, crystal field in Steven's operator formalism, and Zeeman contributions, respectively. Assuming a weak-field octahedral cobalt term (S = 3/2, L= 1) which is the Figure 4.24 green line fit, the best fitting scenarios suggest the magnitude of |D| is on the order of approximately 300 cm^{-1} with a g value of 2.1 and E = -3.1 cm^{-1}. This value represents a record for any cobalt containg molecule. If the orbital component is removed, and the data are fit according to a S = 3/2 system, the magnitude of |D| is reduced to 100 cm^{-1} with E = -1.1 and g = 2.6. Such values would be more reasonable but the fitting of static magntic susceptibility is not as accurate as one can see from the red line in Figure 4.24. In either scenario, the zero-field splitting parameter in compound **26** is very large. Supporting evidence for the large anisotropy is that the magnetization up to 7 tesla at 1.8 K does not saturate, Figure 4.25. The value of 2.21 β is much lower than the expected value of 3 β. Remnant magnetization measurements were performed which show a non-superposition of the isofield lines which is another indication of large magnetic anisotropy, Figure 4.26. Further analysis of the sign and magnitude of the zero-field splitting parameter is presented in the calculation section. Because of these promising static measurements, the dynamic AC susceptibility measurements were also pursued.

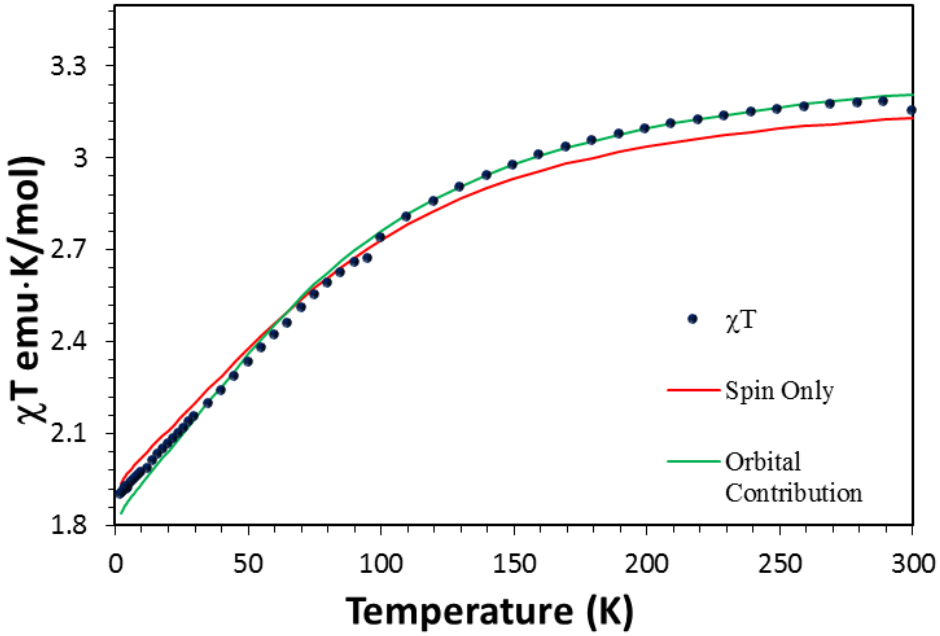

Figure 4.24 The DC susceptibility χT vs T plot for **26** fit with equation 4.7, assuming both (green line) spin-orbit (S = 3/2, L = 1) or (red line) spin-only contributions.

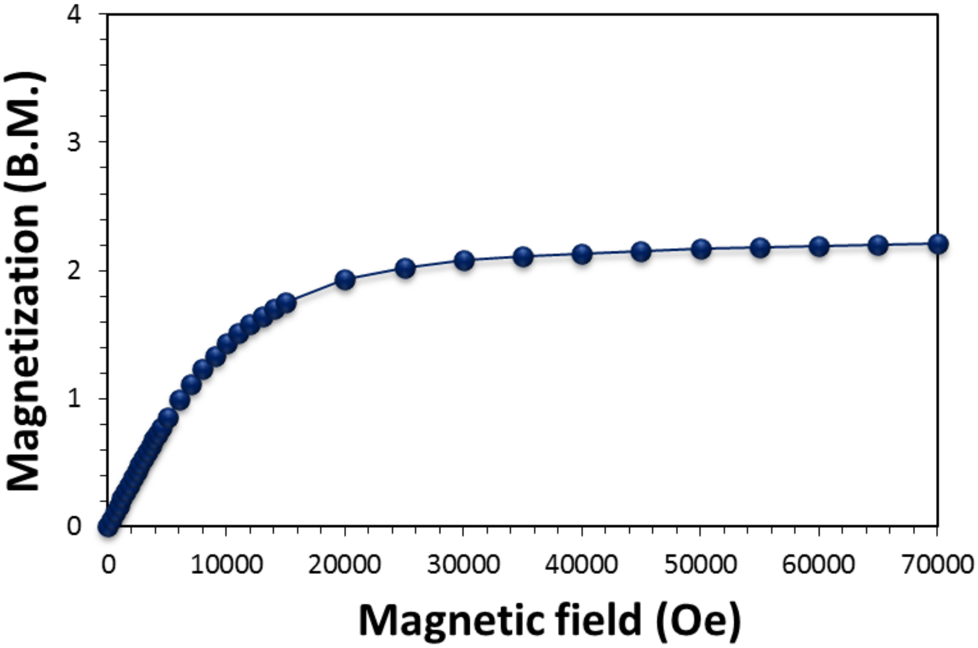

Figure 4.25 Magnetization vs magnetic field plot for **26**.

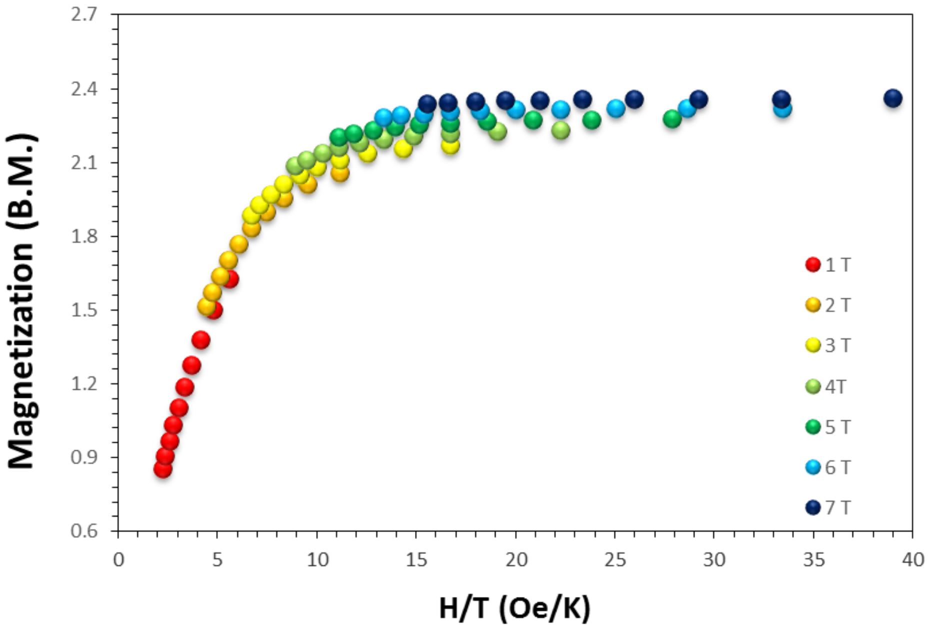

Figure 4.26 Remnant magnetization plot for **26**. Data were collected over the temperature range of 1.8-4.7 K.

An AC susceptibility measurement leads to a time-dependent magnetic response in the sample due to the application of a small oscillating applied field, typically 3-5 Oe at certain frequencies (1-1500 Hz) . Due to the presence of a barrier to spin reversal in SMMs, there is a frequency at which the thermal energy is no longer sufficient for the molecule to continue to track the oscillating field. This situation causes a phase shift, φ, which gives rise to in-phase (χ’) and out-of-phase (χ") components to the magnetic susceptibility, equations 4.8 and 4.9:

$$\chi' = \chi \cos\varphi \qquad \textbf{Equation 4.8}$$

$$\chi'' = \chi \sin\varphi \qquad \textbf{Equation 4.9}$$

The temperature at which the relaxation time of the molecule is equal to the timescale of the measurement is known as the blocking temperature, T_B, above which the molecule behaves as a simple paramagnet and below which the molecule behaves as a SMM. The collection of blocking temperatures can be analyzed by the Arrhenius equation to elucidate the effective barrier height. The inverse of the frequency at which the molecule is thermally blocked is the relaxation time at that particular temperature. Because the relaxation times are temperature dependent, a common definition of a blocking temperature is needed to compare SMMs. In this regard, the temperature at which the molecules take 100 s to relax is becoming a useful standard.

Compound **26** shows interesting temperature dependence of the AC magnetic susceptibility under 5 K in an applied DC field of 2000 Oe, Figure 4.27. The 1500 and 781 Hz lines for **26** exhibit two relaxation processes. The 1500 Hz line is well resolved with a peak at ~ 4.5 K and another at ~ 2.5 K. Because of the difficulty in selecting maxima of the out-of-phase suceptibility signal, Figure 4.27b, we collected AC susceptibility data as a function of frequency, Figure 4.28. For this experiment, 12 temperatures between 2.1 and 5.7 K were chosen. Each isotherm exhibits a frequency dependence to the maxima in the χ'' vs T plot up to 4.2 K and the beginning of a maxima up the highest temperature selected (4.2 - 5.7 K). The inverse of the frequencies coorseponding to the maxima in the temperature range 2.1 – 4.2 K were selected as the relaxation times of compound **26**.

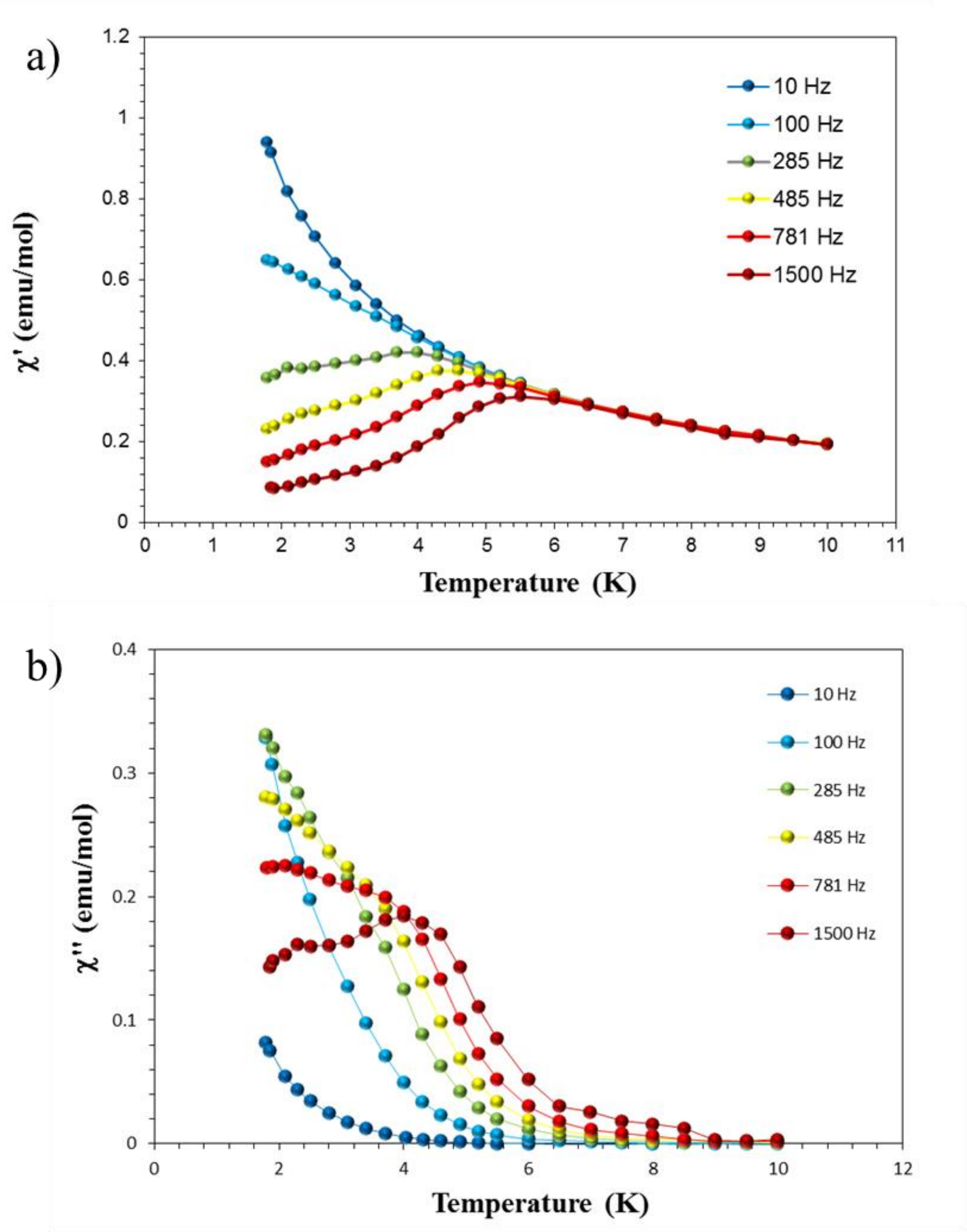

Figure 4.27 (a) The χ' vs T and (b) χ'' vs T plots in a 2000 Oe DC field for compound **26**.

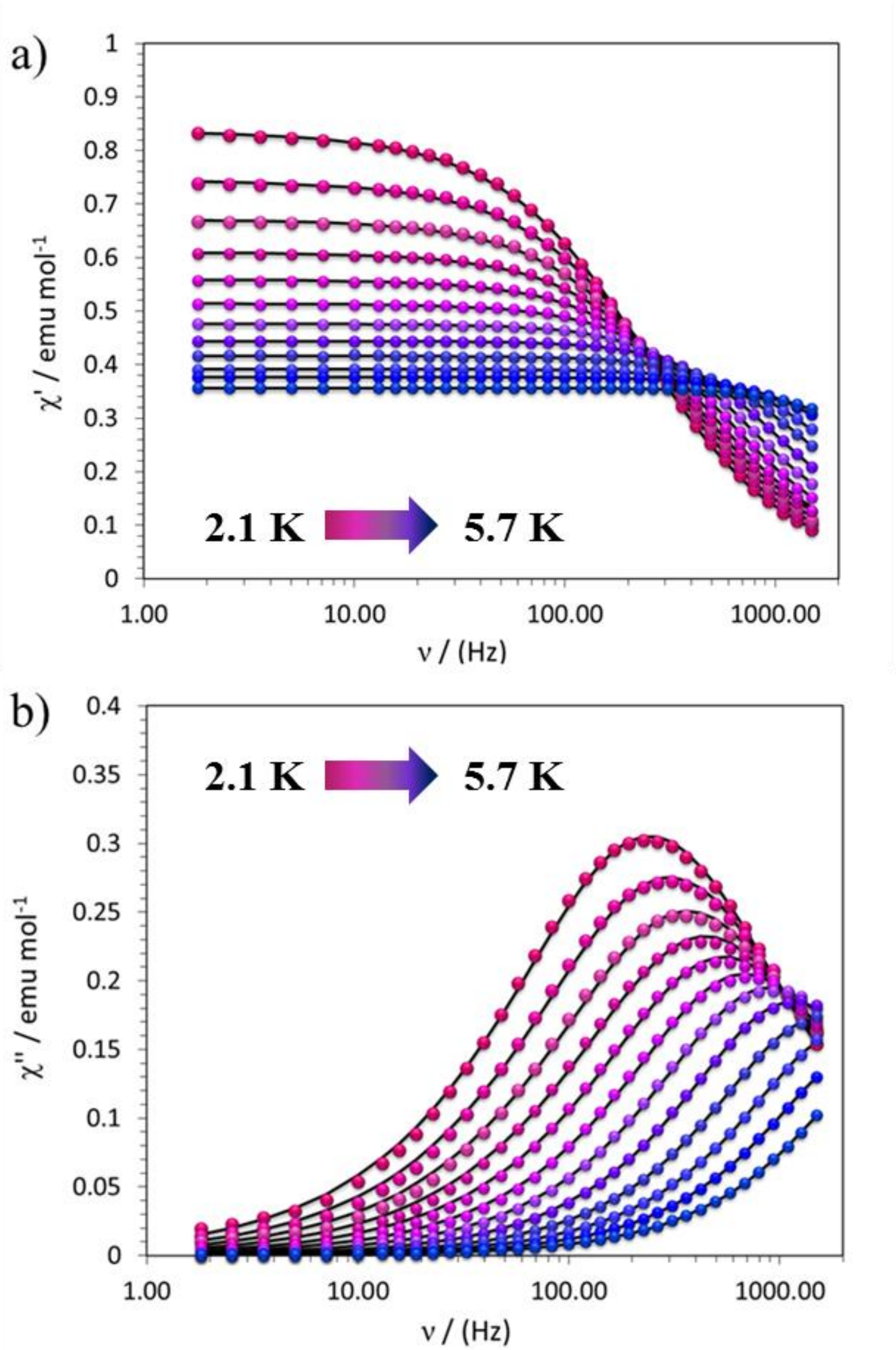

Figure 4.28 In-phase (a) and out-of-phase (b) components of the AC magnetic susceptibility data plotted vs frequency for **26**. Lines represent fitting of the experimental data at different temperatures using the modified Debye model.

The relaxation times obtained from Figure 4.28 were plotted vs temperature using the Arrhenius relationship, equation 4.10:

$$\tau = \tau_o e^{\frac{-U_{eff}}{k_B T}}$$ **Equation 4.10**

where τ is the relaxation time, τ_o is the preexponential constant (or attempt frequency), U_{eff} is the thermal energy barrier, k_B is the Boltzman constant, and T is temperature in Kelvin. By plotting $\ln(\tau^{-1})$ vs T^{-1}, the energy barrier, $U_{eff,}$ is extracted from the slope. Compound **26** was found to have an energy barrier of 32 K, or 22.5 cm^{-1}, with a preexponential constant of 8.64 x 10^{-8} s, Figure 4.29. Extrapolation of the Arrhenius equation leads to a 100 s relaxation time for compound **26** at approximately 1.56 K. This result is suprising given the huge anistropy parameter.

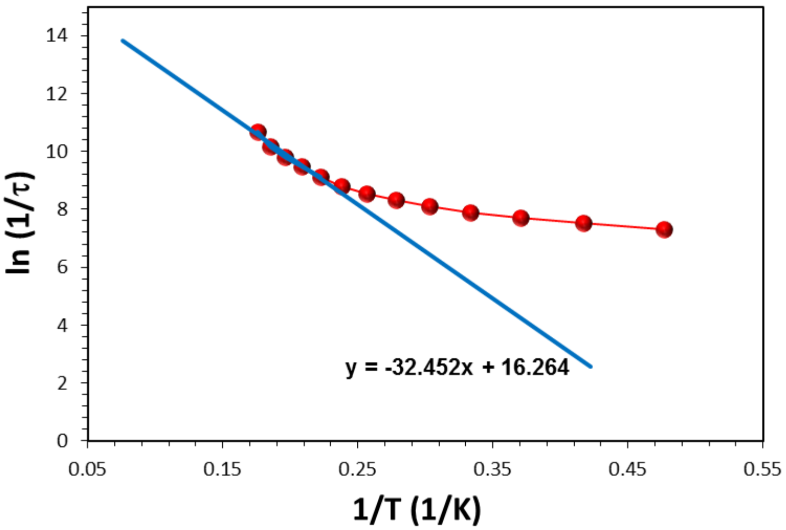

Figure 4.29 Fitting of the Arrhenius plot based on eq. 4.9 and relaxation times obtained by simultaneous fitting of χ' and χ'' vs υ plots for compound **26**. Fitting of the thermal regime is represented by a linear fit of selected data points.

Mitigating the relaxation parameters other than the Orbach process represents the future of this field, as **26** represents an excellent example of successful tuning of the D value but without leading to the ultimate goal which is to achieve a high blocking temperature for slow relaxation. To probe the distribution of relaxation pathways, the Cole-Cole plot in Figure 4.30 was fit with the Debye[284] equations 4.11 and 4.12:

$$\chi' = \chi_S + (\chi_T - \chi_S)\frac{1 + (\omega\tau)^{1-\alpha}\sin(\frac{\pi\alpha}{2})}{1 + 2(\omega\tau)^{1-\alpha}\sin\left(\frac{\pi\alpha}{2}\right) + (\omega\tau)^{2-2\alpha}} \qquad \textbf{Equation 4.11}$$

$$\chi'' = (\chi_T - \chi_S)\frac{(\omega\tau)^{1-\alpha}\cos(\frac{\pi\alpha}{2})}{1 + 2(\omega\tau)^{1-\alpha}\sin\left(\frac{\pi\alpha}{2}\right) + (\omega\tau)^{2-2\alpha}} \qquad \textbf{Equation 4.12}$$

where χ_S and χ_T represent the adiabatic and isothermal susceptibilities, ω is the frequency in radians, τ is the relaxation time is seconds, and α is the Cole-Cole parameter. From these equations it can be seen that χ” reaches a maximum when the relaxation time exactly cancels the oscillating frequency, $\omega\tau = 1$. The α value provides information about the number of different relaxation pathways operating at a given isotherm. The Cole-Cole plot for **26** exhibits a semi-circle overlay between χ’ and χ”. The program CC-Fit was used to fit the Debye equations to the experimental data, Table 4.3. The output yielded α–parameters below 0.2 over all temperature ranges which is indicative of a narrow distribution of single-relaxation processes. An α value of 0 indicates a single relaxation process. CC-Fit also predicts $\chi_{S,}$ χ_T, and the relaxation times at each temperature under investigation.

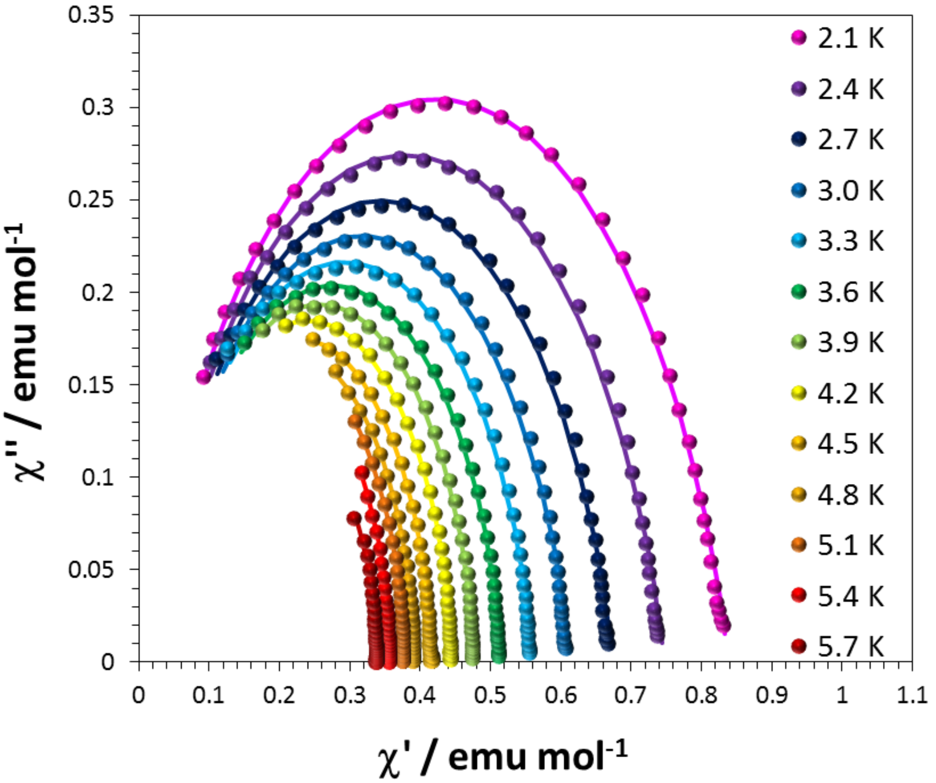

Figure 4.30 Cole-Cole plot for compound **26**. The solid lines represent the best fit to the Debye equations using CC-FIT program (see Nick Chilton's website at http://www.nfchilton.com/cc-fit.html).

Table 4.3 Output parameters from CC fit.

T	χ_S	χ_T	Tau	Alpha
2.1	0.00722	0.83844	6.62E-04	0.1943
2.4	0.01230	0.74726	5.32E-04	0.1827
2.7	0.01755	0.67407	4.38E-04	0.1716
3.0	0.02355	0.61242	3.61E-04	0.1534
3.3	0.02579	0.56046	2.93E-04	0.1326
3.6	0.03192	0.51567	2.33E-04	0.1080
3.9	0.03350	0.47776	1.78E-04	0.0862
4.2	0.03706	0.44535	1.34E-04	0.0623
4.5	0.03473	0.41666	9.67E-05	0.0537
4.8	0.03559	0.39167	7.14E-05	0.0340
5.1	0.03644	0.37676	5.24E-05	0.0262
5.4	0.02685	0.35644	3.73E-05	0.0200
5.7	0.09926	0.33836	3.79E-05	0.0000

The relaxation times listed in Table 4.3 obtained from fitting the Cole-Cole plot were used to construct the Arrhenious plot shown in Figure 4.31. The results give a similar barrier of 28 K. This method is more accurate because of the simultaneous fit of χ’ and χ".

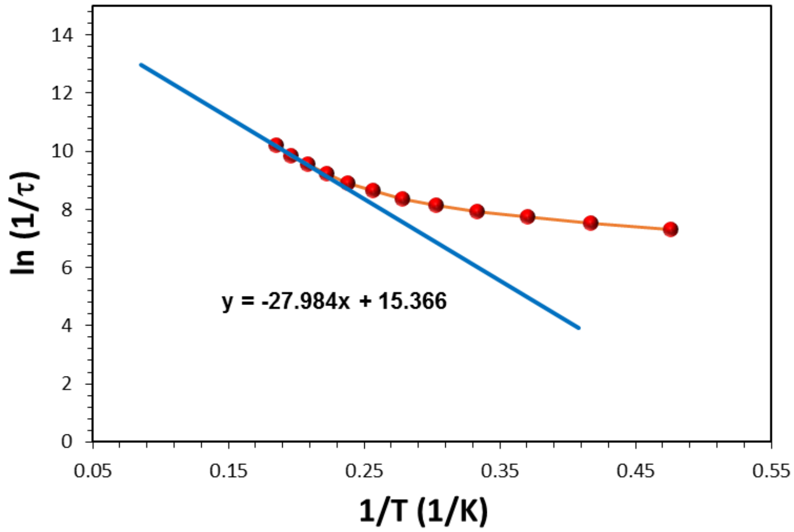

Figure 4.31 Arrhenius plot of **26** plotted using the relaxation times obtained from CC-Fit program.

Previously, different relaxation processes have been observed in mononuclear systems.[107] These encompass interaction of the spin with the crystal lattice in a one phonon (or direct) process and a two phonons (or Raman) process. A recent study of $[Co(acac)_2(H_2O)_2]$ (acac = acetylacetonate) revealed that the nuclear spin of the ^{59}Co (I = 7/2) ion also plays an important role in the spin lattice relaxation dynamics.[102] In this case the dependence of the relaxation time with the field could only be simulated if the nuclear spin and nuclear spin-lattice interactions were included. At low temperature only the lowest Kramers doublet is populated and the $[Co(acac)_2(H_2O)_2]$ complex can be described as an effective S = 1/2. The direct transition from S = +1/2 to S = -1/2 is formally forbidden by time reversal symmetry and only Raman and Orbach relaxation pathways are expected. However, the authors discovered that hyperfine interaction between the nuclear spin and the Kramers doublet split the doublet into 16 electronuclear spin states making some direct transitions allowed. Further application of a magnetic field and spin-lattice nuclear interactions make all direct transitions accessible, as depicted in Figure 4.32.

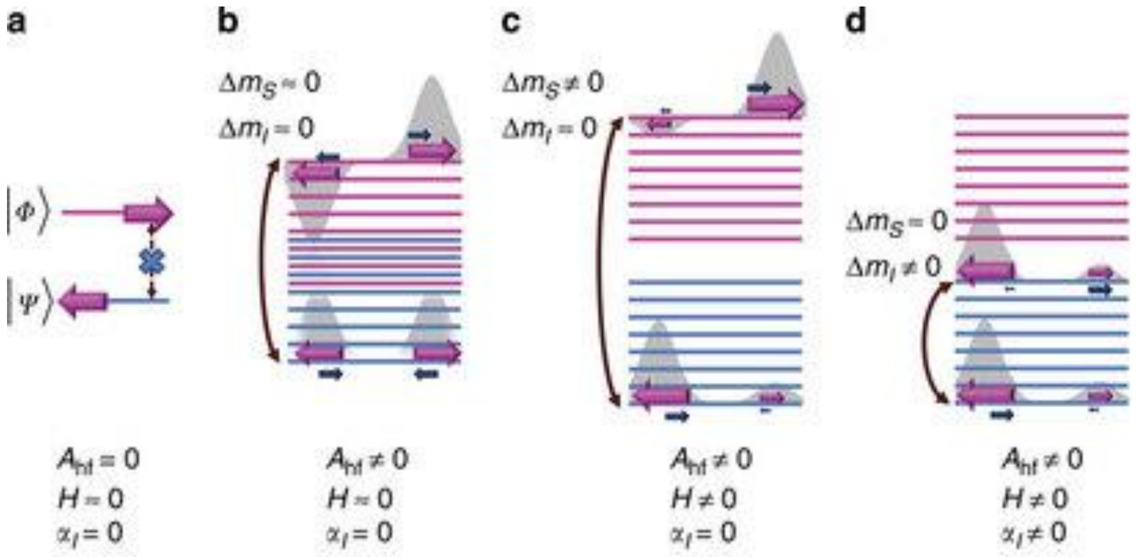

Figure 4.32 Representation of ground state relaxation pathways in $[Co(acac)_2(H_2O)_2]$. a) Approximate zero magnetic field electronic states |ψ> and |φ> are related by time-reversal symmetry (represented by magenta arrows). Direct transitions are forbidden. (b) Hyperfine coupling to a nuclear spin (blue arrow) allows phonon-induced transitions between states having approximately the same nuclear spin state ($\Delta m_I \approx 0$). (c) The Zeeman interaction further splits the levels, giving each state a net magnetic moment. The transitions are now detectable by magnetic susceptibility measurements. (d) A nuclear spin–lattice interaction, characterized by a parameter α_I, compromises the selection rule $\Delta m_I \approx 0$, making all transitions allowed. Reprinted by permission from Macmillan Publishers Ltd: Nature Communications, from reference[102], Copyright 2014.

In order to analyze the discrepancy between the obtained D value and energy barrier in $\{(Tp^*Ti^{IV})(\mu_2\text{-}OAc)_2(\mu_2\text{-}O)Co^{II}(\mu_2\text{-}O)(\mu_2\text{-}OAc)_2(Ti^{IV}Tp^*)\}\cdot 4(CH_3CN)$, **26**, further analysis of the dynamic susceptibility was performed taking into account the different relaxation mechanisms and previous analysis of $[Co(acac)_2(H_2O)_2]$. The dynamic magnetic susceptibility data were collected at 1.8 K with a 5 Oe AC field with an applied DC field ranging from 0 to 5000 Oe. The resulting Cole-Cole plot was fitted using the modified Debye equation as implemented in CC-Fit code, Figure 4.33 and Table 4.4. The dependence of τ^{-1} with field is shown in Figure 4.34.

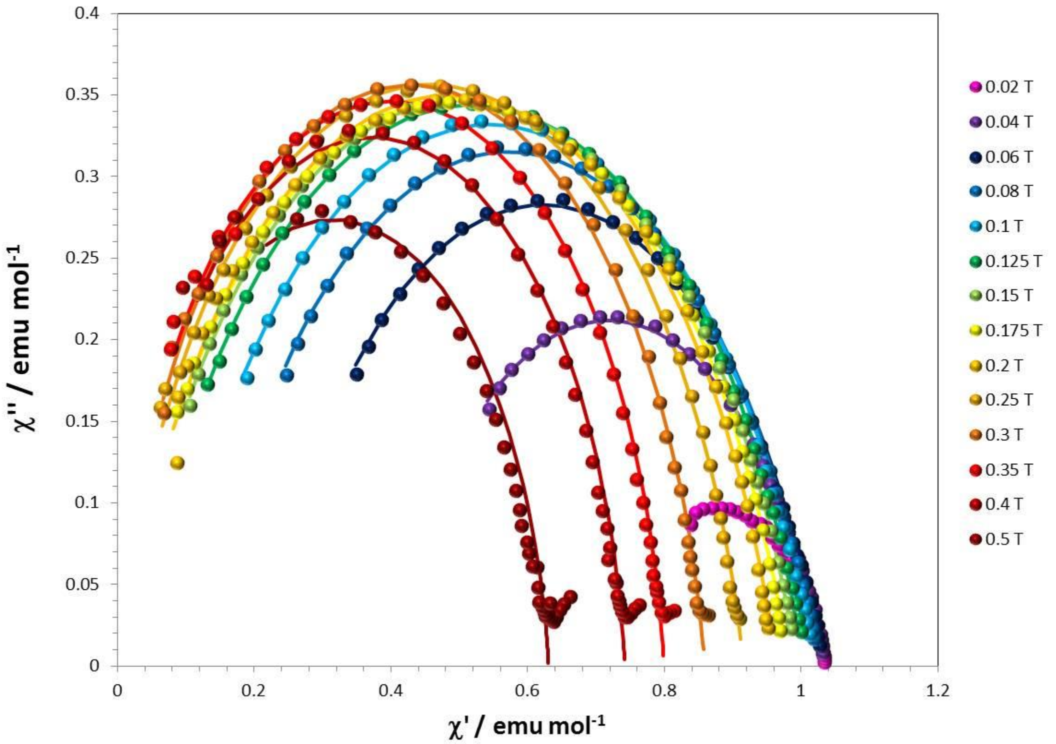

Figure 4.33 Cole-Cole plot for compound **26** at 1.8 K and different applied DC fields. The solid lines represent the best fit to the Debye equations using CC-FIT.

Table 4.4 Relaxation time and α values obtained from CC fit at 1.8 K and different applied DC fields for **26**.

DC Field	χ_S	χ_T	τ	α
200	0.729157	1.03713	0.000202702	0.288786
400	0.402679	1.0334	0.000347937	0.246314
600	0.218092	1.02662	0.000459014	0.222685
800	0.126916	1.0201	0.000554605	0.217249
1000	0.0753913	1.01316	0.000630807	0.215402
1250	0.0294904	1.00378	0.000704032	0.21697
1500	0.00940105	0.993609	0.000780845	0.218085
1750	0.00338494	0.981645	0.000848866	0.213388
2000	0.00770151	0.96398	0.00088619	0.195458
2500	0.000660288	0.916079	0.000782847	0.156979
3000	1.09666E-14	0.859138	0.00060053	0.118376
4000	1.50312E-14	0.799738	0.000436448	0.0906938
5000	1.45883E-14	0.742021	0.000308787	0.0855604

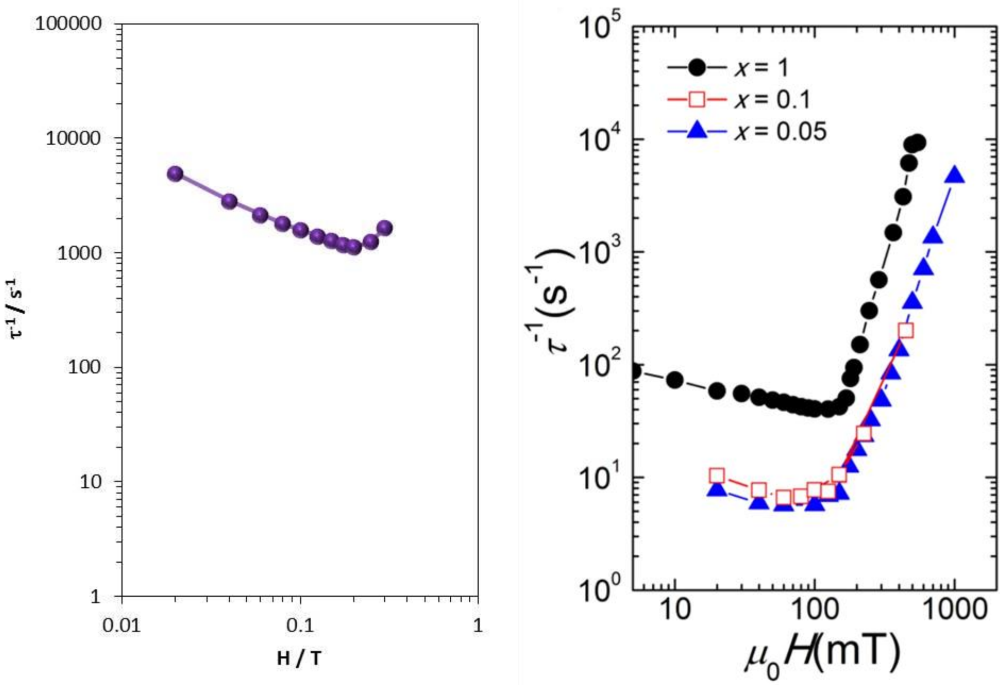

Figure 4.34 Dependence of the relaxation time with the applied DC field of **26** (left) and $[Co_xZn_{1-x}(acac)_2(H_2O)_2]$ (right). Reprinted by permission from Macmillan Publishers Ltd: Nature Communications, reference[102], Copyright 2014.

As shown in Figure 4.34 the behavior of **26** is very similar to that previously observed for [$Co_xZn_{1-x}(acac)_2(H_2O)_2$], which also has a strong dependence with the concentration due to spin-spin coupling. Although the values of τ^{-1} are larger for **26**, the shape is similar indicating the presence of spin-spin and hyperfine interactions, which allow direct phonon-induced transitions between the states of the ground Kramers doublet.

The dynamic susceptibility was collected also at an applied DC field of 1500 Oe and analyzed using the modified Debye function with CC-fit, Figure 4.35 and Table 4.5.

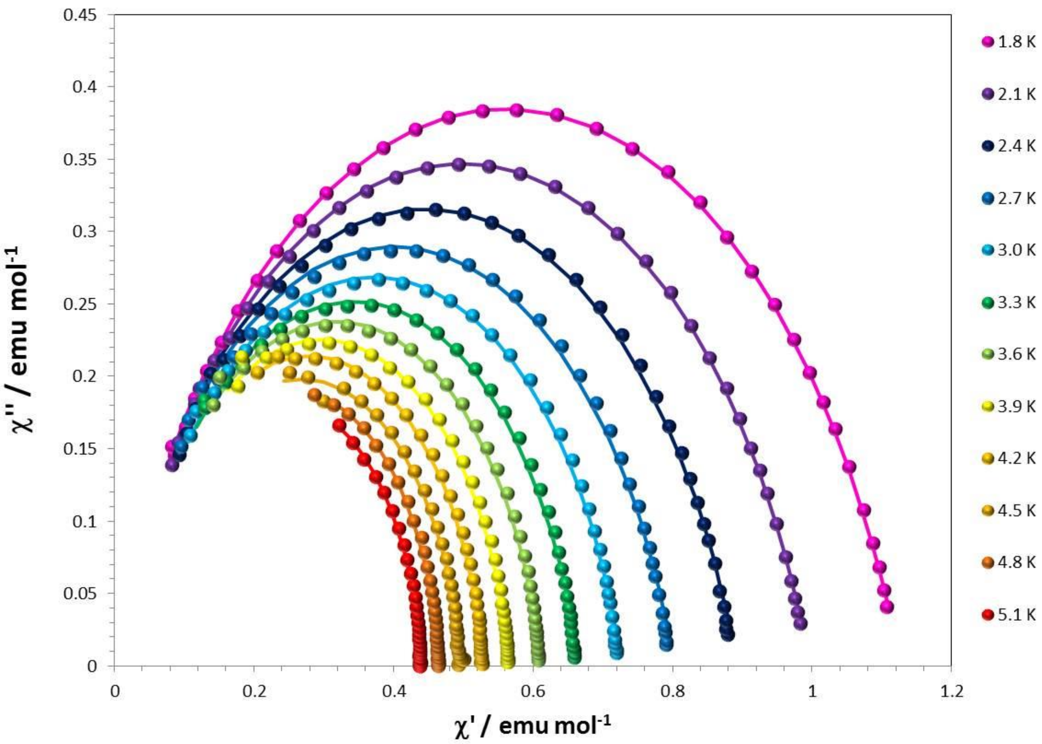

Figure 4.35 Cole-Cole plot for compound **26** at 0.15 T and different temperatures. The solid lines represent the best fit to the Debye equations using CC-FIT.

Table 4.5 Relaxation time and α values obtained from CC fit at 0.15 T and different temperatures for **26**.

T	χ_S	χ_T	τ	α
1.8	1.23676E-05	1.12652	0.00127893	0.236704
2.1	0.000017882	0.996932	0.000991362	0.22548
2.4	2.82881E-05	0.89236	0.000782712	0.21603
2.7	4.02195E-05	0.802392	0.000615839	0.203887
3.0	0.0179182	0.726337	0.000501548	0.173496
3.3	0.0196487	0.664666	0.000389508	0.155905
3.6	0.0233871	0.611714	0.000298074	0.133574
3.9	0.026478	0.566842	0.000222393	0.11435
4.2	0.0302441	0.528239	0.000164556	0.0957034
4.5	0.0442137	0.495383	0.000123745	0.0823411
4.8	0.050069	0.464392	9.31843E-05	0.0566338
5.1	0.0446356	0.43835	6.73689E-05	0.0485737

The dependence with the temperature at 1500 and 2000 Oe was analyzed simultaneously using equation 4.13, which includes direct and Raman processes. As the direct term is dependent on the applied DC field, two A parameters, one for each field, have been considered. The best fit has been obtained for A = 460 s^{-1} K^{-1} and 947 s^{-1} K^{-1} for 1500 and 2000 Oe respectively, with C = 0.14 s^{-1} $K^{-7.07}$ and n = 7.07, Figure 4.36. In this case the best fit for the exponent gave a Raman term of 7.07, which is smaller than 9- the expected value for transition metal Kramers ions. The difference is attributable to dipolar and intermolecular interactions.[286]

$$\tau^{-1} = AT + CT^n \qquad \textbf{Equation 4.13}$$

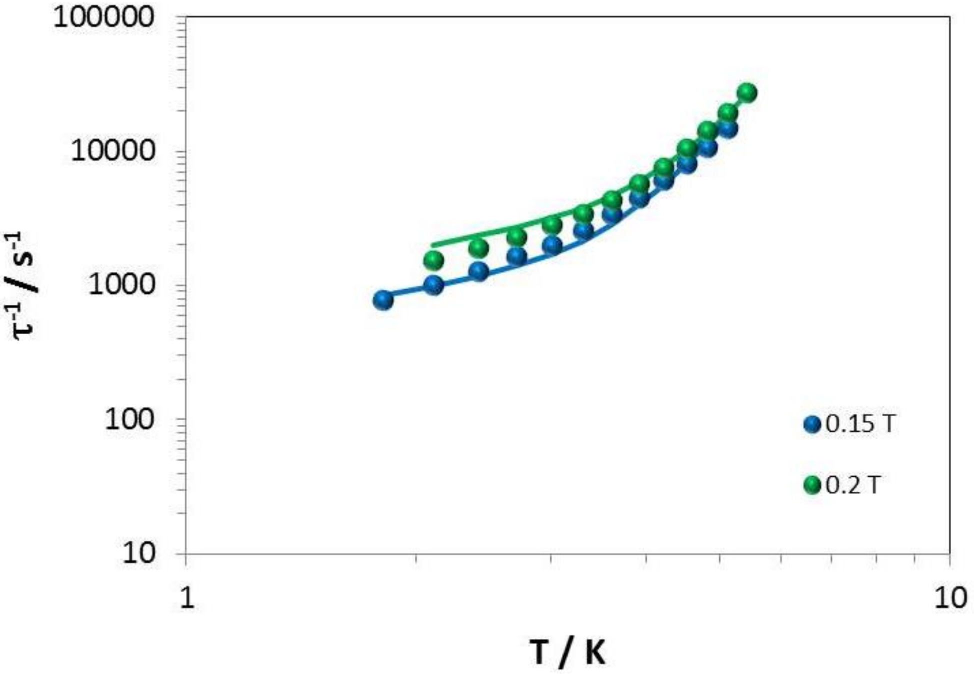

Figure 4.36 Dependence of the relaxation time with temperature of **26.**

As can be observed in the analysis of the dynamic susceptibility for compound **26**, both direct (which is allowed due to the nuclear spin-lattice interaction) and Raman processes are dominant instead of an Orbach process, Figure 4.37. At high temperature the predominant mechanism will be Raman or Orbach processes depending on the Debye temperature (availability of phonons) and the energy barrier. We conclude however, that the predominant mechanism is Raman because the small effective energy barrier of **26**, compared to the obtained D value.

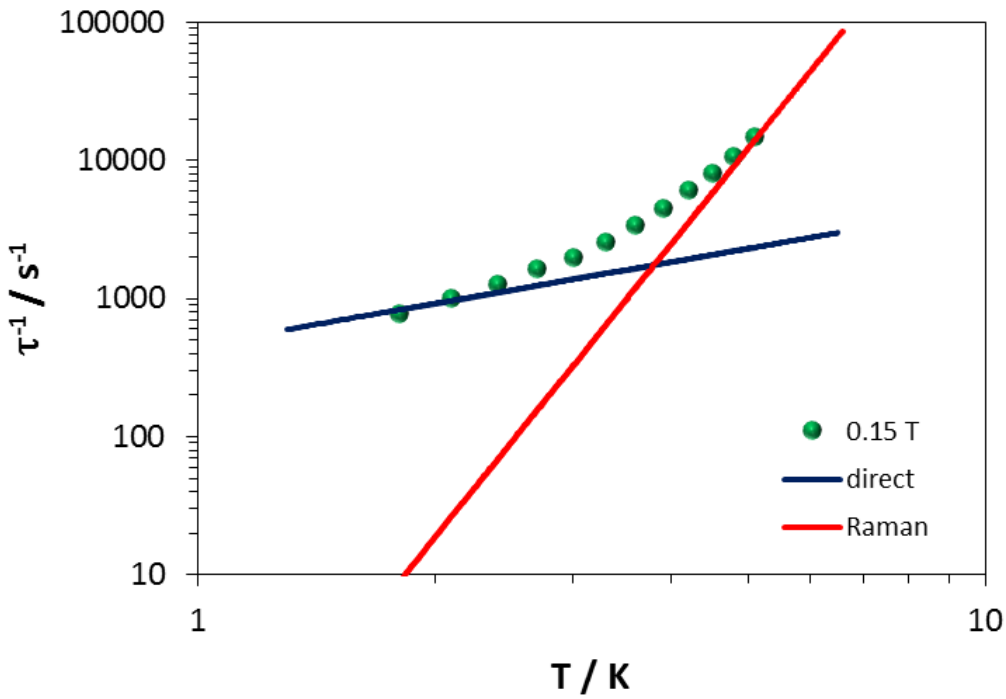

Figure 4.37 Temperature depenence of relaxation times reveal direct and Raman processes operative at low and high temperatures, respectively for **26**. Data was collected under 0.15T DC field.

Thermal Gravimetric Analysis

Because fitting the zero-field splitting parameter using static DC magnetic measurements is extremely sensitive to the molecular weight of the sample, TGA analysis was performed on compound **26**. The TGA sample preparation was conducted in the same manner as those prepared for SQUID measurements and elemental analysis. The TGA, shown in Figure 4.38, was prepared by isolating the crystals from the reaction solution and washing with DMF/MeCN (using MeCN rinses at the end to remove any DMF). The crystals were pipetted from the final MeCN wash and palced into a mortar and pestal and allowed to dry. The crystalline solid was then crushed into a light orange powder. The light orange powder was loaded into a pear shaped flask and pumped *in vacuo* for approximately 1 hour.

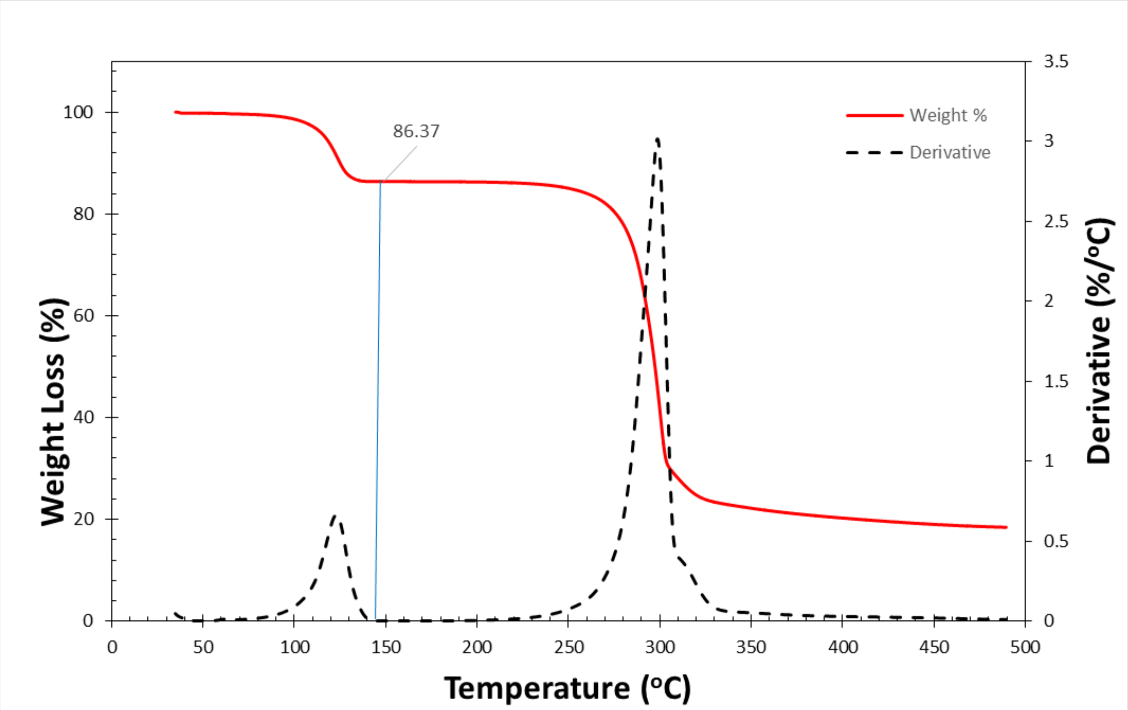

Figure 4.38 Thermal gravimetric analysis (TGA) of compound **26**.

The resulting TGA plot revealed solvent loss over the 100-140 ^{o}C temperature regime that is approximately 14% of the total sample mass. Assuming this mass loss is due to the solvent, 14% of the weight corresponds nicely with four acetonitrile molecules which is the same value as those located in the crystal structure refinement. The sample decomposes after heating to 250 ^{o}C. Assuming a solvent-free base weight of 101.238 g·mol^{-1}: 13.61% = (41.05x·100%)/(1017.238 + 41.05x), x = 3.904.

Computational Studies

[(CH$_3$CH$_2$)$_4$N][Tp*TiCl$_3$] (19) and [(CH$_3$CH$_2$)$_4$N][Tp*TiCl$_3$] (21). For both compounds, the coordination geometry around the titanium ion is approximately octahedral but the actual symmetry is distorted C_{3v}. The CASPT2 energies in Table 4.6 indicate that this descent in symmetry lead to smaller ligand field perturbations. The strongest field is the octahedral field, separating the t_{2g} from the e_g levels, followed by a weaker trigonal field, which splits t_{2g} into a_1 and e orbitals, and finally followed by a low symmetry C_1 field which further splits the e shells. We can define the octahedral field strength as the energy difference between the barycenters of the $^2T_{2g}$ and ^2E_g terms:

$$[\mathrm{Tp^*TiCl_3}]^- : 10Dq \approx 15300\mathrm{cm}^{-1}$$

$$[\mathrm{Tp^*Ti(CN)_3}]^- : 10Dq \approx 22300\mathrm{cm}^{-1}$$

The different $10Dq$ values can be explained on the basis of the known fact that CN$^-$ is a much stronger field ligand than Cl$^-$.

Table 4.6 Calculated ligand field energies (cm^{-1}) for **19** and **21**.

State		**19**		**21**	
Oh	C3v	CASPT2	SOC	CASPT2	SOC
2T2g	2A1	0	0	0	0
	2E	1220	1180	1420	1380
		1310	1380	1480	1550
2Eg	2E	15900	15910	22910	22920
		16410	16420	23630	23640

The magnetic properties of the complexes are determined primarily by the trigonal splitting of the $^2T_{2g}$ term. This splitting is very similar in the two compounds; the ground state is the orbitally nondegenerate $^2A_1$, separated by more than 1000 cm^{-1} from the orbital doublet ^2E (for simplicity we use the notation of an idealized C_{3v} symmetry). The a_1 orbital that is occupied by the single d electron in the ground state is a d_{z2} orbital oriented along the C_3 axis. It can be seen that the introduction of spin-orbit coupling does not dramatically alter the energy level structure. This is consistent with the SOC constant of Ti(III), $\zeta \approx$ 150cm^{-1}, which is small in comparison to the ligand field splittings. The important effect of SOC, however, is that the g factors of the ground state are smaller than the spin only value of $g = 2$. The computed values are:

$[Tp^*TiCl_3]^-$: $g_{\|} = 1.96$, $g_{\perp} = 1.71$

$[Tp^*Ti(CN)_3]^-$: $g_{\|} = 1.97$, $g_{\perp} = 1.77$

Note that, because of the distorted trigonal symmetry, two different $g_{\perp}$ values were obtained for each complex. The difference between the two was however very small and we give only the average $g_{\perp}$ for simplicity.

Figure 4.39 compares the computed susceptibility with the experimental data. Based on the energies in Table 4.6, the computations predict that only the ground state is occupied in the temperature range 0–300K. Consequently the computed χT is in each case a straight line whose slope is the temperature-independent paramagnetism (TIP) of the ground state. The slopes are 3.1×10^{-4} cm^3mol^{-1} for the chloride complex and 2.6×10^{-4} cm^3mol^{-1} for the cyanide derivative. The TIP arises mainly from Zeeman interactions with the states of the first excited ^2E level. Figure 4.39 reveals that the computed χT values agree very well with the experimental data for **19** and **21**.

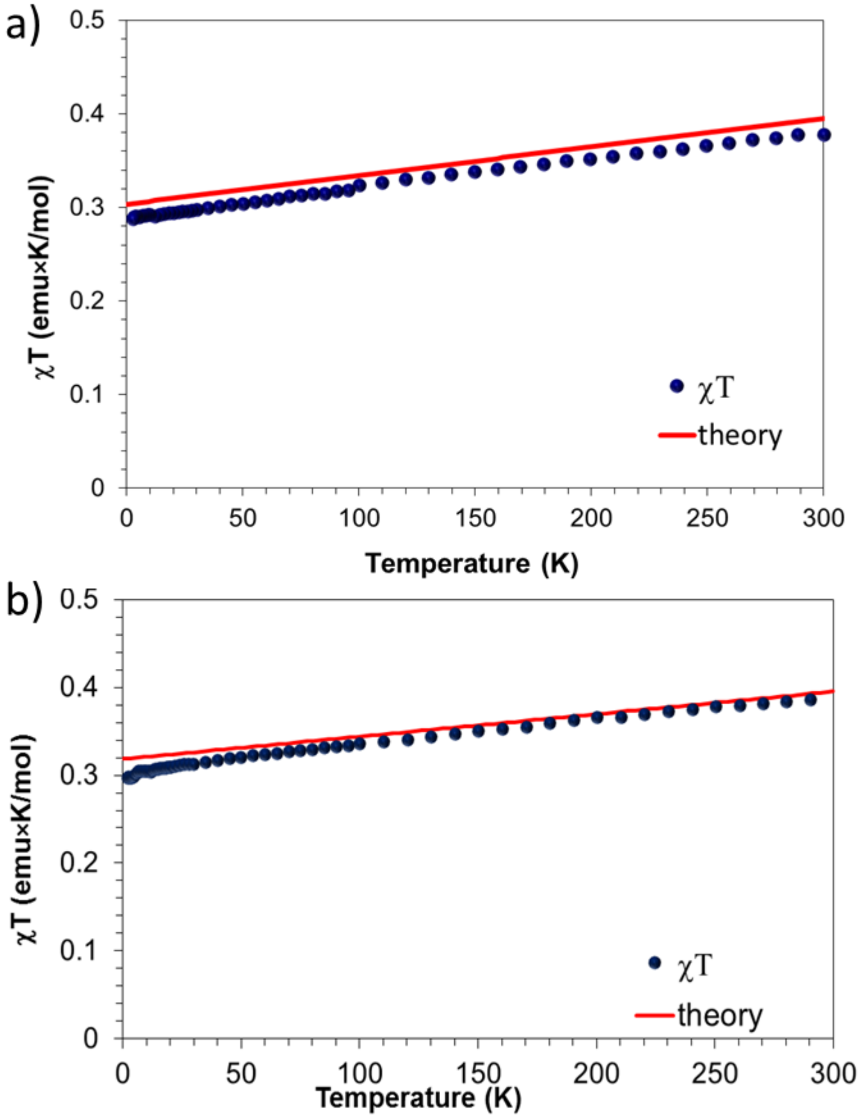

Figure 4.39 Temperature dependence of χT for (a) **19** and (b) **21**. The solid red lines correspond to the modelling from *ab intio* calculations.

The effect of a small trigonal ligand field on an octahedral $^2T_{2g}$ ground term has been described in the literature by a parametric model.[287,288] The parameters are Δ, the splitting of the t_{2g} orbitals into a_1 and e components, *k*, the orbital reduction factor, and ζ, the spin-orbit coupling constant. We can obtain Δ from the CASPT2 energies in Table 4.6

as the barycenter of the weakly split first ^{2}E level. This gives $\Delta = 1260\text{cm}^{-1}$ for $[\text{Tp*TiCl}_3]^-$ and $\Delta = 1450\text{cm}^{-1}$ for $[\text{Tp*Ti(CN)}_3]^-$. Furthermore, k can be estimated from the computed matrix elements of the orbital angular momentum in the CASSCF states. It turns out that $k = 1.0$ for both compounds, which means that the t_{2g} orbitals are almost pure 3d, with negligible covalent mixing with the ligand orbitals. Using $\zeta = 150\text{cm}^{-1}$, we find that this model agrees with the computed g values and the TIP for about 90%. The remaining 10% is due to interaction with the octahedral ^2E_g level, which is not considered in this simple model.

$\{(\text{Tp*Ti}^{\text{IV}})(\mu_2\text{-OAc})_2(\mu_2\text{-O})\text{Co}^{\text{II}}(\mu_2\text{-O})(\mu_2\text{-OAc})_2(\text{Ti}^{\text{IV}}\text{Tp*})\}\cdot 4(\text{CH}_3\text{CN})$ (26). In the case of complex **26**, there are two diamagnetic Ti(IV) centers and one paramagnetic Co(II) center in a compressed octahedral geometry. To further verify the experimental magnetic data and the large D value obtained for **26**, CASSCF and NEVPT2 calculations have been performed. The obtained zero-field splitting (ZFS) parameters are showed in Table 4.7. The results show a large and positive D value with a large E value and a small effect of the dynamic correlation; NEVPT2 results are very similar to CASSCF. The energy difference between the ground state and the first excited state before the SOC is very small, which has been previously related with a large anisotropy.[115]

Table 4.7 Calculated D and E values for **26** and energy differences (in cm^{-1}) between the ground and first excited state before the SOC (ΔE) and between the two Kramers' doublets after the SOC (δE).

	D	E	ΔE	δE
CASSCF	124	34.1	36.2	274.7
NEVPT2	121.5	37.1	44.0	274.8

For a Co(II) ion in an octahedral compressed geometry the predicted D value is large and negative because the orbitals involved in the first excitation are d_{xz} and d_{yz}, which have a small difference in energy and the same $|m_l|$ value. For compound **26** the obtained D values are positive indicating that the system is more complex and cannot by described by a model which only considers the first excitation. The same conclusion was reached recently for a similar Co(II) SMM in a compressed octahedral environment.[289] The calculation of **6** reveals the contribution from different excited states to D and E values, Table 4.8. An important and positive contribution is obtained not only from the first excited state but also from the second excited state. Also in both compounds the E value is very close to the limit E/D < 1/3, indicating a situation between easy plane and easy axis. The preceeding disccusions support the recent theory that a cobalt in an octahedral environment will exhibit large D-values,[115] however the calculations found for **26**, also reveal that the excited state contributions are complicated.

Table 4.8 Contribution to D and E values from the excited states for **26**. ΔE is the difference in energy between the excited state and the ground state.

		CASSCF			NEVPT2		
State	Multiplicity	ΔE	D	E	ΔE	D	E
1	4	36.2	69.02	68.78	44.0	69.12	68.78
2	4	734.2	30.27	-30.00	847.5	33.44	-33.08
3	4	6171.7	0.68	0.68	7779.3	0.86	0.84
4	4	6284.6	5.60	1.83	7875.9	7.04	2.41
5	4	6428.1	-0.07	-2.45	7925.4	-0.09	-3.06
6	4	13429.0	-0.003	0.002	11194.8	-0.004	0.002

Concluding Remarks

A new trigonally distorted titanium(III) cyanide building block has been synthesized and added to the arsenal of cyanide-based building blocks for the geometric design of ansiotropic molecules. Although *ab initio* calculations revealed the ground state to be an orbital singlet, this situation can change with coordination to other metal centers with bulky ligands, thereby engendering single-ion anisotropy in the titanium center. Although none of the attempted reactions produced an SMM with the intact $[Tp^*Ti(CN)_3]^-$ anion, the molecule is available to future synthetic chemists with ambition to tackle such a difficult building block. Promising reactions of **21** with other Tp*M complexes and fully solvated metal ions provided promising IR evidence for product formation. Reactions that were unintentionally compromised by moisture led to the realization that facile hydrolysis of **21** to afford trinuclear carboxylate complexes with various central metal ions coordinated to titanium(IV) units is a reproducible, general method to make magnetic molecules from divalent carboxylate precursors. The Tp^*Ti^{IV} moieties in the compounds, $\{(Tp^*Ti^{IV})(\mu_2\text{-}OAc)_2(\mu_2\text{-}O)M^{II}(\mu_2\text{-}O)(\mu_2\text{-}OAc)_2(Ti^{IV}Tp^*)\}\cdot 4(CH_3CN)$, ($M = Mn^{II}$, Co^{II}), serve as an “inorganic capping ligand” in that the only paramagnetic ion is the central metal ion. Such an intriguing structure motif allowed for testing theory of achieving large anisotropy through geometric control. The large magnitude of D observed for compound **26** is impressive although the effective barrier height of the compound is smaller than expected. These results poise us for the next stage of improving the barriers of SMMs which is to determine how to control non-Orbach relaxation processes. It is interesting to note, that completely switching off quantum tunneling to engender larger barriers, in and of itself, undermines the goal of quantum computing applications for such molecules.[290] It is more reasonable to propose that very high temperature SMMs are not required as long as the properties can be controlled and tuned for the particular needs of the device.

CHAPTER V

INVESTIGATING PROLATE LANTHANIDE COMPLEXES FOR SINGLE-MOLECULE MAGNET BEHAVIOR [*]

Introduction

Lanthanide-containing mononuclear single-molecule magnets (SMMs) have received much attention in the last five years,[124] as they are emerging as the best candidates in the field of molecular magnetism for application in high density data storage, molecular spintronics, and quantum processing.[81,83,291,292] The advantages of 4f elements stem from their inherent anisotropy imparted by high ground state spin values and strong spin-orbit coupling which produces an oblate or prolate shape for the 4f electron density which can be stabilized by a ligand field of the appropriate symmetry.[118]

By using geometric design principles to minimize electronic repulsions between the electron densities of the lanthanide ions and the ligands, researchers have prepared SMMs with extremely high barriers and magnetic hysteresis as compared to previous literature reports.[100] While most examples of the rare earth SMMs are based on the oblate terbium and dysprosium ions, particularly the latter,[293] more recent work has revealed that prolate ions can also engender SMM behavior, with the erbium(III) ion being the main choice for such systems.[76,128,130,294] The first reported erbium(III) mononuclear SMM is the organometallic complex (Cp*)Er(COT) (Cp* = pentamethyl-cyclopentadienide; COT = cyclooctatetraenide), reported by Gao and coworkers, which exhibits two relaxation

---

[*] A portion of this chapter was reprinted with permission from "A Trigonal Pyramidal Erbium(III) Single-Molecule Magnet" by Andrew J. Brown, Dawid Pinkowicz, Mohamed Saber, and Kim R. Dunbar, 2015. Angew. Chemie., 54, 5864-5868, Copyright [2015] by Wiley Online Library (VCH). http://onlinelibrary.wiley.com/doi/10.1002/anie.201411190/abstract

processes with energy barriers $\Delta E_{eff}/k_B$ of 197 and 323 K and a butterfly hysteresis loop as high as 5 K.[128] More recently, Long and coworkers prepared $[Er(COT)_2]^-$ which exhibits enhanced SMM properties because the equatorial nature of the ligands is more compatible with preserving the prolate nature of the erbium(III) ion electron density and the molecule is symmetrical. The compound exhibits a high energy barrier of $\Delta E_{eff}/k_B = 216$ K with waist-restricted hysteresis being observed at temperatures up to 10 K for a diluted sample in a yttrium matrix.[76] Murugesu and coworkers also studied this system[295] and derivatized the COT ligand with trimethylsilyl appendages in order to study the effects of lowering the symmetry. Both $[Er(COT'')_2]$- and $[Er_2(COT'')_3]$ (COT″ = 1,4-bis(trimethylsilyl)cyclooctatetraenyl dianion) were prepared[130] and it was found that the double-decker sandwich compound exhibits $\Delta E_{eff}/k_B = 335$ K and hysteresis up to 14 K in solution.[131]

In addition to the rare earth organometallic sandwich compounds, there are also low-coordinate species of the type $Ln[N(SiMe_3)_2]_3$ which have been studied for catalysis.[296-303] The bis(trimethylsilyl)amide ligand is known to enforce a trigonal planar geometry in transition metal complexes[304,305] but the lanthanide analogs are distorted towards a trigonal pyramidal structure due to agostic interactions between the lanthanide center with the β-Si-C bond of the ligand, as well as bonding considerations involving the d-orbitals of the lanthanide ion.[306] Tang and coworkers recently reported the magnetic properties of $Er[N(SiMe_3)_2]$, the first example of an equatorially coordinated mononuclear lanthanide SMM; the molecule exhibits a blocking temperature of ~13 K based on the $\chi''(T)$ maximum at a frequency of 1488 Hz and a barrier to the reversal of magnetization

$\Delta E_{eff}/k_B$ = 122 K with hysteresis reported to occur at 1.9 K.[307] They also reported $Er(NHPhiPr_2)_3(THF)_2$ which exhibits SMM behavior only in the presence of a DC field.

Recently we also prepared $Er[N(SiMe_3)_2]_3$ for the aforementioned reasons but, during the course of this work, the results of Tang and coworkers appeared in the literature. We therefore decided to pursue the properties of a related compound that exhibits a bridging or terminal chloride which was isolated from one of the syntheses under specific conditions. This chapter contains results of the preparation, crystal structure, and magnetic characterization of $[Li(THF)_4]\{Er[N(SiMe_3)_2]_3Cl\}\cdot 2(THF)$ (**27**). The effects of solid state dilution with the yttrium complex are also reported. While analogs with other lanthanide ions exist,[308,309] the erbium(III) congener was not reported previously. Interestingly, compound **27** exhibits improved magnetic properties as compared with $Er(NHPhiPr_2)_3(THF)_2$ despite the presence of a negatively charged chloride. These results are not easily understood in the framework of the simple oblate versus prolate theory that has been proposed for designing mononuclear lanthanide SMMs,[118] a point that was recently made in the literature by another group for a different Er(III) compound.[310]

To highlight the importance of the Er(III) ion as the best candidate for prolate lanthanide ions, the more prolate ion, Tm(III), was also prepared for the sake of comparison. It was found that the compound $\{[(Me_3Si)_2N]_3Tm(\mu\text{-}Cl)Li(THF)_3\cdot[Li(THF)_4]\{Tm[N(SiMe_3)_2]_3Cl\}\cdot 2THF\}$ (**31**), does not exhibit out-of-phase signals in AC susceptibility measurements under zero DC field. This highlights the importance of using Kramers rare earth ions because the ground state tunnelling transition is formally forbidden with half-interger m_J states.[286] Nonetheless, compound **31** does exhibit the beginning of out-of-phase signals under application of 1000 Oe DC field, placing it in a rare class of mononuclear SMMs containing thulium.[311] Other interesting structure variants are also reported with the thulium analog.

Experimental Section

Syntheses

The acetonitrile solvent was pre-dried over 3 Å molecular sieves and distilled under N_2. Anhydrous *n*-pentane, anhydrous diethyl ether, $ErCl_3$, $TmCl_3$, hexamethyldisilazane, and 1.0 M n-BuLi in hexanes were purchased from Sigma-aldrich and used as received. All manipulations were conducted using standard Schlenk-line or drybox techniques unless otherwise stated.

Preparation of $\{Li(THF)(\mu\text{-}N(SiMe_3)_2)\}_2$. An increased yeild is obtained by first isolating the ligand to prevent reduction of the metal halides by the excess n-BuLi. A 50 mL Schlenk tube was charged with 10 mL of anhydrous diethyl ether, which was then subjected to 5 freeze-pump-thaw cycles to remove dissolved oxygen. The solvent was then treated with 3.5 mL of $HN(SiMe_3)_2$ under a blanket of nitrogen using cannula transfer with an oven-dried syringe that was cooled to room temperature in a desiccator and flushed with nitrogen before use. The flask was then placed in a $MeCN/N_2$ cold bath. Using a pre-dried syringe, 8 mL of a 1.6 M solution of n-BuLi in hexanes was slowly transferred to the hexamethyldisilazane solution. The reaction solution was slowly warmed to room temperature and the reaction solution was stirred for 12 hours. The solvent was then removed in vacuo into a trap filled with heptane/isopropanol. The resulting white powder was re-dissolved in 10 mL of THF and 5 mL of Et_2O. The resulting solution was filtered and stored in the freezer which led to a crop of crystals of $\{Li(THF)(\mu\text{-}N(SiMe_3)_2)\}_2$. Yield: 1.4 g (32% based on $HN(SiMe_3)_2$.

Preparation of $[Li(THF)_4]\{Er[N(SiMe_3)_2]_3Cl\}\cdot 2THF$ (27). Complex **27** was prepared by charging a flask with 73.0 mg of $ErCl_3$ (0.27 mmol) and 210 mg of $\{Li(THF)(\mu\text{-}N(SiMe_3)_2)\}_2$ (0.44mmol) with 10.7 mL of THF at room temperature. The resulting mixture was stirred for 12 hours because $ErCl_3$ does not readily dissolve in THF. The resulting slightly orange/pink solution was reduced to dryness and extracted with 50 mL of pentane. The pentane solution was concentrated to approximately 10 mL. During this time, light pink crystals began to form. The concentrated solution was placed in the freezer to induce more crystal formation. After another 12 hours, the crystals were isolated by removing the supernatant by cannulation and rinsed with cold pentane until the washings were colorless, yield: 170 mg (57% based on $ErCl_3$). The resulting crystals were stored under a minimal amount of pentane in the freezer inside a dry-box. Note: If crystals of compound **27** are sublimed, the pseudo-trigonal planar complex, $Er[N(SiMe_3)_2]_3$, is obtained as is the case with other analogs as well.[302,308] Additionally, temperature may play a key role, as our synthetic method was carried out a room temperature for the initial mixing of reactants. Tang and coworkers employed a similar procedure but they used the sodium salt $Na[N(SiMe_3)_2]$ which also results in the formation of $Er[N(SiMe_3)_2]_3$ without the need for sublimation.[307] The reaction procedure employed for compound **27** also produces variant structural types. Compounds **28** and **29** have both been isolated from different attempts of the same reaction procedure. Collection of unit cell information on multiple crystals was required before collecting magnetic data.

Preparation of $\{Er_{0.1}Y_{0.9}[N(SiMe_3)_2]_3(\mu\text{-}Cl)[Li(THF)_3]\}\cdot$pentane (30). The compound, $[(Me_3Si)_2N]_3Y(\mu\text{-}Cl)Li(THF)_3]$, was prepared is an analogous fashion to the erbium analog. A vial was charged with 110 mg (0.097 mmol) of **27** and 914 mg (0.82 mmol) of $[(Me_3Si)_2N]_3Y(\mu\text{-}Cl)Li(THF)_3]$. The mixture was dissolved in 5 mL of THF and 20 mL of pentane. The resulting concentrated solution was stored in the freezer inside the drybox for 12 hours. Large needle crystals of **30** were obtained and rinsed with cold pentane.

Preparation of $\{[(Me_3Si)_2N]_3Tm(\mu\text{-}Cl)Li(THF)_3\cdot[Li(THF)_4]\{Tm[N(SiMe_3)_2]_3Cl\}\cdot 2THF\}$ (31). To a 100 mL Erlenmeyer flask was added 80 mg $TmCl_3$ and 230 mg $\{Li(THF)(\mu\text{-}N(SiMe_3)_2)\}_2$ in 50 mL THF. The reaction solution was stirred overnight to give a faint yellowish orange solution and was reduced to a paste. The product was extracted with 50 mL of anhydrous pentane and the resulting mixture was filtered and concentrated to 15 mL. After 3 days in the freezer at -15 °C, crystals were harvested and stored under a minimal amount of pentane in the freezer.

Preparation of $[Na(THF)_3((Me_3Si)_2N)_2Tm(CH_2)SiMe_2N(SiMe_3)]$ (32). A solution of $Na\{N(SiMe_3)_2\}$ (0.94g in 20 mL THF) was added to a stirring solution of $TmCl_3$ (0.41g in 40 mL THF). The addition of the reactants was performed at room temperature in the glovebox. The reaction mixture was stirred for 6 hours and then concentrated to 25 mL and filtered through a medium porosity fritted funnel. The resulting filtrate was stored in the glovebox freezer at -15 °C for 3 days after which time yellow platelet crystals were harvested and rinsed with cold pentane until the washings were colorless. The crystals were stored under a small volume of pentane in the freezer.

Preparation of [Tm(N(SiMe$_3$)$_2$)$_2$]$_2$(μ$_2$-OLi(THF)$_2$)$_2$ (33). A 150 mL Schlenk flask was charged with 0.5 g TmCl$_3$ and 1.07 g LiHMDS. The solids were dissolved simultaneously in 70 mL THF. The reaction mixture was stirred for 1 hour, concentrated to 30 mL, and filtered through a fritted funnel with medium porosity. The filtrate was further concentrated to approximately 15 mL and then stored in the freezer at -15 ^{o}C. After one month, white crystals suitable for X-ray diffraction were harvested.

Instrumentation

Single crystal X-ray data were collected at 110 K on a Bruker APEX II diffractometer equipped with a CCD detector. The X-rays were generated with graphite monochromatic Mo Kα radiation (λ = 0.71073 Å). Magnetic susceptibility and magnetization measurements were collected using a Quantum Design MPMS-XL SQUID magnetometer.

Physical Methods

Single crystal X-ray data sets were recorded as ω-scans at 0.3^{o} step width. Integration was performed with the Bruker SAINT Software package and absorption corrections were empirically applied using SADABS. The crystal structures were refined using the SHELXL[173] suite of programs and the graphical interface Olex2.[171] Images of the crystal structure were rendered using the crystal structure visualization software DIAMOND or CCDC Mercury.[217,312] All of the structures were solved by direct methods. Any remaining non-hydrogen atoms were located by alternating cycles of least squares refinements and difference Fourier maps. All hydrogen atoms were placed at calculated positions (riding model). Anisotropic thermal parameters were added for all non-hydrogen atoms. Magnetic susceptibility and magnetization measurements were collected using a Quantum Design MPMS-XL SQUID magnetometer. To prevent torqueing, the samples for magnetic measurements were prepared using crushed crystals immobilized in an eicosane matrix sealed in quartz tubes. DC magnetic susceptibility measurements were performed at an applied field of 1000 Oe over the temperature range 2-300 K. AC magnetic susceptibility measurements were performed in a 5 Oe oscillating field at operating frequencies of 1-1500 Hz. The data were corrected for diamagnetic contributions of the sample holder and as calculated from Pascal's constants.

Results and Discussion

Syntheses

The ligand $LiN(SiMe_3)_2$ was synthesized by reaction of excess *n*-BuLi with $HN(SiMe_3)_2$ followed by recrystallization from THF/hexanes mixture to yield the dimeric species $\{Li(THF)\text{-}\mu\text{-}N(SiMe_3)\}_2$ as confirmed by X-ray crystallography.[313,314] The ligand was reacted with a stoichiometric amount of $ErCl_3$ in THF, the solution was reduced to a paste and then finally extracted with pentane which led to the formation of light pink crystals of **27** upon concentration and cooling to -15 °C. Using this procedure, three distinct structural polymorphs were isolated (compounds **27, 28, and 29**). Rates of crystallization and the amount of time the crystals are stored under solvent appear to be the main factor in determining the structural type that is favored. A 10% diluted sample was prepared by combining an approximate 1:10 mass ratio of $[Li(THF)_4]\{Er[N(SiMe_3)_2]_3Cl\}\cdot 2(THF)$ with the corresponding yttrium analog in a THF/n-pentane mixture. Placing the solution in the freezer at -15 °C led to crystals of

$\{Er_{0.1}Y_{0.9}[(Me_3Si)_2N]_3\text{-}(\mu\text{-}Cl)[Li(THF)_3]\}\cdot$pentane (**30**). Only one structure type was obtained using the yttrium dilution (bridging chloride species) as confirmed by multiple reproducible isolations of the compound under the same conditions.

Related structural variance was observed for the thulium analogs depending on the synthetic conditions. Reactions of $\{Li(THF)\text{-}\mu\text{-}N(SiMe_3)\}_2$ with $TmCl_3$ leads to compound **31** which is the structural analog of compound **28** (erbium with two structural archetypes). Interestingly, during the reaction of $TmCl_3$ with $NaN(SiMe_3)_2$, a methyl group on the silyl appendage of the ligand was deprotonated, which led to the formation of a three-center bonding interaction between the CH_2 group, the thulium center, and a solvated sodium cation. This structural anomaly has been noted for other lanthanide analogs.[315,316] With prolonged storage in the glovebox which apparently led to some exposure to air/water, the new dimeric compound **33** was obtained which contains bridging oxo- ligands.

X-ray Crystallographic Studies

The crystal parameters and information pertaining to the data collection and refinement for **27-33** are summarized in Tables 5.1 and 5.2.

Table 5.1 Crystal structure refinement data for erbium compounds, **27-30**.

	27	**28**	**29**	**30**
Formula	C42H102ClEr LiN3O6Si6	$C_{71.5}H_{182}Cl_2Er_2Li_2N_6O_7Si_{12}$	$C_{30}H_{78}LiN_3O_3Si_6ClEr$	C35H84ClEr0.1Li N3O3Si6Y0.9
Formula weight	1123.46	1994.6	907.14	902.73
Temperature/ K	110	110	110	110
Crystal system	monoclinic	triclinic	monoclinic	monoclinic
Space group	P21/n	P-1	$P2_1/c$	C2/c
a/Å	17.207(3)	14.099(17)	25.559(9)	36.726(10)
b/Å	15.720(3)	16.035(19)	17.642(6)	15.611(4)
c/Å	23.973(4)	24.67(3)	22.497(8)	25.021(7)
α/°	90	89.315(18)	90	90
β/°	109.264(2)	84.852(18)	109.644(4)	131.469(3)
γ/°	90	78.593(18)	90	90
Volume/Å3	6121.5(19)	5445(11)	9554(5)	10749(5)
Z	4	2	8	8
ρcalcg/cm3	1.219	1.217	1.261	1.116
Radiation	MoKα (λ = 0.71073)	MoKα (λ = 0.71073)	MoKα (λ = 0.71073)	MoKα (λ = 0.71073)
2Θ range /°	2.558 to 56.464	2.592 to 50.11	2.862 to 46.168	2.96 to 53.38
Index ranges	-22 ≤ h ≤ 22, -20 ≤ k ≤ 20, -31 ≤ l ≤ 31	-16 ≤ h ≤ 16, -18 ≤ k ≤ 18, -29 ≤ l ≤ 29	-27 ≤ h ≤ 28, -19 ≤ k ≤ 19, -24 ≤ l ≤ 24	-45 ≤ h ≤ 45, -19 ≤ k ≤ 19, -31 ≤ l ≤ 31
Reflections collected	71170	64622	74855	56380
Independent reflections	14777 [Rint = 0.0397, R_{sigma} = 0.0348]	17236 [R_{int} = 0.1721, R_{sigma} = 0.2584]	13362 [R_{int} = 0.0680, R_{sigma} = 0.0500]	11025 [Rint = 0.0648, R_{sigma} = 0.0549]
Data/restraints /parameters	14777/600/650	17236/69/985	13362/390/847	11025/4/451
GOF	1.162	1.033	1.099	1.016
Final R indexes [all data]	R1 = 0.0880, wR2 = 0.1849	R_1 = 0.1498, wR_2 = 0.1862	R_1 = 0.1182, wR_2 = 0.2191	R1 = 0.0856, wR2 = 0.1343
Largest diff. peak/hole	1.88/-1.86	1.39/-0.81	4.70/-3.98	0.73/-0.71

$^{a}R = \sum||F_o|-|F_c||/\sum|F_o|$. $^{b}wR = \{\sum[w(F_o^2 - F_c^2)^2]/\sum w(F_o^2)^2]\}^{1/2}$. ^{c}Goodness-of-fit = $\{\sum[w(F_o^2- F_c^2)^2]/(n-p)\}^{1/2}$, where *n* is the number of reflections and *p* is the total number of parameters refined.

Table 5.2 Crystal structure refinement data for erbium compounds, **31-33**.

	31	**32**	**33**
Formula	$C_{69}H_{176}Li_2N_6O_7Si_{12}Cl_2Tm_2$	$C_{30}HN_3O_3NaSi_6ClTm$	$C_{20}H_{52}LiN_2O_3Si_4ClTm$
Formula weight	1961.87	810.79	656.86
Temperature/K	110	110	110
Crystal system	triclinic	monoclinic	monoclinic
Space group	P-1	$P2_1/n$	$P2_1/n$
a/Å	14.156(10)	29.234(6)	11.671(2)
b/Å	16.097(11)	12.137(2)	13.729(3)
c/Å	24.843(17)	29.246(6)	19.383(4)
α/°	89.221(8)	90	90
β/°	84.805(8)	113.887(2)	90
γ/°	78.729(8)	90	90
Volume/Å3	5529(7)	9488(3)	3105.7(11)
Z	2	8	4
ρcalcg/cm3	1.178	1.135	1.4047
F(000)	2068	3112	1353
Radiation	MoKα (λ = 0.71073)	MoKα (λ = 0.71073)	Mo Kα (λ = 0.71073)
2Θ range /°	2.58 to 52.33	2.554 to 55.012	3.64 to 57.8
Index ranges	$-17 \le h \le 17$, $-19 \le k \le 19$, $-30 \le l \le 30$	$-34 \le h \le 37$, $-15 \le k \le 15$, $-37 \le l \le 37$	$-15 \le h \le 15$, $-18 \le k \le 18$, $-25 \le l \le 25$
Reflections collected	45709	86079	21986
Independent reflections	19300 [R_{int} = 0.1592, R_{sigma} = 0.3501]	21682 [R_{int} = 0.0839, R_{sigma} = 0.0832]	5510 [R_{int} = 0.0336, R_{sigma} = 0.0481]
Data/restraints/parameters	19300/578/939	21682/0/793	5510/0/291
Goodness-of-fit on F2	0.81	1.043	0.887
Final R indexes [all data]	R_1 = 0.1805, wR_2 = 0.2160	R_1 = 0.1092, wR_2 = 0.1650	R_1 = 0.0278, wR_2 = 0.0477
Largest diff. peak/hole /e Å-3	1.49/-1.50	0.93/-1.39	0.90/-0.39

$^{a}R = \sum||F_o|-|F_c||/\sum|F_o|$. $^{b}wR = \{\sum[w(F_o^2 - F_c^2)^2]/\sum w(F_o^2)^2]\}^{1/2}$. ^{c}Goodness-of-fit = $\{\sum[w(F_o^2 - F_c^2)^2]/(n-p)\}^{1/2}$, where n is the number of reflections and p is the total number of parameters refined.

[Li(THF)$_4$]{Er[N(SiMe$_3$)$_2$]$_3$Cl}·2THF (27). Compound **27** crystallizes in a monoclinic space group P21/n (Figure 5.1, Table 5.1). The Er1-N bond distances are in the 2.231-2.251 Å range which is slightly longer than the reported ones for Er[N(SiMe$_3$)$_2$]$_3$;[307] the Er1-Cl bond distance is 2.528(2) Å. The N-Er1-N bond angles are flattened with an average N-Er-N angle of 115.98(19)°, which is closer to an ideal trigonal planar angle than in the case of Er[N(SiMe$_3$)$_2$]$_3$ (113.4°); the average Cl-Er-N bond angle is 101.71(14)°. The closest Er-Er distance is 11.175(2) Å.

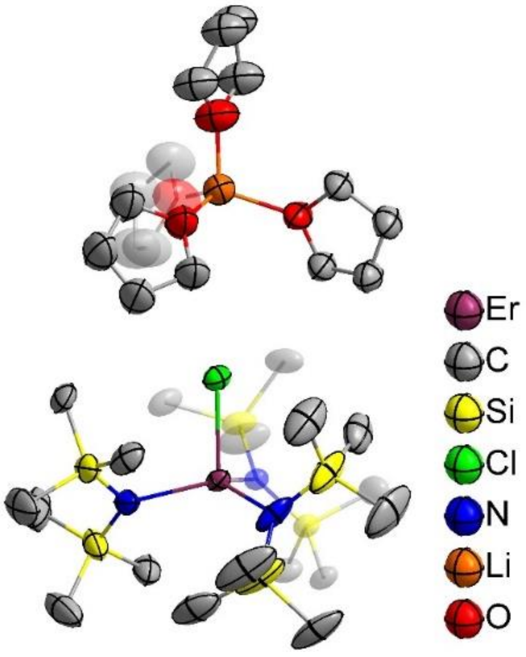

Figure 5.1 Thermal ellipsoid plot of compound **27** at the 50% probability level. Hydrogen atoms and disordered solvent molecules are omitted for the sake of clarity.

{[(Me$_3$Si)$_2$N]$_3$Er(μ-Cl)Li(THF)$_3$·[Li(THF)$_4$]{Er[N(SiMe$_3$)$_2$]$_3$Cl}·2THF} (28). Compound **28** which contains two different structural archetypes, Figure 5.2, crystallizes in the low symmetry triclinic space group, P-1. The structures differ by the presence of a bridging versus terminal chloride. For the bridging chloride molecule the average Er-N bond distance is 2.234(10) Å. The Er-Cl bond distance is 2.580(4) Å. The average N-Er-N bond angle is 116.4(4)$^{o.}$ The average Cl-Er-N bond angle is 101.1(3)^{o}. The Er-Cl-Li bond angle is 170.0(6)^{o}. For the molecule with the terminal chloride, the average Er-N bond distance is 2.250(10) Å. The Er-Cl bond distance is 2.547(4) Å. The average N-Er-N bond angle is 115.9(4)^{o}. The average Cl-Er-N bond angle is 101.8(3)^{o}. As such, each structural type exhibits similar goemetries despite different connectivity. Taken together (averaging both structure types), the overall Er-N bond distance is 2.242(7) Å. The average Er-Cl bond distance is 2.564(3) Å. The average N-Er-N and Cl-Er-N bond angles are 116.2(3)^{o} and 101.4(2)^{o}, respectively. The closest Er-Er contact is 10.722(11) Å. The percent difference relative to compound **27**, |compound **27** – compound **28**|/compound **27**, is as follows: d_{Er-N} 0%; d_{Er-Cl} 1.4%; B.A.$_{N-Er-N}$ 0.14%; and B.A.$_{Cl-Er-N}$ 0.27%, where d and B.A. represent bond distance and bond angle, respectively.

[(Me$_3$Si)$_2$N]$_3$Er(μ-Cl)Li(THF)$_3$ (29). Compound **29**, Figure 5.3, crystallizes in a monoclinic space group, which is consistent with one structural archetype. The structure consist of only bridging chloride anions. The average distances and angles in comparison to **27** are given as [value (relative percent error)]: d_{Er-N} [2.235(12) Å (0.26%)]; d_{Er-Cl} [2.574(4) Å (1.8%)]; B.A.$_{N-Er-N}$ [116.0(4)^{o} (0.03%)]; B.A.$_{Cl-Er-N}$ [101.7(3) ^{o} (0%)]. Again the geometry for compound **29** is reasonably similar to compound **27** with the Er-Cl bond being the most sensitive change, as the electrostatic solvated lithium cation bond is created. The closest Er-Er contact is 11.170(11) Å.

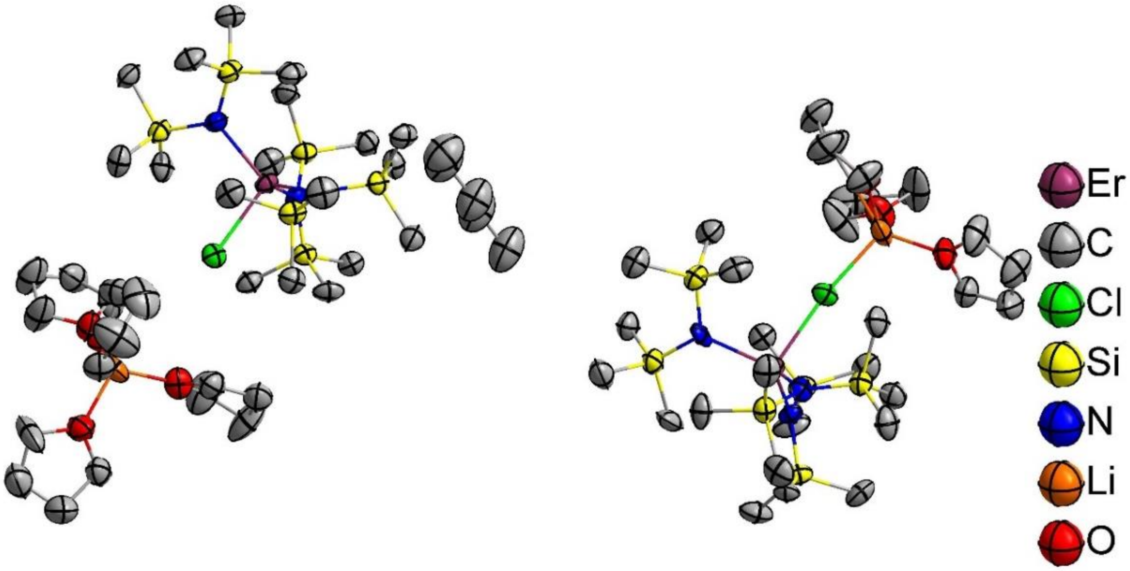

Figure 5.2 Crystal structure of $\{[(Me_3Si)_2N]_3Er(\mu\text{-}Cl)Li(THF)_3\cdot[Li(THF)_4]\{Er[N(SiMe_3)_2]_3Cl\}\cdot 2THF\}$, **28**, in which two different structure types, *viz*., with bridging and terminal chloride connectivities co-crystallize.

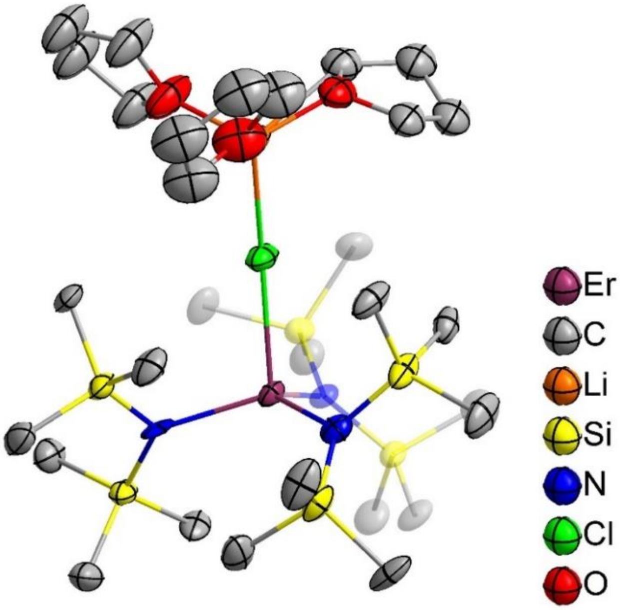

Figure 5.3 Crystal structure of $[(Me_3Si)_2N]_3Er(\mu\text{-}Cl)Li(THF)_3$, **29**, drawn at 50% probability in which there is only one structure type with a bridging chloride.

$\{Er_{0.1}Y_{0.9}[N(SiMe_3)_2]_3(\mu\text{-}Cl)[Li(THF)_3]\}\cdot$pentane (30). Single crystal XRD structural analysis of **30** revealed an analogous crystal structure to what was observed for **29** in that the $[Li(THF)_3]^+$ cation is connected to the Cl^- bridge, Figure 5.4. The average distances and angles in comparison to **27** are: $d_{Er\text{-}N}$ [2.300(15) Å (2.63%)]; $d_{Er\text{-}Cl}$ [2.388(11) Å (5.54%)]; B.A.$_{N\text{-}Er\text{-}N}$ [113.4(7) ^{o} (2.20%)]; B.A.$_{Cl\text{-}Er\text{-}N}$ [105.1(6) ^{o} (3.35%)]. As discussed in the magnetic studies section, the yttrium dilution causes a substantial change in the geometry of the compound, which may have an effect on the magnetic properties.

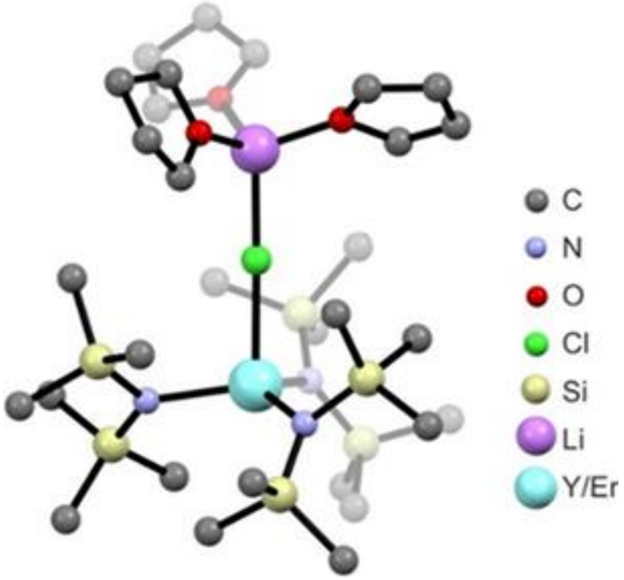

Figure 5.4 Crystal structure of compound **30**. Hydrogen atoms omitted for the sake of clarity.

$\{[(Me_3Si)_2N]_3Tm(\mu\text{-}Cl)Li(THF)_3\cdot[Li(THF)_4]\{Tm[N(SiMe_3)_2]_3Cl\}\cdot 2THF\}$ (31). The thulium analog depicted in Figure 5.5 of compound **28** crystallizes in a triclinic unit cell. For the bridging molecule, the average Tm-N bond distance is 2.246(10) Å. The Tm-Cl bond distance is 2.584(4) Å. The average N-Tm-N bond angle is 116.4(4)° and the average N-Tm-Cl bond angle is 101.0(3)°. The Tm-Cl-Li bond angle is substantially bent at 169.9(8)°. For the molecule with the terminal chloride, the average Tm-N bond distance is 2.260(10) Å. The Tm-Cl bond distance is 2.562(4) Å. The average N-Tm-N bond angle is 116.4(4)°. The average Cl-Tm-N bond angle is 101.05(3)°. The shortest Tm-Tm through space distance is 10.743(7) Å. Overall, the geometry of compound **31** is very similar to compound **28**.

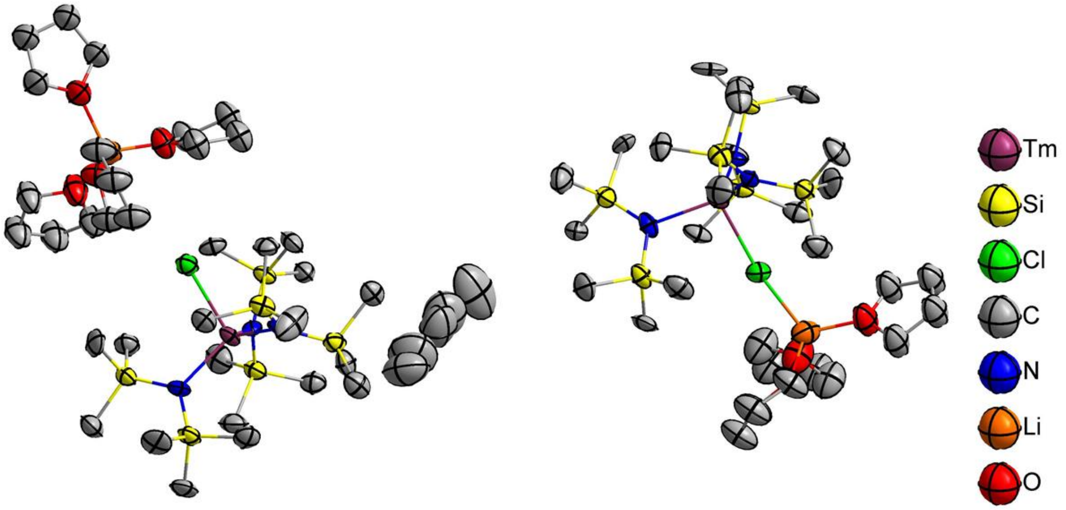

Figure 5.5 Thermal ellipsoid plot for **31** at the 50% probability level. Hydrogen atoms omitted for the sake of clarity. Both structural types are present in the same crystal along with a pentane solvent molecule.

[Na(THF)$_3$((Me$_3$Si)$_2$N)$_2$Tm(CH$_2$)SiMe$_2$N(SiMe$_3$)] (32). The bonding involving one of the three amide ligands changes the symmetry of compound **32**, Figure 5.6. The Tm-N bond distance containing the deprotonated methyl group is slighty shorter than the remain two bond distances at 2.201(6) Å, 2.261(6) Å, and 2.236(6) Å, respectively. The same holds true for the through-space distance between the Tm center and silicon atoms. The silcon bearing the CH_2 group is located 2.946(2) Å from the Tm ion. The remaining silicon distances are 3.260 (2) Å, 3.393(2) Å, 3.462(2) Å, 3.483(2) Å, and 3.622(2) Å. Due to steric strain, one of the N-Tm-N bond angles is quite different from the other two. The bond angles are 111.66(2)°, 118.07(2)°, and 119.74(2)°. The Tm-CH_2 and Na-CH_2 bond length are 2.410(7) Å and 2.612(8) Å, respectively, which are similar to other reported lanthanide compounds. The shortest Tm-Tm through space distance is 10.646(2) Å.

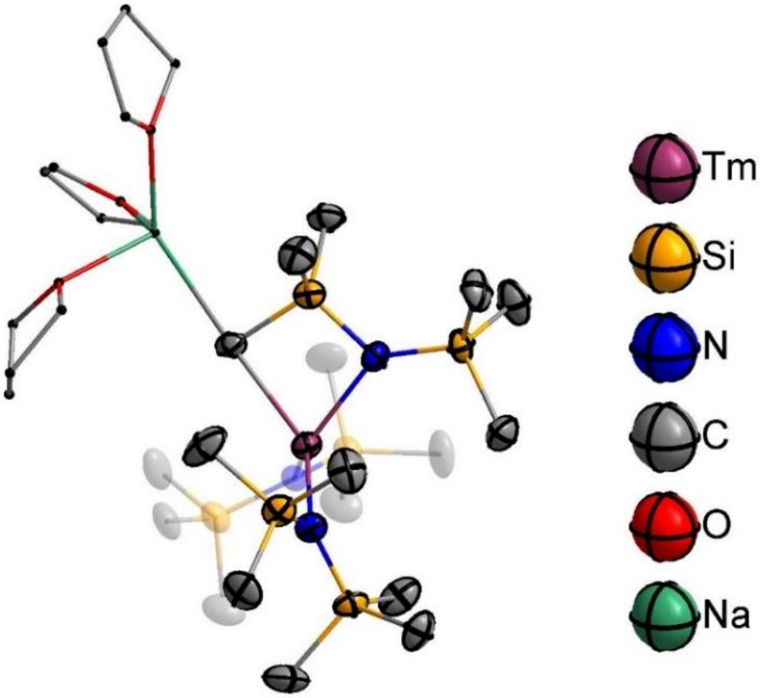

Figure 5.6 Thermal ellipsoid plot for compound **32** at the 50% probability level. Hydrogen atoms omitted for the sake of clarity.

$[Tm(N(SiMe_3)_2)_2]_2(\mu_2\text{-}OLi(THF)_2)_2$ (33). After prolonged storage in the glovebox freezer, decomposition of **31** occurs to form the dioxygen bridged dinuclear compound **33**. The molecule crystallizes in a monoclinic space group, $P2_1/n$, and sits on an inversion center. The asymmetric unit includes one Tm(III) ion bridged to one oxide ligand, two HMDS ligands, and a lithium cation solvated by two THF molecules. The molecule grows to complete the dinuclear complex shown in Figure 5.7. The average Tm-N bond length is 2.284(3) Å and the Tm-O bond length is 2.103(7) Å.

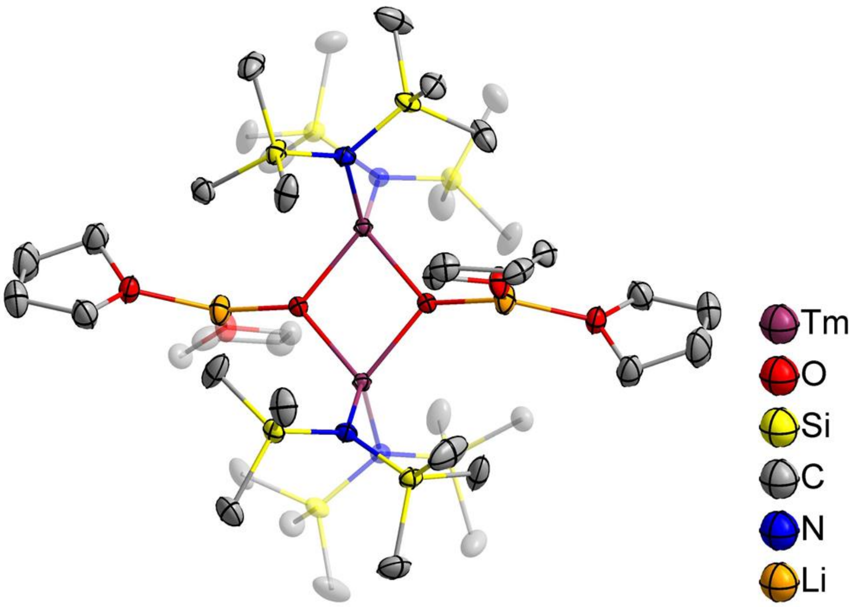

Figure 5.7 Thermal ellipsoid plot for compound **33** at the 50% probability level. Hydrogen atoms omitted for the sake of clarity.

Magnetic Studies

$[Li(THF)_4]\{Er[N(SiMe_3)_2]_3Cl\}\cdot 2THF$ (27). The static magnetic properties of **27** were measured on a sample of crushed crystals using a MPMS SQUID magnetometer under a

1000 Oe DC field. The temperature dependence of the DC magnetic susceptibility is very similar to previously reported Er compounds.[76,128,130,294,295] The room temperature χT value of 11.47 emu/mol·K, Figure 5.8, is consistent with an isolated Er(III) center (J = 15/2, g = 1.2 with the expected χT value of 11.48 emu/mol·K). For lanthanide complexes, the expected magnetic susceptibility was assessed using equations 5.1 and 5.2.[10,317] Equation 5.1 is the general equation for magnetic susceptibility of lanthanide ions, where the first term is a free-ion approximation of molar susceptibility and the second term accounts for mixing between ground and excited states through Zeeman perturbation. χ is the magnetic susceptibility, J is the spin-orbit quantum number, N is Avogadro's number, μ_B is the Bohr magneton, k is the Boltzmann constant, g is the Landé g-value, λ is the spin-orbital coupling constant, and T is temperature. Equation 5.2 is the general equation for calculating g_J value for lanthanide ions in the Russell-Saunders coupling scheme.

$$\chi(\mathrm{J}) = \frac{N g_J^2 {\mu_B}^2 J(J+1)}{3kT} + \frac{2N{\mu_B}^2(g_J-1)(g_J-2)}{3\lambda} \qquad \textbf{Equation 5.1}$$

$$g_{J=}\ \frac{3}{2} + \frac{S(S+1)-L(L+1)}{2J(J+1)} \qquad \textbf{Equation 5.2}$$

At lower temperatures the χT value slowly decreases to reach 9.55 emu/mol·K at 2K which is attributed to the depopulation of m_J sublevels and magnetic anisotropy.

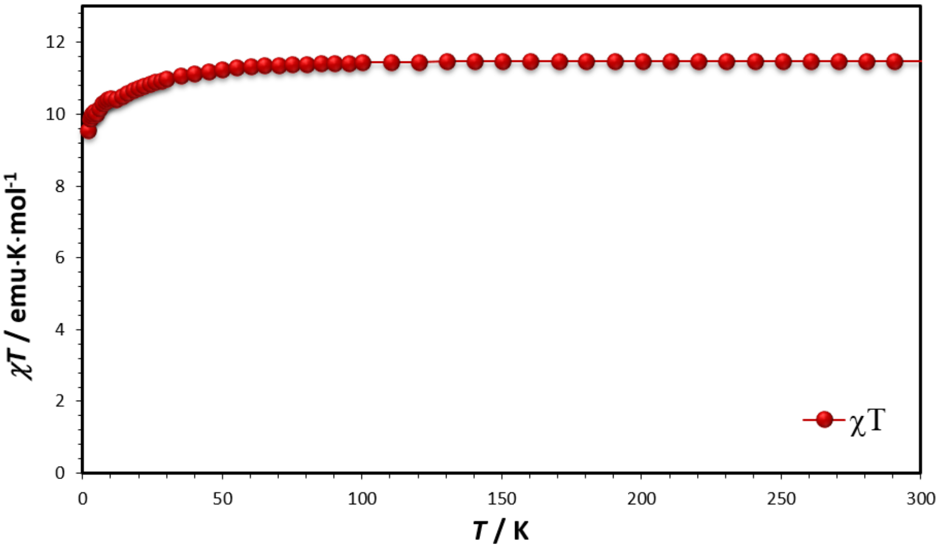

Figure 5.8 DC susceptibility χT vs T plot for **27**.

The dynamic properties of **27** were investigated using AC magnetic susceptibility measurements over the frequency range 1-1500 Hz and temperature range 1.8 – 11 K. The AC magnetic susceptibility was plotted as a function of temperature, Figure 5.9, and as a function of frequency, Figure 5.10. The out-of-phase AC magnetic susceptibility versus frequency plot recorded in the 1.8 – 11 K range under zero applied DC magnetic field reveals slow magnetic relaxation behavior typical of SMMs. The relaxation times obtained from fitting the AC magnetic susceptibility data using the generalized Debye model[13] were plotted vs. $1/T$ to give an Arrhenius plot with two obvious regimes: a temperature dependent regime above approximately 5 K and a temperature independent regime below 5 K, Figure 5.10 inset. The selected high temperature, linear region (7.5 – 11 K), of the Arrhenius plot was used to calculate the thermal energy barrier to the magnetization reversal $\Delta E_{eff}/k_B = 63.3$ K and $\tau_0 = 1.07 \cdot 10^{-7}$ s. The low-temperature regime is expected to be controlled by quantum tunnelling effects (direct relaxation process).

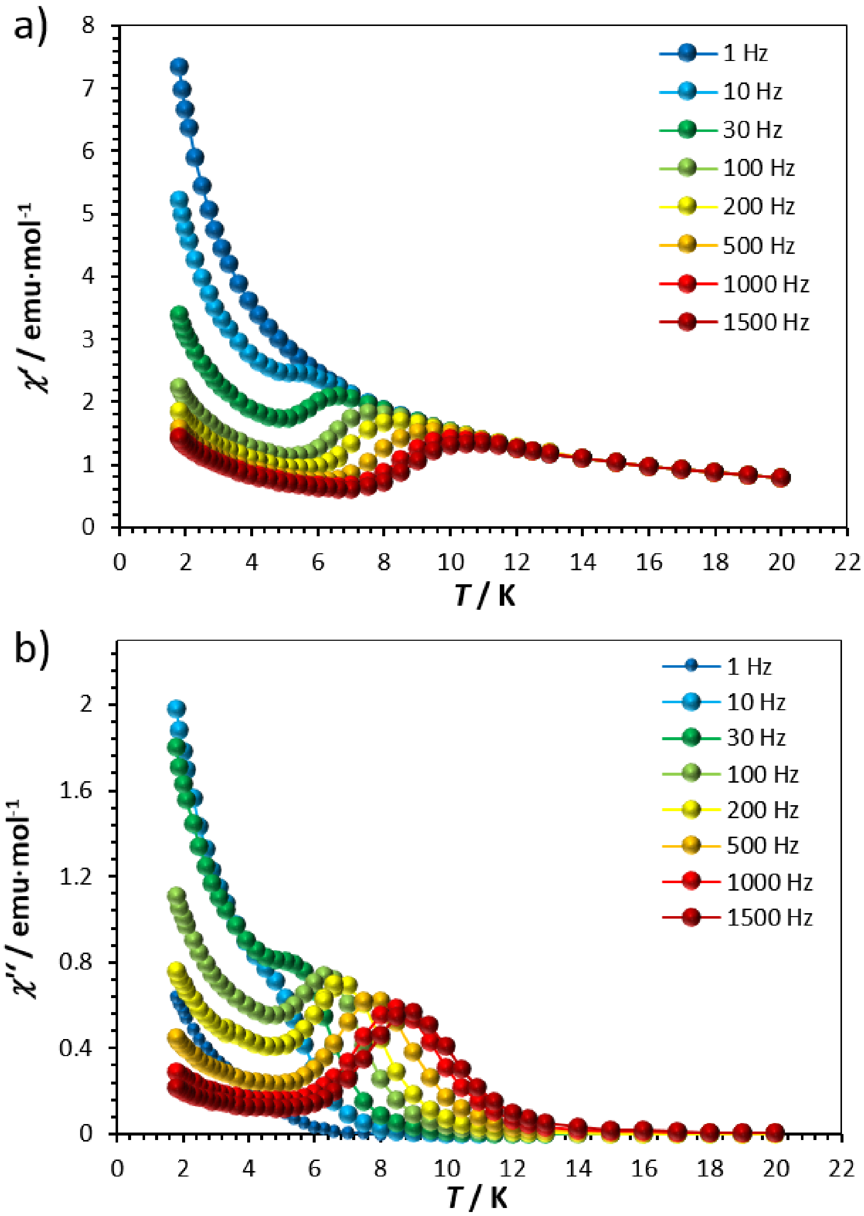

Figure 5.9 (a) The χ' vs T and (b) χ'' vs T plot in zero-applied DC field for compound **27**, which exhibits large adiabatic susceptibility.

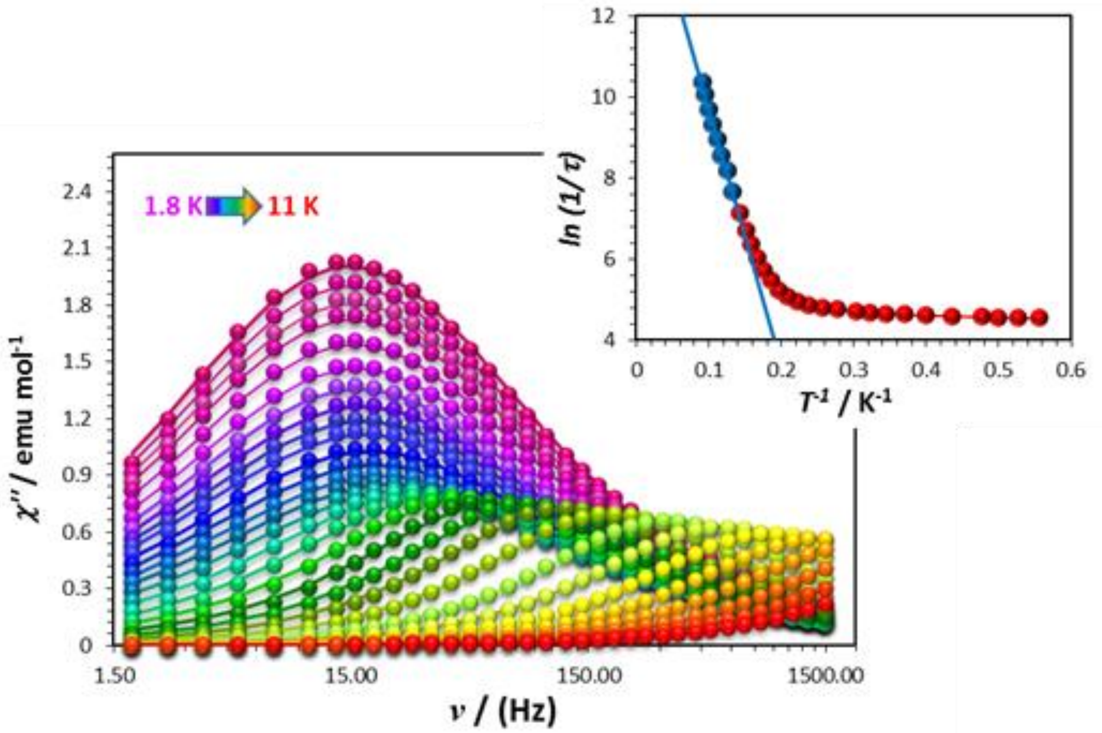

Figure 5.10 Imaginary component of the AC magnetic susceptibility data plotted vs frequency for **27**. Lines represent fitting of the experimental data at different temperatures using the generalized Debye model. Inset: Arrhenius plot of ln(1/τ) vs T^{-1}. Fitting of the thermal regime is represented by linear fit of selected blue data points.

The Cole-Cole plot, Figure 5.11, suggests the existence of only one thermal relaxation process, as evidenced by the semi-circle overlay of χ'' and χ' and α values below 0.29. On the other hand, because the Arrhenius plot does exhibit some curvature below 6.3 K, perhaps another relaxation pathway is also operative. Data in the entire 1.8-11 K temperature range were analysed by equation 5.3.[318]

$$\tau^{-1} = AT + C + BT^{n} + \tau_{o}^{-1} exp\left(\frac{-\Delta E_{eff}}{k_{B}T}\right)$$ **Equation 5.3**

where $AT + C$, BT^{n}, and $\tau_o^{-1}\exp(-\Delta E_{\mathrm{eff}}/k_BT)$ represent direct, Raman, and Orbach relaxation processes, respectively. In order to fit the Arrhenius plot to eq. 1, the values of τ_o and

$\Delta E_{eff}/k_B$ were fixed based on the linear fit to the thermal regime (7.0 - 9.5 K; red dotted line, Figure 5.12). The values of the A and C parameters were also fixed based on the linear fit to the τ^{-1} vs T^1 dependence (direct process; gray dotted curve, Figure 5.12) in the range of 1.8 - 3.1 K. With these restraints, the temperature range 1.8 - 9.5 K was fitted using eq. 1 assuming n = 5, 7, or 9 and letting the B parameter to vary freely. The best fit was obtained for n = 5 and B = 0.00585 $s^{-1}K^{-5}$, Figure 5.12. Thus we conclude that the curvature of the Arrhenius plot is due to Raman relaxation.

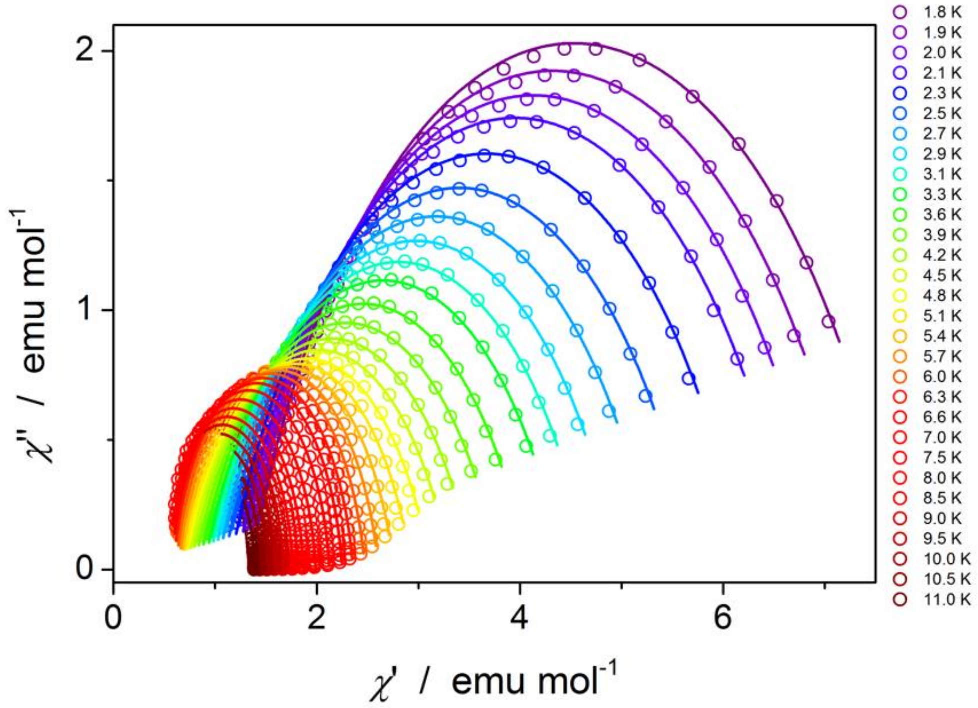

Figure 5.11. Cole-Cole plot of [Li(THF)$_4$]{Er[N(SiMe$_3$)$_2$]$_3$Cl}·2THF.

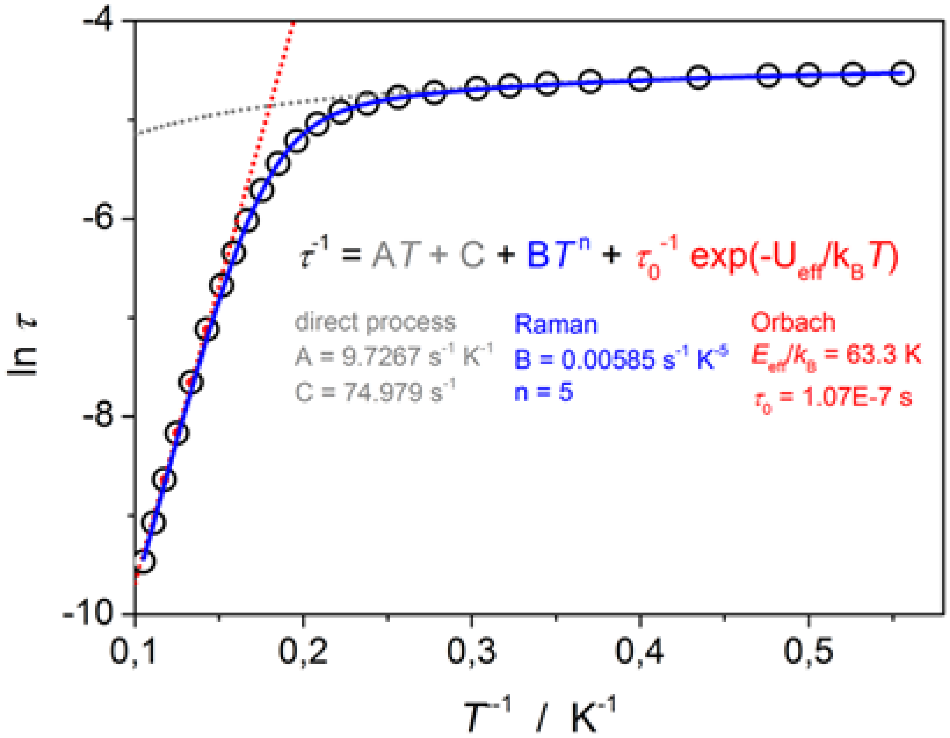

Figure 5.12 Fitting of Arrhenius plot for **27** based on equation 5.3 and relaxation times obtained by simultaneous fitting of χ' and χ'' vs υ plots. Red dotted line represents fitting of Orbach/thermal regime. Gray dotted line represents fitting of low temperature regime. The variables obtained from these two fits were then fixed in the fitting of the full temperature regime (blue line), the curved part of which represents the Raman relaxation regime.

The AC data indicate very slow magnetic relaxation at temperatures below 3.1 K, on the order of 100 s, therefore hysteresis measurements were performed at a conventional sweep rate of 3.46 mT/s. The shape of the hysteresis loop at 1.8 K, Figure 5.13, for **27** is best described as "waist-restricted" or "butterfly-like", similar to what was observed for other Er(III) SMMs.[76,130] A tunneling feature (reflection point) is observed at both negative and positive fields.

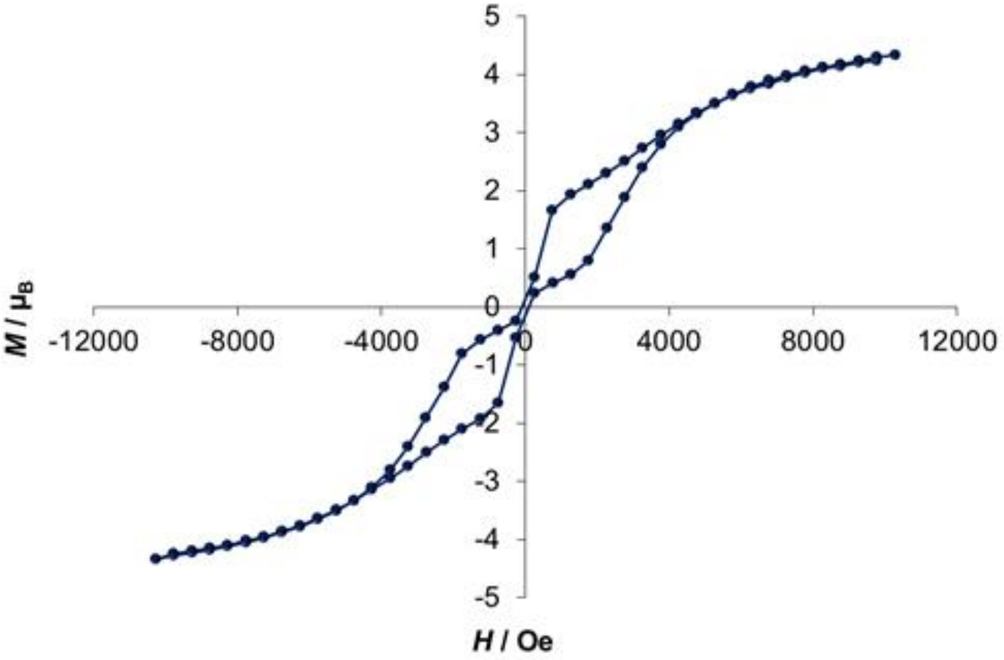

Figure 5.13 Magnetic hysteresis loop for **27** collected at 1.8 K and at a 3.46 mT/s sweep rate.

Due to the structural variance of compound **27**, different sample preparation was employed to demonstrate that the magnetic data are determined by inner sphere coordination to the erbium center. As shown in Figure 5.14, solid-state samples that had been pumped under vacuum exhibit the same blocking temperatures as crystals immobilized in *n*-pentane. We believe this to be solid evidence that the magnetic properties of the different analogs are identical since we could not achieve structural control over which analog was synthesized.

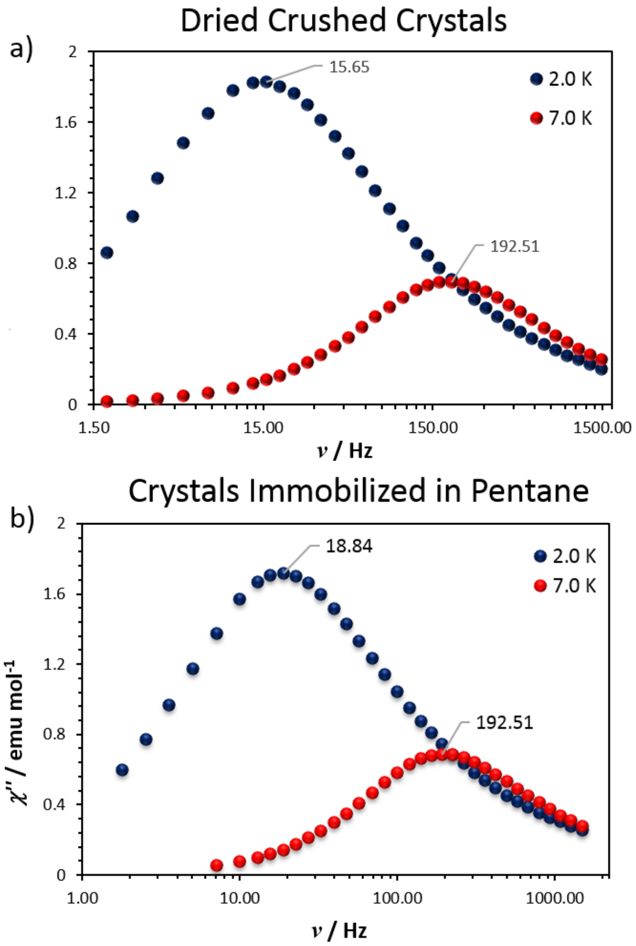

Figure 5.14 Comparison of χ'' vs. ν dependences at 2 K and 7 K by two different preparative methods of compound **27**. The magnetic data shown in (a) were collected on crushed crystalline solid that was dried and measured in a plastic bag, while (b) were collected on fresh crystals immobolized in pentane and sealed in a quartz EPR tube.

$\{Er_{0.1}Y_{0.9}[N(SiMe_3)_2]_3(\mu\text{-}Cl)[Li(THF)_3]\}\cdot$pentane (30). Quantum tunneling is enhanced by weak intermolecular dipole-dipole interactions which can be suppressed by dilution in a diamagnetic matrix or by applying an external DC field. AC measurements were performed on crushed crystals of the diluted sample, **30**, revealing the retention of the out-of-phase signal with partial suppression of the quantum tunneling regime, Figure 5.15 and Figure 5.16.

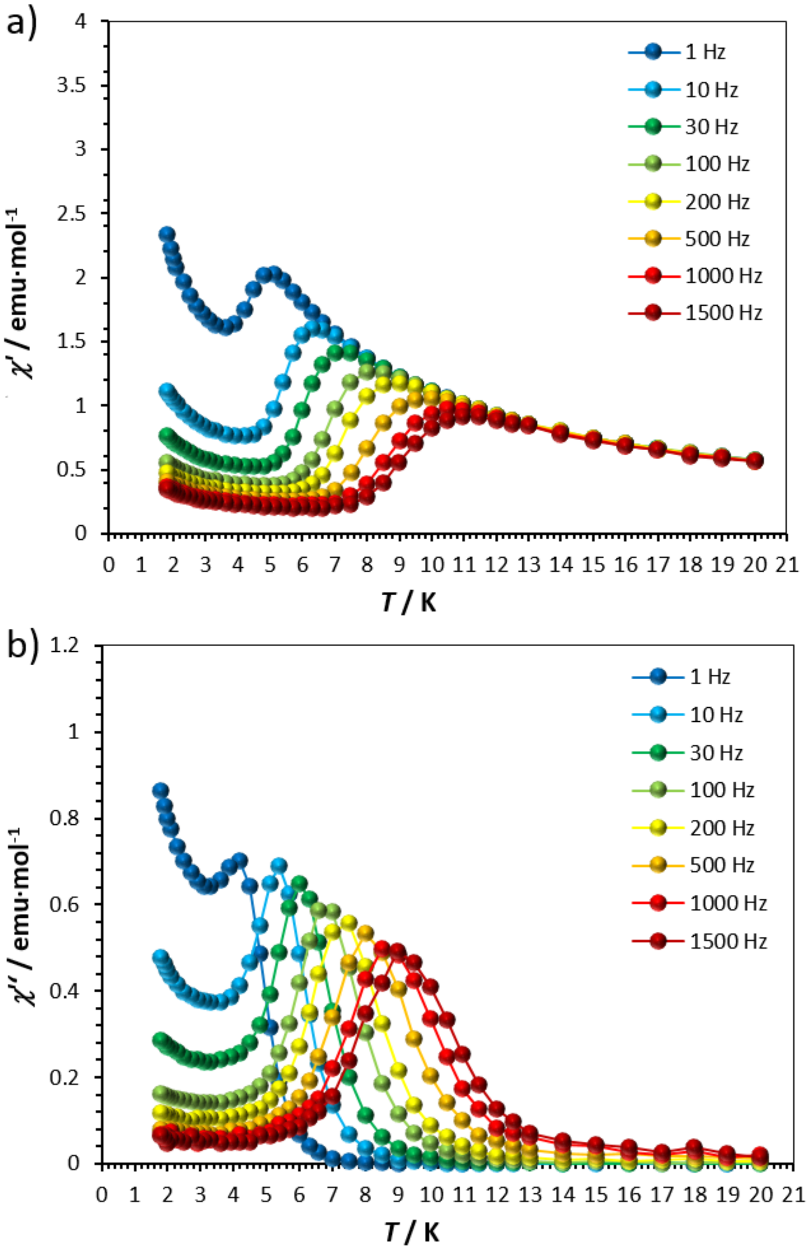

Figure 5.15 (a) The χ' vs T and (b) χ'' vs T plot of **30** in zero-applied DC field showing partial suppression of the quantum tunnelling regime.

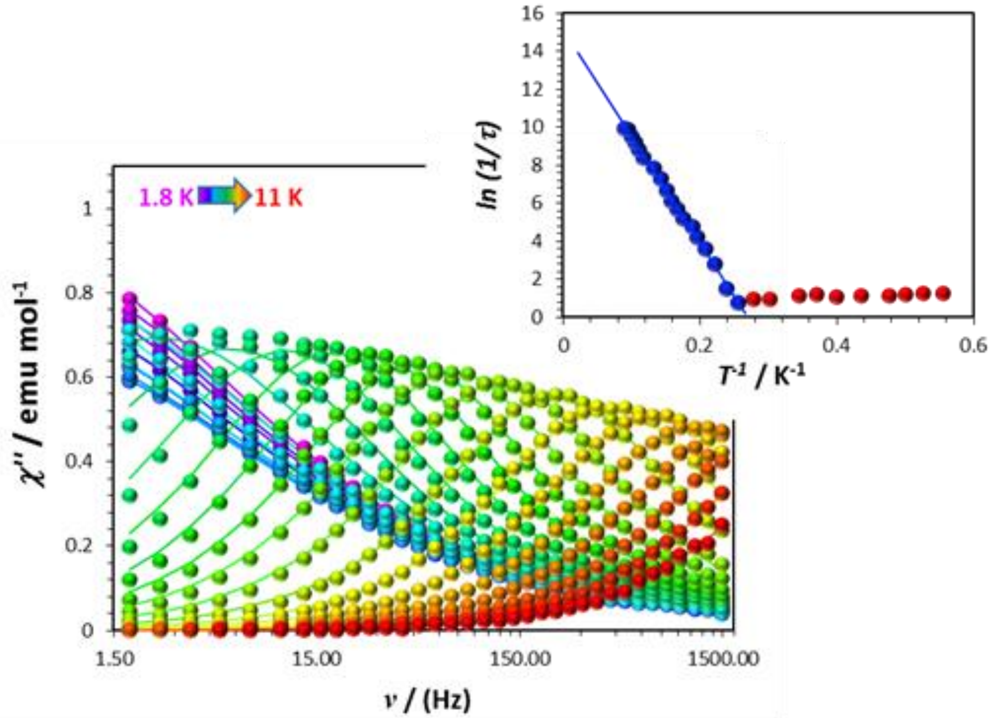

Figure 5.16 Imaginary component of the AC susceptibility plotted vs. frequency for **30**. Lines represent fitting of the experimental data at different temperatures using the generalized Debye model. Inset: Arrhenius plot of ln(1/τ) vs T^{-1}. The blue line is the best fit of the thermal regime (blue data points).

These results support the molecular nature of the slow magnetic relaxation in **27**. The AC data shown in Figure 5.16 were fitted using a generalized Debye model.[10,13] The resulting relaxation times were plotted versus 1/*T* and the data reveal that there is a temperature dependent regime above 3.8 K and a temperature independent one below 3.8 K. The high-temperature region (above 3.8 K) was fitted using the Arrhenius law, which resulted in an estimated effective energy barrier to the magnetization reversal of $\Delta E_{eff}/k_B$ = 55.8 K and pre-exponential factor $\tau_0 = 2.84 \cdot 10^{-7}$ s. The estimated effective energy barriers for **27** and **30** are different by ~7-8 K. We attribute this difference to the slightly altered coordination sphere of the two analogs as well as the selection of points used to ascertain the energy barrier. The low-temperature regime for **30** is most likely controlled by quantum tunneling of the magnetization. Repeating the AC measurements of **30** under a 1000 Oe static DC field shows a further suppression of the quantum tunneling as expected, Figure 5.17. The yttrium dilution sample exhibits sharper hysteresis up to 3 K, Figure 5.18.

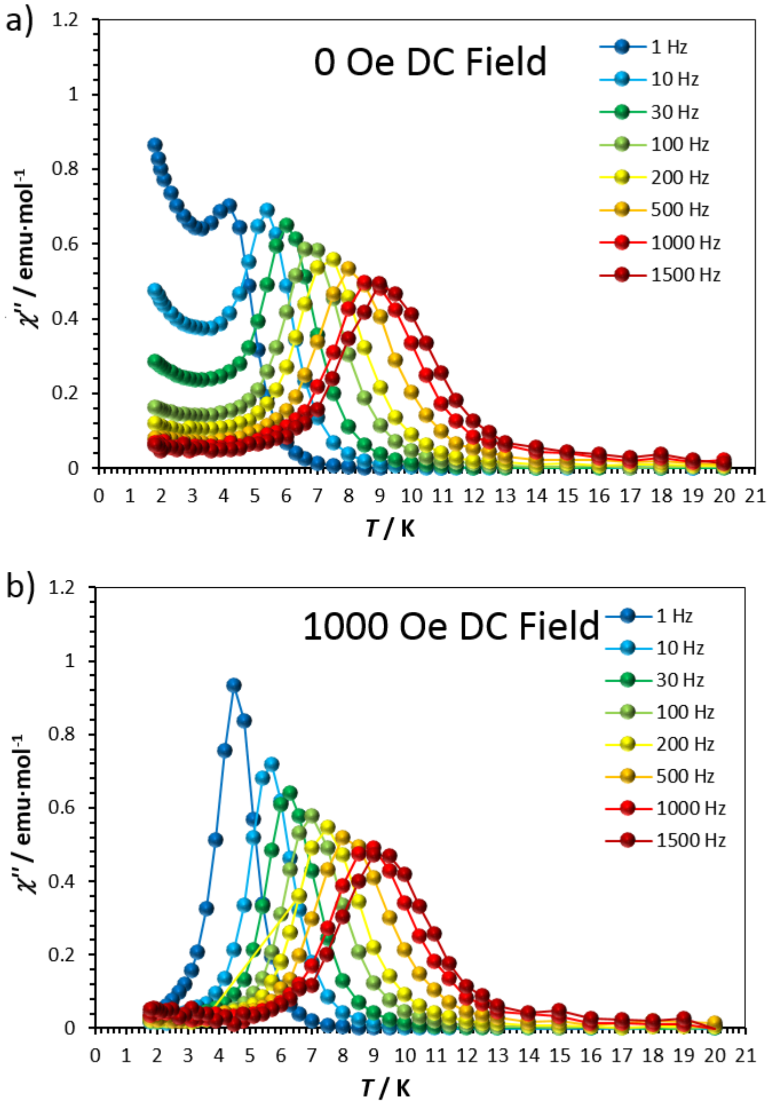

Figure 5.17 The (a) χ" vs T plot of **30** in zero-applied DC field and (b) in a 1000 Oe DC field.

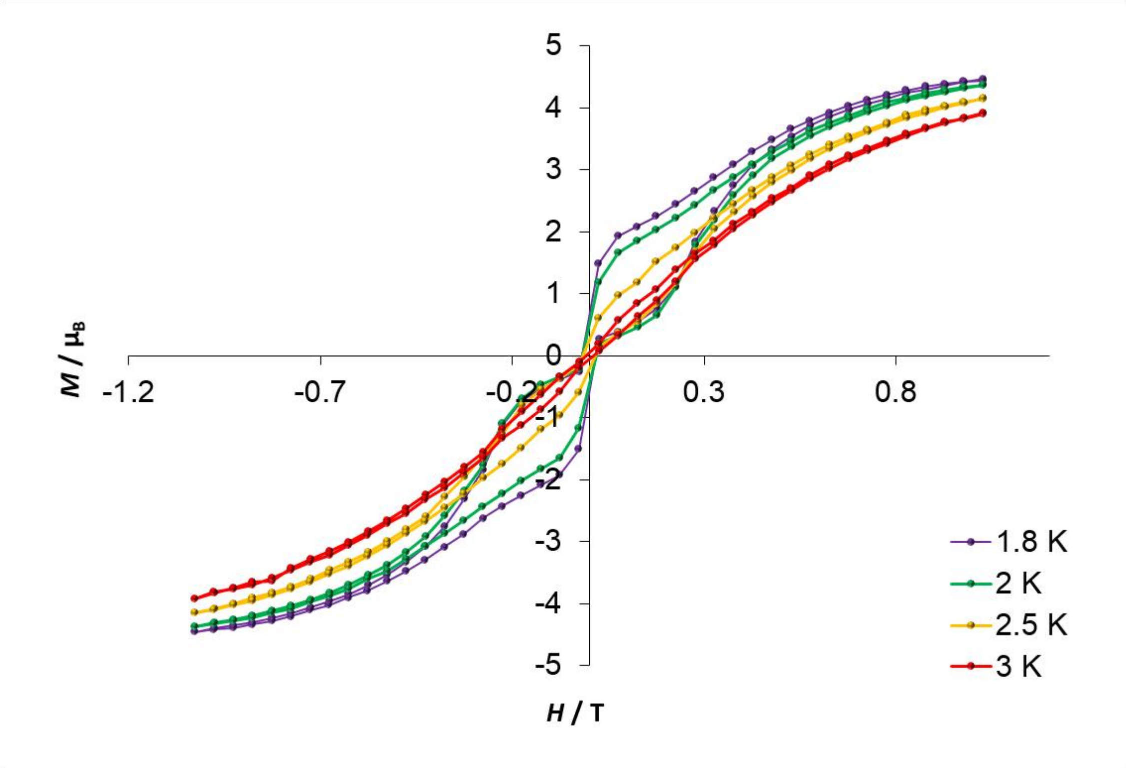

Figure 5.18 Hysteresis loops of compound **30** from 1.8 to 3 K.

$\{[(Me_3Si)_2N]_3Tm(\mu\text{-}Cl)Li(THF)_3\cdot[Li(THF)_4]\{Tm[N(SiMe_3)_2]_3Cl\}\cdot 2THF\}$ (31). The static magnetic properties of **31** were measured on a sample of crushed crystals using a MPMS SQUID magnetometer under a 1000 Oe DC field. The magnetic susceptibility of compound **31** is shown in Figure 5.19. The compound exhibits similar behavior to the erbium analog in that the χT product slowly decreases as the temperature is lowered. The low susceptibility as compared to the erbium analog is clear evidence of the lower magnetic moment of the thulium ion (S = 1, L = 5). As compared to the expected value of 7.15 emu·K/mol from equations 5.1 and 5.2, the slightly high χT value at room temperature of 7.73 emu·K/mol is attributed to solvent loss which leads to a minor mass error. The crystals are highly unstable and will readily lose solvent when removed from the mother liquor.

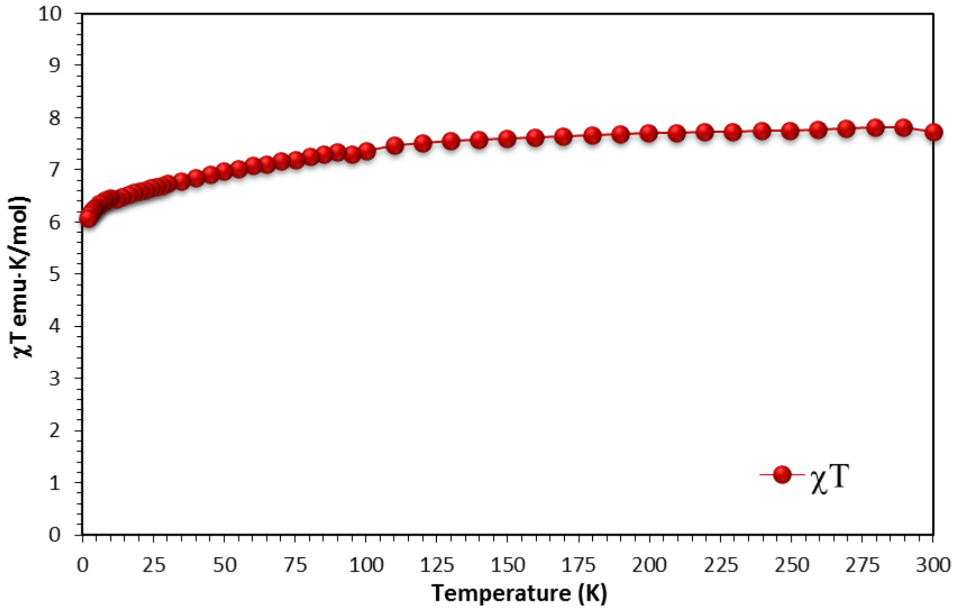

Figure 5.19 DC susceptibility χT vs T plot for **32** from 300-2 K.

The dynamic susceptibility of **31** was measured in anticipation of observing similar SMM behavior as found for **27**. Despite the fact that thulium possesses more prolate f electron density, compound **31** only exhibits the beginning of an out-of-phase signal in the imaginary component of the AC susceptibility signal under an applied DC field of 1000 Oe, Figure 5.20.

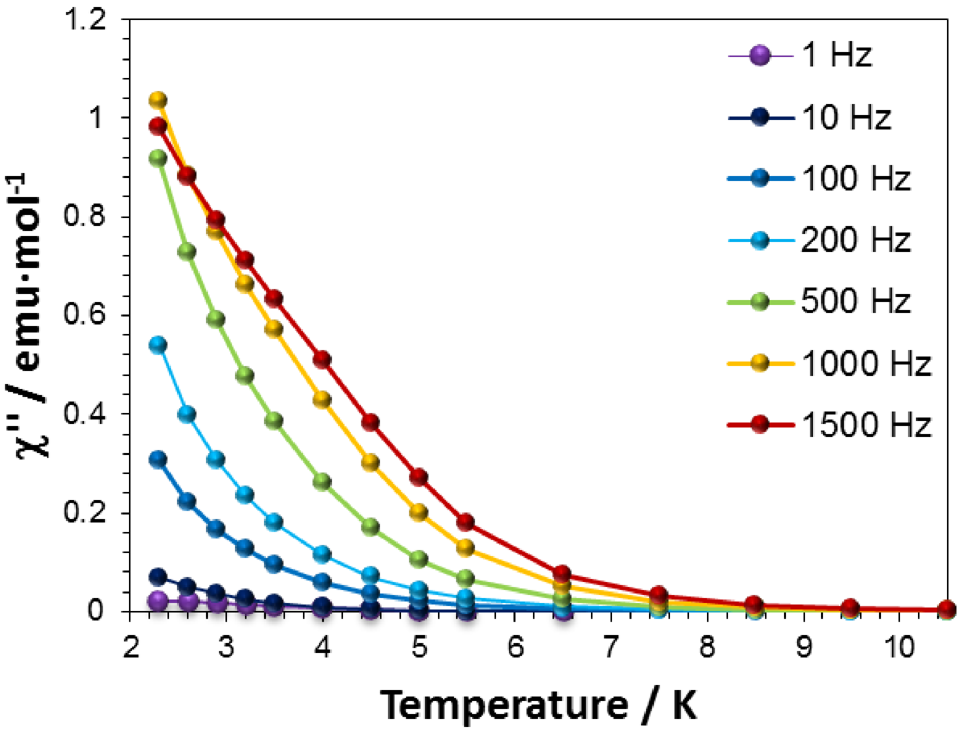

Figure 5.20 (a) The χ“ vs T plot in 1000 Oe DC field for compound **32**, which exhibits the beginning of out-of-phase signals at low temperature.

In order to determine a possible barrier height to the reversal of the magnetization, the ratio of χ”/ χ’ was plotted using Kramers-Kronig equation 5.4.[319] Under these conditions, the thulium analog was found to have a U_{eff}/k_B of ~12 K, Figure 5.21 and Table 5.3. This value is conservative, as the points selected are in the region that marks the beginning of non-zero slope.

$$\ln\frac{\chi''}{\chi'} = \ln(2\pi\upsilon\tau_o) + \frac{U_{eff}}{kT}$$ **Equation 5.4**

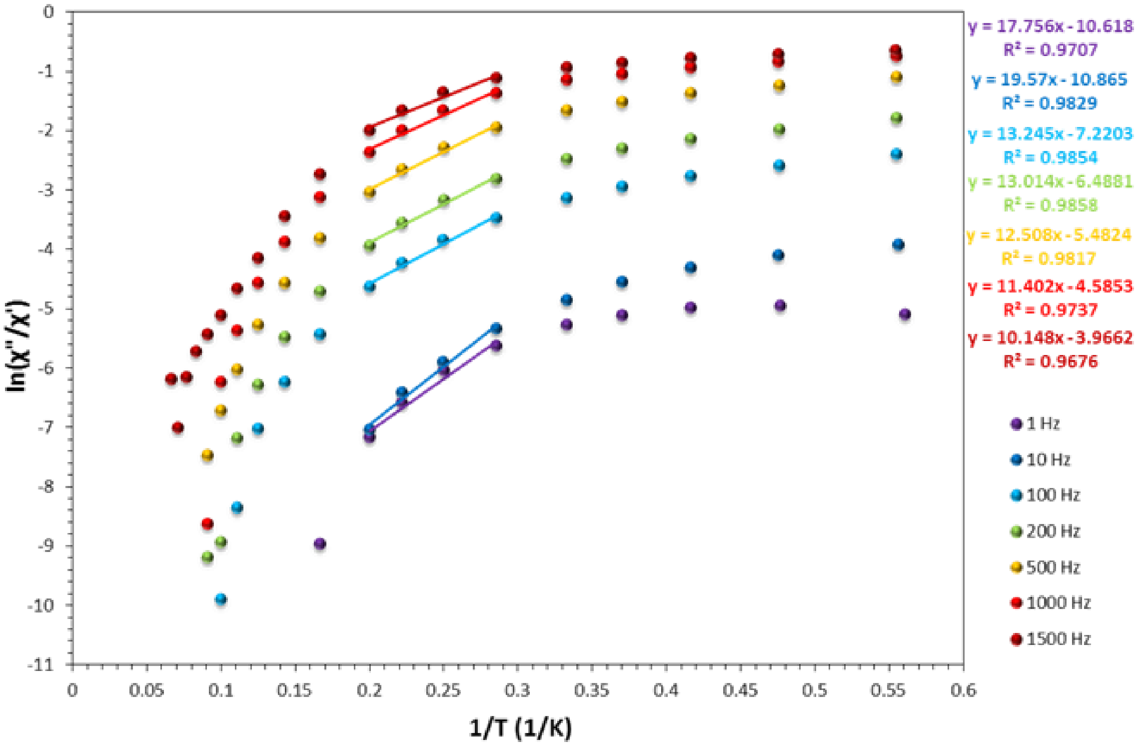

Figure 5.21 (a) The χ“ vs T plot in 1000 Oe DC field for compound **32**, which exhibits the beginning of out-of-phase signals at low temperature.

Table 5.3 Fitting of barrier height for **32** from equation 5.4 at different frequencies. Average over all frequencies leads to an approximate barrier of 12 K.

Frequency	**Barrier, Δ/k_b**	**τ_0**
100 Hz	13.2 K	1.16 X 10^{-6}
200 Hz	13.0 K	1.21 X 10^{-6}
500 Hz	12.5 K	1.32 X 10^{-6}
1000 Hz	11.4 K	1.62 X 10^{-6}
1500 Hz	10.1 K	2.03 X 10^{-6}

[Na(THF)$_3$((Me$_3$Si)$_2$N)$_2$Tm(CH$_2$)SiMe$_2$N(SiMe$_3$)] (32). The static magnetic properties of **32** were measured on a sample of crushed crystals sealed in a quartz EPR tube under an eicosane matrix, Figure 5.22. Eicosane was used to suspend the crystals in random orientations to prevent torqueing upon the application of an applied DC field.

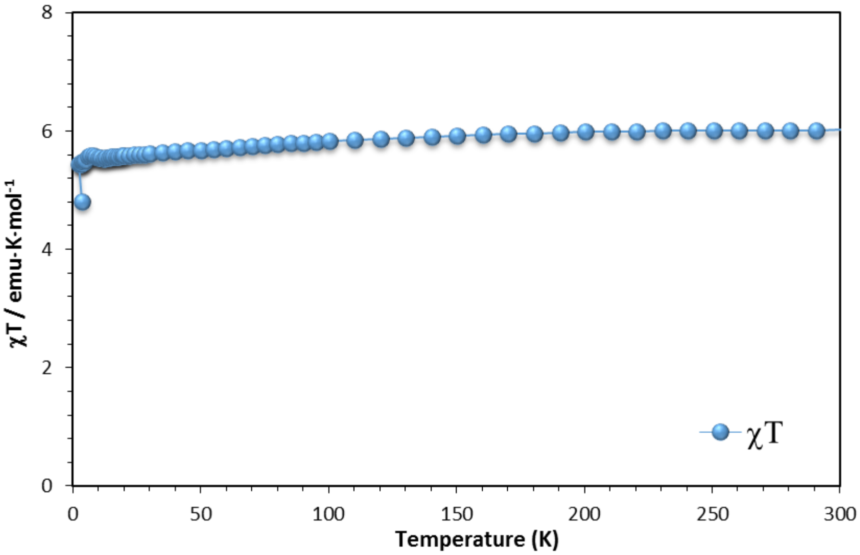

Figure 5.22 DC susceptibility χT vs T plot for **33** from 300-2 K.

The low value of χT at room temperature (6.2 emu·K/mol) is curious given the structural similarity between **31** and **32**. The disparity is most likely due to unaccounted for solvent and the error in measuring the sample's mass is amplified with the addition of eicosane in an EPR tube. Nonetheless, the dynamic AC susceptibility measurements were measured on compound **32** with no frequency dependence being observed. This is somewhat bewildering given that the axial chloride in compound **31** has been removed in compound **32**, which should further stabilize the $m_J = 6$ magnetic ground state of the ion.

Concluding Remarks

Magnetic parameters for compound **27** compared with other known mononuclear erbium(III) SMMs are compiled in Table 5.4. It is interesting at this stage to point out that the magnetic properties of the trigonal bipyramidal molecule $Er(NHPh^{i}Pr_2)_3(THF)_2$ compared to those of $Er[N(SiMe_3)_2]_3$ by Tang *et al.*, indicate that the former compound exhibits fast quantum tunneling presumably due to increased transverse anisotropy owing to the presence of the two axial THF molecules.[307] The compound exhibits out-of-phase signals in the χ" versus ν plots albeit with the necessity of applying a DC field. Given these findings, we reasoned that the presence of the axial chloride ligand in **27** and **30** might likewise eliminate the dynamic susceptibility properties; however, the effect of the chloride appears to only slightly destabilize the ground state yielding a smaller effective energy barrier as compared to $Er[N(SiMe_3)_2]_3$. Compound **27** is the first mononuclear erbium SMM with an axial negatively charged ligand reported to exhibit SMM behavior in the absence of an applied static DC field. The lower barrier observed for the new compound as compared to the trigonal $Er[N(SiMe_3)_2]_3$ complex is entirely reasonable although it can be said that, *a priori*, it would not have been possible to predict that compound **27** with the lower geometry would exhibit an appreciable axial anistropy[118] - especially after considering the results for the $Er(NHPh^{i}Pr_2)_3(THF)_2$ complex reported by Tang.

Table 5.4 Comparison of mononuclear erbium(III) SMM's.

Compound	U_{eff}/k_B	Hysteresis	DC Field?	Source
27	66.4 K	3 K	No	----
30	55.1 K	3 K	No	----
$Er[N(SiMe_3)_2]_3$	122 K	1.9 K*	No	[307]
$Er(NHPh^iPr_2)_3(THF)_2$	25 K	-----	Yes	[307]
(Cp*)Er(COT)	197, 323 K	5 K	No	[128]
$[Er(COT)_2]$	216 - 286 K	10 - 12 K	No	[295]
Er(trensal)	77.7 K**	-----	Yes	[310]
$[Er(COT'')_2]$	187 K	8 K	No	[130]
$[Er_2(COT'')_3]$	335 K	14 K	No	[131]

[*] Higher temperature magnetic hysteresis measurement not attempted/reported. [**] Calculated.

In summary, the first trigonal pyramidal erbium SMM is reported, the magnetic data of which indicate that strictly prolate *f*-electron density is not required to stabilize a crystal field that favors SMM behavior. The relaxation dynamics are interesting in that the presence of the axial chloride ligand does not quench the slow relaxation of the magnetization in zero DC field. While the ligand framework may primarily stabilize the $m_J = 15/2$ ground state, it is noteworthy that this molecule exhibits strikingly different magnetic behavior than the trigonal bipyramidal compound $Er(NHPh^iPr_2)_3(THF)_2$. The current findings support the hypothesis that erbium(III) ions in lower symmetry ligand environments other than those that are strictly limited to the oblate crystal field geometry are prospects for interesting SMM behavior. These results provide a nice backdrop for future theoretical studies as it hints that simple models are not entirely adequate for accurate prediction of slow magnetic relaxation in lanthanide-based SMMs - a conclusion also supported by the study of Dy-based SMMs.[320] Additional experimental and theoretical studies are underway to explain the origins of zero-field SMM behavior of the magnetization in **27**. Importantly, the axial chloride poises this molecule to be a convenient precursor for the preparation of a family of derivatives and even the possibility of device applications by attaching the molecule to surfaces.

The unimpressive dynamic susceptibility properties of the thulium analogs is evidence of the necessity of using Kramers ions in the rational design of lanthanide single-molecule magnets. With integer m_J lanthanide ions, tunneling within the ground state may occur, whereas this transition is formally forbidden in half integer ground states due to time-reversal symmetry arguments.[286] This chapter experimentally confirms this fact.

CHAPTER VI

CONCLUSIONS AND FUTURE OUTLOOK

Summary and Device Applications

The work presented in this dissertation encompasses structural and magnetic studies of molecular nanomagnets of different dimensionalities. In Chapter II, an in-depth structural study of Prussian Blue was presented which ultimately revealed that the formulation of this material is inherently complex. A detailed systematic approach to the synthesis of the “classical” Prussian Blue compound, $Fe^{III}_4[Fe^{II}(CN)_6]_3 \cdot 14\text{-}16H_2O$, and related materials was undertaken, the results of which indicated that the products are exquisitely sensitive to synthetic parameters including acid concentration and timing/aging of the reaction. The results of energy dispersive X-ray spectroscopy indicate that the formation of Prussian Blue under microwave assisted oxidation of ferrocyanide is composed of an inner shell of what is known in the literature as Prussian White, $K_2Fe^{II}[Fe^{II}(CN)_6]$. A new synthetic approach was presented for the growth of crystals suitable for single-crystal X-ray diffraction studies which sets the stage for a better understanding of the intricate nature of site vacancies and host-guest properties. The goal for future work will be to employ this synthetic method to grow large crystals of structurally related analogs with systematic variations to the crystal structure such as those described (potassium content, water content, number of defects, *etc.*). Such work would eliminate the main drawback of Prussian Blue chemistry- the inability to make a direct comparison of structure-property relationships. This problem is the main reason many researchers, including our research group, focus on the use of blocking ligands to make lower dimensional cyanide complexes that mimic Prussian Blue parent compounds.

Besides growing crystals, the work discussed in chapter II also underscores the problem of structural variance which was addressed by testing the properties of a family of Prussian Blue products. This concept was employed by Dr. Carolina Avendano, a former Dunbar group member, whose research included a study of Prussian Blue analogs of general formula $AI_xCo^{II}_4[Os^{III}(CN)_6]_{(8+x)/3}$ where A^+ = Li , Na, K, Rb, and Cs.[321] Her work revealed photomagnetic and charge transfer induced spin transition (CTIST) behavior that are dependent on the identity of the alkali metal cation incorporated into the Prussian Blue framework- the highest ordering temperature being observed for the K^+ analog which exhibits a $T_C = 28.5$ K. The results obtained for the Co^{II}-Os^{III} Prussian Blue analog and the results presented herein, serve as a future guide on how to analyze Prussian Blue material properties. In addition, obtaining crystal structures of Prussian Blue analogs would allow researchers to further understand Prussian Blue properties in the vast technologies and applications achieved already with powders and amorphous solids.[322-331]

Chapter III presents three new heterobimetallic chains based on octacyanometallates of W^V and Mo^V. While no impressive SCM behavior was observed, this work revealed the application of the building-block approach in reducing dimensionality of compounds. The *mer*-tridentate tptz ligand efficiently controls the molecular archetype to form a ladder or square type structural motif which can be used as a platform for future studies involving different combinations of 3d/4d and 3d/5d metal ions.

Both chapters IV and V present results on SMMs with a single metal center contibuting to the slow relaxation and no exchange interacations. These materials are receiving enromous attention in the field primarily for the following reasons: (1) their small size and simplicity allows for investigations with *ab initio* or DFT calculations; (2) their ease of tunability through ligand modification permits a direct method for testing computational predictions, and (3) mononuclear SMMs exhibit larger magnetic anisotropies as compared to low dimensional SCMs and polynuclear SMMs.[113,121,122,332]

Single-molecule magnets in general (polynuclear or mononuclear) afford the smallest sized "object" for device implementation. In 2006, Heersche and coworkers fabricated a molecular spin transistor by making a derivative of $Mn_{12}OAc$ with dangling acetyl-protected thiol groups and attaching the molecule to a break-junction between two gold electrodes using electromigration.[333] The results showed negative differential conductance due to a blocking mechanism of the current on the energy scale of the anisotropy barrier in the molecule. In 2008, Bogani and Wernsdorfer published an article outlining how SMMs could be used for the manipulation of spin and charges in electronic devices.[38] In one example, SMMs were discussed as a potential molecular spin-transistor as depicted in Figure 6.1. In this device, current passes through the source and drain of non-magnetic electrodes and the electronic transport properties are tuned as a function of the applied gate voltage across the SMM.

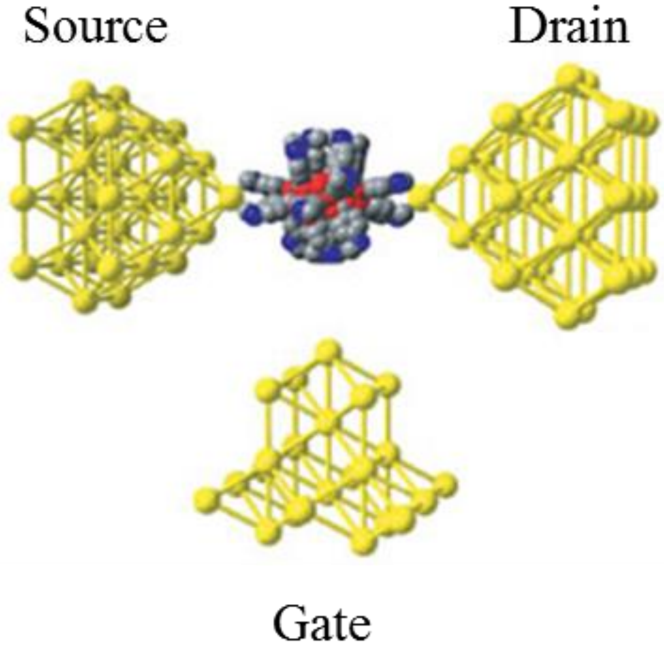

Figure 6.1 Schematic of SMM-based molecular transistors, in which a gate voltage can modulate transport. Reprinted by permission from Macmillan Publishers Ltd, copyright 2008.

Another device similar to transistors is the molecular spin-valve, Figure 6.2. In this device, the orientation of the net magnetization of a SMM can be used to filter spin-polarized currents. In other words, only spins in the magnetic source electrode perfectly aligned with the SMM can be transported to the drain electrode and this effect is known as "giant spin amplification". This type of device offers a means for measuring the magnetic state of the molecule, and spin polarized current itself can be used to orient the direction of the SMM magnetization in between two magnetically aligned electrodes.

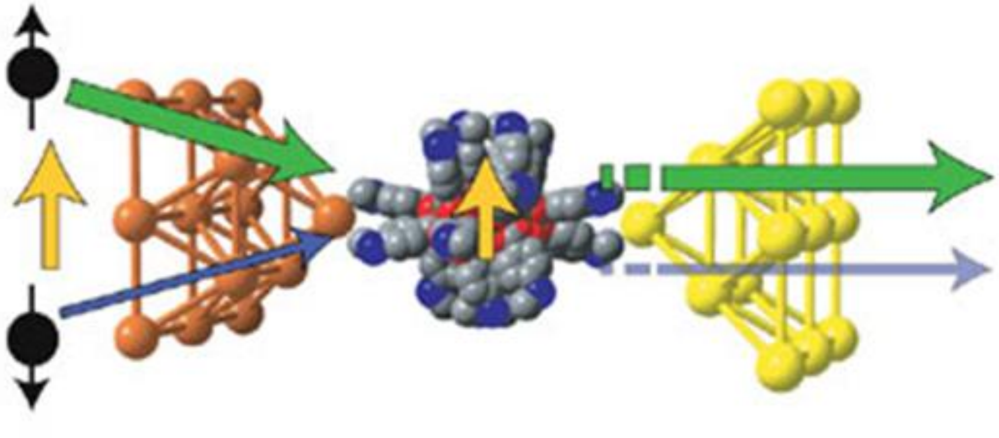

Figure 6.2 Parallel configuration of the magnetic source electrode (orange) and spin moment on SMM. Yellow electrode is diamagnetic drain electrode. Spin-up majority carriers represented by the green arrow are not affected by the molecular magnetization, whereas the spin-down minority carriers represented by blue arrow are blocked. Reprinted by permission from Macmillan Publishers Ltd, copyright 2008.

For SMMs to be implemented in mainstream technology and for these applications to be realized, higher blocking temperatures and effective barrier heights, Ueff, are needed. In this regard, the results in this dissertation followed strategies based on theoretical predictions for enhancing magnetic anisotropy.[118,233] Chapter IV reports the diamagnetic inorganic capping ligand, {Tp*Ti(IV)}, which forms a sandwich around a central magnetic ion to give an excellent platform for testing mononuclear SMM properties in a compressed octahedral environment. The cobalt complex, $\{(Tp^*Ti^{IV})(\mu_2\text{-}OAc)_2(\mu_2\text{-}O)Co^{II}(\mu_2\text{-}O)(\mu_2\text{-}OAc)_2(Ti^{IV}Tp^*)\}$, exhibits large magnetic anisotropy as evidenced by the zero-field splitting parameter of $|D| = 100$ or $300\ cm^{-1}$ (depending on the orbital contribution of the cobalt ion). The results confirm recent theory pertaining to a d^7 ion in a octahedral crystal field, suggesting that relative splitting of the d-orbitals is directly related to the magnitude of D.[115] In chapter V, the complex

$[Li(THF)_4]\{Er[N(SiMe_3)_2]_3Cl\}\cdot 2(THF)$ was shown to exhibit a large magnetic anisotropy with $U_{eff} = 63$ K. These results are attributed to the fact that erbium is a Kramers ion with a large spin-orbital m_J ground state that is stabilized by interaction of the prolate Er(III) center with the equatorially coordinating trimethylsilylamide ligands. The compound exhibits hysteresis up to 3 K which is an impressive achievement given that the great majority of SMMs have lower effective energy barriers to the reversal of magnetization.

While the D value for $\{(Tp^{*}Ti^{IV})(\mu_2\text{-}OAc)_2(\mu_2\text{-}O)Co^{II}(\mu_2\text{-}O)(\mu_2\text{-}OAc)_2(Ti^{IV}Tp^{*})\}$ is quite large, the small effective barrier height, $U_{eff} = 32$ K, exemplifies the need to determine a way to avoid non-Orbach relaxation processes. Simply designing an SMM with large anisotropy is not enough to ensure SMM behavior, as anticipating zero DC field relaxation dynamics is still somewhat unpredictable.[334] Transition metal and lanthanide-based mononuclear SMMs typically exhibit fast quantum tunneling under a zero-applied DC field. Moving forward, the study of Kramers ions will be of great value because the ground state tunneling is formally forbidden by time-reversal symmetry arguments. However the transition can still occur in low-symmetry complexes where transverse anisotropy components become substantial or when hyperfine interactions exist.[98] For non-Kramers, or integer molecules, the ground state tunneling is permitted and, in addition, the requirement of bistability of the ground states is only obtained in highly symmetric coordination environments.[118] As discussed in this dissertation, the typical relaxation pathways of SMMs include one-phonon direct processes, two-phonon Raman and Orbach processes, quantum tunneling, thermally assisted quantum tunneling, nuclear hyperfine interactions, and low symmetry transversal components.

Improving SMMs

Lanthanide SMMs typically exhibit energy barriers that are related to a spin-phonon mechanism occurring via the first excited state. This is attributed to low symmetry distortions, which result in transverse components as well as non-coincident anisotropy axes between the ground and first excited Kramers doublets.[98] In order to observe effective barriers based on transitions through higher energy excited states, a crystal field that enforces rigorously axial symmetry represents the best strategy and may very well be the future of SMMs. Recent theoretical predictions reveal that a linear dysprosium oxide compound, $[DyO]^+$ would exhibit perfect axial symmetry, making a full projection of the M_J states aligned with the molecular axis.[335] The scenario is predicted to eliminate the transverse magnetic field ($g_\perp=0$) up to the highest $M_J = \pm½$ manifold, Figure 6.3. The barrier height of such a compound was proposed to be on the order of U_{eff} = 3000 K. Experimentalists have already begun applying these principles and achieved lanthanide SMMs with relaxation occurring through the second excited state due to strong axial bonds.[295,336,337]

In conclusion, from fundamental science to applications, the study of molecular nanomagnets is a fascinating subject and is sure to continue to blossom in a collaborative environment between experimentalists, physicists, materials scientists and engineers.

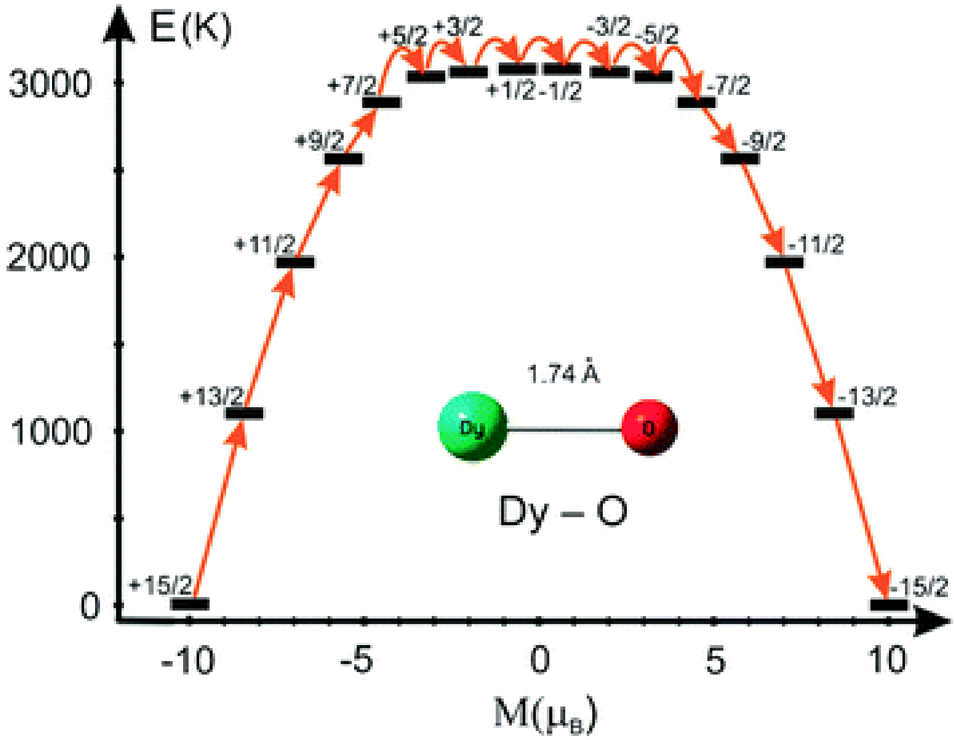

Figure 6.3 Barrier for reversal of magnetization in a hypothetical $[DyO]^+$ complex.. The arrows show the path for the reversal of magnetization. Reproduced from reference[335] with permission from the Royal Society of Chemistry.

REFERENCES

(1) Munro, U.; Munro, J. A.; Phillips, J. B.; Wiltschko, R.; Wiltschko, W. *Naturwissenschaften* **1997**, *84*, 26.

(2) Walker, M. M.; Diebel, C. E.; Haugh, C. V.; Pankhurst, P. M.; Montgomery, J. C.; Green, C. R. *Nature* **1997**, *390*, 371.

(3) Fischer, J. H.; Freake, M. J.; Borland, S. C.; Phillips, J. B. *Anim. Behav.* **2001**, *62*, 1.

(4) Lohmann, K. J.; Cain, S. D.; Dodge, S. A.; Lohmann, C. M. F. *Science* **2001**, *294*, 364.

(5) Boles, L. C.; Lohmann, K. J. *Nature* **2003**, *421*, 60.

(6) Brothers, J. R.; Lohmann, Kenneth J. *Curr. Biol.* **2015**, *25*, 392.

(7) Mora, C. V.; Davison, M.; Wild, J. M.; Walker, M. M. *Nature* **2004**, *432*, 508.

(8) McCallum, R. W.; Lewis, L. H.; Skomski, R.; Kramer, M. J.; Anderson, I. E. *Annu. Rev. Mater. Res.* **2014**, *44*, 451.

(9) Jalan, R. *Permanent Magnets: Technologies and Global Markets*; BCC Research: Wellesley, MA, 2014.

(10) Kahn, O. *Molecular Magnetism*; Wiley: New York, NY, 1993.

(11) Goodenough, J. B. *Phys. Chem. Solids* **1958**, *6*, 287.

(12) Kanamori, J. *Phys. Chem. Solids* **1959**, *10*, 87.

(13) Gatteschi, D.; Sessoli, R.; Villain, R. *Molecular Nanomagnets*; Oxford University Press: Oxford, 2006.

(14) Shatruk, M.; Avendano, C.; Dunbar, K. R. Cyanide-Bridged Complexes of Transition Metals: A Molecular Magnetism Perspective; Karlin, K. D., Ed.; John Wiley & Sons, Inc.: Hoboken, NJ, 2009; Vol. 56, p 155.

(15) Gadet, V.; Bujolidoeuff, M.; Force, L.; Verdaguer, M.; Elmalkhi, K.; Deroy, A.; Besse, J. P.; Chappert, C.; Veillet, P.; Renard, J. P.; Beauvillain, P. *Towards High-Tc Ferro And Ferrimagnetic Bi And Tridimensional Materials From Molecular Precursors*; Kluwer Academic: Boston, 1991; Vol. 198.

(16) Verdaguer, M.; Girolami, G. S. Magnetic Prussian Blue Analogs; Miller, J., Drillon, M., Eds.; Wiley-VCH: Germany, 2005, p 283.

(17) Herren, F.; Fischer, P.; Ludi, A.; Haelg, W. *Inorg. Chem.* **1980**, *19*, 956.

(18) Holmes, S. M.; Girolami, G. S. *J. Am. Chem. Soc.* **1999**, *121*, 5593.

(19) Sato, O. *Nat Chem* **2010**, *2*, 10.

(20) Ricci, F.; Palleschi, G. *Biosens. Bioelectron.* **2005**, *21*, 389.

(21) Berlinguette, C. P.; Vaughn, D.; Canada-Vilalta, C.; Galan-Mascaros, J. R.; Dunbar, K. R. *Angew. Chem., Int. Ed.* **2003**, *42*, 1523.

(22) Schelter, E. J.; Prosvirin, A. V.; Dunbar, K. R. *J. Am. Chem. Soc.* **2004**, *126*, 15004.

(23) Wang, S.; Zuo, J. L.; Zhou, H. C.; Choi, H. J.; Ke, Y.; Long, J. R.; You, X. Z. *Angew. Chem., Int. Ed.* **2004**, *43*, 5940.

(24) Boskovic, C.; Brechin, E. K.; Streib, W. E.; Folting, K.; Bollinger, J. C.; Hendrickson, D. N.; Christou, G. *J. Am. Chem. Soc.* **2002**, *124*, 3725.

(25) Goodwin, J. C.; Sessoli, R.; Gatteschi, D.; Wernsdorfer, W.; Powell, A. K.; Heath, S. L. *J. Chem. Soc., Dalton Trans.* **2000**, 1835.

(26) Eppley, H. J.; Tsai, H. L.; Devries, N.; Folting, K.; Christou, G.; Hendrickson, D. N. *J. Am. Chem. Soc.* **1995**, *117*, 301.

(27) Sessoli, R.; Gatteschi, D.; Caneschi, A.; Novak, M. A. *Nature (London, U. K.)* **1993**, *365*, 141.

(28) Seo, D. M.; Meenakshi, V.; Teizer, W.; Zhao, H.; Dunbar, K. R. *J. Magn. Magn. Mater*. **2006**, *301*, 31.

(29) Coronado, E., Dunbar, K. R. *Inorg. Chem.* **2009**, 3293.

(30) Gatteschi, D.; Sessoli, R. *Angew. Chem., Int. Ed. Engl.* **2003**, *42*, 268.

(31) Wernsdorfer, W. *Nat. Mater.* **2007**, *6,* 174.

(32) Tejada, J.; Chudnovsky, E. M.; del Barco, E.; Hernandez, J. M.; Spiller, T. P. *Nanotechnology* **2001**, *12*, 181.

(33) Affronte, M.; Troiani, F.; Ghirri, A.; Carretta, S.; Santini, P.; Corradini, V.; Schuecker, R.; Muryn, C.; Timco, G.; Winpenny, R. E. *Dalton Trans.* **2006**, 2810.

(34) Bertaina, S.; Gambarelli, S.; Tkachuk, A.; Kurkin, I. N.; Malkin, B.; Stepanov, A.; Barbara, B. *Nat. Nanotechnol.* **2007**, *2,* 39.

(35) Timco, G. A.; Carretta, S.; Troiani, F.; Tuna, F.; Pritchard, R. J.; Muryn, C. A.; McInnes, E. J. L.; Ghirri, A.; Candini, A.; Santini, P.; Amoretti, G.; Affronte, M.; Winpenny, R. E. P. *Nat. Nanotechnol.* **2009**, *4*, 173.

(36) Lehmann, J.; Gaita-Arino, A.; Coronado, E.; Loss, D. *J. Mater. Chem.* **2009**, *19*, 1672.

(37) Bertaina, S.; Shim, J. H.; Gambarelli, S.; Malkin, B. Z.; Barbara, B. *Phys. Rev. Lett.* **2009**, *103,* 226402.

(38) Bogani, L.; Wernsdorfer, W. *Nat. Mater.* **2008**, *7*, 179.

(39) Stamp, P. C. E. *Nature* **2008**, *453*, 167.

(40) Stepanenko, D.; Trif, M.; Loss, D. *Inorg. Chim. Acta* **2008**, *361*, 3740.

(41) Schlegel, C.; van Slageren, J.; Manoli, M.; Brechin, E. K.; Dressel, M. *Phys. Rev. Lett.* **2008**, *101*.

(42) Lehmann, J.; Gaita-Arino, A.; Coronado, E.; Loss, D. *Nat. Nanotechnol.* **2007**, *2*, 312.

(43) Leuenberger, M. N.; Loss, D.; Poggio, M.; Awschalom, D. D. *Phys. Rev. Lett.* **2002**, *89*.

(44) Leuenberger, M. N.; Loss, D. *Nature* **2001**, *410*, 789.

(45) Tejada, J. *Polyhedron* **2001**, *20*, 1751.

(46) Camarero, J.; Coronado, E. *J. Mater. Chem.* **2009**, *19*, 1678.

(47) Sanvito, S. Molecular Spintronics; Taylor & Francias: 2012.

(48) Katoh, K.; Isshiki, H.; Komeda, T.; Yamashita, M. *Chem. - Asian J.* **2012**, *7*, 1154.

(49) Chappert, C.; Fert, A.; Van Dau, F. N. *Nat. Mater.* **2007**, *6*, 813.

(50) Bogani, L.; Wernsdorfer, W. *Inorg. Chim. Acta* **2008**, *361*, 3807.

(51) Caneschi, A.; Gatteschi, D.; Lalioti, N.; Sangregorio, C.; Sessoli, R.; Venturi, G.; Vindigni, A.; Rettori, A.; Pini, M. G.; Novak, M. A. *Angew. Chem., Int. Ed.* **2001**, *40*, 1760.

(52) Glauber, R. J. *J. Math. Phys.* **1963**, *4*, 294.

(53) Miyasaka, H.; Julve, M.; Yamashita, M.; Clérac, R. *Inorg. Chem.* **2009**, *48*, 3420.

(54) Sun, H. L.; Wang, Z. M.; Gao, S. *Coord. Chem. Rev.* **2010**, *254*, 1081.

(55) Wang, X. Y.; Avendano, C.; Dunbar, K. R. *Chem. Soc. Rev.* **2011**, *40*, 3213.

(56) Boeckmann, J.; Wriedt, M.; Nather, C. *Chem. - Eur. J.* **2012**, *18*, 5284.

(57) Zhang, W. X.; Shiga, T.; Miyasaka, H.; Yamashita, M. *J. Am. Chem. Soc.* **2012**, *134*, 6908.

(58) Ababei, R.; Pichon, C.; Roubeau, O.; Li, Y. G.; Brefuel, N.; Buisson, L.; Guionneau, P.; Mathoniere, C.; Clerac, R. *J. Am. Chem. Soc.* **2013**, *135*, 14840.

(59) Liu, T.; Zheng, H.; Kang, S.; Shiota, Y.; Hayami, S.; Mito, M.; Sato, O.; Yoshizawa, K.; Kanegawa, S.; Duan, C. Y. *Nat. Commun.* **2013**, *4*.

(60) Tangoulis, V.; Lalia-Kantouri, M.; Gdaniec, M.; Papadopoulos, C.; Miletic, V.; Czapik, A. *Inorg. Chem.* **2013**, *52*, 6559.

(61) Zhang, W. X.; Ishikawa, R.; Breedlove, B.; Yamashita, M. *RSC Adv.* **2013**, *3*, 3772.

(62) Ghosh, S.; Ida, Y.; Ishida, T.; Ghosh, A. *Cryst. Growth Des.* **2014**, *14*, 2588.

(63) Vaz, M. G. F.; Cassaro, R. A. A.; Akpinar, H.; Schlueter, J. A.; Lahti, P. M.; Novak, M. A. *Chem. - Eur. J.* **2014**, *20*, 5460.

(64) Wang, T. T.; Ren, M.; Bao, S. S.; Liu, B.; Pi, L.; Cai, Z. S.; Zheng, Z. H.; Xu, Z. L.; Zheng, L. M. *Inorg. Chem.* **2014**, *53*, 3117.

(65) Harris, T. D.; Bennett, M. V.; Clerac, R.; Long, J. R. *J. Am. Chem. Soc.* **2010**, *132*, 3980.

(66) Bhowmick, I.; Hillard, E. A.; Dechambenoit, P.; Coulon, C.; Harris, T. D.; Clerac, R. *Chem. Commun.* **2012**, *48*, 9717.

(67) Feng, X.; Liu, J.; Harris, T. D.; Hill, S.; Long, J. R. *J. Am. Chem. Soc.* **2012**, *134*, 7521.

(68) Hoshino, N.; Iijima, F.; Newton, G. N.; Yoshida, N.; Shiga, T.; Nojiri, H.; Nakao, A.; Kumai, R.; Murakami, Y.; Oshio, H. *Nat. Chem.* **2012**, *4*, 921.

(69) Pedersen, K. S.; Bendix, J.; Clerac, R. *Chem. Commun.* **2014**, *50*, 4396.

(70) Cui, L.; Zhu, F.; Leong, C.; Ru, J.; Gao, F.; D'Alessandro, D.; Zuo, J. *Sci. China: Chem.* **2015**, *58*, 650.

(71) Gatteschi, D.; Vindigni, A. Single-Chain Magnets; Bartolome, S. J., Luis, F., Fernández, J. F., Eds.; Springer-Verlag Berlin Heidelberg: New York, 2014, p 191.

(72) Ferbinteanu, M.; Miyasaka, H.; Wernsdorfer, W.; Nakata, K.; Sugiura, K.; Yamashita, M.; Coulon, C.; Clerac, R. *J. Am. Chem. Soc.* **2005**, *127*, 3090.

(73) Zhao, H.; Shatruk, M.; Prosvirin, A. V.; Dunbar, K. R. *Chem. - Eur. J.* **2007**, *13*, 6573.

(74) Wang, X. Y.; Avendano, C.; Dunbar, K. R. *Chem. Soc. Rev.* **2011**, *40*, 3213.

(75) Sessoli, R.; Powell, A. K. *Coord. Chem. Rev.* **2009**, *253*, 2328.

(76) Meihaus, K. R.; Long, J. R. *J. Am. Chem. Soc.* **2013**, *135*, 17952.

(77) Rinehart, J. D.; Harris, T. D.; Kozimor, S. A.; Bartlett, B. M.; Long, J. R. *Inorg. Chem.* **2009**, *48*, 3382.

(78) Weihe, H.; Gudel, H. U. *Comments Inorg. Chem.* **2000**, *22*, 75.

(79) Entley, W. R.; Treadway, C. R.; Girolami, G. S. *Mol. Cryst. Liq. Cryst. Sci. Technol., Sect. A* **1995**, *273*, 153.

(80) Coronado, E.; Epsetin, A. J. *J. Mater. Chem.* **2009**, *19*, 1670.

(81) Stamp, P. C. E.; Gaita-Arino, A. *J. Mater. Chem.* **2009**, *19*, 1718.

(82) Gomez-Coca, S.; Ruiz, E. *Can. J. Chem.* **2013**, *91*, 866.

(83) Jenkins, M.; Hummer, T.; Martinez-Perez, M. J.; Garcia-Ripoll, J.; Zueco, D.; Luis, F. *New J. Phys.* **2013**, *15*.

(84) Jiang, L.; Liu, X.; Zhang, Z. Z.; Wang, R. Q. *Phys. Lett. A* **2014**, *378*, 426.

(85) Zhang, Z. Z.; Jiang, L. *Nanotechnology* **2014**, *25*.

(86) Vincent, R.; Klyatskaya, S.; Ruben, M.; Wernsdorfer, W.; Balestro, F. *Nature* **2012**, *488*, 357.

(87) Raman, K. V.; Kamerbeek, A. M.; Mukherjee, A.; Atodiresei, N.; Sen, T. K.; Lazic, P.; Caciuc, V.; Michel, R.; Stalke, D.; Mandal, S. K.; Blugel, S.; Munzenberg, M.; Moodera, J. S. *Nature* **2013**, *493*, 509.

(88) Inose, T.; Tanaka, D.; Tanaka, H.; Ivasenko, O.; Nagata, T.; Ohta, Y.; De Feyter, S.; Ishikawa, N.; Ogawa, T. *Chem. - Eur. J.* **2014**, *20*, 11362.

(89) Mannini, M.; Bertani, F.; Tudisco, C.; Malavolti, L.; Poggini, L.; Misztal, K.; Menozzi, D.; Motta, A.; Otero, E.; Ohresser, P.; Sainctavit, P.; Condorelli, G. G.; Dalcanale, E.; Sessoli, R. *Nat. Commun.* **2014**, *5*.

(90) Totaro, P.; Poggini, L.; Favre, A.; Mannini, M.; Sainctavit, P.; Cornia, A.; Magnani, A.; Sessoli, R. *Langmuir* **2014**, *30*, 8645.

(91) Ganzhorn, M.; Klyatskaya, S.; Ruben, M.; Wernsdorfer, W. *ACS Nano* **2013**, *7*, 6225.

(92) Christou, G.; Gatteschi, D.; Hendrickson, D. N.; Sessoli, R. *MRS Bull.* **2000**, *25*, 66.

(93) Ruiz-Molina, D.; Christou, G.; Hendrickson, D. N. *Mol. Cryst. Liq. Cryst.* **2000**, *343*, 335.

(94) Sessoli, R.; Tsai, H. L.; Schake, A. R.; Wang, S.; Vincent, J. B.; Folting, K.; Gatteschi, D.; Christou, G.; Hendrickson, D. N. *J. Am. Chem. Soc.* **1993**, *115*, 1804.

(95) Aubin, S. M. J.; Wemple, M. W.; Adams, D. M.; Tsai, H.-L.; Christou, G.; Hendrickson, D. N. *J. Am. Chem. Soc.* **1996**, *118*, 7746.

(96) Caneschi, A.; Gatteschi, D.; Sessoli, R.; Barra, A. L.; Brunel, L. C.; Guillot, M. *J. Am. Chem. Soc.* **1991**, *113*, 5873.

(97) Wernsdorfer, W.; Aliaga-Alcalde, N.; Hendrickson, D. N.; Christou, G. *Nature* **2002**, *416*, 406.

(98) Tang, J.; Zhang, P. *Lanthanide Single Molecule Magnets*; Springer-Verlag Berlin Heidelberg: New York, 2015.

(99) Qian, K.; Huang, X. C.; Zhou, C.; You, X. Z.; Wang, X. Y.; Dunbar, K. R. *J. Am. Chem. Soc.* **2013**, *135*, 13302.

(100) Rinehart, J. D.; Fang, M.; Evans, W. J.; Long, J. R. *J. Am. Chem. Soc.* **2011**, *133*, 14236.

(101) Nemec, I.; Marx, R.; Herchel, R.; Neugebauer, P.; van Slageren, J.; Travnicek, Z. *Dalton Trans.* **2015**, *44*, 15014.

(102) Gomez-Coca, S.; Urtizberea, A.; Cremades, E.; Alonso, P. J.; Camon, A.; Ruiz, E.; Luis, F. *Nat. Commun.* **2014**, *5*, 4300.

(103) Freedman, D. E.; Harman, W. H.; Harris, T. D.; Long, G. J.; Chang, C. J.; Long, J. R. *J. Am. Chem. Soc.* **2010**, *132*, 1224.

(104) Friedman, J. R.; Sarachik, M. P.; Tejada, J.; Ziolo, R. *Phys. Rev. Lett.* **1996**, *76*, 3830.

(105) Thomas, L.; Lionti, F.; Ballou, R.; Gatteschi, D.; Sessoli, R.; Barbara, B. *Nature* **1996**, *383*, 145.

(106) Sangregorio, C.; Ohm, T.; Paulsen, C.; Sessoli, R.; Gatteschi, D. *Phys. Rev. Lett.* **1997**, *78*, 4645.

(107) Harman, W. H.; Harris, T. D.; Freedman, D. E.; Fong, H.; Chang, A.; Rinehart, J. D.; Ozarowski, A.; Sougrati, M. T.; Grandjean, F.; Long, G. J.; Long, J. R.; Chang, C. J. *J. Am. Chem. Soc.* **2010**, *132*, 18115.

(108) Dattagupta, S.; Blume, M. *Phys. Rev. B* **1974**, *10*, 4540.

(109) Weismann, D.; Sun, Y.; Lan, Y. H.; Wolmershauser, G.; Powell, A. K.; Sitzmann, H. *Chem. - Eur. J.* **2011**, *17*, 4700.

(110) Zadrozny, J. M.; Long, J. R. *J. Am. Chem. Soc.* **2011**, *133*, 20732.

(111) Poulten, R. C.; Page, M. J.; Algarra, A. G.; Le Roy, J. J.; Lopez, I.; Carter, E.; Llobet, A.; Macgregor, S. A.; Mahon, M. F.; Murphy, D. M.; Murugesu, M.; Whittlesey, M. K. *J. Am. Chem. Soc.* **2013**, *135*, 13640.

(112) Zadrozny, J. M.; Atanasov, M.; Bryan, A. M.; Lin, C. Y.; Rekken, B. D.; Power, P. P.; Neese, F.; Long, J. R. *Chem. Sci.* **2013**, *4*, 125.

(113) Gómez-Coca, S.; Aravena, D.; Morales, R.; Ruiz, E. *Coord. Chem. Rev.* **2015**, *289–290*, 379.

(114) Neese, F.; Solomon, E. I. *Inorg. Chem.* **1998**, *37*, 6568.

(115) Gomez-Coca, S.; Cremades, E.; Aliaga-Alcalde, N.; Ruiz, E. *J. Am. Chem. Soc.* **2013**, *135*, 7010.

(116) Rinehart, J. D.; Long, J. R. *J. Am. Chem. Soc.* **2009**, *131*, 12558.

(117) Magnani, N.; Apostolidis, C.; Morgenstern, A.; Colineau, E.; Griveau, J.-C.; Bolvin , H.; Walter, O.; Caciuffo, R. *Angew. Chem., Int. Ed.* **2011**, *50*, 1696.

(118) Rinehart, J. D.; Long, J. R. *Chem. Sci.* **2011**, *2*, 2078.

(119) Rivera, V. A. G.; Ferri, F. A.; E. Marega, J. Localized Surface Plasmon Resonances: Noble Metal Nanoparticle Interaction with Rare-Earth Ions; Kim, K. Y., Ed.; InTech: Brazil, 2012, p 558.

(120) Benelli, C.; Gatteschi, D. *Chem. Rev.* **2002**, *102*, 2369.

(121) Ishikawa, N.; Sugita, M.; Ishikawa, T.; Koshihara, S.-y.; Kaizu, Y. *J. Am. Chem. Soc.* **2003**, *125*, 8694.

(122) Ganivet, C. R.; Ballesteros, B.; de la Torre, G.; Clemente-Juan, J. M.; Coronado, E.; Torres, T. *Chem. - Eur. J.* **2013**, *19*, 1457.

(123) Damen, M. A.; Clemente, J. M.; Coronado, E.; Martí-Gastaldo, C.; Gaita-Ariño, A. *J. Am. Chem. Soc.* **2008**, *130*, 8874.

(124) Woodruff, D. N.; Winpenny, R. E. P.; Layfield, R. A. *Chem. Rev.* **2013**, *113*, 5110.

(125) Feltham, H. L. C.; Brooker, S. *Coord. Chem. Rev.* **2014**, *276*, 1.

(126) Jiang, S.-D.; Wang, B.-W.; Su, G.; Wang, Z.-M.; Gao, S. *Angew. Chem., Int. Ed.* **2010**, *49*, 7448.

(127) Chen, G. J.; Guo, Y. N.; Tian, J. L.; Tang, J.; Gu, W.; Liu, X.; Yan, S. P.; Cheng, P.; Liao, D. Z. *Chem. - Eur. J.* **2012**, *18*, 2484.

(128) Jiang, S. D.; Wang, B. W.; Sun, H. L.; Wang, Z. M.; Gao, S. *J. Am. Chem. Soc.* **2011**, *133*, 4730.

(129) Liu, J. L.; Chen, Y. C.; Zheng, Y. Z.; Lin, W. Q.; Ungur, L.; Wernsdorfer, W.; Chibotaru, L. F.; Tong, M. L. *Chem. Sci.* **2013**, *4*, 3310.

(130) Le Roy, J. J.; Korobkov, I.; Murugesu, M. *Chem. Commun.* **2014**, *50*, 1602.

(131) Le Roy, J. J.; Ungur, L.; Korobkov, I.; Chibotaru, L. F.; Murugesu, M. *J. Am. Chem. Soc.* **2014**, *136*, 8003.

(132) Rafalska-Łasocha, A.; Podulka, K.; Łasocha, W. *Powder Diffr.* **2011**, *26*, 39.

(133) Anonymous *Miscellanea Berolinensia ad Incrementum Scientiarum* **1710**, *1*, 377.

(134) Woodward, J. *Phil. Trans.* **1724**, *33*, 15.

(135) Brown, J. *Phil. Trans.* **1724**, *33*, 19.

(136) Ludi, A. *J. Chem. Educ.* **1981**, *58*, 1013.

(137) Ludi, A.; Güdel, H. Structural chemistry of polynuclear transition metal cyanides; Springer Berlin Heidelberg: New York, 1973; Vol. 14, p 1.

(138) Kirby, J. S., D. *National Gallery Technical Bulletin* **2004**, *25*, 73.

(139) Hansen, L. D.; Litchman, W. M.; Daub, G. H. *J. Chem. Educ.* **1969**, *46*, 46.

(140) Cosgrove, J. G.; Collins, R. L.; Murty, D. S. *J. Am. Chem. Soc.* **1973**, *95*, 1083.

(141) Samain, L.; Grandjean, F.; Long, G. J.; Martinetto, P.; Bordet, P.; Strivay, D. *J. Phys. Chem. C* **2013**, *117*, 9693.

(142) Buser, H. J.; Schwarzenbach, D.; Petter, W.; Ludi, A. *Inorg. Chem.* **1977**, *16*, 2704.

(143) Buser, H. J.; Ludi, A.; Petter, W.; Schwarzenbach, D. *J. Chem. Soc., Chem. Commun.* **1972**, 1299.

(144) Keggin, J. F. M., F. D. *Nature* **1936**, *137*, 557.

(145) Bueno, P. R.; Ferreira, F. F.; Giménez-Romero, D.; Oliveira Setti, G.; Faria, R. C.; Gabrielli, C.; Perrot, H.; Garcia-Jareño, J. J.; Vicente, F. *J. Phys. Chem. C* **2008**, *112*, 13264.

(146) Garcia-Jareno, J.; Sanmatias, A.; Navarro-Laboulais, J.; Vicente, F. *Electrochim. Acta* **1998**, *44*, 395.

(147) Huggins, R. A. *Advanced Batteries: Materials Science Aspects*; Springer Science: New York, 2009.

(148) Granqvist, C. G. *Handbook of Inorganic Electrochromic Materials*; Elsevier: Amsterdam, 1995.

(149) Agrisuelas, J.; García-Jareño, J. J.; Moreno, C.; Vicente, F. *Electrochim. Acta* **2014**, *138*, 200.

(150) Mohammad, A.; Yang, Y.; Khan, M. A.; Faustino, P. J. *J. Pharm. Biomed. Anal.* **2014**, *103c*, 85.

(151) Faustino, P. J.; Yang, Y.; Progar, J. J.; Brownell, C. R.; Sadrieh, N.; May, J. C.; Leutzinger, E.; Place, D. A.; Duffy, E. P.; Houn, F.; Loewke, S. A.; Mecozzi, V. J.; Ellison, C. D.; Khan, M. A.; Hussain, A. S.; Lyon, R. C. *J. Pharm. Biomed. Anal.* **2008**, *47*, 114.

(152) Mohammad, A.; Faustino, P. J.; Khan, M. A.; Yang, Y. *Int. J. Pharm.* **2014**, *477*, 122.

(153) Yang, Y.; Faustino, P. J.; Progar, J. J.; Brownell, C. R.; Sadrieh, N.; May, J. C.; Leutzinger, E.; Place, D. A.; Duffy, E. P.; Yu, L. X.; Khan, M. A.; Lyon, R. C. *Int. J. Pharm.* **2008**, *353*, 187.

(154) Yang, Y.; Brownell, C.; Sadrieh, N.; May, J.; Del, A. *Clin Toxicol (Phila)* **2007**, *45*, 776.

(155) Yang, Y.; Brownell, C. R.; Sadrieh, N.; May, J. C.; Del Grosso, A. V.; Lyon, R. C.; Faustino, P. J. *J. Pharm. Biomed. Anal.* **2007**, *43*, 1358.

(156) Khan, S. R.; Kona, R.; Faustino, P. J.; Gupta, A.; Taylor, J. S.; Porter, D. A.; Khan, M. *J. Pharm. Sci.* **2014**, *103*, 1331.

(157) Robin, M. B. D., P. *Adv. Inorg. Chem. and Radiochem.* **1967**, *10*, 248.

(158) Mayoh, B.; Day, P. *Dalton Trans.* **1976**, 1483.

(159) Ferlay, S.; Mallah, T.; Ouahes, R.; Veillet, P.; Verdaguer, M. *Nature* **1995**, *378*, 701.

(160) Verdaguer, M. *Science* **1996**, *272*, 698.

(161) Kosaka, W.; Nomura, K.; Hashimoto, K.; Ohkoshi, S.-i. *J. Am. Chem. Soc.* **2005**, *127*, 8590.

(162) Sato, O.; Einaga, Y.; Fujishima, A.; Hashimoto, K. *Inorg. Chem.* **1999**, *38*, 4405.

(163) Sato, O.; Iyoda, T.; Fujishima, A.; Hashimoto, K. *Science* **1996**, *272*, 704.

(164) Pejakovic, D. A.; Manson, J. L.; Miller, J. S.; Epstein, A. J. *J. Appl. Phys.* **2000**, *88*, 4457.

(165) Bleuzen, A.; Lomenech, C.; Escax, V.; Villain, F.; Varret, F.; Cartier dit Moulin, C.; Verdaguer, M. *J. Am. Chem. Soc.* **2000**, *122*, 6648.

(166) Sato, O.; Einaga, Y.; Iyoda, T.; Fujishima, A.; Hashimoto, K. *J. Electrochem. Soc.* **1997**, *144*, L11.

(167) Escax, V.; Bleuzen, A.; Cartier dit Moulin, C.; Villain, F.; Goujon, A.; Varret, F.; Verdaguer, M. *J. Am. Chem. Soc.* **2001**, *123*, 12536.

(168) Shimamoto, N.; Ohkoshi, S.; Sato, O.; Hashimoto, K. *Inorg. Chem.* **2002**, *41*, 678.

(169) Lee, S. H., Y. *Bull. Korean Chem. Soc.* **2012**, *32*, 1078.

(170) Sheldrick, G. M. *SADABS. Program for Empirical Absorption Correction.*; University of Gottingen: Germany, 1996.

(171) Dolomanov, O. V.; Bourhis, L. J.; Gildea, R. J.; Howard, J. A. K.; Puschmann, H. *J. Appl. Crystallogr.* **2009**, *42*, 339.

(172) Sheldrick, G. M. *Acta Crystallogr., Sect. A: Found. Crystallogr.* **2015**, *71*, 3.

(173) Sheldrick, G. M. *Acta Crystallogr., Sect. A.* **2008**, *64*, 112.

(174) Pennington, W. *J. Appl. Crystallogr.* **1999**, *32*, 1028.

(175) Ganguli, S.; Bhattacharya, M. *J. Chem. Soc., Faraday Trans.* **1983**, *79*, 1513.

(176) Reen, G. S. *Solid State Physics*; Dorling Kindersley: India, 2012.

(177) Nossol, E.; Nossol, A. B. S.; Abdelhamid, M. E.; Martin, L. L.; Zarbin, A. J. G.; Bond, A. M. *J. Phys. Chem. C* **2014**, *118*, 13157.

(178) Machala, L.; Zoppellaro, G.; Tucek, J.; Safarova, K.; Marusak, Z.; Filip, J.; Pechousek, J.; Zboril, R. *RSC Adv.* **2013**, *3*, 19591.

(179) Aparicio, C.; Machala, L.; Marusak, Z. *J. Therm. Anal. Calorim.* **2012**, *110*, 661.

(180) Giménez-Romero, D.; Bueno, P. R.; García-Jareño, J. J.; Gabrielli, C.; Perrot, H.; Vicente, F. *J. Phys. Chem. B* **2006**, *110*, 2715.

(181) Giménez-Romero, D.; Bueno, P. R.; Gabrielli, C.; García-Jareño, J. J.; Perrot, H.; Vicente, F. *J. Phys. Chem. B* **2006**, *110*, 19352.

(182) Bogani, L.; Vindigni, A.; Sessoli, R.; Gatteschi, D. *J. Mater. Chem.* **2008**, *18*, 4750.

(183) Zhang, W. X.; Ishikawa, R.; Breedlove, B.; Yamashita, M. *RSC Adv.* **2013**, *3*, 3772.

(184) Zhang, Y.; Mallik, U. P.; Rath, N.; Yee, G. T.; Clerac, R.; Holmes, S. M. *Chem. Commun.* **2010**, *46*, 4953.

(185) Zhang, Y.-Z.; Mallik, U. P.; Rath, N. P.; Clérac, R.; Holmes, S. M. *Inorg. Chem.* **2011**, *50*, 10537.

(186) Coulon, C.; Miyasaka, H.; Clérac, R. Single-Chain Magnets: Theoretical Approach and Experimental Systems; Winpenny, R., Ed.; Springer Berlin Heidelberg: New York, 2006; Vol. 122, p 163.

(187) Song, Y.; Zhang, P.; Ren, X. M.; Shen, X. F.; Li, Y. Z.; You, X. Z. *J. Am. Chem. Soc.* **2005**, *127*, 3708.

(188) Lim, J. H.; Yoon, J. H.; Kim, H. C.; Hong, C. S. *Angew. Chem., Int. Ed.* **2006**, *45*, 7424.

(189) Muetterties, E. L. *Inorg. Chem.* **1973**, *12*, 1963.

(190) Burdett, J. K.; Hoffmann, R.; Fay, R. C. *Inorg. Chem.* **1978**, *17*, 2553.

(191) Sieklucka, B.; Podgajny, R.; Przychodzeń, P.; Korzeniak, T. *Coord. Chem. Rev.* **2005**, *249*, 2203.

(192) Przychodzeń, P.; Korzeniak, T.; Podgajny, R.; Sieklucka, B. *Coord. Chem. Rev.* **2006**, *250*, 2234.

(193) Sieklucka, B.; Podgajny, R.; Pinkowicz, D.; Nowicka, B.; Korzeniak, T.; Balanda, M.; Wasiutynski, T.; Pelka, R.; Makarewicz, M.; Czapla, M.; Rams, M.; Gawel, B.; Lasocha, W. *CrystEngComm* **2009**, *11*, 2032.

(194) Sieklucka, B.; Podgajny, R.; Korzeniak, T.; Nowicka, B.; Pinkowicz, D.; Kozieł, M. *Eur. J. Inorg. Chem.* **2011**, *2011*, 305.

(195) Lim, J. H.; You, Y. S.; Yoo, H. S.; Yoon, J. H.; Kim, J. I.; Koh, E. K.; Hong, C. S. *Inorg. Chem.* **2007**, *46*, 10578.

(196) Ma, S. L.; Ma, Y.; Ren, S.; Yan, S. P.; Liao, D. Z. *Struct. Chem.* **2008**, *19*, 329.

(197) Liu, B.; Xiao, H.; Song, Y.; You, X. *Sci. China B: Chem.* **2009**, *52*, 1801.

(198) Wang, J.; Xu, Y. L.; Zhou, H. B.; Wang, H. S.; Song, X. J.; Song, Y.; You, X. Z. *Dalton Trans.* **2010**, *39*, 3489.

(199) Stefanczyk, O.; Korzeniak, T.; Nitek, W.; Rams, M.; Sieklucka, B. *Inorg. Chem.* **2011**, *50*, 8808.

(200) Podgajny, R.; Pełka, R.; Desplanches, C.; Ducasse, L.; Nitek, W.; Korzeniak, T.; Stefanczyk, O.; Rams, M.; Sieklucka, B.; Verdaguer, M. *Inorg. Chem.* **2011**, *50*, 3213.

(201) Yuan, A.-H.; Qian, S.-Y.; Liu, W.-Y.; Zhou, H.; Song, Y. *Dalton Trans.* **2011**, *40*, 5302.

(202) Nowicka, B.; Korzeniak, T.; Stefańczyk, O.; Pinkowicz, D.; Chorąży, S.; Podgajny, R.; Sieklucka, B. *Coord. Chem. Rev.* **2012**, *256*, 1946.

(203) Kania, R.; Lewinski, K.; Sieklucka, B. *Dalton Trans.* **2003**, 1033.

(204) Podgajny, R.; Korzeniak, T.; Stadnicka, K.; Dromzee, Y.; Alcock, N. W.; Errington, W.; Kruczala, K.; Balanda, M.; Kemp, T. J.; Verdaguer, M.; Sieklucka, B. *Dalton Trans.* **2003**, 3458.

(205) Li, D..; Gao, S.; Zheng, L..; Tang, W. *J. Chem. Soc., Dalton Trans.* **2002**, 2805.

(206) Li, D.; Zheng, L.; Zhang, Y.; Huang, J.; Gao, S.; Tang, W. *Inorg. Chem.* **2003**, *42*, 6123.

(207) Rombaut, G.; Golhen, S.; Ouahab, L.; Mathoniere, C.; Kahn, O. *J. Chem. Soc., Dalton Trans.* **2000**, 3609.

(208) Ma, S. L.; Ren, S. *J. Inorg. Organomet. Polym. Mater.* **2009**, *19*, 382.

(209) Ma, S. L.; Ren, S. *Synth. React. Inorg., Met.-Org., Nano-Met. Chem.* **2010**, *40*, 299.

(210) Qian, S. Y.; Zhou, H.; Zhang, Y.; Yuan, A.-H. *Z. Anorg. Allg. Chem.* **2010**, *636*, 2671.

(211) Ma, S. L.; Ren, S. *Russ. J. Inorg. Chem.* **2011**, *56*, 1390.

(212) Wang, Z. X.; Liu, B. L.; Wang, J.; Song, Y. *Inorg. Chem. Commun.* **2009**, *12*, 1179.

(213) Bok, L. D. C.; Leipoldt, J. G.; Basson, S. S. *Z. Anorg. Allg. Chem.* **1975**, *415*, 81.

(214) Zhao, H.; Clérac, R.; Sun, J. S.; Ouyang, X.; Clemente-Juan, J. M.; Gómez-García, C. J.; Coronado, E.; Dunbar, K. R. *J. Solid State Chem.* **2001**, *159*, 281.

(215) Carlin, R. L. *Magnetochemistry*; Springer-Verlag: Berlin, 1986.

(216) SMART and SAINT, Siemens Analytical X-Ray Instruments, I. Madison, WI, USA, 1996.

(217) Barbour, L. J. *J. Supramol. Chem.* **2001**, *1*, 189.

(218) Majumder, A.; Choudhury, C. R.; Mitra, S.; Marschner, C.; Baumgartner, J. *Z. Naturforsch. B* **2005**, *60*, 99.

(219) Holbrey, J.; Vigour, K.; Reichert, W. M.; Rogers, R. *J. Chem. Crystallogr.* **2006**, *36*, 799.

(220) Baker, G. A.; Rushbrooke, G. S.; Gilbert, H. E. *Physical Review* **1964**, *135*, A1272.

(221) Powell, A. K.; Heath, S. L.; Gatteschi, D.; Pardi, L.; Sessoli, R.; Spina, G.; Delgiallo, F.; Pieralli, F. *J. Am. Chem. Soc.* **1995**, *117*, 2491.

(222) Cadiou, C.; Murrie, M.; Paulsen, C.; Villar, V.; Wernsdorfer, W.; Winpenny, R. E. P. *Chem. Commun.* **2001**, 2666.

(223) Ako, A. M.; Hewitt, I. J.; Mereacre, V.; Clerac, R.; Wernsdorfer, W.; Anson, C. E.; Powell, A. K. *Angew. Chem., Int. Ed.* **2006**, *45*, 4926.

(224) Murugesu, M.; Takahashi, S.; Wilson, A.; Abboud, K. A.; Wernsdorfer, W.; Hill, S.; Christou, G. *Inorg. Chem.* **2008**, *47*, 9459.

(225) Moushi, E. E.; Stamatatos, T. C.; Wernsdorfer, W.; Nastopoulos, V.; Christou, G.; Tasiopoulos, A. J. *Inorg. Chem.* **2009**, *48*, 5049.

(226) Wang, X. Y.; Prosvirin, A. V.; Dunbar, K. R. *Angew. Chem., Int. Ed.* **2010**, *49*, 5081.

(227) Mironov, V. S.; Chibotaru, L. F.; Ceulemans, A. *J. Am. Chem. Soc.* **2003**, *125*, 9750.

(228) Mironov, V. S. *Dokl. Phys. Chem.* **2006**, *408*, 130.

(229) Palii, A.; Ostrovsky, S. M.; Klokishner, S. I.; Tsukerblat, B. S.; Dunbar, K. R. *Chem. Phys. Chem.* **2006**, *7*, 871.

(230) Palii, A. V.; Ostrovsky, S. M.; Klokishner, S. I.; Tsukerblat, B. S.; Schelter, E. J.; Prosvirin, A. V.; Dunbar, K. R. *Inorg. Chim. Acta* **2007**, *360*, 3915.

(231) Waldmann, O. *Inorg. Chem.* **2007**, *46*, 10035.

(232) Neese, F.; Pantazis, D. A. *Faraday Discuss.* **2011**, *148*, 229.

(233) Ruamps, R.; Maurice, R.; Batchelor, L.; Boggio-Pasqua, M.; Guillot, R.; Barra, A. L.; Liu, J.; Bendeif, E.-E.; Pillet, S.; Hill, S.; Mallah, T.; Guihéry, N. *J. Am. Chem. Soc.* **2013**, *135*, 3017.

(234) Zadrozny, J. M.; Xiao, D. J.; Atanasov, M.; Long, G. J.; Grandjean, F.; Neese, F.; Long, J. R. *Nat. Chem.* **2013**, *5*, 577.

(235) Craig, G. A.; Murrie, M. *Chem. Soc. Rev.* **2015**, *44*, 2135.

(236) Tsukerblat, B. S.; Palii, A. V.; Ostrovsky, S. M.; Kunitsky, S. V.; Klokishner, S. I.; Dunbar, K. R. *J. Chem. Theory Comput.* **2005**, *1*, 668.

(237) Schelter, E. J.; Karadas, F.; Avendano, C.; Prosvirin, A. V.; Wernsdorfer, W.; Dunbar, K. R. *J. Am. Chem. Soc.* **2007**, *129*, 8139.

(238) Manzer, L. E. *J. Organomet. Chem.* **1975**, *102*, 167.

(239) Burchill, P.; Wallbridge, M. G. H. *Inorg. Nucl. Chem. Lett.* **1976**, *12*, 93.

(240) Kouba, J. K.; Wreford, S. S. *Inorg. Chem.* **1976**, *15*, 2313.

(241) Antinolo, A.; Carrillo-Hermosilla, F.; Corrochano, A.; Fernandez-Baeza, J.; Lanfranchi, M.; Otero, A.; Pellinghelli, M. A. *J. Organomet. Chem.* **1999**, *577*, 174.

(242) Oshiki, T.; Mashima, K.; Kawamura, S.; Tani, K.; Kitaura, K. *Bull. Chem. Soc. Jpn.* **2000**, *73*, 1735.

(243) Otero, A.; Fernandez-Baeza, J.; Antinolo, A.; Carrillo-Hermosilla, F.; Tejeda, J.; Lara-Sanchez, A.; Sanchez-Barba, L.; Fernandez-Lopez, M.; Rodriguez, A. M.; Lopez-Solera, I. *Inorg. Chem.* **2002**, *41*, 5193.

(244) Cai, H.; Lam, W. H.; Yu, X. H.; Liu, X. Z.; Wu, Z. Z.; Chen, T. N.; Lin, Z. Y.; Chen, X. T.; You, X. Z.; Xue, Z. L. *Inorg. Chem.* **2003**, *42*, 3008.

(245) Hughes, D. L.; Leigh, G. J.; Walker, D. G. *J. Chem. Soc., Dalton Trans.* **1988**, 1153.

(246) Jungst, R.; Sekutowski, D.; Stucky, G. *J. Am. Chem. Soc.* **1974**, *96*, 8108.

(247) Sekutowski, D.; Jungst, R.; Stucky, G. D. *Adv. Chem. Ser.* **1974**, 142.

(248) Samuel, E.; Harrod, J. F.; Gourier, D.; Dromzee, Y.; Robert, F.; Jeannin, Y. *Inorg. Chem.* **1992**, *31*, 3252.

(249) Jeske, P.; Wieghardt, K.; Nuber, B. *Inorg. Chem.* **1994**, *33*, 47.

(250) Lukens, W. W.; Andersen, R. A. *Inorg. Chem.* **1995**, *34*, 3440.

(251) Castro, S. L.; Streib, W. E.; Huffman, J. C.; Christou, G. *Chem. Commun.* **1996**, 2177.

(252) Jerzykiewicz, L. B.; Utko, J.; Duczmal, M.; Sobota, P. *Dalton Trans.* **2009**, *28*, 5450.

(253) Davis, P. H.; Wood, J. S. *Chem. Phys. Lett.* **1969**, *4*, 466.

(254) Baker, J.; Figgis, B. N. *Aust. J. Chem.* **1980**, *33*, 2377.

(255) Premovic, P. I.; West, P. R. *Can. J. Chem.* **1975**, *53*, 1630.

(256) Tregenna-Piggott, P. L. W.; Gudel, H. U. *Inorg. Chem.* **2001**, *40*, 5497.

(257) Uudsemaa, M.; Tamm, T. *Chem. Phys. Lett.* **2001**, *342*, 667.

(258) Mink, J.; Nemeth, C.; Hajba, L.; Sandstrom, A.; Goggin, P. L. *J. Mol. Struct.* **2003**, *661*, 141.

(259) Schlafer, H. L.; Lenz, W.; Staab, J. *Z. Phys. Chem.* **1968**, *62*, 290.

(260) Giggenba.W; Brubaker, C. H. *Inorg. Chem.* **1969**, *8*, 1131.

(261) Nassiff, P. J.; Couch, T. W.; Hatfield, W. E.; Villa, J. F. *Inorg. Chem.* **1971**, *10*, 368.

(262) Krebs, B.; Henkel, G. *Z. Anorg. Allg. Chem.* **1981**, *474*, 149.

(263) Hinz, D. J.; Dedecke, T.; Urland, W.; Meyer, G. *Z. Anorg. Allg. Chem.* **1994**, *620*, 801.

(264) Winkelmann, M.; Welz, D.; Baehr, M.; Hinz, D. J.; Dedecke, T.; Urland, W.; Meyer, G. *J. Magn. Magn. Mater.* **1995**, *140*, 1667.

(265) Hinz, D.; Gloger, T.; Moller, A.; Meyer, G. *Z. Anorg. Allg. Chem.* **2000**, *626*, 23.

(266) Jongen, L.; Meyer, G. *Z. Anorg. Allg. Chem.* **2004**, *630*, 211.

(267) Jongen, L.; Gloger, T.; Beekhuizen, J.; Meyer, G. *Z. Anorg. Allg. Chem.* **2005**, *631*, 582.

(268) Ruiz, E.; Rodríguez-Fortea, A.; Alvarez, S.; Verdaguer, M. *Chem. - Eur. J.* **2005**, *11*, 2135.

(269) Borras-Almenar, J. J.; Clemente-Juan, J. M.; Coronado, E.; Palii, A. V.; Tsukerblat, B. S. *J. Chem. Phys.* **2001**, *114*, 1148.

(270) Levy, O.; Bogoslavsky, B.; Bino, A. *Inorg. Chim. Acta* **2012**, *391*, 179.

(271) Hein, F. H., S. *Handbook of Preparative Inorganic Chemistry*; 2 ed.; Academic Press: London, 1965.

(272) Hikichi, S.; Sasakura, Y.; Yoshizawa, M.; Ohzu, Y.; Moro-oka, Y.; Akita, M. *Bull. Chem. Soc. Jpn.* **2002**, *75*, 1255.

(273) Neese, F. *Wiley Interdiscip. Rev.: Comput. Mol. Sci.* **2012**, *2*, 73.

(274) Schafer, A.; Huber, C.; Ahlrichs, R. *J. Chem. Phys.* **1994**, *100*, 5829.

(275) Weigend, F. *Phys. Chem. Chem. Phys.* **2006**, *8*, 1057.

(276) Holmes, S. M.; Whelpley, A. S.; Girolami, G. S. *Polyhedron* **2007**, *26*, 2291.

(277) Nakamoto, K. *Infrared and Raman Spectra of Inorganic and Coordination Compounds, Part A: Theory and Applications in Inorganic Chemistry*; John wiley & Sons, Inc.: New York, 1997.

(278) Dunbar, K. R.; Heintz, R. A. Chemistry of Transition Metal Cyanide Compounds: Modern Perspectives; Karlin, K. D., Ed.; Wiley-Interscience: New York, 1997; Vol. 45, p 283.

(279) Spek, A. L. *Acta Crystallogr., Sect. C: Cryst. Struct. Commun.* **2015**, *71*, 9.

(280) Entley, W. R.; Treadway, C. R.; Wilson, S. R.; Girolami, G. S. *J. Am. Chem. Soc.* **1997**, *119*, 6251.

(281) Miller, J. S.; Epstein, A. J. *Angew. Chem., Int. Ed. Engl.* **1994**, *33*, 385.

(282) Casimir, H. B. G.; Du Pre, F. K. *Physica* **1938**, *5*, 507.

(283) Cole, K. S.; Cole, R. H. *J. Chem. Phys.* **1941**, *9*, 341.

(284) Guo, Y. N.; Xu, G. F.; Guo, Y.; Tang, J. K. *Dalton Trans.* **2011**, *40*, 9953.

(285) Chilton, N. F.; Anderson, R. P.; Turner, L. D.; Soncini, A.; Murray, K. S. *J. Comput. Chem.* **2013**, *34*, 1164.

(286) Abraham, M.; Bleaney, B. *Electron Paramagnetic Resonance of Transitions Ions*; Oxford University Press: Oxford, 2012.

(287) Griffith, J. S. *The Theory of Transition-Metal Ions*; Cambridge University Press: New York, 1961.

(288) Figgis, B. N. *Trans. Faraday Soc.* **1961**, *57*, 198.

(289) Herchel, R.; Vahovska, L.; Potocnak, I.; Travnicek, Z. *Inorg. Chem.* **2014**, *53*, 5896.

(290) Fataftah, M. S.; Zadrozny, J. M.; Rogers, D. M.; Freedman, D. E. *Inorg. Chem.* **2014**, *53*, 10716.

(291) Wernsdorfer, W. *Int. J. Nanotechnol.* **2010**, *7*, 497.

(292) Aromi, G.; Aguila, D.; Gamez, P.; Luis, F.; Roubeau, O. *Chem. Soc. Rev.* **2012**, *41*, 537.

(293) Zhang, P.; Guo, Y. N.; Tang, J. K. *Coord. Chem. Rev.* **2013**, *257*, 1728.

(294) Pedersen, K. S.; Ungur, L.; Sigrist, M.; Sundt, A.; Schau-Magnussen, M.; Vieru, V.; Mutka, H.; Rols, S.; Weihe, H.; Waldmann, O.; Chibotaru, L.; Bendix, J.; Dreiser, J. *Chem. Sci.* **2014**.

(295) Ungur, L.; Le Roy, J. J.; Korobkov, I.; Murugesu, M.; Chibotaru, L. F. *Angew. Chem., Int. Ed.* **2014**, *53*, 4413.

(296) Xie, M. H.; Liu, X. Y.; Wang, S. W.; Liu, L.; Wu, Y. Y.; Yang, G. S.; Zhou, S. L.; Sheng, E. H.; Huang, Z. X. *Chin. J. Chem.* **2004**, *22*, 678.

(297) Sheng, E.; Wang, S.; Yang, G.; Zhou, S.; Cheng, L.; Zhang, K.; Huang, Z. *Organometallics* **2003**, *22*, 684.

(298) Schuetz, S. A.; Day, V. W.; Sommer, R. D.; Rheingold, A. L.; Belot, J. A. *Inorg. Chem.* **2001**, *40*, 5292.

(299) Westerhausen, M.; Hartmann, M.; Pfitzner, A.; Schwarz, W. *Z. Anorg. Allg. Chem.* **1995**, *621*, 837.

(300) Edelmann, F. T.; Steiner, A.; Stalke, D.; Gilje, J. W.; Jagner, S.; Hakansson, M. *Polyhedron* **1994**, *13*, 539.

(301) Andersen, R. A.; Templeton, D. H.; Zalkin, A. *Inorg. Chem.* **1978**, *17*, 2317.

(302) Bradley, D. C.; Ghotra, J. S.; Hart, F. A. *J. Chem. Soc., Dalton Trans.* **1973**, 1021.

(303) Alyea, E. C.; Bradley, D. C.; Copperthwaite, R. G. *J. Chem. Soc., Dalton Trans.* **1972**, 1580.

(304) Bryan, A. M.; Long, G. J.; Grandjean, F.; Power, P. P. *Inorg. Chem.* **2013**, *52*, 12152.

(305) Eichhöfer, A.; Lan, Y.; Mereacre, V.; Bodenstein, T.; Weigend, F. *Inorg. Chem.* **2014**, *53*, 1962.

(306) Brady, E. D.; Clark, D. L.; Gordon, J. C.; Hay, P. J.; Keogh, D. W.; Poli, R.; Scott, B. L.; Watkin, J. G. *Inorg. Chem.* **2003**, *42*, 6682.

(307) Zhang, P.; Zhang, L.; Wang, C.; Xue, S.; Lin, S. Y.; Tang, J. *J. Am. Chem. Soc.* **2014**, *136*, 4484.

(308) Zhou, S. L.; Wang, S. W.; Yang, G. S.; Liu, X. Y.; Sheng, E. H.; Zhang, K. H.; Cheng, L.; Huang, Z. X. *Polyhedron* **2003**, *22*, 1019.

(309) Wu, Q. M.; Zhou, J.; Yao, Z. G.; Xu, F.; Shen, Q. *J. Org. Chem.* **2010**, *75*, 7498.

(310) Lucaccini, E.; Sorace, L.; Perfetti, M.; Costes, J.-P.; Sessoli, R. *Chem. Commun.* **2014**, *50*, 1648.

(311) Magnani, N.; Caciuffo, R.; Colineau, E.; Wastin, F.; Baraldi, A.; Buffagni, E.; Capelletti, R.; Carretta, S.; Mazzera, M.; Adroja, D. T.; Watanabe, M.; Nakamura, A. *Phys. Rev. B* **2009**, *79*.

(312) Macrae, C. F.; Edgington, P. R.; McCabe, P.; Pidcock, E.; Shields, G. P.; Taylor, R.; Towler, M.; van De Streek, J. *J. Appl. Crystallogr.* **2006**, *39*, 453.

(313) Mack, H.; Frenzen, G.; Bendikov, M.; Eisen, M. S. *J. Organomet. Chem.* **1997**, *549*, 39.

(314) Engelhardt, L. M.; Jolly, B. S.; Junk, P. C.; Raston, C. L.; Skelton, B. W.; White, A. H. *Aust. J. Chem.* **1986**, *39*, 1337.

(315) Karl, M.; Harms, K.; Seybert, G.; Massa, W.; Fau, S.; Frenking, G.; Dehnicke, K. *Z. Anorg. Allg. Chem.* **1999**, *625*, 2055.

(316) Han, F. Y.; Zhang, J.; Yi, W. Y.; Zhang, Z. X.; Yu, J. Y.; Weng, L. H.; Zhou, X. G. *Inorg. Chem.* **2010**, *49*, 2793.

(317) Casey, A.; Mitra, S. *In Theory and Applications of Molecular Paramagnetism*; John Wiley: New York, 1976.

(318) Meihaus, K. R.; Minasian, S. G.; Lukens, W. W.; Kozimor, S. A.; Shuh, D. K.; Tyliszczak, T.; Long, J. R. *J. Am. Chem. Soc.* **2014**, *136*, 6056.

(319) Bartolome, J.; Filoti, G.; Kuncser, V.; Schinteie, G.; Mereacre, V.; Anson, C. E.; Powell, A. K.; Prodius, D.; Turta, C. *Phys. Rev. B* **2009**, *80*.

(320) Aravena, D.; Ruiz, E. *Inorg. Chem.* **2013**, *52*, 13770.

(321) Avendano, C. Cyanide Bridged Molecular Magnetic Materials With Anisotropic Transition Metal Ions: Investigation of Bistable Magnetic Phenomena. Ph.D. Thesis, Texas A&M University, 2010.

(322) Charmantray, F.; Touisni, N.; Hecquet, L.; Noguer, T.; Mousty, C. *Electroanalysis* **2015**, *27*, 1341.

(323) Liu, J.; Zhou, W.; Walheim, S.; Wang, Z.; Lindemann, P.; Heissler, S.; Liu, J.; Weidler, P. G.; Schimmel, T.; Woell, C.; Redel, E. *Opt. Express* **2015**, *23*, 13725.

(324) Padigi, P.; Thiebes, J.; Swan, M.; Goncher, G.; Evans, D.; Solanki, R. *Electrochim. Acta* **2015**, *166*, 32.

(325) Scharlach, C.; Kratz, H.; Wiekhorst, F.; Warmuth, C.; Schnorr, J.; Genter, G.; Ebert, M.; Mueller, S.; Schellenberger, E. *Nanomedicine* **2015**, *11*, 1085.

(326) Wang, Q.; Wang, N.; He, S.; Zhao, J.; Fang, J.; Shen, W. *Dalton Trans.* **2015**, *44*, 12878.

(327) Yang, H.; Li, H.; Zhai, J.; Yu, H. *Chem. Eng. J. (Lausanne)* **2015**, *277*, 40.

(328) Yasutaka, T.; Tsuji, H.; Kondo, Y.; Suzuki, Y.; Takahashi, A.; Kawamoto, T. *J. Nucl. Sci. Technol.* **2015**, *52*, 792.

(329) Zakaria, M. B.; Belik, A. A.; Liu, C.-H.; Hsieh, H.-Y.; Liao, Y.-T.; Malgras, V.; Yamauchi, Y.; Wu, K. C. W. *Chem. - Asian J.* **2015**, *10*, 1457.

(330) Zhu, W.; Liu, K.; Sun, X.; Wang, X.; Li, Y.; Cheng, L.; Liu, Z. *ACS Appl. Mater. Interfaces* **2015**, *7*, 11575.

(331) Salazar, P.; Martin, M.; Garcia-Garcia, F. J.; Luis Gonzalez-Mora, J.; Gonzalez-Elipe, A. R. *Sens. Actuators, B* **2015**, *213*, 116.

(332) Zhang, P.; Zhang, L.; Tang, J. *Dalton Trans.* **2015**, *44*, 3923.

(333) Heersche, H. B.; de Groot, Z.; Folk, J. A.; van der Zant, H. S. J.; Romeike, C.; Wegewijs, M. R.; Zobbi, L.; Barreca, D.; Tondello, E.; Cornia, A. *Phys Rev Lett* **2006**, *96*, 206801.

(334) Pedersen, K. S.; Dreiser, J.; Weihe, H.; Sibille, R.; Johannesen, H. V.; Sørensen, M. A.; Nielsen, B. E.; Sigrist, M.; Mutka, H.; Rols, S.; Bendix, J.; Piligkos, S. *Inorg. Chem.* **2015**.

(335) Ungur, L.; Chibotaru, L. F. *Phys. Chem. Chem. Phys.* **2011**, *13*, 20086.

(336) Guo, Y. N.; Ungur, L.; Granroth, G. E.; Powell, A. K.; Wu, C.; Nagler, S. E.; Tang, J.; Chibotaru, L. F.; Cui, D. *Sci. Rep.* **2014**, *4*.

(337) Blagg, R. J.; Ungur, L.; Tuna, F.; Speak, J.; Comar, P.; Collison, D.; Wernsdorfer, W.; McInnes, E. J. L.; Chibotaru, L. F.; Winpenny, R. E. P. *Nat. Chem.* **2013**, *5*, 673.